Assessment of a universal nucleation and crystal growth mechanism in undercooled alloys with orthorhombic CrB-type structure

Von der Fakultät für Georessourcen und Materialtechnik
der Rheinisch-Westfälischen Technischen Hochschule Aachen

zur Erlangung des akademischen Grades eines

Doktors der Ingenieurwissenschaften

genehmigte Dissertation

vorgelegt von

Till Christian Niersbach, M.Sc.

aus Neuss

Berichter: Prof. Dr. rer. nat. Florian Kargl
Univ.-Prof. Dr.-Ing. Andreas Bührig-Polaczek

Tag der mündlichen Prüfung: 29.06.2023

To my family

Abstract

Electrostatic (ESL) and electromagnetic (EML) levitation techniques were utilized to investigate the nucleation and crystal growth in binary intermetallic melts, that solidify in CrB-type structure. The high purity alloying and subsequent contact free processing allowed the systems to stay liquid at substantial undercoolings below the equilibrium melting temperature. The subsequent nucleation event was observed in situ and the microstructure of the solid sample was analyzed by optical and electron microscopy. EBSD analysis was used to obtain a better understanding through crystal-structure evaluation on the mechanisms at play.

Binary, intermetallic ($A_{50}B_{50}$) alloys were chosen that are supposed to solidify in the orthorhombic CrB-type crystal structure. The present work bases on a special nucleation and growth mechanism, found by Kobold in $Ni_{50}Zr_{50}$. Based on these observations, the Hornfeck-Kobold-Kolbe growth model was developed, which connects a quasicrystalline (QC) core structure with a ten-fold twinned microstructure. According to the model, other n-fold symmetries are possible in CrB-structures alloys, based on their respective lattice parameters. This work assesses a part of these CrB-structured alloys in order to show the universal applicability of this model to orthorhombic systems.

Based on the prototype system of NiZr, crucial features are stated, that are necessary for nucleation and growth based on the model. Besides the singular nucleation event and the icosahedral based nucleus structure, especially the orthorhombic unit cell of the CrB-structure (B33 phase) is of importance. It was shown, that the lattice parameter ratio a/b is responsible for the n-fold symmetry, since the twinning boundaries of the model, creating ten differently orientated grains around a point symmetric center, run along the diagonal of the unit cell.

In this work, systems were chosen, based on the expected n-fold symmetry and it will focus on the investigations of the ten-fold ($Ni_{50}Hf_{50}$, $Ni_{50}Zr_{25}Hf_{25}$), nine-fold ($Ni_{50}Gd_{50}$) and eight-fold ($Ni_{50}B_{50}$) systems. It will give an analysis on whether their behavior can be described by the proposed growth model and its crucial features.

$Ni_{50}Hf_{50}$ and $Ni_{50}Zr_{25}Hf_{25}$ were chosen, since Hf and Zr are very similar and almost completely miscible. Additionally, a ten-fold growth was expected. Both systems meet the expectations as most of the crucial features are observed. These systems clearly show a singular nucleation event, the growth front can be observed in situ and connected with the front of the NiZr system. In both systems, a single growth

direction is present, with all grains orientated around one common $[001]$ direction. In NiHf however, no singular growth structure could be identified in the microstructure analysis. Instead, several smaller point-symmetric structures were found, that resemble the symmetric core structure found in NiZr. A solid-solid structural transition was found to disturb the optimal growth. Several nucleation modes are proposed in this work, and described, depending on the exact undercooling and which phase is stable upon nucleation. Only one mode, with the initial nucleation in the orthorhombic B33 phase, and two subsequent solid-solid transitions, can be connected to the growth model. With the latent heat released during nucleation, the system transitions into the high temperature (HT) B2 phase. Upon cooling, all samples transition (back) into the B33 phase. An initial nucleation in the cubic B2 phase results in different features, such as multiple growth directions. Despite the two transitions following the initial B33 nucleation (B33→B2→B33) the microstructure could preserve the singular growth direction and some of the symmetric structures that can be connected to tertiary dendrites of the growth model. In $Ni_{50}Zr_{25}Hf_{25}$, this effect is not that heavily pronounced. The solid-solid transition is present and it disturbs the microstructure. However, a singular underlying growth structure can still be identified in the microstructure. Other crucial features are met, according to the model, just as in NiHf.

$Ni_{50}Gd_{50}$ was the first system with a predicted uneven (nine-fold) symmetry. As the model is based on an icosahedral core structure, disturbances in a stable growth were anticipated. But, despite only small undercoolings reached, the system exhibits a singular common growth direction with several symmetric structures and the expected grain boundary angle. Only incomplete symmetric structures could be found, though. Due to the low undercoolings, modifications had to be made, to explain this microstructure in accordance to the proposed model. A heterogeneous growth front propagates through the melt and symmetric structures are formed regularly due to stacking faults or impurities. These nuclei can act as nucleation sites for the model's QC core structure. As these structures have to compete in growth with the general heterogeneous growth front, they take a cylindrical shape and cannot grow through the whole of the sample. This can also explain the deformations and missing orientations found.

With $Ni_{50}B_{50}$, only small undercoolings could be reached. It was however possible, to connect this system to the proposed model. A singular growth, throughout the whole sample, with the expected eight-fold symmetry was observed. The twinning

boundaries exhibit the expected grain boundary angle, but are highly distorted and shifted and it was shown, that smaller symmetries shift the atomic arrangements, which, in NiZr, extend almost perfectly along twinning boundaries and impose therefore only a small energy barrier.
Other systems were investigated with expected symmetries from 8- to 11-fold. They are shortly described in this work and evaluated. Some systems are promising and should be investigated further, others show no relation to the growth model, e.g. when they solidify in the B2 structure.

The proposed nucleation and growth model, based on the NiZr prototype system, was finally assessed, based on presence of the defined crucial features in the investigated systems. It is concluded, that the model can hold as a universal characteristic in the liquid-solid phase transition of CrB-structured alloys. Especially, the grain boundary angle with the twinning boundary running through the diagonal of the unit cell and the directly dependent n-fold symmetry are highly preserved. The growth in a single direction is another crucial feature, that is observed in basically every case. Despite this, it is often difficult to observe the perfect growth structure, as it was found in NiZr. It was shown to be highly dependent on factors, such as solid-solid transitions ($Ni_{50}Hf_{50}$), inner structural tensions ($Ni_{50}B_{50}$) or disturbances during the formation of the core structure ($Ni_{50}Gd_{50}$). Additionally, modifications were implemented to adapt the model to a broad range of nucleation events.

Kurzfassung

Elektrostatische (ESL) und elektromagnetische (EML) Levitationstechniken wurden benutzt, um die Keimbildung und das Kristallwachstum in binären Legierungsschmelzen, die nach der Erstarrung eine CrB-Struktur aufweisen, zu untersuchen. Das hoch reine Legieren und anschließendes kontaktfreies Prozessieren erlaubt es, dass die Systeme eine substantielle Unterkühlung unter die Gleichgewichts-Schmelztemperatur erreichen können. Die darauf folgende Keimbildung wurde in situ beobachtet und die Mikrostruktur der erstarrten Probe wurde mit optischer- und elektronen-basierter Mikroskopie untersucht. Eine EBSD Analyse der Kristallstrukturen wurde eingesetzt, um Rückschlüsse auf die ablaufenden Mechanismen zu ziehen.

In dieser Arbeit wurden binäre, intermetallische ($A_{50}B_{50}$) Legierungen, bei denen erwartet wird, dass sie in der orthorhombischen CrB-Struktur erstarren, ausgewählt. Dem liegt ein spezieller Keimbildungs- und Wachstumsmechanismus zu Grunde, beschrieben von Kobold in $Ni_{50}Zr_{50}$. Auf Basis dieser Beobachtungen wurde das Hornfeck-Kobold-Kolbe Wachstumsmodell enwickelt, welches einen quasikristallinen Kern mit einer zehn-zähligen, verzwillingten Mikrostruktur verbindet. Darauf basierend sind auch weitere n-zählige Symmetrien in Systemen mit CrB-Struktur, abhängig von den Gitterparametern der jeweiligen Verbindung, möglich. Diese Arbeit bewertet einen Teil dieser CrB-strukturierten Legierungen in Bezug auf die universelle Präsenz des Modells und der Behauptung, dass es sich um ein in diesen orthorhombischen Strukturen allgemein gültiges Modell handelt.

Basierend auf dem Prototyp System NiZr, wurden einige zentral ausschlaggebende Merkmale aufgestellt, die notwendig sind, um das Modell beobachten zu können. Neben der singulären Keimbildung und der Kernstruktur, die auf einem Ikosaeder beruht, ist vor allem die orthorhombische Einheitszelle von Bedeutung. Es wurde gezeigt, dass das Verhältnis der Gitterparameter a/b dafür verantwortlich ist, dass eine n-zählige Symmetrie entsteht, da die Zwillingsgrenzen, die in NiZr zehn unterschiedlich orientierte Körner um ein gemeinsames punkt-symmetrisches Zentrum bilden, auf der Diagonalen der Einheitszelle laufen.

In dieser Arbeit wurden Systeme danach ausgewählt, welche Zähligkeiten zu erwarten waren. Die Arbeit konzentriert sich hauptsächlich auf die Untersuchungen an 10-zähligem ($Ni_{50}Hf_{50}$, $Ni_{50}Zr_{25}Hf_{25}$) neun-zähligem ($Ni_{50}Gd_{50}$) und acht-zähligem ($Ni_{50}B_{50}$). Es wird anschließend analysiert, ob die beobachteten Mechanismen mit

dem vorgeschlagenen Wachstumsmodell in Einklang gebracht werden können. $Ni_{50}Hf_{50}$ und $Ni_{50}Zr_{25}Hf_{25}$ wurden zunächst ausgewählt, weil Hf und Zr fast gänzlich mischbar sind. Außerdem wurde eine zehn-zählige Symmetrie erwartet. Beide Systeme erfüllen die Erwartungen, da die meisten der ausschlaggebenden Merkmale erfüllt werden. Es wird ein singuläres Keimbildungsereignis beobachtet und die Wachstumsfront kann mit der Front von NiZr in Einklang gebracht werden. Zudem orientieren sich die Körner in beiden Systemen um eine gemeinsame $[001]$ Wachstumsrichtung. In NiHf konnten jedoch keine Korngrenzen, welche sich durch die gesamte Probe ziehen, in der Mikrostruktur gefunden werden. Stattdessen wurden mehrere kleinere punkt-symmetrische Strukturen analysiert, die der symmetrischen Wachstumsstruktur von NiZr vollständig gleichen. Es wurde eine Festkörperumwandlung ausgemacht, die das optimale Wachstum dieses Modells stört. Mehrere Keimbildungsarten wurden in dieser Arbeit vorgeschlagen und beschrieben. Diese hängen im Wesentlichen von der erreichten Unterkühlung und damit von der stabilen Phase im Moment der Keimbildung ab. Nur eine Art konnte mit dem Wachstumsmodell in Einklang gebracht werden. In dieser bildet sich zunächst ein Keim in der orthorhombischen B33 Struktur, welcher dann zwei Festkörperumwandlungen passieren muss. Mit dem Freiwerden der latenten Wärme während der Keimbildung, wandelt sich diese Struktur in die Hochtemperatur (HT) B2 Phase um. Beim späteren Abkühlen erfolgt dann wieder die Rückumwandlung in die B33 Phase. Eine initiale Keimbildung der B2 Phase führt zu anderen Merkmalen, wie u.a. vielen verschiedenen Wachstumsrichtungen. Trotz der Festkörperumwandlungen nach der eigentlichen B33 Erstarrung (B33→B2→B33) konnten die einheitliche Wachstumsrichtung und einige der symmetrischen Strukturen, die mit den tertiären Dendriten des Wachstumsmodells beschrieben werden können, erhalten werden. In $Ni_{50}Zr_{25}Hf_{25}$ ist dieser Effekt weniger stark ausgeprägt. Die Umwandlung ist vorhanden und sie verzerrt ebenfalls die Mikrostruktur. Dennoch konnte eine zugrunde liegende Wachstumsrichtung in der gesamten Struktur beobachtet werden. Die weiteren Merkmale decken sich mit NiHf.

$Ni_{50}Gd_{50}$ ist das erste untersuchte System, dass eine ungerade (neun-zählige) Symmetrie aufweisen soll. Da das Modell auf einer ikosaedrischen Kernstruktur beruht, waren Beeinträchtigungen eines stabilen Wachstums erwartbar. Trotz geringer erreichter Unterkühlungen konnte die erwartete gemeinsame Wachstumsrichtung und die Orientierung um diese Richtung mit dem erwarteten Korngrenzenwinkel beobachtet werden. Es konnten allerdings nur unvollständige symmetrische Struk-

turen ausgemacht werden. Das Modell musste entsprechend modifiziert werden um die Beobachtungen in Einklang zu bringen. Eine heterogene Wachstumsfront wächst durch die Schmelze und es werden regelmäßig, durch Stapelfehler oder Verunreinigungen, die als Keimbildner agieren, symmetrische Strukturen gebildet, auf denen die quasikristalline Kernstruktur des Wachstumsmodells aufbaut. Da diese Strukturen mit der allgemeinen Wachstumsfront konkurrieren, nehmen sie eine zylindrische Form an und sind in ihrer Ausdehnung begrenzt. Dies erklärt ebenso, dass es bei der Zähligkeit zu Fehlern kommen kann und nur unvollständige und deformierte Strukturen beobachtet wurden.
Mit $Ni_{50}B_{50}$ konnten nur kleine Unterkühlungen erreicht werden. Es war jedoch möglich, dieses System dem Wachstumsmodell zuzuordnen, da ein singuläres Wachstum, mit einem symmetrischen Zentrum, durch die ganze Probe, beobachtet wurde. Die Zwillingsgrenzen zeigen den erwarteten Winkel, sind jedoch stark verzerrt und deplatziert. Es wurde gezeigt, dass kleinere Symmetrien atomare Positionen verschieben. In NiZr gibt es symmetrische Elemente, die über die Zwillingsgrenze hinaus abgebildet werden können. Mit abnehmender Symmetrie gibt es eine größere Abweichung, die in einer höheren Energiebarriere resultiert.
Weitere Systeme mit erwarteten Symmetrien von acht- bis elf-zählig, wurden analysiert. Diese werden kurz beschrieben, da einige vielversprechende Ergebnisse für zukünftige Arbeiten zeigen. Andere sind für das Wachstumsmodell nicht relevant, da sie z.B. in der kubischen B2 Phase erstarren.

Das vorgeschlagene Keimbildungs- und Wachstumsmodell, basierend auf dem Prototypen System NiZr, wurde abschließend bewertet. Basierend auf den definierten ausschlaggebenden Merkmalen wurden die benannten Systeme analysiert und mit dem Modell verbunden. Daraus kann gefolgert werden, dass das Model als universelle Charakteristik in Flüssig-Fest Phasenumwandlungen von CrB-strukturierten Systemen vorhanden ist. Vor Allem der Korngrenzenwinkel mit der Zwillingsgrenze, die in der Diagonalen der Einheitszelle läuft und die direkt davon abhängige Zähligkeit sind hoch erhalten und sind, zusammen mit der gemeinsamen Wachstumsrichtung, immer zu beobachten. Dennoch ist es schwierig, einen optimalen Ablauf, wie in NiZr, zu beobachten. Es wurde gezeigt, dass dies stark von Faktoren, wie einer Festkörperumwandlung ($Ni_{50}Hf_{50}$), inneren strukturellen Spannungen ($Ni_{50}B_{50}$) oder Beeinträchtigungen während der Ausbildung der Struktur ($Ni_{50}Gd_{50}$), abhängt.

Contents

Nomenclature

Roman alphabet

a_0	interatomic spacing
$\vec{B}$	magnetic field
B	magnetic flux density
b	Burgers vector
C	composition
C_p	specific heat capacity
C^*	ratio factor
D	diffusion coefficient
d	distance
d_0	capillary constant
$\vec{E}$	electrostatic field
$\vec{e}$	unit vector
$\vec{F}$	force
G	thermodynamic potential, Gibbs free energy, free enthalpy
G^*	efficiency ratio
H	enthalpy
I	spectral radiance
$I(t)$	nucleation rate
K_V	pre-exponential factor for nucleation rate
m	atomic mass
N	particle number
n	integer
P	power
p	pressure
Q	heat
q	charge
R	dendrite tip radius
R_g	gas constant
r	radius
r_{eq}	minimal distance to central atom
r^*	critical radius
S	entropy
t	time
T	temperature
T_L	liquidus temperature
T_m	melting temperature
T_S	solidus temperature
T_{SST}	transition temperature of a SST
T_i	interface temperature
U	internal energy

U_z	voltage
V	volume
v	growth velocity
V_{mol}	molar volume

Greek alphabet

α_T	thermal diffusivity
Γ	Gibbs-Thompson coefficient
γ	geometric angle regarding the ratios of the decagonal body
δ	path difference
δ^*	magnetic skin depth
ΔC	concentration change
ΔG_{SL}	change of the Gibbs free energy
ΔG_r	energy balance
ΔG^*	energy barrier
ΔH_f	enthalpy of fusion
ΔH_{SL}	difference in enthalpy
ΔS_f	entropy of fusion
ΔS_{SL}	difference in entropy
ΔT	undercooling
ΔT_{hyp}	hypercooling limit
ϵ	anisotropy of the interface energy
ϵ_T	hemispherical emissivity
ϵ_0	vacuum permittivity
ϵ_λ	emissivity
η	viscosity
Θ	wetting angle
θ	scattering angle
κ	geometrical factor
λ	wavelength
λ^*	interatomic spacing
μ	chemical potential
μ_0	magnetic permeability
μ^*	kinetic undercooling coefficient
ν	frequency
ξ_T	thermal stability function
ρ	density
σ	interfacial energy
σ_B	Stefan-Boltzmann constant
σ_c	conductivity

τ	geometric constant
υ_0	atomic vibration frequency
ϕ	B33 unit cell angle
X	atom concentration
ω	angular frequency

Crystallographic notations

$[hkl]$	specific crystallographic direction
$\langle hkl \rangle$	set of all crystallographic directions equivalent to $[hkl]$
(hkl)	specific crystallographic plane
$\{hkl\}$	set of all crystallographic planes equivalent to (hkl)

Crystallographic structures

B2	cubic structure, based on the CsCl-prototype
B33	orthorhombic structure, based on the CrB- (or TlI)-prototype

Both structures are described and frequently stated in this work, often denoted as *phase*. Their crystallographic parameters are listed in detail in App. 1.

Abbreviations

BSD	backscatter detector
DB	decagonal body, denotation for the *dbp* in this work
dbp	decagonal bi-pyramid
DSC	differential scanning calorimetry
EBSD	electron backscatter diffraction
EML	electromagnetic levitation
EDS	energy dispersive X-ray spectroscopy
ESL	electrostatic levitation
FL method	First Frame - Last frame method to analyze growth velocities
FSD	forward scatter detector
fps	frames per second
GBA	grain boundary angle
HKK	Hornfeck-Kobold-Kolbe model
HSC	high-speed camera
HT	high-temperature

IPF	inverse pole figure
ISRO	icosahedral short-range order
LST	liquid-solid phase transition
MS	microstructure
OM	optical microscopy
PF	pole figure
PSD	position sensitive detector
QC	quasicrystal
RT	room temperature
SEM	scanning electron microscope
SST	structural solid-solid phase transition
SRO	short-range order
TEMPUS	**T**iegelfreies **E**lektro-**M**agnetisches **P**rozessieren **U**nter **S**chwerelosigkeit - μg levitation experiment on parabolic flights
TTP	temperature-time plot
UHV	ultra-high vacuum

CHAPTER 1

Introduction

The law of the conservation of energy states, that the energy of an isolated system is always constant. Energy cannot be created, nor can it be destroyed. It can only be transformed into different forms. The second law of thermodynamic states, that any isolated system in equilibrium reached a state of a maximal entropy for the given internal energy. All elements and their combinations follow these fundamental laws. If external energy is transferred into the system it will change its internal energy and the system has to adapt to a new equilibrium state. In real systems, this will ultimately result in transitions into a different form of matter. This phase change is initiated by nucleation; a phenomenon that forms the new phase within the parent phase and is present in a multitude of phase changes [1]. One prominent example would be the gas nucleation of bubbles in boiling water.

The realization, that these changes can be delayed, as pure water was undercooled below its freezing temperature by Fahrenheit in the 18^{th} century [2], and the observations that metallic melts can be undercooled significantly below their equilibrium melting temperatures [3], opened an entirely new field of basic research. In a general approach, most metallic melts can be undercooled around $\Delta T_{\text{max}} / T_L = 0.18$ [4]. Despite a first description of nucleation by Volmer & Weber in 1926 [5], the phenomenon is still not understood in all its depth. Undercooled melts energetically favor the growth of dendrites, tree-like structures solidifying in branches through the melt, as they have a more advantageous heat and mass distribution in the liquid-solid system. They propagate in crystallographic directions, characteristic in each crystal system, and are therefore crucial in understanding the solidification and shaping of the microstructure of a given system [6, 7].

Undercooling of metallic systems and the subsequent solidification process can be observed with containerless processing techniques, such as levitation, where the gravitational force is compensated, e.g. by electrostatic or electromagnetic forces. If this is combined with high purity elements, heterogeneous nucleation can be avoided to a certain degree, that is sufficient to reach substantial undercoolings below the equilibrium melting temperature. The solidification process can be observed in situ with a high-speed camera and the propagation and shape of the solidification front can be used to deduct the crystallographic growth directions of the dendrites. A macroscopic geometrical shape

can be spanned by the dendrites and with the knowledge of characteristic growth directions, the crystal system can be deducted with simulation software.
The phenomenon of undercooling is essentially the expression of an energy barrier, that needs to be overcome to start the phase change. This energy barrier comes from the reordering of atoms into a solid structure. The atomic arrangement was first connected to dendritic growth by Kepler in 1611, as he questioned if the hexagonal shape of snowflakes has its root in the hexagonal layering of close packed spheres [8]. He further assumed, that such an arrangement must be the tightest occupation of space possible. Regarding metals, this assumption was proven mathematically to hold true and to have a space occupation of around 74% [9]. Metals are commonly modeled by hard spheres, since the metallic bonding favors more direct neighbors. Two of the three most common packing types for periodic arrangements have this maximum volume occupancy. Namely these are the face-centered cubic (fcc), the hexagonal close packed (hcp) arrangements and the body-centered cubic (bcc) with an occupancy of around 68%. More condensed structures can only be realized locally and without the full degree of periodicity.
The highest local symmetry is expressed by the icosahedron, which is an arrangement of 12 atoms around a central one. It has a five-fold symmetry and is as such incompatible with the periodic crystal lattice. It was therefore postulated already 70 years ago by Frank, that icosahedrons are present in metallic melts [10]. If the order of the liquid phase differs substantially from the crystal structure of the solid phase, a high energy barrier must be overcome to initiate the nucleation process. Icosahedrons are not strictly necessary to impose a high energy barrier, but they are commonly observed and serve for the basic idea of a short-range order of atoms in the melt that differs from the crystal ordering in the solid phase [11–13].
With the classical crystallographic restriction theorem it was stated, that every crystal lattice can be described with the mathematical restriction on 2-, 3-, 4- and 6-fold rotational symmetry. These are the only symmetric patterns, that can fill space entirely, while also retaining a translational symmetry. These restrictions were extended by the discovery of a five-fold diffraction pattern in quenched Mn-Al specimens by Shechtman in 1984 [14]. After decades of dispute, whether these observations were not just a mechanism of five-fold twinning, it is now an accepted intermediate state between crystalline and amorphous solids. These solids are called quasicrystals and exhibit only a long range rotational order, but no translational symmetry. They are found in various binary and ternary systems, since their discovery. Due to their five-fold symmetry, they are usually connected with low possible undercoolings, since metallic melts often have the icosahedral short-range order.

Hornfeck, Kobold and Kolbe, connected a quasicrystalline nucleation and core structure with a subsequent transition to a crystalline lattice [15], based on the observations made by Kobold in the binary $Ni_{50}Zr_{50}$ system [16]. Molten NiZr has no icosahedral short-range order and it was possible to reach undercoolings, where homogeneous nucleation was observed [17]. The solidification of NiZr revealed a ten-fold growth front and a point symmetric (2D) growth in its microstructure. The ten-fold symmetry is based on twinned dendrites. Each dendrite constitutes a grain boundary in its stem, which are angled by 36° to each other. According to these observations, an atomic model was designed to connect a quasicrystalline core structure with a subsequent ten-fold twinned microstructure.

In this work, the nucleation and growth model, based on the NiZr system, is assessed on its existence and relevance in other CrB-structured systems. Based on the lattice parameter ratio a/b, of the orthorhombic unit cell in the CrB-type structure, other symmetries can be expected for different alloys. With this ratio, symmetries for 8-fold to 11-fold should be possible, based on the orthorhombic unit cell. For the quantitative assessment, crucial features are defined, that are based on the NiZr-prototype system. Several CrB-structured alloy systems are evaluated based on these features, to conclude whether the model is a universal nucleation and growth mechanism in orthorhombic CrB-type systems.
The solid-solid phase transition between the high-temperature cubic B2 phase and the orthorhombic B33 (CrB-type) phase exists in most of the investigated systems. Its influence on the nucleation and growth mechanism, and the microstructure of respective systems, is discussed with respect to the $Ni_{50}Hf_{50}$ system. For NiHf, the solid-solid transition temperature lies in the vicinity of the reached undercoolings. It was therefore possible to trigger different kinds of nucleation and subsequently also transitions. With these findings, it was possible, to reconstruct the initially grown structure within the microstructure, that was present after the transition.

CHAPTER 2

Crystal growth of undercooled melts

This thesis analyses the transitions between different states of matter. A state is changed when it is energetically favorable for a given system. Within certain conditions however, these changes can be delayed. Almost 300 years ago, in 1724, Fahrenheit [2] observed that water can cool down below it's equilibrium melting temperature, up to 4 K below, for long time periods and still remain liquid. But, as soon as it is disrupted by an air flow or ice crystals, it will suddenly become a solid; it transitions into a different phase. The difference between the equilibrium melting temperature T_L and the actual temperature T of the liquid system is called the undercooling[1] $\Delta T = T_L - T$. Thereafter, the undercoolability of liquids was thoroughly studied. Turnbull established that many metallic melts, as well as alloys, can be deeply undercooled - to about $\Delta T_{\max}/T_L = 0.18$ [4]. With improving technology, this ratio rises. In this work, it was possible to reach $\Delta T/T_L \approx 0.26$.

This chapter gives the essential theoretical background on thermodynamics of undercooled liquids and the mechanics of nucleation for binary alloys. In the first section, the thermodynamic potential is discussed in context of equilibrium conditions. It is shown how different thermodynamic variables and the influence of elemental compositions can be plotted to form phase diagrams and deduct equilibrium melting temperatures for alloys. Sec. 2.2 introduces the concepts of nucleation and the solidification from non-equilibrium conditions. It covers the intrinsic homogeneous, as well as the extrinsic heterogeneous type of nucleation. The following sections will also introduce the concept of atomic short-range order, the implication of interfaces, the dendritic crystal growth and the concept of solid-solid structural transitions. At last, it will also shortly discuss the concept of diffraction.

1 Undercooling may also be referred to as *supercooling*.

2.1 Thermodynamics

2.1.1 Liquid-solid phase transition

The driving force of a phase transition is the thermodynamic potential G, which is also called the Gibbs free energy or free enthalpy. In a closed system the minimum of the Gibbs free energy defines a stable equilibrium. A change of intensive conditions, such as temperature or pressure, leads to different global minima of G and induces phase transitions. For a one-component system G can be calculated, using isothermal and isobaric conditions as well as a constant particle number N, by

$$G(T,p,N) = H(T,p,N) - TS(T,p,N). \tag{2.1}$$

H describes the enthalpy of the system, which is the sum of it's internal energy U and the product of it's pressure p and volume V ($H = U + pV$). The entropy S is a fundamental thermodynamical property and can be understood as a measure for the disorder within a system. For low temperatures, the system will favor a solid configuration as the internal energy is lowest when atoms are bound to each other. At high temperatures, the $-TS$ part dominates the equation and configurations with higher entropy (liquids and gases) will be favored.

The phase transition is visualized based on the thermodynamic potential in Fig. 2.1 (a). It shows the Gibbs free energy for a liquid (G_L) and for a solid (G_S) phase and their dependence on the temperature. It is assumed that both configurations exist at any temperature. In Fig. 2.1 (b) the enthalpies of the liquid (H_L) and the solid (H_S) phase are presented, depending on the temperature as well. The slopes of the functions in (a) correspond to the entropies of the liquid (S_L) and solid (S_S) phases ($S = -(\delta G/\delta T)_p$). In (b) they depend on the specific heat capacity of the liquid (c_p^L) or solid (c_p^S) phases ($c_p = (\delta G/\delta T)_p$). The change of enthalpy between the liquid and the solid phase in (b) is called the enthalpy of fusion ΔH_f. In (a) the different slope of both phases is described as the entropy of fusion ΔS_f. The liquid phase G_L has higher entropy and therefore decreases more rapidly as the temperature increases. This leads to the intersection of both curves, after which, the Gibbs free energy of the liquid phase is lower than the one of the solid phase. The point of intersection is called the equilibrium melting temperature T_m. Since $G_L < G_S$, the liquid phase is favored at temperatures above T_m. The opposite is true for temperatures below T_m, as $G_L > G_S$. If the temperature of the

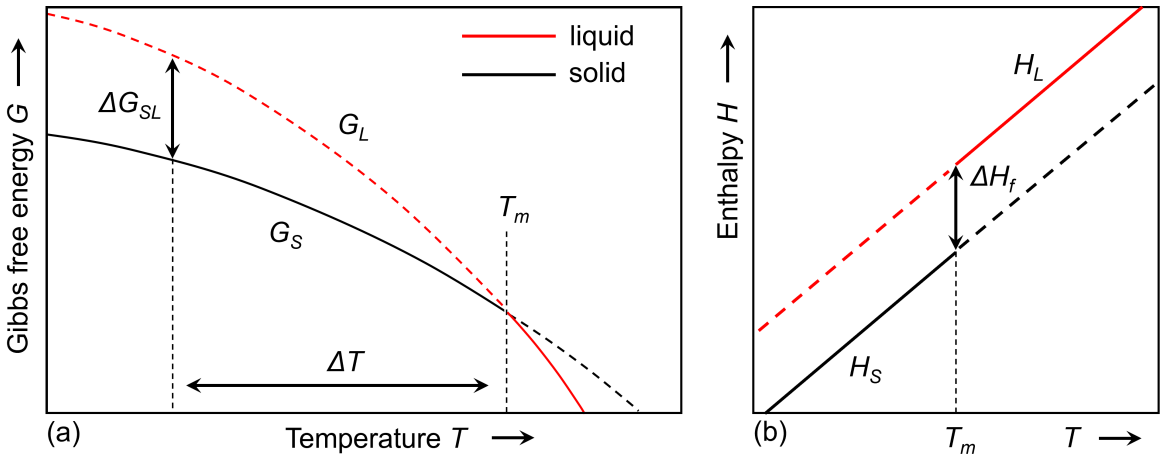

Fig. 2.1: (a) Gibbs free energy G as a function of temperature T. The intersection of the liquid (G_L) and the solid (G_S) phase defines the equilibrium melting temperature (T_m) of the system. **(b)** Enthalpy H as a function of temperature T. At the system's melting temperature T_m the enthalpy increases by the latent heat of fusion ΔH_f.

system is decreased below T_m, but the liquid state persists, it exists in a metastable state. The system is now described as an undercooled liquid with $\Delta T = T_m - T$. Fig. 2.1 (a) also illustrates that the difference between the Gibbs free energy of the solid and the liquid phase (ΔG_{SL}) increases with a rising undercooling ΔT. ΔG_{SL} is the driving force for solidification since the transition to the solid state would decrease the Gibbs free energy of the system:

$$\Delta G_{SL}(T) = \Delta H_{SL}(T) - T\Delta S_{SL}(T) \tag{2.2}$$

with the difference in enthalpy

$$\Delta H_{SL}(T) = \Delta H_f - \int_T^{T_m} \Delta C_p(T) dT \tag{2.3}$$

and the difference in entropy

$$\Delta S_{SL}(T) = \Delta S_f - \int_T^{T_m} \frac{\Delta C_p(T)}{T} dT. \tag{2.4}$$

ΔC_p describes the specific heat difference between the liquid (ΔC_p^L) and the solid (ΔC_p^S) phase. At T_m the difference of the Gibbs free energies is $\Delta G_{SL} = 0$. Therefore, Eq. 2.2 can be expressed as

$$\Delta H_f = T_m \Delta S_f. \tag{2.5}$$

$\Delta G_{SL}(T)$ can now be expressed as

$$\Delta G_{SL}(T) = \Delta H_f \frac{\Delta T}{T_m} - \int_T^{T_m} \Delta C_p(T) dT + \int_T^{T_m} \frac{\Delta C_p(T)}{T} dT. \tag{2.6}$$

For small temperature changes ΔH and ΔS can be assumed constant [4] and ΔG_{SL} can be written as

$$\Delta G_{SL} = \Delta H_f \frac{\Delta T}{T_m} = \Delta S_f \Delta T \tag{2.7}$$

The driving force hence rises proportional to the entropy of fusion and the undercooling ΔT. This is, however, only a first approximation, since ΔC_p is temperature dependent. It is difficult to determine in undercooled melts, still, there are multiple models to get reliable estimates of ΔG_{SL} in undercooled regimes [18–20]. The specific heat difference of pure metallic melts typically only shows small changes [21] and Eq. 2.7 can be used to determine sufficient values for the changes of the Gibbs free energy at low undercoolings [22]. However, the change of the specific heat is not zero. Eq. 2.6 must be changed into

$$\Delta G_{SL}(T) = \Delta H_f \frac{\Delta T}{T_m} - \Delta C_p \left[\Delta T - T \ln\left(\frac{T_m}{T}\right) \right]. \tag{2.8}$$

An assumption made by Jones and Chadwick [18] sets the specific heat difference as the respective one at T_m. This has the advantage to determine $\Delta C_p(T_m)$ through thermoanalytical methods. The Gibbs free energy change can then be written as

$$\Delta G_{SL}(T) = \Delta H_f \frac{\Delta T}{T_m} - \Delta C_p(T_m) \frac{(\Delta T)^2}{T_m + T}. \tag{2.9}$$

2.1.2 Binary systems

In binary systems an additional thermodynamic variable needs to be considered, besides temperature and pressure. The composition n_i (number of atoms of the respective component i) is essential as the interaction between different atoms can influence the Gibbs free energy of a mixture (ΔG_{mix}) It can vary due to an increase of the entropy of mixing ΔS_{mix} (which describes the difference between mixed and unmixed states) and the addition of the enthalpy of mixing ΔH_{mix} (which corresponds to the released heat from mixing), resulting in

$$\Delta G_{\text{mix}} = \Delta H_{\text{mix}} - T \Delta S_{\text{mix}}. \tag{2.10}$$

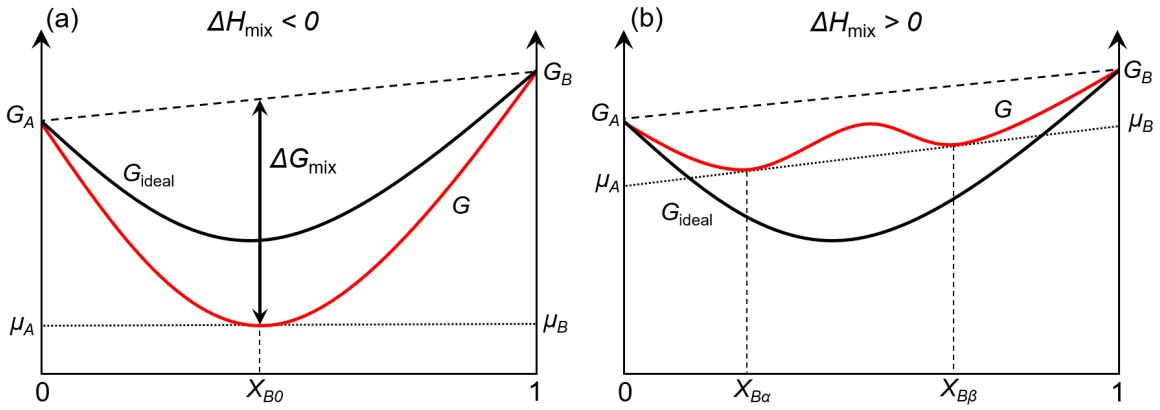

Fig. 2.2: Plots of the Gibbs free energy over the composition. **(a)** illustrates the case of a negative enthalpy of mixing for an ideal and a regular (red) solution. **(b)** shows that a positive enthalpy term can influence the Gibbs free energy resulting in two minima on the curve. With the construction of a common tangent it can be visualized that both phases coexist in equilibrium.

Fig. 2.2 illustrates the Gibbs free energy change for a binary system with (a) negative and (b) positive enthalpies of mixing. With the tangent construction from [23] applied at the local minimum, the chemical potentials μ_A and μ_B can be derived. At $\mu_A = \mu_B$ the slope of G is zero and equilibrium conditions are reached. With positive values for the enthalpy of mixing the Gibbs free energy can develop two minima. Any composition between these minima at $X_{B\alpha}$ and $X_{B\beta}$ separates into two coexisting phases in equilibrium which minimizes the total free energy in the system. Looking further at different phases, the minimum of the total Gibbs free energy is found at the common tangent of the liquid (G_L) and the solid (G_S) phase, which is presented in Fig. 2.3 (a). The respective chemical potentials for the solid and the liquid phase are equal at this temperature. It shows further, that, in equilibrium, compositions of $X < X_{BS}$ are solid, compositions of $X > X_{BL}$ are liquid and in compositions between these values both phases coexist. These tangents and the consequent analysis can be done for a range of temperatures so that stable phases and compositions are identified and plotted in diagrams, that show the temperature over the composition. These are called equilibrium phase diagrams as they translate the local minima of the Gibbs free energy into a composition of stable phase. An idealized section of such a diagram is shown in Fig. 2.3 (b), arranged to show the same composition as the previous figure. The solidus (m_S) and the liquidus (m_L) define the separation between stable phases. A system with the initial composition C_0 will begin solidification when it is cooled slightly below the respective liquidus temperature $T_L(C_0)$. It then has the composition C_S. However, ongoing decrease in temperature leads to a change of the

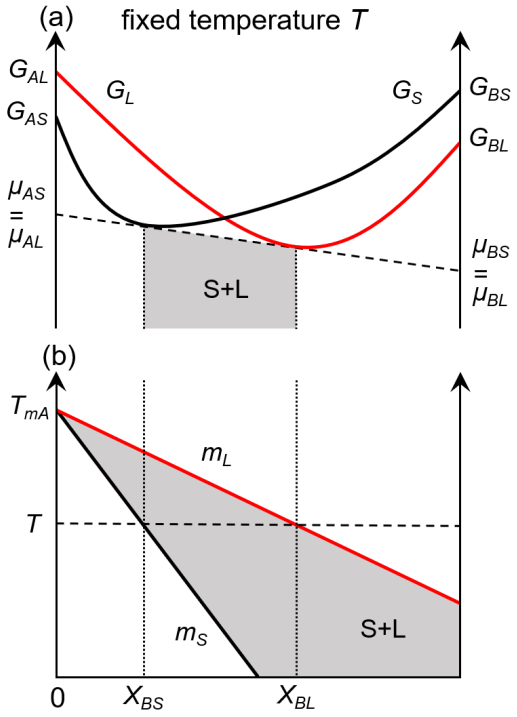

Fig. 2.3: (a) Solid (G_S) and liquid (G_L) Gibbs free energy curves at a fixed temperature. Stable phases and a region with both phases coexisting in equilibrium are indicated by the tangent construction. The respective chemical potentials are equal in this construction. **(b)** Idealized equilibrium phase diagram that visualizes the stable phases for a range of temperatures. The phases are separated by the solidus (m_S) and liquidus (m_L) lines. Illustrations after [23].

composition along solidus or liquidus line. This difference between solid and liquid phase composition is expressed by the partition coefficient $k = C_S/C_L$. It is necessary in order to calculate the solid (f_S) and liquid (f_L) fractions for a specific temperature. This is done by applying the lever rule by

$$f_S = \frac{C_L - C_0}{C_L - C_S} = \frac{C_L - C_0}{(1-k)C_L} \quad \text{and} \quad f_L = \frac{C_0 - C_S}{C_L - C_S} \tag{2.11}$$

with $f_S + f_L = 1$ for binary systems. Idealizing solidus and liquids lines as straight lines (with the slopes m_S and m_L) is useful to calculate the respective compositions for a given temperature via

$$C_L = \frac{T - T_m}{m_L} \quad \text{and} \quad C_S = \frac{T - T_m}{m_S}. \tag{2.12}$$

Consequently, the respective fractions can now be expressed for any temperature with

$$f_S = \frac{T_L(C_0) - T}{(1-k)(T_m - T)}. \tag{2.13}$$

These equations assume, that each phase is in equilibrium. There is enough time for all phases to reach steady-state conditions by diffusion. In reality, this is basically never the case with time being the limiting factor, especially in rapid solidification. Metastable or non-equilibrium phases may be created [24]. When kinetic processes govern, solidifica-

tion might not result in a state of minimal energy, which is not necessarily unstable, but metastable. Energy is not sufficient to transition into a more stable phase, so these states are *frozen*. It requires additional energy to overcome an activation barrier to transform them into a low energetic and stable state.

2.2 Nucleation theory

Temperature is the driving force of all atomic motions. At *absolute zero*[2] all vibrational motion of atoms is at a fundamental minimum. It is the lowest limit of the thermodynamic temperature scale and, referred to an ideal gas, enthalpy and entropy reach their minimum values as well. With rising temperatures phase changes become possible as described previously. Within liquid phases there is an additional movement of atoms, called the *Brownian motion*. In contrast to the solid phase, where bonding between atoms dominates, atoms in a liquid can move freely through the medium. This typically results in a pattern of statistical approaches between atoms creating a fluctuation to the density when several atoms cluster. Such atomic clusters may form spontaneously and can have a solid-like interatomic spacing. Solidification can therefore be initialized from these clusters.
Historically, Volmer and Weber were the first to describe the processes of nucleation in liquid phases phenomenological in 1926 [5]. Becker and Döring followed in 1935 with investigations on nucleation from supersaturated vapors [25]. The fundamentals of nucleation theory were then developed further to condensed matter by Zeldovich [26], as well as Turnbull and Fisher [3, 4]. Nucleation can occur as an intrinsic process, then called *homogeneous nucleation*, which is solely dependent on material parameters. When the influences of an impurity phase, e.g. a crucible wall, act as nucleation catalyst, the process is then called *heterogeneous nucleation*.

2.2.1 Homogeneous nucleation

Atomic clusters will decompose almost instantaneously if the temperature of the system is above its melting temperature ($T > T_m$). When a liquid system cools below the equilibrium melting temperature ($T < T_m$) it will not solidify immediately but remain in this

2 The absolute zero is set to $T = 0$ K or -273.15 °C.

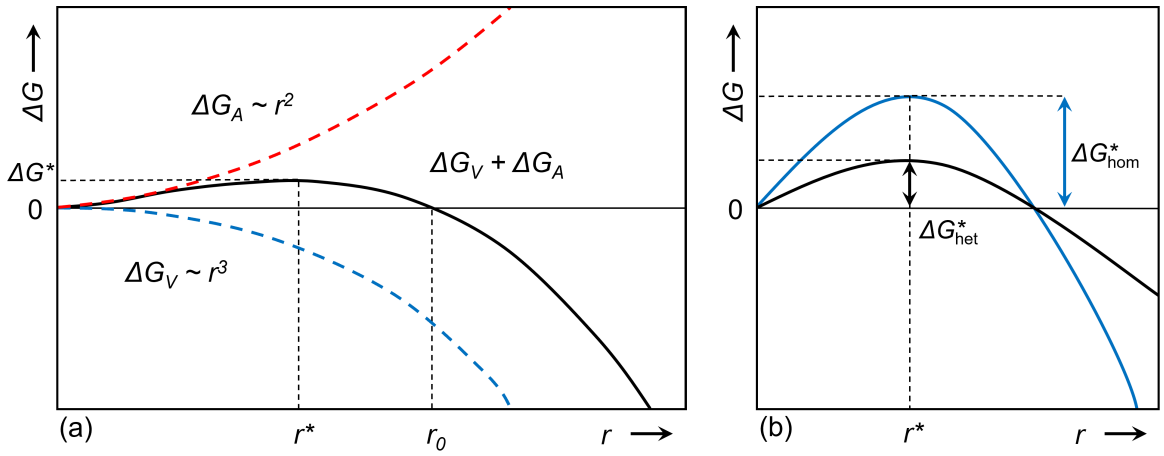

Fig. 2.4: Energy barrier ΔG^* that needs to be overcome at r^* for nucleus formation. **(a)** Plot of the Gibbs free energy difference ΔG over the cluster radius r (black line). Volume energy gain ΔG_V and surface contribution ΔG_A (dashed red and blue lines). **(b)** Comparison between the energy barrier for homogeneous (blue) and heterogeneous (black) nucleation.

meta-stable state. As shown in Fig. 2.1, the energy ΔG_{SL} becomes negative, implying that the system gains energy from forming atomic, solid-like clusters. The energy gain ΔG_V is proportional to ΔG_{SL} and the volume V of the cluster. The formation of such clusters is a physical separation from the liquid phase and makes it necessary to create an interface between both phases. The interface energy is called ΔG_A and is proportional to the (positive) interfacial energy σ and the surface of the interface. With the assumption that solid-like clusters are spherical configurations with a radius r and have an interface of infinitesimal thickness, the energy balance $\Delta G(r)$ is given by

$$\Delta G(r) = \Delta G_V + \Delta G_A = -\frac{4}{3} \cdot \pi \cdot r^3 \cdot \frac{\Delta G_{SL}}{V_{\mathrm{mol}}} + 4 \cdot \pi \cdot r^2 \cdot \sigma \tag{2.14}$$

with V_{mol} as the molar volume and the solid-liquid interfacial energy σ. Fig. 2.4 (a) plots the change of the Gibbs free energy difference over the increasing radius of a cluster. Also shown are the surface contribution (red) with $\Delta G_A \sim r^2$ and the volume energy gain (blue) with $\Delta G_V \sim r^3$. The change of the Gibbs free energy is the sum of both competing contributions. With increasing radius, $\Delta G(r)$ reaches a maximum at the critical radius r^*. The energy barrier ΔG^* needs to be overcome by any atomic cluster to create a nucleus and set off solidification. By setting the derivative $\Delta G'(r)$ of Eq. 2.14 to zero, the critical radius r^* can be written as

$$r^* = 2 \cdot \frac{\sigma V_{\mathrm{mol}}}{\Delta G_{SL}}. \tag{2.15}$$

For $r < r^*$ the system can decrease its free energy with the shrinking of clusters. A

decomposition of these, so called, embryos is most likely. When $r > r^*$ the system can reduce its free energy by growing as the volume contribution predominates. The clusters are then called nuclei. By substituting r^* for r in Eq. 2.14 the activation energy ΔG^* can be expressed as

$$\Delta G^* = \frac{16}{3}\pi \cdot \left(\frac{\sigma^3 V_{\text{mol}^2}}{\Delta G_{SL}^2} \right) \tag{2.16}$$

and the number of atoms that need to agglomerate to form a nucleus is given by

$$n^* = \frac{4\pi N_A}{3V_{\text{mol}}} r^{*3}. \tag{2.17}$$

The undercoolability of liquids is a direct consequence of an activation energy that must be overcome to form a nucleus of critical size. The scale of undercooling of a given system depends on ΔG^* as well. A higher barrier leads to higher undercoolings.

2.2.1.1 Nucleation rate

Volmer and Weber [5] were the first to introduce estimations on the formation rate of critical nuclei. They introduced the nucleation rate $I(t)$. It gives the frequency of cluster formation (clusters with $r > r^*$), when a sufficient amount of atoms is present $n > n^*$ as

$$I(t) = K_{n^*}^+ N_{n^*}(t) - K_{n^*+1}^- N_{n^*+1}(t), \tag{2.18}$$

with the atomic attachment rate $K_{n^*}^+$. The number of clusters N_n that have n atoms per unit of volume follows a Boltzmann distribution and is expressed as

$$N_n = \frac{N_A}{V_{\text{mol}}} \exp\left(-\frac{\Delta G_n}{k_B T} \right). \tag{2.19}$$

$G(n)$ describes the required energy to form a cluster with n atoms per unit of volume. Volmer and Weber further assumed that at $n > n^*$ clusters start to grow into the melt continuously and therefore they are ignored. From Eq. 2.18 and Eq. 2.19 follows

$$I_{SS} = K_{n^*}^+ N_{n^*} = K_{n^*}^+ \frac{N_A}{V_{\text{mol}}} \exp\left(-\frac{\Delta G_n}{k_B T} \right) \quad \text{(steady-state)}. \tag{2.20}$$

Becker and Döring [25] ensured particle number conservation (at clusters with $n > n^*$) by introducing the Zeldovich-factor Γ_Z, which is defined as the second derivative of ΔG

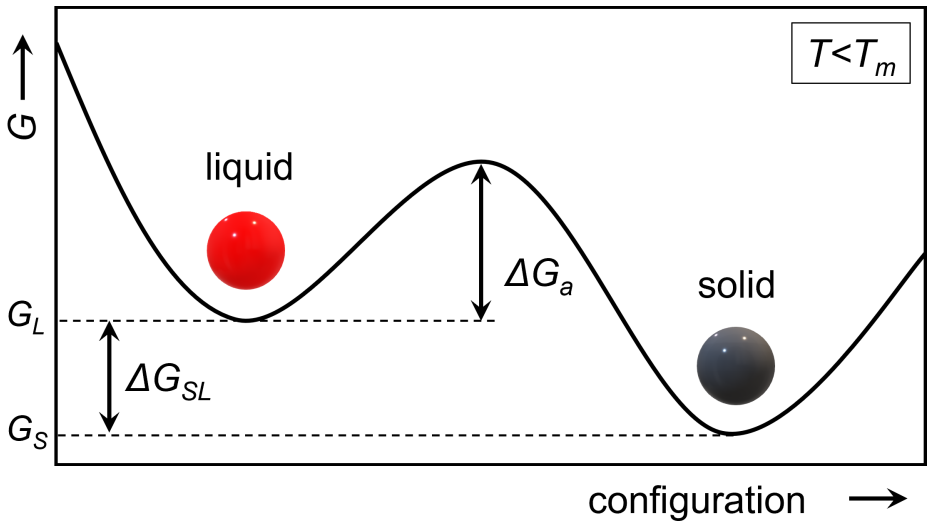

Fig. 2.5: Attachment kinetics of atoms in thermally activated nucleation. The potential wells of both states of matter visualize that ΔG_a needs to be overcome to form atomic clusters.

at $n = n^*$. According to them the steady state nucleation rate density is therefore given by

$$I_{SS} = K^+_{n^*} \frac{N_A}{V_{\mathrm{mol}}} \Gamma_Z \exp\left(-\frac{\Delta G_n}{k_B T}\right). \tag{2.21}$$

The atomic attachment rate $K^+_{n^*}$ is described with the assumption that the growth of clusters is affected by atomic diffusion through the solid-liquid interface [3, 27]. In order to attach to the cluster, atoms must overcome this activation energy of diffusion ΔG_a. This is also called thermally activated nucleation. The interplay of the atomic attachment kinetics is depicted in Fig. 2.5, which shows the energy needed (ΔG_a) to overcome to form clusters. The diffusion coefficient D and the interatomic spacing a_0 can be correlated with ΔG_a [28] (when ΔG_a is equal to the activation energy for atomic self diffusion)

$$D = \frac{1}{6} a_0^2 \nu_0 \exp\left(-\frac{\Delta G_a}{k_b T}\right) \tag{2.22}$$

showing the atomic vibration frequency $\nu_0 = k_b T/h$, with the Planck constant h. The viscosity of the system $\eta(T)$ and the diffusion coefficient D are correlated according to the Einstein-Stokes equation by

$$D_\eta = \frac{k_b T}{6\pi r_H} \tag{2.23}$$

where r_H is the hydrodynamic radius of the solvent [1]. However, contrary to the Einstein-Stokes equation, Brillo et al. [29] found that D_η = const.. They also showed that this is not true for some liquid metals or glass-forming liquids such as Zr-based metal-

lic melts. The steady state nucleation rate density can now be expressed for homogeneous nucleation with further assumptions from Turnbull [3] and Porter et al. [28] as

$$I_{SS}(T) = K_V^{\text{hom}} \exp\left(-\frac{\Delta G^*}{k_b T}\right). \tag{2.24}$$

For homogeneous nucleation the pre-exponential factor is found to be approximately $K_V^{\text{hom}} \approx 10^{39}\text{m}^{-3}\text{s}^{-1}$ [4]. It gives an impression of the number of atoms that act as potential nucleation starting sites.
Intrinsic homogeneous nucleation occurs almost exclusively under experimental conditions, given high purity elements and a liquid system that has no contact to different phases to prevent crystal nucleation by extrinsic sources. Most often these extrinsic sources act as catalysts and prevent further undercooling of the melt. This type of nucleation is called heterogeneous and will be attended in the next section. The different energy barriers for homogeneous and heterogeneous nucleation are shown in Fig. 2.4 (b).

2.2.2 Heterogeneous nucleation

The contact to other phases, such as impurities or container walls, lowers the energy barrier that needs to be overcome for nucleation. Homogeneous nucleation, as described in the last section (Sec. 2.2.1), is only achieved under special, experimental conditions as it has a high activation barrier. Nucleation in contact with a third phase - heterogeneous nucleation - is therefore energetically favorable for the system and almost exclusively present in practice. In a first description of this process in 1929, Volmer [30] assumed that a nucleus forms on a planar surface of a third foreign phase. This formation between the liquid phase (l), the solid nucleus (s) and the foreign phase (f) is shown in Fig. 2.6. Three interfacial energies σ_{sf}, σ_{ls} and σ_{lf} can be assumed. Their subscripted letters denote which two phases are in contact. The Young equation [31]

$$\sigma_{\text{lf}} = \sigma_{\text{sf}} + \sigma_{\text{ls}} \cos\Theta \tag{2.25}$$

is used to calculate the wetting angle Θ, that depends on the different interfacial energies. Ideally, in homogeneous nucleation, the nucleus will be a sphere. The ratio between a spherical volume and the spherical-capped volume of a nucleus in contact with another

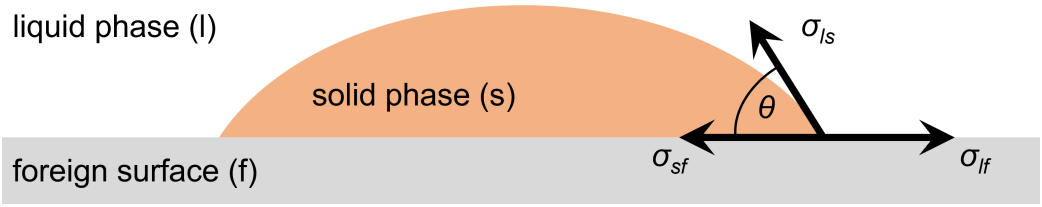

Fig. 2.6: Concept of heterogeneous nucleation. A nucleus forms on a planar foreign surface. It has a spherical-capped geometry with the wetting angle Θ, which results from the interplay of the different interfacial energies.

phase can be expressed by a catalytic potency factor $f(\Theta)$ [1, 32]

$$f(\Theta) = \frac{2 - 3 \cdot \cos\Theta + \cos^3\Theta}{4} \tag{2.26}$$

with the wetting angle Θ between 0° and 180°, $\Theta = [0, 180]$. In homogeneous nucleation there is no contact, so $\Theta = 180°$ and $f(\Theta) = 1$. As $f(\Theta)$ lies between zero and one ($0 \leq f(\Theta) \leq 1$) heterogeneous nucleation can be described as

$$\Delta G^*_{\text{het}} = \Delta G^*_{\text{hom}} \cdot f(\Theta). \tag{2.27}$$

In conclusion, ΔG^*_{het} is always lower than ΔG^*_{hom}. The case of $f(\Theta) = 0$ prohibits any undercooling of the melt since it implies a complete wetting as would be the case e.g. in *epitaxial growth*.

With the reduction of the activation energy in heterogeneous nucleation, the number of atoms, that are essential to form a nucleation site, are reduced as well. They are reduced by a factor $\xi \leq 1$. The nucleation rate density, introduced in Eq. 2.24, can then be expressed as

$$I^{\text{het}}_{SS}(T) = \xi K^{\text{hom}}_V \exp\left(-\frac{\Delta G^*_{\text{het}}}{k_B T}\right) = K^{\text{het}}_V \exp\left(-\frac{\Delta G^*_{\text{het}}}{k_B T}\right). \tag{2.28}$$

The strong temperature dependence of the nucleation rate was shown by Dantzig and Rappaz [23]. They calculated that in pure liquid Al, an increase of the undercooling by $\approx 30\,\text{K}$ will affect the nucleation rate tremendously. The time to form one nucleus of critical size in a volume of one cm^3 accelerates from 450.000 years to 0.1 μs.

Turnbull estimated certain pre-exponential factors to be $K^{\text{hom}}_V \approx 10^{39}\text{m}^{-3}\text{s}^{-1}$ for homogeneous nucleation and $K^{\text{het}}_V \approx 10^{29}\text{m}^{-2}\text{s}^{-1}$ for heterogeneous nucleation [4].

Skripov analysis: The pre-exponential factor K_V in the nucleation rate can be used to experimentally distinguish between homogeneous and heterogeneous nucleation. Skripov [33, 34] describes that a large number of experimentally well conducted undercoolings can be used to apply a *Poisson distribution*. The distribution gives a probability on how many independent events happen during a fixed time frame. It will output certain parameters that can be used to make a reasonable assumption about the type of nucleation in a system at a given undercooling. Essentially, a sufficiently large K_V can be assumed to indicate towards homogeneous nucleation. By applying the Skripov analysis, Kobold [17] showed with 200 consecutive undercoolings of a single sample, that homogeneous nucleation is present in the $Ni_{50}Zr_{50}$ system at $\Delta T = 300$ K with $K_V = 1.034 \times 10^{35} \mathrm{m}^{-3}\mathrm{s}^{-1}$ and a solid-liquid interfacial energy of $\sigma = 0.2107(6)\,\mathrm{J\,m}^{-2}$.

2.2.3 Nucleation in alloys

Up to now, only nucleation in pure liquids was discussed. A mayor thermodynamic variable that needs to be considered in multi-component systems is the concentration of each component, since the Gibbs free energies of the solid (G_S) and the liquid (G_L) phase and the entropy of fusion S_f depend on it. By implementing the atom concentration X_i^Φ, with component $i = A, B$ and the corresponding phase Φ, Eq. 2.14 can be rewritten as

$$\Delta G = -\frac{4}{3}\pi r^3 \frac{\Delta G_{SL}(X_i^\Phi, r)}{V_{\mathrm{mol}}} + 4\pi r^2 \sigma(X_i^\Phi). \tag{2.29}$$

The melt composition can differ from the one of the solid nucleus. ΔS_f is slightly dependent on the composition and the interfacial energy [28, 35]. With these dependencies it is assumed that the largest difference of the free energy ΔG_{SL} is the most probable to initiate nucleation. The composition of the nucleus is then set by the maximum of ΔG_{SL} [35]. This is discussed in more detail, together with a description on how to calculate ΔG_{SL} in multi-component systems, in [36].

2.3 Interfacial energy

Eq. 2.14 introduces the solid-liquid interfacial energy σ and shows that it has a certain effect on the nucleation of undercooled melts. It is defined as the (excess) Gibbs free

energy that is needed to build the solid-liquid interface per unit area ($[\sigma] = \mathrm{J/m^2}$). It consists of an entropic and an enthalpic part. The entropic part describes the excess of internal energy of broken bonds between atoms. This excess is created as atoms at the interface are missing some of their direct neighbors, in contrast to atoms in the bulk. The enthalpic part takes into account that, again compared to atoms in the bulk, atoms near the interface have a lower thermal entropy as they have less options of movement.
The first model for the solid-liquid interface was introduced by Spaepen and Thompson as the negentropic model [37–39]. It is a structural model for monoatomic systems and looks at the crystal structure of the solid phase as well as a polytetrahedral short-range order of the liquid phase. They considered this packing to result in a *maximum short-range density*. The model combines two systems and their free energies. The interfacial energy σ is defined as this difference between a system, that has a solid-liquid interface and a system (hypothetical reference system), which has a discontinuous change of the free energy upon the phase boundary. It is also assumed, that there is no change in density, so that ρ is constant in both phases and up to the boundary. Fig. 2.7 shows a solid-liquid interface. The discontinuous change of the density ρ is drawn, as well as the different contributions to the interfacial energy σ itself. With Eq. 2.2, Eq. 2.5 and at the melting temperature T_m one can conclude, that

$$G_S(T_m) = G_L(T_m) \Rightarrow \Delta G_{SL}(T_m) = 0 \tag{2.30}$$

and

$$\Delta S_f = \frac{\Delta H_f}{T_m}, \tag{2.31}$$

where $G_L(T_m) = H_L(T_m) - T_m S_L(T_m)$. Also, $G_S(T_m) = H_S(T_m) - T_m S_S(T_m)$ and $\Delta S_f = \Delta S_{\mathrm{conf}} + \Delta S_{\mathrm{vib}}$, with a configurational and a vibrational contribution to the possible atomic arrangements. The former is due to a certain number of available configurations of atoms in the liquid phase, for a given energy. The latter can be discarded in this model, since the density changes discontinuously at the interface. Therefore, $\Delta S_f \approx \Delta S_{\mathrm{conf}}$. There is a difference between atoms in the interface and atoms in the bulk lattice. These atoms also have higher ΔS_{conf} than these in the interface. The interfacial energy within the model can now be expressed as

$$\sigma_{SL}(T_L) = \frac{N_i}{N_S} T_L \left(\Delta S_{\mathrm{conf}}^{\mathrm{liq}} - \Delta S_{\mathrm{conf}}^{\mathrm{int}}\right). \tag{2.32}$$

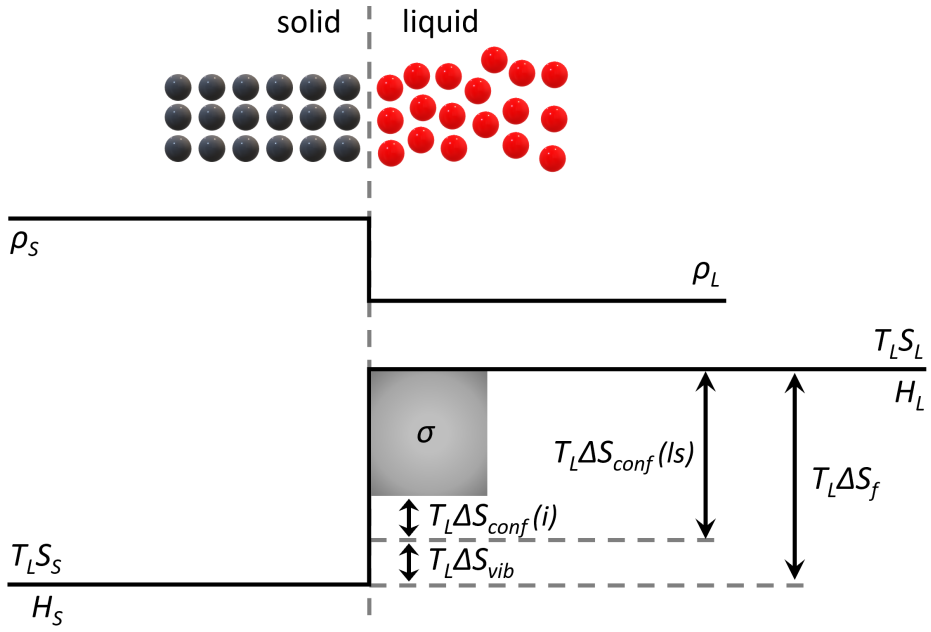

Fig. 2.7: The negentropic model by Spaepen and Thompson. It visualizes the solid-liquid interface, the discontinuous change of density and the interfacial energy σ, as well as the different entropic and enthalpic contributions.

N_i denotes the atoms per unit area of the interface, N_S the atoms of the bulk crystal. A dimensionless factor, the α-factor, that is independent of the temperature and used to describe the structure of the solid-liquid interface is introduced as

$$\alpha = \frac{\sigma_{SL}(T_L)}{\Delta H_f}. \tag{2.33}$$

With the premise of a linear temperature dependence (i.e. $T_m = T$) and the use of α, the solid-liquid interfacial energy σ per surface atom can then be expressed as

$$\sigma = \alpha \frac{\Delta S_f T}{(N_A V_m^2)^{1/3}}. \tag{2.34}$$

Thompson and Spaepen [38, 39] were able to calculate different α-factors for simple structures (bcc: 0.70; fcc/ hcp: 0.86) and only for pure element systems. With more complex systems, an analytic determination with the negentropic model is not possible anymore. A numerical procedure was developed by Holland-Moritz [40] to determine α for such complex systems.

2.4 Solidification in non-equilibrium conditions

The previous sections about thermodynamics and the solid-liquid interface are discussed by considering equilibrium conditions. These conditions apply, when the actual temperature of a given system during solidification stays at the system's T_m. This work mainly analyses the effects of undercooling prior to nucleation and the subsequent microstructure evolution. Non-equilibrium conditions need to be discussed. This section will give an overview on the different undercooling contributions and an introduction to the concept of dendritic growth.

Current theories on dendritic growth take a detailed look on how the solid-liquid interface propagates through the melt. Two broadly known models are the *phase field model* and the *sharp interface model*. The First is mainly based on statistical mechanics. The Latter is used in experimental works as thermodynamic parameters can be determined. The solid-liquid interface is considered to be a sharp boundary between the two phases. It only has a thickness of one atomic layer. The model utilizes heat and mass transfer equations and can describe the dendrite growth velocity even of deeply undercooled melts [36]. Convection and local deviations (anisotropy) from equilibrium conditions are modeled at the interface, as well as the anisotropy of the kinetic growth coefficient.
Equiaxed dendritic growth models for undercooled regimes were introduced by Lipton-Kurz-Trivedi [41–43] and Boettinger-Coriell-Trivedi [44]. They describe the total undercooling ΔT and break it down into the main contributions:

$$\Delta T = \Delta T_T + \Delta T_K + \Delta T_R + \Delta T_C \tag{2.35}$$

Thermal undercooling ΔT_T; defined as the difference between the temperature of the undercooled melt far from the interface T_∞ and the temperature at the dendrite tip T_i.

Kinetic undercooling ΔT_K; defined by the growth velocity v and the kinetic growth coefficient, as $\Delta T_K = v/\mu^*$, with the coefficient

$$\mu^* = \frac{v_0 \Delta S_f}{k_b T_L}. \tag{2.36}$$

Here, ΔS_f denotes the entropy of fusion and k_b is the Boltzmann constant[3]. The speed of sound within a phase is a limiting factor of the total undercooling.

Curvature undercooling ΔT_R; it is the difference between a planar interface melting temperature T_L and the temperature at the curved dendrite tip T_{LR} due to the Gibbs-Thompson effect and is expressed as

$$\Delta T_R = \frac{2 d_0 Q}{C_p R}. \tag{2.37}$$

d_0 denotes the capillary constant, Q is the heat of solidification, C_p the heat capacity and R is the dendrite tip radius. It can also be expressed as

$$\Delta T_R = 2\Gamma / R, \tag{2.38}$$

with the Gibbs-Thomson coefficient

$$\Gamma = \sigma V_m / \Delta S_f, \tag{2.39}$$

which, for most metals, is in the order of 10^{-7} K m [45].

Constitutional undercooling ΔT_C; it is based on the different concentrations between the dendrite tip and the melt. By solving the mass transfer equations one can get the concentration at the tip C_L° and the nominal concentration C_0 to calculate

$$\Delta T_C = m_L (C_L^\circ - C_0) \tag{2.40}$$

with the slope of the liquidus line m_L at the alloy concentration in the phase diagram and visualized in Fig. 2.8. It gives an impression on the interplay of concentration and temperature at the interface to form ΔT_C. The difference in concentration ΔC is directly correlated by m_L to the constitutional undercooling. The previously mentioned planar interface is based on the size of the dendrite tip, that is much larger than interatomic distances. In the kinetic undercooling contribution, the liquid-solid interface was therefore assumed to be planar. Wilson and Frenkel [46, 47] were the first to describe the velocity v of the progression of such a planar interface. This progression depends on the self-diffusion of atoms between the solid and liquid phase (potential well, compare

3 Boltzmann constant: $k_b = 1.3807 \times 10^{-23}$ J K^{-1}

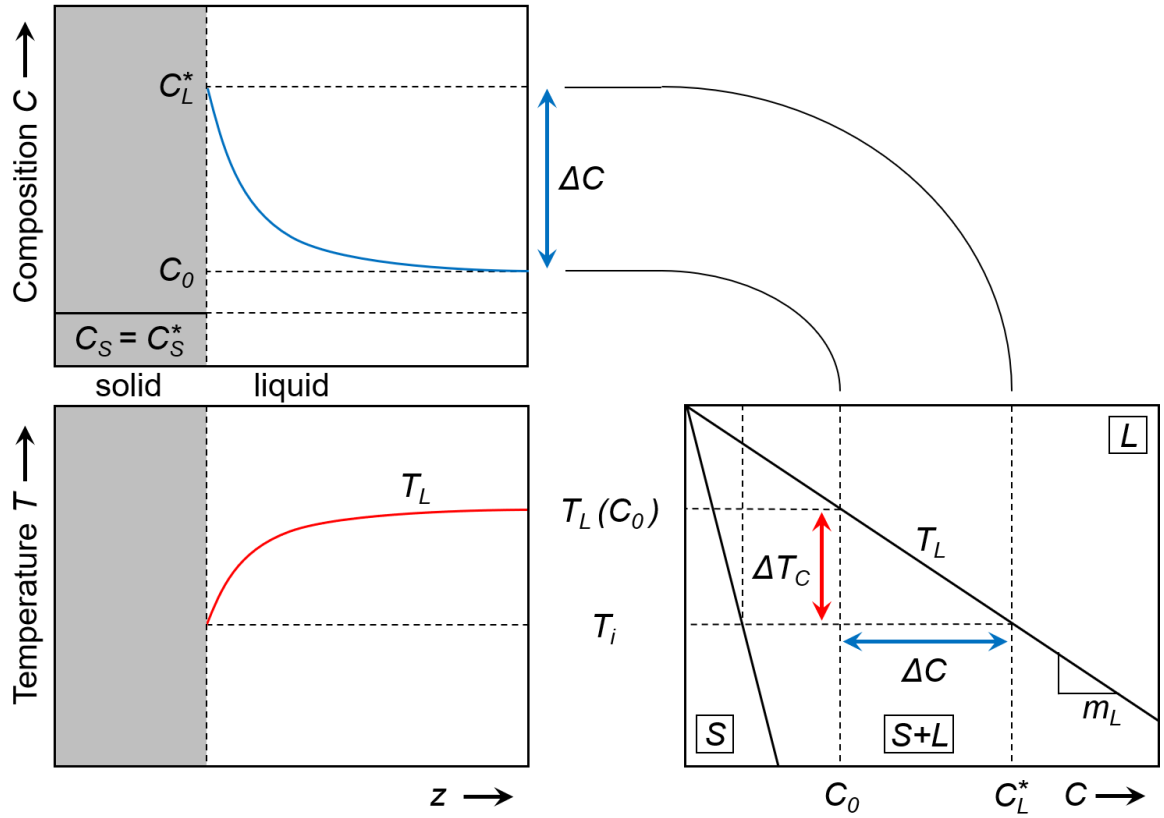

Fig. 2.8: Scheme of the contributions of different concentrations and the liquidus line to the constitutional undercooling ΔT_C at the solid-liquid interface. Illustration after Kurz & Fischer [45].

Fig. 2.5). The velocity can be described as

$$v = v_0 \left[1 - \exp\left(\frac{\Delta G}{R_g T_i}\right)\right] \tag{2.41}$$

with the interface temperature T_i and the gas constant R_g. ΔG is a thermodynamic contribution of the equation and v_0 represents a kinetic part, as it is equivalent to the upper limit of the interface velocity. It is equal to the speed of sound v_S of the respective system if the atoms at the interface and their attachment kinetics are *collision-limited* [48]. The crystal growth velocity is then also limited to v_S. In a *thermal-limited* growth process the limit of the growth velocity is $v_{th} = \sqrt{3k_bT/m}$, with the atomic mass m. In intermetallic systems the attachment kinetics are expected to be *diffusion-limited* [49]. With the atomic diffusion speed v_d the growth velocity at the interface is as follows:

$$v_d = C^* D_l = C^* D_0 \exp\left(-\frac{E_A}{k_b T_i}\right) \tag{2.42}$$

with the diffusion coefficient of the liquid phase D_l and the activation energy of diffusion E_A. C^* is a ratio factor and defined as $C^* = f/\lambda^*$ with f being a geometrical factor and the interatomic spacing λ^* [50]. The growth velocity can now be connected to the Gibbs free energy. If $\Delta G = 0$, as it is at T_L the velocity is zero. It is not yet favorable for the system to change phases. Crystal- and therefore dendritic growth is now dependent on $\Delta G \leq 0$, in other words undercooling, in order to let a solidification front advance through the melt. The thermal undercooling can also be expressed as the product of the hypercooling limit ΔT_{hyp}[4] and the Ivantsov function $Iv(Pe_T)$ [51] as

$$\Delta T_T = \Delta T_{\text{hyp}} Iv(Pe_T). \tag{2.43}$$

This introduces the Peclet number $Pe_T = vR/2a_l$, which quantifies the transport of heat in a dimensionless number, with a_l being the thermal diffusion coefficient and the factor R, which is calculated by utilizing the solvability theory [52]

$$R = \left(\frac{\Gamma}{\sigma_0 \epsilon^{7/4}}\right) 2Pe_T \Delta T_{\text{hyp}} \xi_T. \tag{2.44}$$

ϵ denotes the anisotropy of the interface energy and a thermal stability function is given by $\xi_T = 1/(a_T \epsilon Pe_T^2)$. The Gibbs-Thompson coefficient is expressed as $\Gamma = \sigma V_m/\Delta S_f$ with the molar volume V_m. The growth of the solid-liquid interface, the dendrite tip and the shape of the tip can be determined by solving such equations. Dendrite growth is additionally also influenced by the anisotropy of the interfacial energy [53, 54]. The microscopic solvability theory then leads to a prediction of the radius of the dendrite tip and also on the tip velocity [52, 55]. This is done by expanding Ivantsov's theory [55, 56]. Additionally, anisotropy can influence the shape of the tip, when the point of maximal curvature is not the region with lowest temperature. This leads to a reduction of the heat flow to the tip, which, in turn, can decrease the growth velocity. The affinity for splitting is increased [57, 58], which is also observed in experiments [59].

The experimental conditions are a significant factor on how to utilize Eq. 2.35. At slow growth velocities ($\leq$ 1mm/s) equilibrium conditions can be assumed locally, despite temperature and concentration gradients [60]. It follows that the use of equilibrium phase diagram is possible and therefore, that the attachment kinetic effects are negligible, which leads to $\Delta T_K = 0$. Fig. 2.9 now shows the different contributions of undercoolings in

4 In hypercooling the stored latent heat in the liquid phase is no longer sufficient to heat the sample up to the melting plateau at T_L. The hypercooling limit is introduced in more detail in Sec. 3.2.3.

relation to the dendrite tip (left boundary of the figure). It visualizes the new assumptions and changes Eq. 2.35 into

$$\Delta T = T_L(C_0) - T_\infty = \Delta T_T + \Delta T_C + \Delta T_R. \tag{2.45}$$

2.4.1 Dendritic growth

The solid-liquid interface will eventually become unstable due to its anisotropy. Gradients in temperature and the inherent crystallography define the growth direction of the interface. In an undercooled, single component system, a spherical interface will increase its free energy by $\Delta G = \Delta pV$, since surface tension will increase pressure. This leads to a reduction of the sphere's melting temperature - compared to a planar interface (Gibbs-Thomson effect) [61]. The temperature of the particle surface, especially considering a moving interface, can be expressed as a function to the corresponding interface normal [62, 63]. This holds true when the interfacial energy σ is anisotropic, which is crucial for growth direction and growth velocity of the interface. In the end, the crystal orientation with the highest interfacial growth rate is expected to have the highest crystal growth velocity [64]. During the phase change from the undercooled liquid to solid, a type of morphology is created by the inherent drive of the system to minimize

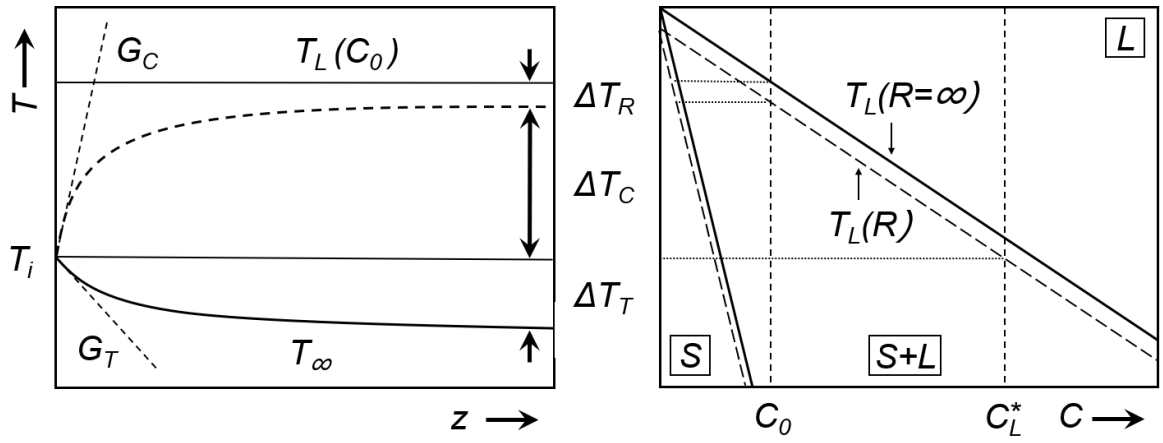

Fig. 2.9: Undercooling contributions during growth at the dendrite tip. It is shown, how the different contributions affect temperature of the system in respect to the distance z to the solid-liquid interface, as well as the correlations between temperature and concentration during dendritic growth.

its interfacial energy. The ideal structural arrangement, as described by Jackson [65, 66], depends largely on the entropy of fusion ΔS_f. With $\Delta S_f / R_G$[5] ≈ 2, a critical value is created that can be used to sufficiently approximate the interfacial morphology. If this value is < 2 there will be a rough interface and with a value > 2 this will result in a faceted growth. The origin of dendrite growth is analyzed by starting with the assumption of a spherical shaped nucleus with $r > r^*$ that grows into an infinite undercooled melt while releasing latent heat. This results in a negative temperature gradient G_t between the solid and the undercooled liquid phase. It influences the solidification and interface stability as small protrusions can build up at the interface due to local fluctuations of the growth rate v. This is also referred to as *destabilization of the interface*. It evolves to the shape of a tip and ultimately leads to more effective heat flow between the two phases phases at the interface. The reason is the increased surface to volume area when transforming away from a planar interface. This further drives G_t and the interface will remain unstable and even develop the destabilization further. This development is counteracted by the Gibbs-Thompson effect, that limits the increasing curvature of the interface. A balance is formed between both phenomena and a specific shape is created, based on the respective system's parameters. Depending on the crystal structure of the system, these shapes will grow along certain, preferred crystallographic directions. These shapes are now called *dendrites*[6]. Fig. 2.10 gives a simulated example of the solid-liquid interface for an undercooled melt ($\Delta T = 87\,\mathrm{K}$) of Ni. It becomes clear, that certain growth directions are more favorable than others. In the cubic crystal system of Ni shown here, this is the case for the <100> directions. Ivantsov [51, 67] solved the transport equations, which were first suggested by Papapetrou [68] that result in the dendrite tip radius and velocity. It is assumed that the dendrite interface is isothermal ($T_i = T_L$) and isoconcentrate. It is further known from experiments, that for each undercooling a pair (r, v) exists, that defines a constant velocity of the tip, as well as a certain shape-preserving effect [69, 70], so there is not one unique solution. Further theories were developed to find a more

Fig. 2.10: Solid-liquid interface simulation of an undercooled Ni melt at an undercooling of $\Delta T = 87\,\mathrm{K}$. It reveals that the cubic Ni system develops dendrites in the six <100> directions [64].

5 R_G denotes a rate at which atoms attach to a crystal per unit area.
6 The name comes from the Greek word dendron ($\delta\epsilon\nu\delta\rho\sigma\nu$), meaning "tree".

realistic operating state of the dendrite tip. The marginal stability theory [71, 72] and the microscopic solvability theory [52, 53] utilize a scaling factor σ^* and provide explanations for the preferred growth directions of dendrites. Together with Ivantsov's equations unique values for the velocity and the shape (r, v) at a certain undercooling can be identified.

The described models concentrated on an assumed infinite undercooled melt with a single dendrite tip growing. In practice, dendrites grow in many configurations close to each other. Considering free growing dendrites is only possible in the first moments of solidification. With many dendrites next to each others, their thermal and solutal fields (their influence on temperature and concentration, that reaches into the liquid phase) overlap each other. Especially in multi-component systems, such as alloys, there is (in addition to G_t) also a concentration gradient G_c, which contributes even further to the destabilization of the phase boundary. A model extension has been developed for isothermal systems, which considers the concentration change in front of the dendrite tip [73, 74]. Additional analysis and mathematical descriptions to describe the dendrite tip growth can be found in [67, 70, 75, 76].

2.5 Atomic short-range order

Atoms in a liquid phase are not entirely free to move. Local structures will form and decompose, almost instantly, again. A closer packing and more bonds between atoms will result in a lower energetic state. In order to discuss these local structures an interaction potential must be defined. The Mie-potential [77] can be used to describe the interaction of atoms in metallic systems as

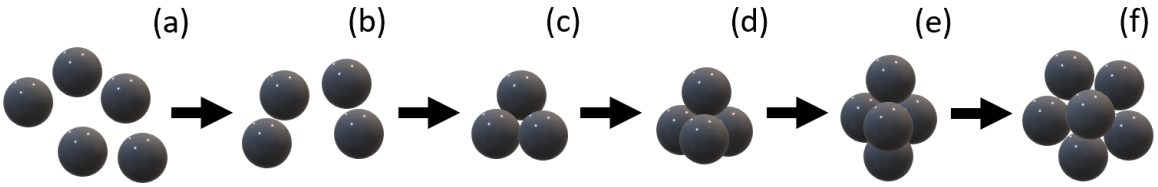

Fig. 2.11: Formation of short-range order of atoms in metallic melts **(a)**. The atoms will form dimers **(b)** with an equilibrium distance r_{eq} based on atomic bonds. The energy will decrease with more bonds. Forming triangular clusters **(c)** and regular tetrahedrons **(d)** is favorable. This process continues with **(e, f)** and will result in an icosahedron (Fig. 2.12). Adapted from [78, 79]

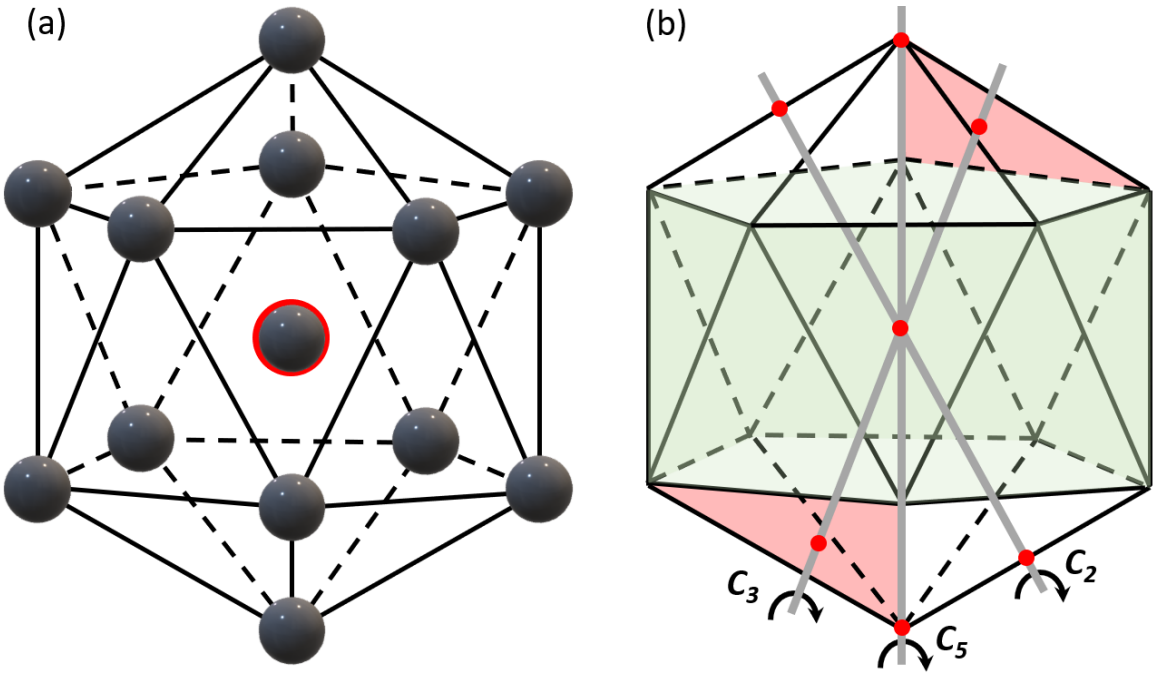

Fig. 2.12: Icosahedral cluster consisting of 13 atoms. **(a)** The red circled, central atom having 12 nearest neighbor atoms. Spacing not to scale. **(b)** Geometric scheme of the symmetry axes of a regular icosahedron with highlighted relations.

$$V(r) = c\left[\left(\frac{\epsilon_{p1}}{r}\right)^{\nu_1} - \left(\frac{\epsilon_{p2}}{r}\right)^{\nu_2}\right]. \tag{2.46}$$

ϵ_{pi} and ν_i, with $i = [1,2]$, are constants that depend on the used model. For metallic interaction the Lennard-Jones potential is frequently used as a special case of the Mie-potential with $\nu_1 = 12$ and $\nu_2 = 6$. It results in an equilibrium distance r_{eq} between two atoms, where the attractive and repulsive term (or atomic forces) cancel out. A point of minimized energy between two atoms. With additional bonds, the total energy can be decreased further. Considering a third atom, as in Fig. 2.11 (c), results in the formation of a regular triangle, the resulting base shape of atomic clusters. Fig 2.11 (d) shows a tetrahedron, which is formed by adding a fourth atom. It reduces the energy significantly again. All four atoms are distanced to each other by r_{eq}. The tetrahedron has the lowest energetic state of four-atomic systems (with isotropical bonding), since it shows the highest packing fraction.

By adding further atoms, several tetrahedra will start to develop into polytetrahedral clusters and ultimately form an icosahedron. This atomic structure is shown in Fig. 2.12 a and is composed of 20 equal triangular faces. It is build from 20, slightly deformed, tetrahedra [79]. It was proven by Benson & Shuttleworth in 1951 that the icosahedral cluster is

about 8% more densely packed than fcc or hcp structures (74% packing density).
All 12 outer atoms have the same minimal distance r_{eq} to central atom. The icosahedron is locally the atomic cluster with the lowest energetic state. It has six five-fold symmetry axes, but has no translational periodicity like crystal structures [80]. This discrepancy was used by Frank [10] to explain the high undercoolability of metallic melts, observed by Turnbull [4]. He proposed an icosahedral short-range order (ISRO), which interactions could be very well described with the Lennard-Jones potential. The incompatibility of this ISRO and the crystal structure of the solid phase are the reason of large undercoolings. This is backed up by recent neutron scattering and X-ray diffraction experiments on undercooled melts [11, 81, 82]. The regular icosahedron is a *platonic solid*, a convex regular polyhedron, meaning that all its faces, edges and angles are congruent (identical in shape and size). It has six five-fold (C_5), ten three-fold (C_3) and 15 two-fold (C_2) axes of rotation. These symmetry axes are shown in Fig. 2.12 b. Each two directly opposing triangular faces share the same plane in 3D space (highlighted in red). In relation to the C_5 axis, there are ten outer facets (green).

2.6 Solid-solid phase transitions

Unlike liquid-solid transitions (LST), introduced in Sec. 2.1.1, solid-solid phase transitions (SST) are a structural reordering of atoms in a solid system. Thermodynamically, two crystalline phases are stable at different temperature ranges and at T_{SST}[7] both phases coexist in equilibrium. Similar to a LST, an activation barrier needs to be overcome to realize a net energy gain after transition [83, 84]. In principle, the energy gain rises with increasing temperature deviation from T_{SST} (see Fig. 2.1). The actual transitioned fraction in the microstructure is therefore a function of time and temperature. SSTs usually propagate much slower through the system, than the transition from liquid to solid[8] and can be actively interrupted, e.g. by holding a certain temperature, the martensitic transformation in steels can be controlled [85].

7 The transition temperature in literature is often denoted as T_0.
8 This relates to the context of this work, where usually far-from equilibrium transitions, in deeply undercooled systems, are analyzed.

The kinetics of a SST are dependent on the nucleation, the growth and also the interplay of already transitioned structures. In the main contribution, the growth part, interfacial-controlled (athermal) and diffusion-controlled (thermal) transitions are distinguished. [83, 86] Due to their low temperature, martensitic transformations in steel occur basically without diffusion and only by structural rearrangements. There is a competition between the rising drive to transition and simultaneous obstruction of diffusion. Both increase by the cooling of the system. At some point, whole regions of the microstructure will suddenly transform. A re-transition, back to the high temperature (HT) phase, in these low-temperature transitions is usually only possible after a strong overheating to release structural tensions. A hysteresis is formed around T_{SST} [85, 87–89].
At more elevated temperatures, the phenomenon of overheating reaches lower values, as diffusional parts help with re-transitioning. It is only of subsidiary importance in practice [87]. By looking at it from the standpoint of chemical reactivity, driving patterns and atomic rearrangements are favorable above the respective transition temperature and thus, a transition must propagate through the sample [90]. This holds true for temperature regions, where diffusion-controlled processes are suppressed. The undercooling however, will remain relevant, as a SST can also be undercooled, quenched or even passed entirely [91, 92].

In LSTs, overheating is also a more theoretical construct. It can happen, but the required conditions are not met in practical processes. It was shown for lead crystals, that overheating above the equilibrium melting temperature of 3 K was possible. This was however, highly dependent on the grown facets of these micro-crystals [93].

2.7 Crystal scattering

Scattering is a characteristic interaction of waves and particles with atom cores. This interaction is used to determine crystal structures (ordered structures), as well as short-range order of atoms in liquid (disordered) structures. It uses the interaction of waves and particles with the sample that result in a defined deflection. These experiments can be executed with high energetic photons (X-rays) or particles (neutrons or electrons). The structural ordering that needs to be resolved, requires wavelengths as small as the

atomic distances. With smaller structures, higher energetic radiation is needed. The principle of X-ray scattering was proposed by Bragg in 1913 [94]. Crystal structures are defined by periodicity. The structure can be constructed by a set of characteristic lattice parameters, that form a *unit cell*, which repeats throughout the structure in all directions. Bragg realized, that the distance between the atomic net planes d and the wavelength λ of the photon or particle used directly result in a specific diffraction (or scattering) angle θ

$$n\lambda = 2d_{\mathrm{hkl}} \sin\theta_{\mathrm{hkl}}. \tag{2.47}$$

This is illustrated in Fig. 2.13. When the path difference δ equals an integer multiple (n) of the wavelength, the scattered waves will interfere constructively. The intensity of diffraction can be plotted for each angle, which results in a so called diffraction pattern. They usually consist of several large spikes of constructive interference. These spikes are causally directly connected to the crystal structure. This causality results in a characteristic pattern for each structure [95].

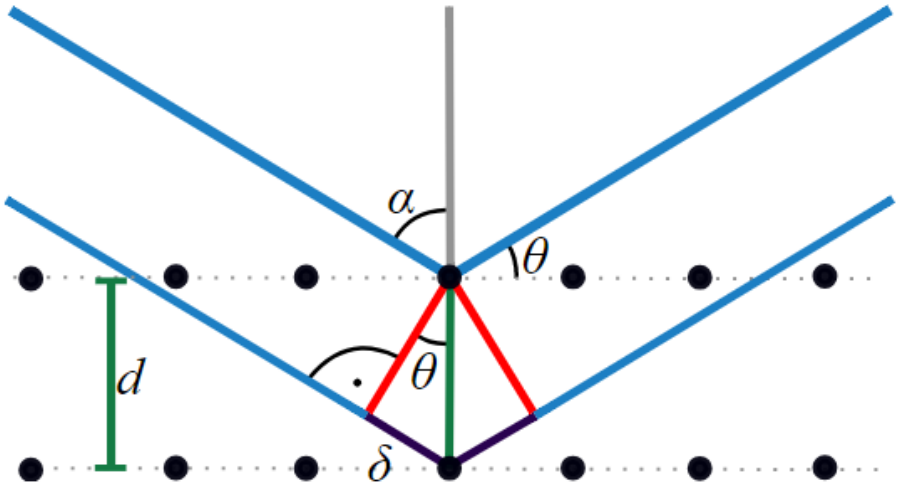

Fig. 2.13: Schematic visualization of Bragg's law. A wave is diffracted on an atomic plane by the angle θ, based on the wavelength of the source and the net plane of the crystal lattice d.

CHAPTER 3

Experimental methods and analysis

Most solidification processes, such as industrial casting, take place in or near equilibrium. Heterogeneous nucleation is in fact often purposely used, e.g. with cooled crucibles or seed crystals, to control the process. Deep undercoolings, rapid solidification or even homogeneous nucleation are achieved only in special experimental conditions. The reduction of heterogeneous nucleation sites is achieved by using high purity elements and experimental techniques, that keep the sample from other phases, such as crucible walls. The selection of said elements and their preparation is described in Sec. 3.1. Subsequently, levitation techniques are introduced in Sec. 3.2, together with discussion of temperature analysis and in situ visualization. After the experiments, samples need to be inspected and prepared for a microstructure analysis. Optical microscopy and electron microscopy methods, such as electron backscatter diffraction, are discussed in Sec. 3.5.

3.1 Sample preparation

High-purity raw elements are used for sample alloying. They are listed with the respective purity in Tab. 3.1. Many alloys investigated in this work contain elements that are affine to oxidization or are difficult to produce free from oxides or other elements. That concerns primarily the elements in the 3rd group as well as elements from the lanthanide group, also called *rare-earth elements*, of which gadolinium is used in this work. They have strong reducing potential and up to seven unpaired electrons in the 4f orbitals; these electrons won't participate in bonding as they penetrate the [Xe] core and are isolated [96–98]. Their similar chemical properties are also the reason for difficulties in separation from each other during the refining processes. Therefore, even high purity elements often contain chemically similar elemental constituents, that cannot be easily separated, or certain impurities, such as oxides.

Table 3.1: Purity and distributor of elements used for the investigated alloys.

Element	Purity [%]	Shape	Vendor
Zr	99.99	crystal bar	Alfa Aesar
Co	99.996	small cylinders	Alfa Aesar
Ni	99.995	pellets	Alfa Aesar
Gd	99.99	small pieces	Alfa Aesar
B	99.995	small pieces	Alfa Aesar
Hf	99.9	small pieces	Alfa Aesar
Si	99.999	plate	Alfa Aesar
Al	99.9999	block	Hydro
Au	99.9985	small rod	Alfa Aesar
Pd	99.95	wire	Alfa Aesar
Fe	99.99	wire	Goodfellow
Y	99.9	small pieces	Alfa Aesar

All elements, that are especially affine to oxidization or similar reactions, are stored within a *glove box*, which is basically a closed chamber with a separated inert gas atmosphere. Within the chamber, oxygen and water content are carefully monitored and maintained below 0.1 ppm.
The samples are alloyed in an arc-melting furnace that can be evacuated to 10^{-7}mbar in reasonable times. The volume is then backfilled with argon inert gas (6N). Before the actual alloying process, a small titanium sample is melted repeatably to reduce the oxygen content of the furnace atmosphere even further (since Ti is a strong oxygen absorber). A high-energy electric arc is then induced between a tungsten electrode and a water-cooled copper crucible, in which the elemental pieces are positioned. Since the tungsten electrode is movable, the arc can be steered onto the alloy constituents and they can be carefully melted while monitored and adjusted. The mass loss during this process is found to be negligible, as it ranges only up to 0.2% of the sample mass. This, of course, depends highly on the respective elements used, but unlike in vacuum processes (as in levitation, which will be described later on) evaporation is reduced.
After processing in respective experiments, the specimens must be prepared for the microstructure analysis. Typically, a cross-sectional area is prepared to be investigated, e.g. inside an electron microscope. The samples are embedded, in the desired orientation, into a electrically conducting material (*Struers Polyfast*), by hot embedding. A cold

embedding into an epoxy resin can be used for samples, which might be transformed by the temperature or pressure applied in hot embedding. The cross-sectional area must be grinded and polished to reach a plain surface, that can be analyzed even by electron backscatter diffraction. In a last polishing step, the specimens are treated with a 0.05 μm alumina suspension (*Buehler MasterPrep*) and a final, slightly basic, 0.05 μm silica suspension (*Schmitz O.P.S.*).

3.2 Levitation techniques

Levitation is a process that compensates the gravitational force by an opposite external force, without direct contact to the levitated object. Levitation can even be achieved acoustically or aerodynamically. Material science mainly focuses on electromagnetic and electrostatic levitation.

3.2.1 Electrostatic levitation

The electrostatic levitation (ESL) technique is based on Coulomb forces that are exerted on an electrically charged sample in an electrostatic field [99]. It is sufficient to create a force, that is able to counteract the gravitational force, as seen in Fig. 3.1. With this technique, conducting and non-conducting samples can be processed. However, in an arrangement of fixed electric charges there cannot be a stabilizing minima for the sample's position (Earnshaw theorem [100]). To realize a stable positioning of the sample within the electrostatic field, it's position has to be adjusted in real-time. A first levitation for samples of several mm diameter was successful in 1984 at the JPL [1] and in 1987 it was also achieved to levitate molten droplets. [101, 102]. A detailed description on the functionality and structure of an ESL can be found in the dissertation of Meister [103], who developed an ESL system in 1998. Further descriptions can be found in [104–106].

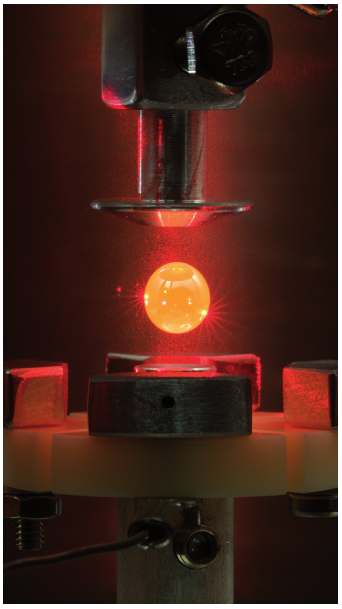

Fig. 3.1: Picture of the NESL at DLR-MP with a levitating sphere (ø = 4 mm).

1 The NASA **J**et **P**ropulsion **L**aboratory is part of the California Institute of Technology (Caltech).

Fig. 3.2 pictures an overview of typical ESL components. The ESL system is designed with two main electrodes (z-axis) that apply a voltage of up to 40 kV and induce the main force upon the sample. Four additional electrodes are placed in the horizontal plane (xy-plane) and are used for correction of the sample's position. The system corrects the position based on the cast shadow on photosensitive detectors (PSD) by two He/Ne-lasers placed orthogonal to each other. Heating lasers ($P = 75\,\mathrm{W}$, $\lambda = 808\,\mathrm{nm}$) are used to heat and melt the specimen (usually $r \approx 1.5 - 2.5\,\mathrm{mm}$) during levitation. Temperature measurements are contactless as well with a pyrometer (Impac IGA 120-TV, 100-5000 Hz, accuracy ±5 K). In the first heating cycle there is an evaporation of positive Ions from the surface of the sample. This highly impacts the levitation and can even push the specimen out of the stable configuration. It is therefore irradiated with ultra violet light to utilize the photoelectric effect [107] and create a positive surface charge for stable levitation. Under normal atmosphere conditions, the main current of the electrodes will result in flash-overs between the two main electrodes. High vacuum pressure of $p = 2 \times 10^{-5}\,\mathrm{mbar}$ is necessary to prevent such arcs. The ESL-facilities used for this work reach pressures of $10^{-7} - 10^{-8}\,\mathrm{mbar}$ in a reasonable time and therefore operate in ultra high vacuum (UHV) conditions. In terms of purity, the reached vacuum together with the high elemental purities used, result in state-of-the-art conditions for alloy investigations. Flash-overs can also be created by evaporated substances that deposit at the electrodes, which sets restrictions based on the respective vapor pressure of a given system or its elemental components. This can also have an impact on the performance of the levitation as it could disturb the electrostatic field or deposit on surfaces used for positioning of the sample.

3.2.1.1 Sample positioning in electric fields

The electrostatic field $\vec{E}$ that is generated to oppose the gravitational force in a sample with mass m and a surface charge q can be written out as

$$\vec{E} = -\frac{mg}{q}\vec{e}_z. \tag{3.1}$$

In z-direction two main forces are acting on the sample. The gravitational force $\vec{F}_g$ and the force of the electrical field $\vec{F}_z$.

$$\vec{F}_g = -mg\vec{e}_z \qquad \vec{F}_z = -q\frac{U_z}{d_z}\vec{e}_z \tag{3.2}$$

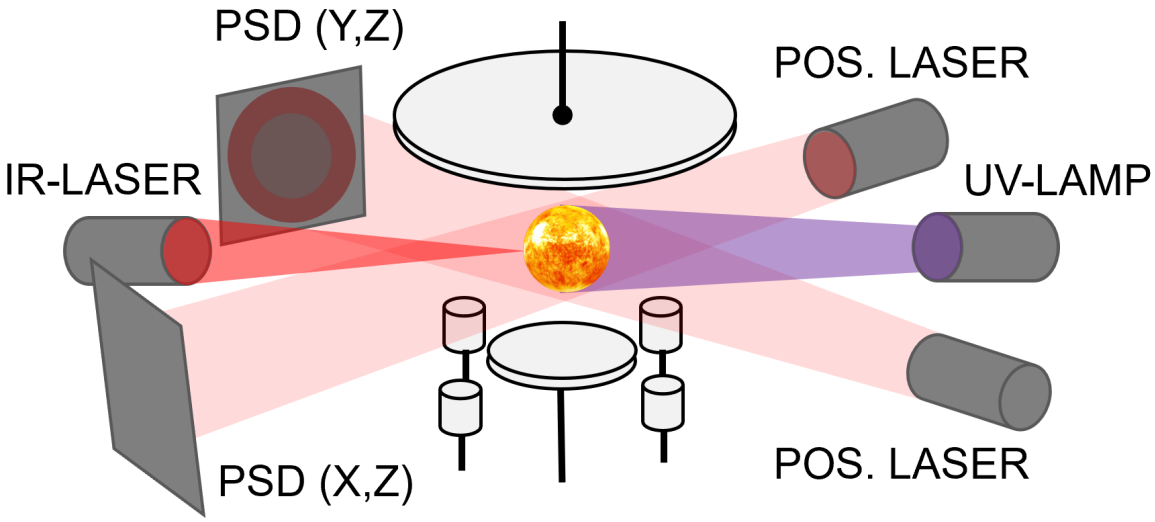

Fig. 3.2: Scheme of principal components inside an electrostatic levitator. The electrode system is positioned in the center, surrounded by the positioning system (PSD), the heating laser and an optional UV-lamp.

with the gravitational acceleration[2] g, the voltage U_z and the distance of the electrodes d_z. The overall force acting on the sample can now be derived as

$$F(z) = \frac{q^2}{4\pi\epsilon_0}\left(\sum_{n=1}^{\infty}\frac{1}{(2d_z n - 2z)^2} - \sum_{n=0}^{\infty}\frac{1}{(2d_z n - 2z)^2}\right) \tag{3.3}$$

with the sample position z, the vacuum permittivity[3] ϵ_0 and the number of reflections n. Reflections can be neglected to approximate the force as

$$F(z) \approx -\frac{q^2}{4\pi\epsilon_0}\left(\frac{1}{(2z)^2} - \frac{1}{(2d_z - 2z)^2}\right). \tag{3.4}$$

The forces acting on the sample cancel out when the sample is in the middle, between both electrodes. The equation for motion in z-direction is then given by

$$m\ddot{z} = -mg - q\frac{U_z}{d_z} - \frac{q^2}{4\pi\epsilon_0}\left(\frac{1}{(2z)^2} - \frac{1}{(2d_z - 2z)^2}\right). \tag{3.5}$$

The motion in x and y direction can be derived similarly. Together with the assumption, that the respective fields are between two parallel electrodes and the geometrical factor κ,

2 gravitational acceleration: $9.78 - 9.82\ \mathrm{m\ s^{-2}}$
3 vacuum permittivity: $\epsilon_0 = 8.8542 \times 10^{-12}\ \mathrm{C\ Vm^{-1}}$

which comprises the distance of sample and electrodes [103]:

$$m\ddot{x} = -2q\frac{1}{\kappa}\frac{U_x}{d_x} \quad \text{with} \quad \kappa = \sqrt{\left(\frac{2z}{d_x}\right)^2 + 1}. \tag{3.6}$$

3.2.1.2 Levitation of a charged sample

The sample is placed on top of the bottom main electrode. To initiate the levitation, (negative) voltage is applied at the top electrode. This leads to a change of the charge distribution, because of a field change in z-direction. The sample becomes positively charged, which can be expressed by

$$q^i = -4\pi\epsilon_0\tau\frac{U_z}{d_z r^2} \tag{3.7}$$

with the radius of the sample r and a geometric constant $\tau = 1.645$ [105]. In the initial time frame of levitation the charge at the bottom electrode dominates the voltage. The lifting force on a spherical sample is then part of the power balance in z-direction:

$$F_z^i = \frac{4}{3}\pi r^3\rho g - q\frac{U_z^i}{d_z} - \frac{q^2}{4\pi\epsilon_0}\frac{1}{(2r)^2} = 0. \tag{3.8}$$

This can be combined with Eq. 3.7 to express the voltage needed to initiate levitation

$$U_z^i = \pm\sqrt{\frac{4\rho g r}{3\tau(4-\tau)\epsilon_0}} \tag{3.9}$$

By using Eq. 3.4 and Eq. 3.7 the voltage U_z^0, that is needed to levitate the sample in the middle between both electrodes, can be written as

$$U_z^0 = \frac{4-\tau}{4}U_z^i. \tag{3.10}$$

It becomes clear, that the initial voltage is higher, than the voltage needed for continuous levitation. The needed rate to reevaluate the voltage in order to keep the sample stable in the middle between both electrodes can be approximated. The time elapsed after applying the initial voltage and until the sample hits the top electrode is used to estimate a minimum rate, which is required for a continuous stable positioning. With a Silicon sample of 2 mm diameter, Panofen concludes a sampling rate of 2×10^{-3} s [108].

As mentioned earlier, a UV-lamp is used to utilize the photoelectric effect and create a positive surface charge to ensure a stable levitation. This is needed, because in ESL the heating and the levitation are decoupled. Evaporation of atoms (impurities) and ions will result in a decreasing surface charge. Hardware can only compensate this up to the maximum voltage. Evaporation would eventually lead to an insufficient surface charge and ultimately stop levitation. The UV-lamp ($\lambda = 115-350\,\text{nm}$) recharges the sample at low temperatures. At high temperatures the loss of charge is counteracted by thermionic emission and the UV-lamp is, in principle, not required anymore.

3.2.2 Electromagnetic levitation

Similar to the ESL technique, Electromagnetic levitation (EML) is a contactless processing technique. The sample is positioned and heated through induced currents in an inhomogeneous electromagnetic field, based on Maxwell's equations. It is limited to electrically conducting samples. The field is generated with radio frequency alternating current ($150-1000\,\text{kHz}$) running through copper coils. These coils are hollow and have cooling water running through them. They are positioned below and above the sample, with opposite magnetic field on either side. Eddy currents are created in the sample by the alternating field, as electrons start to move according to it. The direction of the eddy currents is opposite to the current flow in the coils. A magnetic field is generated in the sample that is basically opposing the field from the coils, with a phase shift of 180°. As shown in Fig. 3.3, the charged particles of the eddy currents and the magnetic field will result in a force $\vec{F}_{em}$ pointed perpendicular to the eddy current and the field lines. This repulsive force holds the sample in levitation against the gravitational force. The sample behaves basically like a diamagnet, that is repelled from the coils. Additionally, through the magnetic fields, small changes of the sample position are instantly compensated.
By utilizing several coil spirals ($5-10$ windings) below and also above (reversed winding direction) the sample, it is kept in a stable cage within the electromagnetic fields. The samples usually range from $6-10\,\text{mm}$ diameter. The system always operates in an inert gas atmosphere. The chamber will be evacuated to high vacuum conditions ($< 10^{-6}\,\text{mbar}$) and refilled with high-purity (6N) inert gas (Ar or He) to 800 mbar. The lower atmospheric pressure allows for a more stable temperature control at low temperatures, but also limits evaporation during heating. In contrast to the ESL, in EML levitation and heating are coupled. Through Ohmic losses of the eddy currents, the sample always has some power absorption during levitation and is always heated.

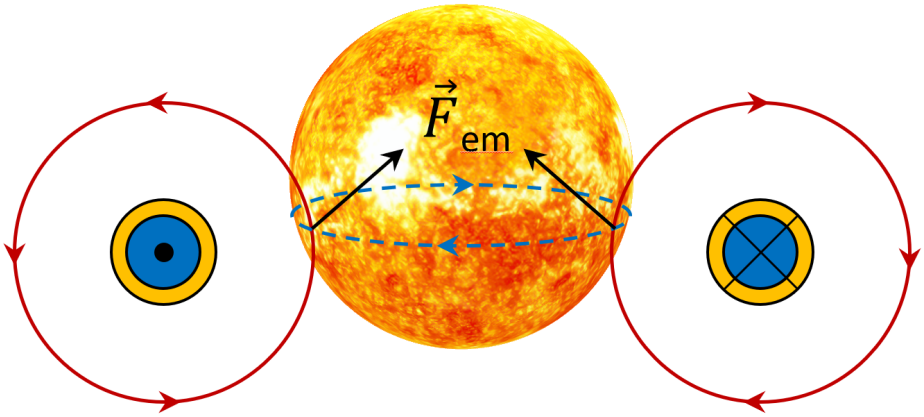

Fig. 3.3: Principle of electromagnetic levitation. The red arrows represent field lines of the electromagnetic field induced by the coil. The field lines interact with the surface region of the sample and induce eddy currents (blue arrows). This interaction results in a force $\vec{F}_{em}$ indicated by the black arrows.

Alternating magnetic fields generate eddy currents in the sample. These induced currents will lead to a magnetic moment $\vec{m}$ opposing the primary field $\vec{B}$. This results in the Lorentz force $\vec{F}$ expressed by

$$\vec{F} = -\vec{\nabla}(\vec{m}\vec{B}). \tag{3.11}$$

With the assumption of a spherical, non-ferromagnetic sample and with the magnetic flux density B, the mean force, according to Rony [109], can be written as

$$\vec{F}_{em} = -\frac{4\pi r^3}{3}\frac{\vec{\nabla}B^2}{2\mu_0}G^*(q) \tag{3.12}$$

with the magnetic permeability μ_0 and the efficiency ratio G^*:

$$G^*(q) = \frac{3}{4}\left(1 - \frac{3}{2q}\frac{\sinh(2q) - \sin(2q)}{\cosh(2q) - \cos(2q)}\right). \tag{3.13}$$

q is a dimensionless parameter and gives the ratio of the sample radius r and the magnetic skin depth δ^* as

$$q = \frac{r}{\delta^*} \quad \text{with} \quad \delta^* = \sqrt{\frac{2}{\mu\omega\sigma_c}}. \tag{3.14}$$

This introduces the angular frequency ω of the current and the conductivity σ_c. It shows, that sample size, the frequency of the field and the conductivity all influence G^*. Non conducting samples ($q \to 0$) cannot be levitated, whereas a good conductivity ($q \to \infty$) results in a constant $G^*(q) = 3/4$. The force $\vec{F}_{em}$ acting on the sample has to be strong

enough to counteract the gravitational force $\vec{F}_g$. If this is true, a stable levitation is possible.

$$\vec{F}_{em} = -\vec{F}_g \tag{3.15}$$

The gravitational force equals

$$\vec{F}_g = m\vec{g} = \frac{4\pi r^3}{3}\rho\vec{g} \tag{3.16}$$

with the material density ρ. This can be combined with Eq. 3.12 for an expression of the acceleration in the z-axis as

$$\frac{\partial \vec{B}^2}{\partial z} = \frac{2\mu_0 g}{G^*(q)}\rho. \tag{3.17}$$

Now, one can derive the mean power absorption P

$$P = \frac{B^2}{2\mu_0}\omega\frac{4\pi r^3}{3}H(q) \tag{3.18}$$

with the efficiency of power absorption $H(q)$

$$H(q) = \frac{9}{4q^2}\left(q\frac{\sinh(2q)-\sin(2q)}{\cosh(2q)-\cos(2q)}-1\right). \tag{3.19}$$

The conductivity of the sample is again crucial. With $q \to 0$ the field and the sample have no interaction. With $q \to \infty$, as would be the case with an ideal conductor, there is no resistance and $H(q) \to 0$. However, the function its maximum at $q \approx 2$, resulting in the mentioned typical sample size.
It should be mentioned, that Eq. 3.15 is simplified. For example a standard EML (1g conditions) also has coils positioned above the sample to force a stable positioning cage. The force upon the sample from these coils is $\vec{F}_{\text{top}}$ The sum of forces necessary to get a sample levitating in the centre between the coils is then given by

$$\vec{F}_{em} - \vec{F}_g - \vec{F}_{\text{top}} = 0. \tag{3.20}$$

The publications of Lohöfer [110, 111] and Herlach [112] provide a detailed look into the theoretical details of electromagnetic levitation.
To reduce convections, that are also induced by the positioning field, a special EML, named TEMPUS[4] [113], was fitted for use in parabolic flights. Fig. 3.4 shows a typical parabola during such a flight with a μg-phase of about 22 seconds, where the gravitational

4 **T**iegelfreies **E**lektro-**M**agnetisches **P**rozessieren **U**nter **S**chwerelosigkeit. *Containerless electromagnetic processing in microgravity.*

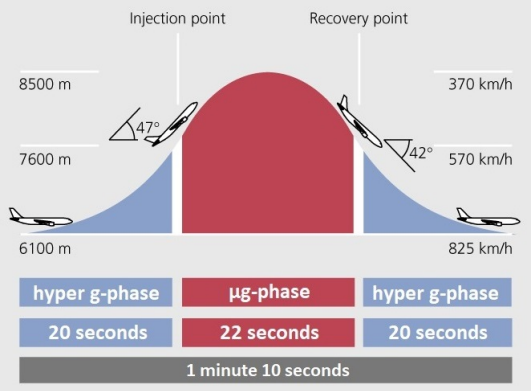

Fig. 3.4: Typical parabola during a parabolic flight with a 22 second μg-phase, where the gravitational force is compensated by inertia.

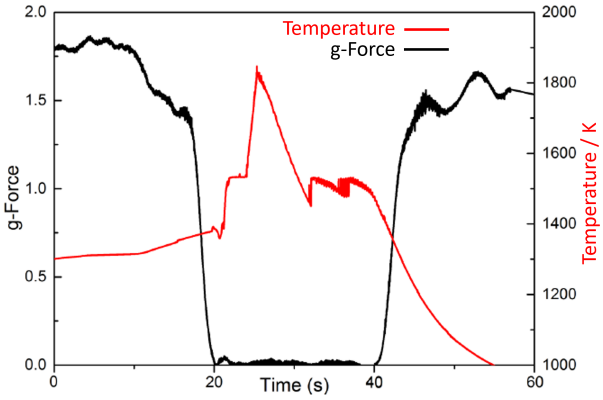

Fig. 3.5: Graph of the g-force and the temperature of a sample during one parabola. The heating and cooling of the sample is happening within the reduced g-force segment.

pull is compensated by inertia. EML in μg-environment reduces the needed power for positioning by a factor of $100 - 1000$ in relation to $1g$ conditions. This is visualized with Fig. 3.5 as the g-force is dropped to basically zero during the μg-phase, normally around $10^{-2}\,g$. During this time frame the experiment itself is conducted. Here, the heating and the positioning are decoupled. They are realized by two sets of coils, as depicted in Fig. 3.6. The quadrupole positioning field is at least one magnitude weaker than the dipole heating field. The sample can be preheated on a positioning stand in reduced inert (Ar) atmosphere, but levitation itself is only possible in the μg-phase, because the positioning field is only able to hold the sample in place without the gravitational force. Upon entering the μg-phase, the stand is retracted and the positioning field controls the position of the sample. Heating is then done with both fields on full power. Cooling down is done by turning of the heating field and reducing the positioning field to a minimum. Additional cooling can be achieved (as in 1g EML facilities) by a short Helium quench into the chamber.

3.2.3 Temperature measurement

The spectral radiance [5] I is used in pyrometry to reliably determine the temperature. It is the radiance of a surface related to the unit frequency or wavelength. It can be expressed

5 Generally denoted as B. To avoid confusion with the magnetic field, the spectral radiance is denoted with I in this work.

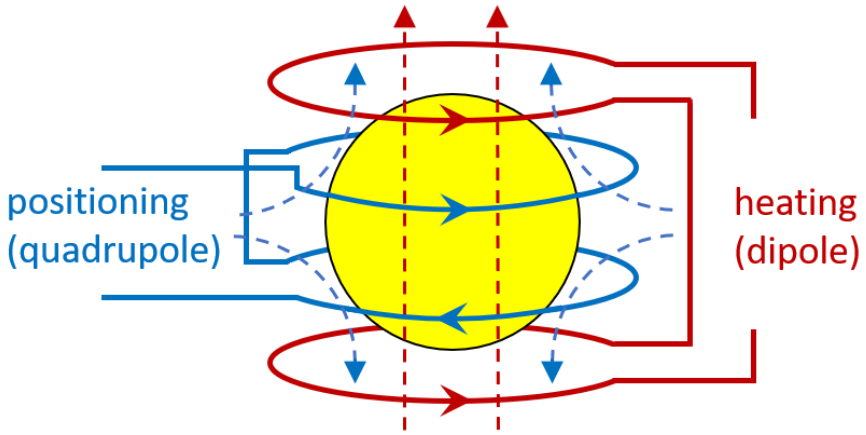

Fig. 3.6: Coil systems and resulting fields of TEMPUS used on parabolic flights. A dipole field is used solely during heating of the sample. A quadrupole field is sufficient to hold the sample in position during a μg-phase.

as a function of the frequency ν by Planck's law [114] as

$$I_{\epsilon_\nu}(\nu, T) = \epsilon_\nu \frac{2h\nu^3}{c^2} \frac{1}{\exp\left(\frac{h\nu}{k_B T}\right) - 1} \tag{3.21}$$

or as a function of the wavelength, by using $c = \lambda\nu$,

$$I_{\epsilon_\lambda}(\lambda, T) = \epsilon_\lambda \frac{2hc^2}{\lambda^5} \frac{1}{\exp\left(\frac{hc}{\lambda k_B T}\right) - 1}. \tag{3.22}$$

The emissivity $\epsilon(\lambda, T)$ is hereby the ratio between the radiated energy by the respective material in contrast to the radiated energy of a black body ($0 < \epsilon(\lambda, T) < 1 = \epsilon_{bb}(\lambda, T)$). It needs to be adjusted before the experiment. If it is unknown, a appropriate value is assumed based on the elemental partners. For small wavelengths Wien's approximation [115] can be used on Eq. 3.22:

$$I_{\epsilon_\lambda}(\lambda, T) = \epsilon_\lambda \frac{2hc^2}{\lambda^5} \exp\left(-\frac{hc}{\lambda k_B T}\right) \tag{3.23}$$

With the approximation and the relation between different emissivities $\epsilon_1 I_1(\lambda, T) = \epsilon_2 I_2(\lambda, T)$, they can be related to the respective temperatures by

$$\frac{1}{T_2} - \frac{1}{T_1} = \frac{\lambda k_B}{hc} \ln \frac{\epsilon_2}{\epsilon_1}. \tag{3.24}$$

If the liquidus temperature T_L^{lit} is well known from literature and a clear experimental liquidus temperature T_{exp} is measured, a correction can be implemented with

$$\frac{1}{T_{\text{real}}} - \frac{1}{T_{\text{exp}}} = \frac{\lambda k_B}{hc} \ln \frac{\epsilon_{\text{real}}}{\epsilon_{\text{exp}}}, \tag{3.25}$$

since T_{real} and T_L^{lit} must be the same and therefore have the same emissivity. The same can be done for T_L^{lit} and the experimentally obtained T_L^{exp}:

$$\frac{1}{T_L^{\text{lit}}} - \frac{1}{T_L^{\text{exp}}} = \frac{\lambda k_B}{hc} \ln \frac{\epsilon_L^{\text{lit}}}{\epsilon_{\text{exp}}}. \tag{3.26}$$

It follows, that

$$\frac{1}{T_{\text{real}}} - \frac{1}{T_{\text{exp}}} = \frac{1}{T_L^{\text{lit}}} - \frac{1}{T_L^{\text{exp}}}, \tag{3.27}$$

which can be rewritten to

$$T_{\text{real}} = \frac{1}{\frac{1}{T_{\text{exp}}} + \frac{1}{T_L^{\text{lit}}} - \frac{1}{T_L^{\text{exp}}}}. \tag{3.28}$$

This formula is used practically, when the emissivity is unknown, to correct the temperature-time profiles of the pyrometer. The exact value of T_{real} depends on the accuracy of the pyrometer, with typical mean deviations of ± 2 K, as well as the literature values for T_L^{lit}, which are frequently assumed with ± 4 K.

With temperature correction, the temperature-time profiles acquired with the pyrometer can be plotted. In general, the samples are heated, melted and cooled down again several times to evaporate impurities, reach deeper undercoolings and get a broad understanding of an alloy. A typical heating cycle is presented in the temperature-time profile (TTP) of Fig. 3.7 (a). The sample is heated by the respective source (ESL: heating laser; EML: induction heating) up to the point where it reaches its melting temperature. The supplied energy is now consumed by the phase change from solid to liquid and increases the heat of fusion, i.e. the latent heat of the system. An actual plateau (melting plateau) is shown in the plotted data. This applies for congruently melting systems (such as intermetallics) when $T_L = T_S$. In non-congruently melting systems the phase transition will start at T_S and end at T_L which will result in a gradient plateau. Only after the sample is completely molten, the temperature will rise again. It is then purposely over-heated [6] to melt away

6 It is over-heated above its melting temperature, not as in a thermodynamic context.

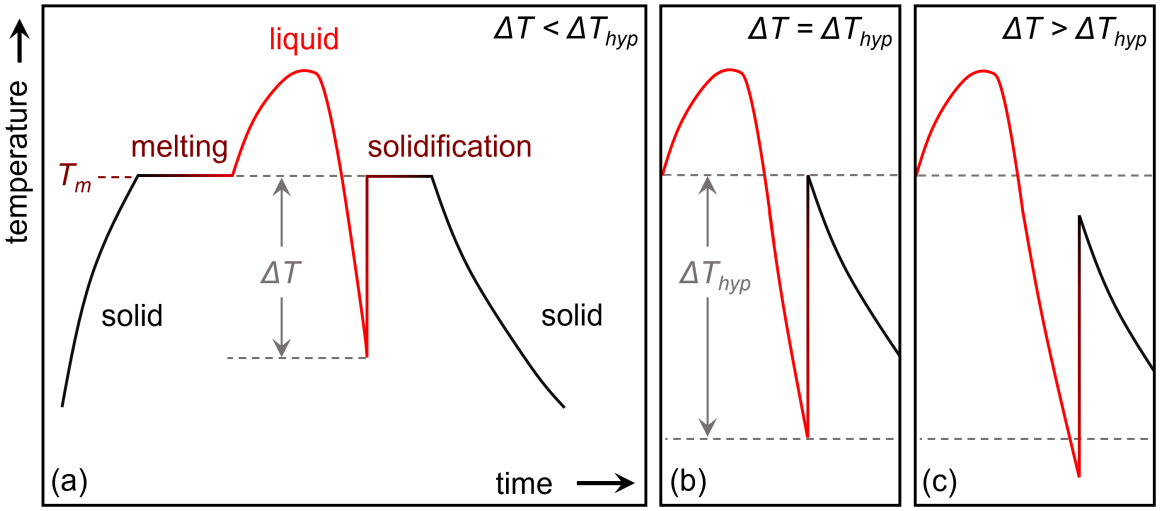

Fig. 3.7: Illustration of different temperature-time profiles (TTP) of undercooled samples. **(a)** A typical heating cycle with an undercooling ΔT below T_m and a subsequent recalescence. **(b)** At the hypercooling limit ΔT_{hyp}, the stored latent heat is just sufficient to heat the sample up to T_m and no post-recalescence plateau is present. **(c)** At even higher undercoolings $\Delta T > \Delta T_{\mathrm{hyp}}$ the latent heat is not sufficient to even reach T_m.

remaining microscopic crystals within the melt and to remove any impurities from the surface by evaporation or dissolving them into the melt.

The heat source is then turned off and the sample starts to cool down. In ESL this is happening solely through radiation, which is highly dependent of the temperature (T^4), as doubling it results in radiated power risen by a factor of 16. This is expressed in the Stefan-Boltzmann law for the radiated power P of a real body by

$$P_{\mathrm{vacuum}} = -\sigma_{SB} \cdot A \cdot \epsilon_T \left(T^4 - T_0^4\right) \tag{3.29}$$

with the Stefan-Boltzmann constant[7] σ_{SB}, the sample surface A, the total hemispherical emissivity ϵ_T ($\epsilon_T = 1$ for a black body), the sample temperature T and the ambient temperature T_0. The emissivity is independent of the temperature for pure metals, as well as intermetallic alloys, provided that there is no phase change [117–119]. Additionally, the cooling rate, that is expected experimentally, depends also on thermal conductivity, the sample's heat capacity and it's dimensions [120]. In EML it is also influenced by the active positioning field, the quench-cooling or the present inert atmosphere.

At a certain point, the phase transition from liquid to solid will take place. The latent heat ΔH_f, that is stored in the undercooled liquid, is released, which is called the recalescence.

7 Stefan-Boltzmann constant: $\sigma_{SB} = 5.6704 \times 10^{-8}$ W m^{-2} K^{-4} [116]

As a consequence, the temperature will rise again rapidly up to the melting temperature where it will reside until the sample is completely solidified. Then it will cool down, until the heat source is turned on again. The undercooling ΔT can be determined by the difference between T_m and the temperature, at which the sample starts to solidify. An undercooling is denoted as hypercooling if the latent heat is not sufficient anymore to reach the melting temperature of the system. In this case, no post-recalescence plateau of solidification is present. This is shown in Fig. 3.7 (b). With $\Delta T = \Delta T_{\mathrm{hyp}}$ the latent heat is just enough to heat the sample up to T_m. It will however, not form a plateau, which implies, that at this point, the sample is already completely solidified. This is called the hypercooling limit. Even deeper undercoolings will not change the height of the recalescence anymore (as there is a defined latent heat in a given system), but shift it, as in Fig. 3.7 (c). Thermodynamically, hypercooling can be expressed by

$$\Delta T_{\mathrm{hyp}} = \frac{\Delta H_f}{C_p} \tag{3.30}$$

with the enthalpy of formation ΔH_f and the specific heat capacity C_p. Both are intrinsic material properties and so ΔT_{hyp} must be a specific point in a respective system. Hypercooling, and the total solidification during the recalescence, can be exploited to conserve metastable phases within the microstructure [121] More detailed explanation of the hypercooling limit in congruently and non-congruently melting systems, as well as a description of unique effects that occur in relation to the hypercooling limit, can be found in [122].

3.2.4 In situ visualization

In situ observations were obtained with a *Photron Ultima APX 775k* high-speed camera (HSC). Levitated samples are freely suspended and their whole surface can be observed directly. The HSC provides the necessary contrast, space resolution and, most importantly, time resolution to resolve the ongoing solidification. Fig. 3.8 shows exemplary HSC recording of moving heat front on a levitating sample in ESL. The frames are always denoted with the time passed, either regarding to the onset of solidification or in relation to the first frame shown. For the latter case, the first frame is denoted with "0 ms".

As mentioned in Sec. 3.2.3, the latent heat, that is released during the recalescence, leads to a rise in temperature. With higher temperature, the radiation of the sample is shifted inversely proportional, due to *Wien's displacement law* [123], to smaller, i.e. visible,

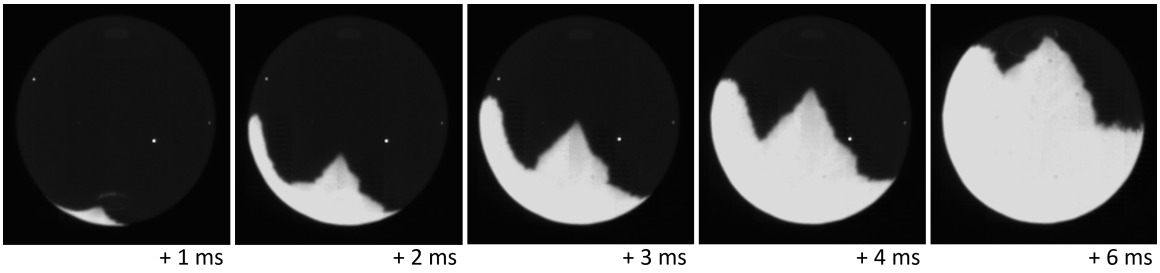

Fig. 3.8: Consecutive frames showing the expanding heat front on the surface of a NiHf sample. Latent heat gets released by the phase transition, which can be observed with the HSC.

wavelengths. This allows direct observation of the moving heat front on the sample. It needs to be noted, that this emission of light solely represents the heat release at or near the surface of the specimen. These observations also only visualize the recalescence until the heat front has engulfed the whole sample and the temperature has increased to the equilibrium melting temperature again. Further ongoing parts of the solidification are mostly not visible as the whole sample has reached a basically uniform temperature. The residual melt is then outshone due to radiation of the whole sample. Hypercooling allows to visualize the whole solidification during the initial recalescence, since the temperature does not reach T_m (T_S in non-congruently melting systems) again and there is no residual melt left.

Observing a sample with the HSC naturally only allows 50% of it to be visible. To analyze the ongoing heat front and derive growth directions or velocities it is necessary to observe the whole sample. In the ESL, this is achieved by a mirror that is placed behind the sample, which was implemented by Kobold [16]. He calculated, that this results in a visibility of 97 – 98 % of the sample.

The velocity of the heat front can be used to identify the growth velocity. In a simple case both are the same. This depends on the system's preferred dendritic growth direction. This direction needs to be identified and correlated to the heat front to calculate the growth velocity. Either way, the surface growth velocity can be measured by the relation between on- and offset of solidification. This is referred to as the First Frame - Last Frame (FL) method and the velocity can be calculated by $v = 2R/t$. The in situ observations are analyzed to identify distinct features, such as kinks, in the heat front. With these features the heat front can be simulated using the 3D-animation software *Blender*[8]. A 3D shape of the heat front within the sample can be constructed, which can be used to identify the growing dendrites and consequently the dendritic growth velocities. The calculated

8 Blender is a free 3D creation suite software released under the GNU General Public License [124].

velocities presented in this work are always written out with a deviation. This deviation was reduced to under 3 %, if the mirror was present during the experiment. Without the mirror, only events could be analyzed, where the growth direction was perpendicular to the camera. The deviation was however larger, mostly in the region of 10 % of the given velocity.

3.3 Differential scanning calorimetry

The differential scanning calorimetry (DSC), developed by [125] is a thermo-analytical method that measures the required heat to increase the temperature of a sample in a standard crucible in relation to an empty crucible. The difference of heat flux is measured for both, the crucible with the sample and the reference crucible, and plotted against the temperature, which is elevated constantly. At physical transformation, e.g. phase changes, the energy input needed, to keep both crucibles at the same temperature, is changed. This results in a negative, or positive input, which is directly connected to the thermodynamic nature of the transformation. An exothermic reaction will result in a negative energy input, since the sample will give away energy in form of heat and the system will consequently need less energy to have both crucibles at the same temperature. Vise versa, the endothermic reaction will demand more energy and the plot will show a positive curve. Practical and more detailed information about different types of DSC and the respective applications can be found in [126]. In this work a NETZSCH DSC 404 C Pegasus with heating and cooling rates of 5, 10, 15 or 20 K/min was used. A rate of 20 K/min was set with alumina crucibles and a purging gas (Ar, 5N) with a volumetric flow rate of 50 mL/min was used. The DSC is calibrated with sapphire calibration standards. The samples had around 150 mg in mass, with a glass embedding of roughly the same mass. The embedding was used to shield the sample from the alumina crucible and to take advantage of the effect, that the the molten glass has a high affinity to absorb oxides, resulting in a purer sample. Together, this can result in deeper undercoolings.

3.4 Drop tube - free fall solidification

Drop tubes are frequently used to simply analyze alloys in a free fall environment together with high cooling rates. Detailed description and a schematic drawing of a drop tube construction can be found in [127]. An alloy sample of about 1 g is put in a zirconia tube crucible with a small puncture of about 0.5 mm diameter at its bottom. The crucible is placed in the top of the 13.4 m vacuum chamber of the construction. The drop tube is evacuated to a pressure of 10^{-6} mbar and backfilled with pure 5N helium gas to ~ 0.5 bar. The specimen is then inductively heated and melted. The temperature is kept sufficiently above the melting temperature of the respective alloy for at least one minute to ensure complete melting. After this, the zirconia tube is over-pressured, so that the molten alloy is ejected through the puncture hole. It is then immediately disintegrated into a large number of small droplets (around 500 - 1000) ranging roughly from $0.01 - 2$ mm. These droplets experience high cooling rates and solidify rapidly. This solidification is happening in free fall in a containerless environment. It was shown for intermetallic alloys that large undercoolings, of over one-third of the equilibrium melting temperature, can be reached in this type of experiment [128]. The droplets were collected and sieved using assorted wire meshes to assort them to several size groups. The cooling rates are directly influenced by the size of the droplets, with smaller diameter leading to faster cooling rates; spheres with a diameter of 300 μm should roughly be in the magnitude of 10^4 K/s [129].

3.5 Microscopy

After successful experimentation, the microstructure of the sample needs to be analyzed to extract information on nucleation, crystal or dendritic growth and grain structure. This is done mostly by microscopical methods that can be differentiated by their wavelength, which is responsible for the spatial resolution of the method. Typically, the specimen is first inspected visually, with optical magnification and then embedded for further grinding and polishing, as described in Sec. 3.1, to allow for a more detailed microscopical analysis.

3.5.1 Optical microscopy

A first qualitative look of the specimen can be made with an optical stereo microscope (*Leitz Ortholux II*, $2 - 50$ x). Features on the surface of the samples can be identified as indications for onset or end of the solidification process. This helps to align the samples in the embedding process.
The polished cross-section can be studied in more detail with a *Zeiss Axioimager A2M* upright microscope. It allows optical magnifications of $12.5 - 1500$ x and is equipped with a polarization filter to highlight certain features within the microstructure, such as grain boundaries or different orientations.

3.5.2 Scanning electron microscopy

Elemental analysis, surface structure and microstructure characterization are investigated by scanning electron microscopy (SEM). A *LEO 1530 VP Gemini* microscope is used with an *INCA* energy dispersive X-ray spectroscopy (EDS) detector and a *Nordlys 2* electron backscatter diffraction (EBSD) detector from *Oxford hkl* together with the *Channel 5* software.
Whereas optical microscopy utilizes the visible spectrum of electromagnetic waves ($\sim 400 - 700$ nm), SEM uses electrons with wavelengths in the range of $0.007 - 0.123$ nm (for 30 and 0.1 kV respectively). Two examples of SEM images, taken with two different detectors are shown in Fig. 3.9. The sample is scanned in a grid pattern with a focused beam of electrons at acceleration voltages ranging from $0.1 - 30$ kV. At 20 kV a resolution of about 1 nm can be reached. Several different scattering processes are detected for each grid point and an artificial image can be processed from the results.
Primary electrons (PE) are created in the system's hot cathode. They are accelerated and focused by multiple magnetic lenses to reach the sample's surface with a sufficiently high resolution. Different detectors can now record the different interactions of the primary electrons with the sample's atoms. Fig. 3.10 illustrates these scattering mechanisms. The PE can be scattered inelastically by interacting with electrons of the element and thereby creating a secondary electron (SE) or a characteristic X-ray quanta. They can also be reflected with high energy by elastic scattering at the atomic core and are than called backscattered electrons (BSE). These mechanisms, their detection and the extracted information are explained in this section. A more detailed breakdown of scanning electron

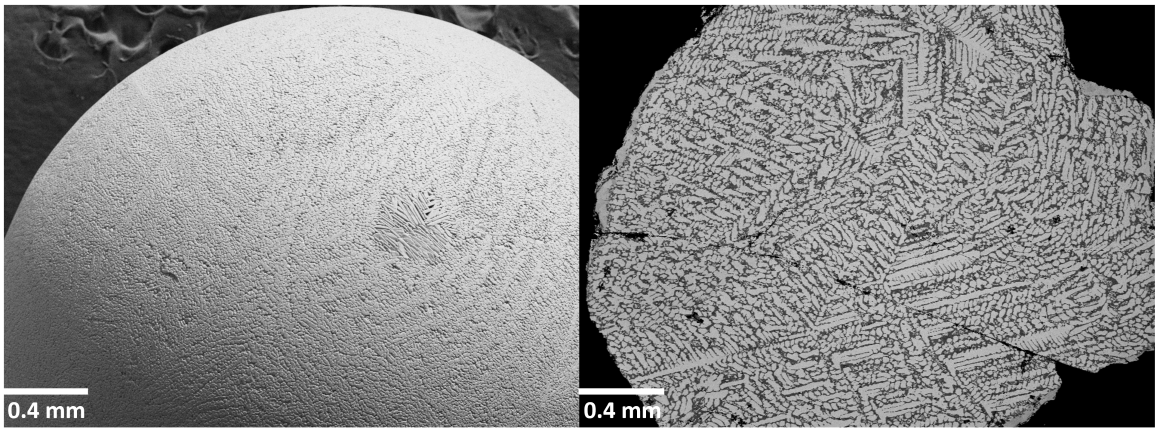

Fig. 3.9: Left: SEM image, taken with the SE detector, from an ESL processed $Ni_{50}Zr_{50}$ sample solidified at an undercooling of 236 K. Right: Image taken with the BSE detector of a polished cross-section of a DSC processed $Ni_{44}Gd_{56}$ sample that solidified without significant undercooling.

microscopy and the underlying physical basis can be found in [130, 131].

Secondary electrons

The detection of secondary electrons is the most common analyzing method of electron microscopes. The detector collects low energetic (< 50 eV) electrons, that are emitted from the outer shell of the sample's atom. This is shown in the left example of Fig. 3.10. At these low energies, the electrons are emitted near the surface of the sample (depth of a few nm). If they would be emitted deeper inside the sample, they would interact with the bulk sample due to their low energies. The designated detector will read different intensities of

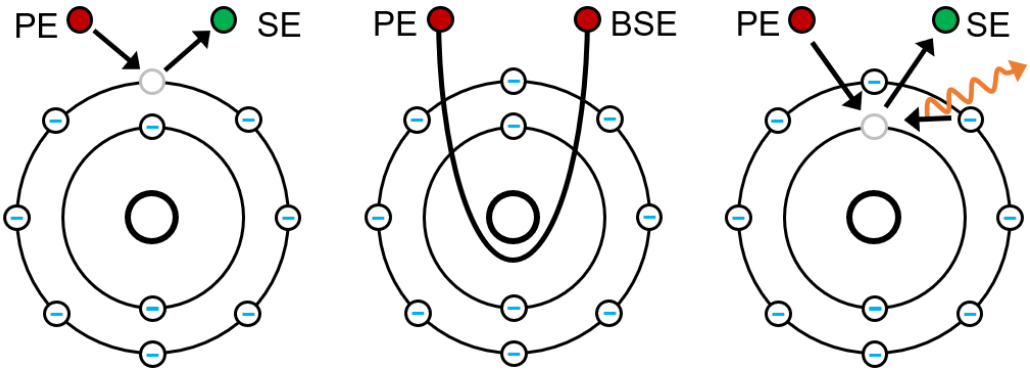

Fig. 3.10: Different scattering mechanisms of electrons with atoms. Elastic scattering is an interaction with the atom's core, whereas inelastic scattering involves the emission of the atom's electrons.

SE it receives based on the sample's topological features. Steep surfaces, that are inclined towards the detector, will generate a brighter spot, as more SE are detected. This method creates topological images of the sample's surface with an appearance comparable to optical microscopy.

Characteristic X-rays

When a PE interacts with a lower shell of an atom, the emitted SE has to be replaced with an electron from an outer shell, i.e. a higher energy level. This process results in an energy difference that is emitted in form of an X-ray quanta. The process is illustrated in the third example of Fig. 3.10. Each element has its characteristic transition energies. By detecting the energy from the emitted X-rays with an energy-dispersive spectrometer (EDS), present chemical elements and their relative abundance can be determined, e.g. to the exact composition of a certain alloy. Detailed descriptions can be found in [132, 133].

3.5.2.1 Electron backscatter diffraction

Electrons can also be elastically scattered at the atom core. These backscattered electrons (BSE), as presented in the central example of Fig. 3.10, have approximately the same energy as the primary electrons (PE). Up to 100 million diffuse scattered electrons can emerge from the sample per second with a penetration depth of the PE beam of a few nm. The sample is tilted 70° and the detector is positioned close to the sample to detect a sufficient amount of BSE. The probability of the elastic scattering is proportional to the mass of the elements at the particular point, where the PE beam hits the sample. BSD (backscatter detector) create contrast images of the specimen.
Additionally, BSE can be detected, based on their specific scattering direction. If some BSE leave the sample aligned to the atomic lattice planes of the material they may create a constructive interference based on the Bragg condition (see Sec. 2.7). This diffraction is visible on a phosphor screen of the EBSD (electron backscatter diffraction) detector, as a so called *Kikuchi* line [134]. Fig. 3.11 illustrates the constructive interference. In 3D space the *Kikuchi* bands represent cones known as *Kossel cones*. The location and orientation of the *Kikuchi* lines to each other correspond to a certain crystal lattice and also to definitive orientations of this lattice. If the geometry of the system is well described, each line can be indexed to specific Miller indices. It is possible to detect a certain crystalline phase

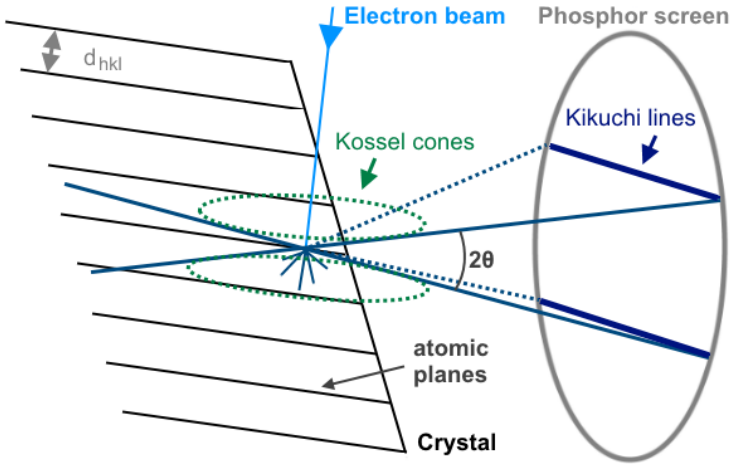

Fig. 3.11: Constructive interference based on the Bragg condition to create *Kikuchi* lines on a phosphor screen. These lines are characteristic to the crystal lattice. They can be used to index the specific orientation of each grain in a given sample.

and its orientation for every grid point to create an EBSD image.
Each indexed pixel can now be color coded as well, to create an EBSD image that displays the differently orientated grains of the analyzed area. Fig. 3.12 shows such an image with the corresponding color code on the right.
Differently colored grains can also be interpreted to visualize the corresponding grain boundaries themselves. The structure of a grain boundary depends (in 3D space) on eight parameters [60]. These are:

- 1) The geometric plane of the grain boundary that is characterized by the *normal vector* $\vec{n} = (n_1, n_2, n_3)$ of the grain boundary. By setting the length of the vector to unity, the geometry can be determined by just n_1 and n_2.
- 2) The rotation of the grain is determined by the *Euler angles* (ψ, θ, ϕ). They are independent from each other (generalized coordinates).
- 3) The structure of grain boundary depends, at the microscopic scale, on a *translation vector* $\vec{t} = (t_1, t_2, t_3)$. It adapts itself, so that the grain boundary energy is at minimum.

The microstructure of a crystal can contain a high number of differently orientated grains. Just with a 2D image of different colored grains, it can be difficult to understand the crystallographic relations between different orientations. Pole figures are constructions to visualize the 3D crystal orientations onto a 2D plane [135]. They are frequently used together with the EBSD technique to analyze the relations between different grains in a

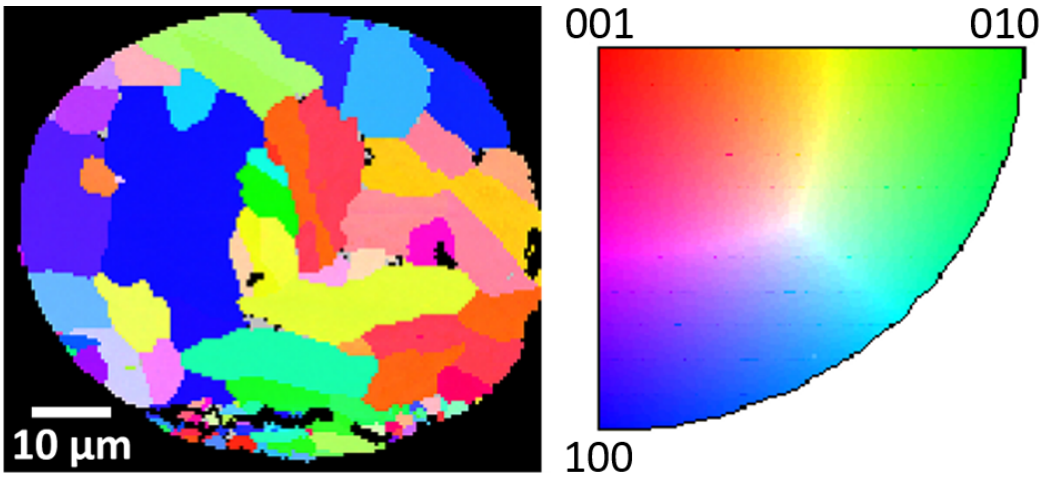

Fig. 3.12: False color EBSD image of a small NiB droplet that was processed in a drop tube. It was grinded and polished before EBSD measurement. It visualizes the different orientations of each grain.

sample. In Fig. 3.13 this construction is depicted. A cubic crystal with a given orientation is placed in the center of a sphere. A direct line from the directions and planes of this crystal is drawn to a point on the sphere. All of these points are then connected to the south pole of the sphere. The intersection of these connections with the equatorial plane creates a plane, that visualizes the crystal orientations and relations as points in an equiangular view. This particular construction is called the *Stereographic projection*.
The inverse pole figure (IPF) is used complementary to visualize orientations related to the crystal reference system, instead of the sample reference frame, that is used in the pole figure. By assigning a color code to the IPF, a color key can be implemented in a respective EBSD image and the corresponding pole figures. Fig. 3.12 illustrates this, as the color legend used is actually an IPF. In practice, IPFs and pole figures are combined to present color and orientation in one pole figure image.
Relations between different structure elements of the crystal can be derived by overlaying the pole figure with a *Wulff net*. This is a stereographic projection of a sphere onto a plane, that preserves angles, but not area. Angular relations between different directions can be deducted easier with an underlying *Wulff net*. An orthorhombic crystal cell and some specific directions are shown in Fig. 3.14. By placing the stereographic projection of the sphere into the pole figure, its great circles can be used to derive relations between different directions. In this example it can be seen, that direction on the highlighted great circle are angled 90° to the [001] direction, since each great circle presents an angle of 10°.
There is an additional detector connected to the EBS detector, whose images are fre-

quently shown in this work and is therefore shortly introduced. The forward scattering dectector (FSD) is positioned below the phosphor screen of the EBSD. It enhances the orientation contrast in imaging and reveals grain boundaries clearly. The EBSD method is thoroughly described in [133] and a detailed work on the current technical status of the EBSD technique is given in [136]. Additional information regarding pole figures and crystal orientations can be found in [135].

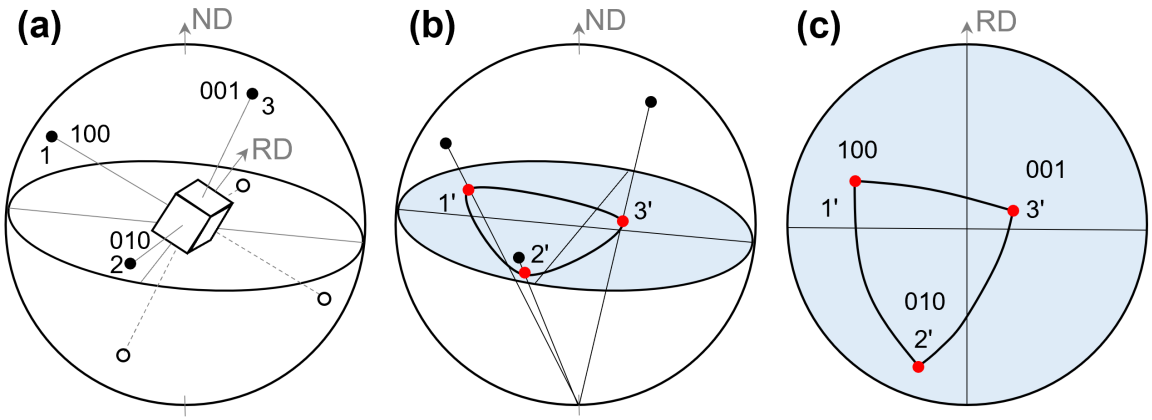

Fig. 3.13: Construction of a pole figure for the ⟨100⟩ directions of a cubic crystal. **(a)** Orientation of the crystal, centered in a sphere. **(b)** Stereographic projection of the crystals directions. **(c)** Pole figure for the ⟨100⟩ directions of the cubic crystal. Illustrations after Gottstein [137].

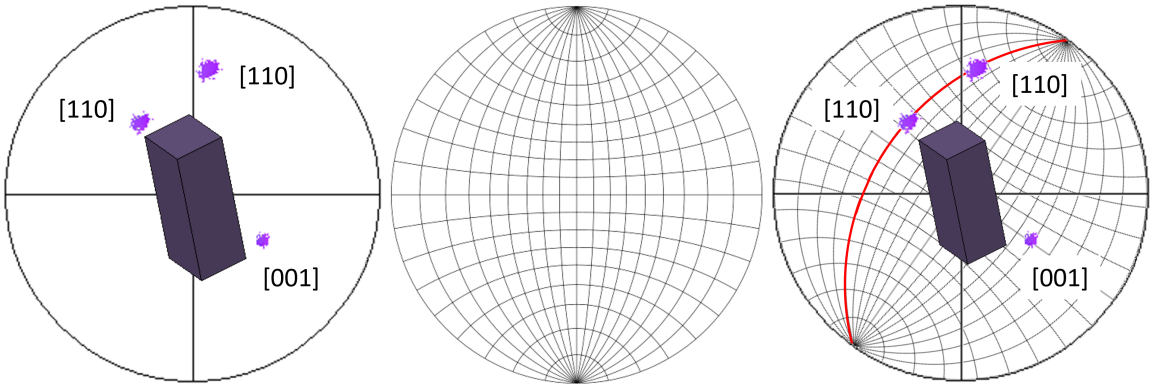

Fig. 3.14: The use of a Wulff net to depict different crystallographic relations and angles to each other. **(a)** IPF plot of specific directions and the visualized crystal orientation of an orthorhombic grain. **(b)** A stereographic projection of the great and small circles of a sphere, called a Wulff net. **(c)** Orientating the Wulff net onto a specific direction reveals crystallographic relations. The directions on the red great circle are angled 90° to the [001] direction.

CHAPTER 4

Symmetric nucleation and growth model in the $Ni_{50}Zr_{50}$ system

This chapter will give a concise summary on the findings of Kobold regarding nucleation and solidification in the NiZr system [16] and the consequent development of a nucleation and growth model by Hornfeck, Kobold and Kolbe (HKK-model) [15]. The motivation for this work was the extension of the model on other systems, that solidify in orthorhombic structure, and a more detailed understanding of the mechanisms at play. The NiZr prototype system solidifies in the CrB-type structure, which properties are crucial for the growth model. The orthorhombic structure is described in detail in Sec. 4.1. With the structure and its characteristics noted, the nucleation and growth model is introduced in Sec. 4.2. A number of crucial features, necessary for the formation of this model, are identified and listed. Sec. 4.3 explains the simulation of other variants of this model, as well as its existence in other CrB-structured systems apart from NiZr. Together with the defined features, other alloys systems can be assessed on whether they follow the same rules during nucleation and growth, which is the subject of Chap. 5.

4.1 The orthorhombic CrB-type structure

$Ni_{50}Zr_{50}$ solidifies in the CrB-type structure (B33 phase). It consists of an orthorhombic, base centered unit cell and contains eight atoms within one cell. The orthorhombic crystal system is defined by three distinct lattice parameters, whereas the bases intersect at 90° angles.

$$a \neq b \neq c \qquad \alpha = \beta = \gamma = 90^\circ \tag{4.1}$$

The CrB-structure has the space group type Cmcm, No. 63. As depicted in Fig. 4.1, it has an elongated lattice parameter b, on which it is centered. The first discovery of this structure type was made by Sindeband and Frueh in 1949 [138, 139], which was later confirmed by using single crystal diffraction [140]. Additional information on the CrB system itself can be found in [141].

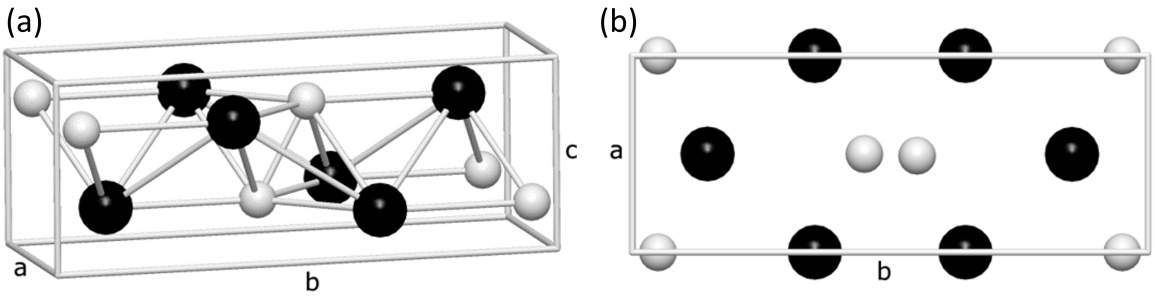

Fig. 4.1: Unit cell depiction of the CrB-type structure. **(a)** Atomic arrangement of the unit cell in a 3D view. **(b)** Top view in c-direction.

Cubic B2 into orthorhombic B33 transformation

The cubic B2 phase and the orthorhombic B33 (CrB-type) phase are closely related energetically, as well as structurally in the alloy systems analyzed in this work[1]. Usually, the B2 phase occurs as a high-temperature (HT) phase with a solid phase transition (SST) into the B33 phase at lower temperatures. It is a first order, structural solid-solid transformation, reordering atoms, based on a temperature change [28]. This transition can also be passed in multiple steps, including the intermediate B19, B19' and other phases [142, 143]. Which phase is stable at a given temperature depends highly on the respective system. In the NiTi system, known for several compositions with shape memory effect [144], it was shown, that the consequent transformation steps to the different B19 phases result in lower energy per atom and an overall lower tension in respect to the B2 phase [145]. This was confirmed as well by ab initio calculations, for the transition from B2 into B19 and B19' [146, 147]. In the CoZr system, both phases (B2 and B33) are energetically close and applied pressure can change the existing stable phase rapidly [148]. Because of such changes, specimens have to be embedded in an epoxy resin, instead of the plastic hot embedding, if it was reasonable to assume a phase change due to the hot embedding for any given system. However, in a previous work, a change between cold and hot embedding, regarding the observed phase, was not determined for the CoZr system [149].

In the context of undercooling it was presented for the NiZr system, that nucleation can occur in the B2 phase with a subsequent SST into the B33 phase [150]. This was shown for $\Delta T = 200$ K. It was presented recently in a nucleation study by Kobold, that homogeneous nucleation is present in intermetallic NiZr at $\Delta T = 300$ K in the B33 phase [17]. Here, B33

1 See App. 1 for a detailed description of the B2 and B33 structures.

solidification was detected for broad range of undercoolings between $\Delta T = 125 - 300$ K with NiZr. In fact, B2 phase nucleation in the NiZr system was only triggered for special cases. This is in line with simulation results, that predict the B33 phase as the primary stable phase in this system [151]. In this work, B33 nucleation was observed as well, with the B2 nucleation being present only very rarely. For other Ni- and Zr-based alloys B2 phase nucleation was determined at various undercoolings [152]. It will be shown in the next section, that the results from Kobold [16] to reach high undercoolings in NiZr were reproducible.

The orthorhombic CrB-type structure itself results from a periodic unit cell twinning from cubic close-packed structures into the orthorhombic cell [153, 154]. It can also be described as a series of stacking faults of $\frac{1}{2}$ [100] $(011)_{B2}$ [155]. The transition itself was worked out by adapting the Kurdjumov-Sachs relation [156] of the well understood Fe-C system and Bain's model [157] to: $\{110\}_{bcc} \parallel (010)_{pO}$ with $b = \frac{a}{2}\langle 100\rangle$ [2]. This is illustrated in App. 5.4, with certain atoms highlighted in color to show the position of the former B2 phase within the B33 lattice after the subsequent transition. The glide direction is indicated by a red arrow. The transition also induces a certain compression to the cubic symmetry element, that is now present in the B33 structure. This is shown in Fig. 4.2 to visualize the orientation of the former B2 phase (green dashed line) within the B33 lattice. The red square indicates a perfect cubic B2 structure. The visible compression in $[001]_{B33}$ direction results in an angle $\alpha \approx 80°$ (as shown in App. 5.3).

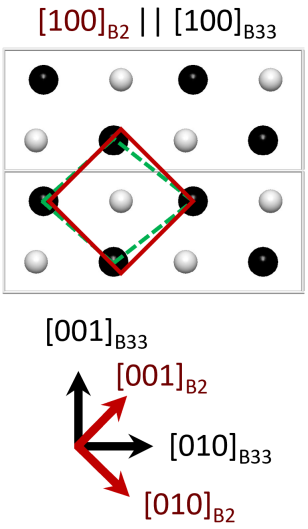

Fig. 4.2: Orthorhombic B33 lattice. The orientation of the formerly B2 phase is indicated with the green dashed line. The perfect B2 structure is shown in red.

Due to this compression, the symmetric element in the orthorhombic structure has to be described by a monoclinic cell with

$$a \neq b \neq c \qquad \alpha \neq \beta = \gamma = 90°, \tag{4.2}$$

instead of a cubic unit cell. Additionally, for this specific cell, the lattice parameters b and c are equal: $b = c$.

2 The abbreviation "pO" means "primitive orthorhombic".

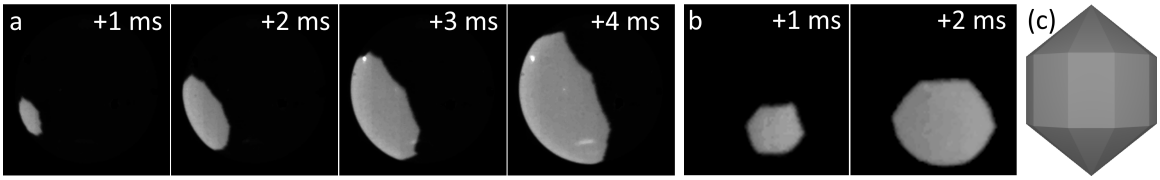

Fig. 4.3: Two sequences of the NiZr heat front in different orientations, as also observed and described by Kobold. **(a)** Four frames of the ten-fold heat front with the characteristic peaks. These peaks are described in [16] and in Fig. 5.1 (as they appear in the NiHf system.). **(b)** The apparent six-fold front, which can be observed when the ⟨001⟩ direction axis of the growing body is aligned with the surface of the sample. **(c)** Simulated 3D shape, which is consistent with such characteristics.

4.2 $Ni_{50}Zr_{50}$ - the prototype system

At undercoolings of $\Delta T > 125$ K a novel nucleation and growth mechanism was described by Hornfeck, Kobold and Kolbe for the $Ni_{50}Zr_{50}$ system [15]. The development of this growth model was based on the in situ HSC observations during solidification made by Kobold [16, 17, 158], that are now discussed briefly as a guided introduction to explain the nucleation and growth mechanisms in this model.

The recalescence of NiZr samples, undercooled more than 125 K, showed a characteristic heat front, that is shown in Fig. 4.3 (a), as a time series of the propagating heat front. This propagation was observed with a ten-fold symmetric structure, identified by the edges of the growing front. Kobold connected this front to a physical shape, he named as *extended decagonal bi-pyramid (dbp)*, but will be referenced in this work with *decagonal body (DB)* for simplicity. This body represents the growing crystal structure within the sample. The DB is shown in Fig. 4.3 (c). If the DB is aligned differently, with it's central axis (upper pyramidal spike to the lower pyramidal spike) perpendicular to the surface of the sample, a seemingly six-fold front is observed, as seen in Fig. 4.3 (b). The microstructure was analyzed by EBSD, where a ten-fold, point-symmetric alignment of grains was observed, which is presented in Fig. 4.4. The pole figures show that all grains are orientated around a common [001] direction, with each orientation being clearly separated to its neighbors. The EBSD and FSD image both show straight grain boundaries that exhibit an angle of approximately 36° between each other. With the lattice parameters of the orthorhombic NiZr unit cell (a: 0.3268(8) nm, b: 0.9937(4) nm, c: 0.4101(5) nm [159]) it was determined, that the diagonal of the unit cell (in respect to the top view in the c-axis, as shown in Fig.4.5, is angled 18.2° to the b-axis of the cell. For better visualization, all cell orientations are

shown above their respective grains. This is calculated by

$$\phi = 2 \arctan(a/b). \tag{4.3}$$

The angle of the diagonal is highlighted in Fig. 4.5. It was shown, that for two unit cells, angled to each other by 36.4°, the diagonal of the cell will form the boundary between both grains. This led to the conclusion, that the grain boundaries of the microstructure presented earlier, make up this diagonal of the unit cell as well. It is implied, that this is a most favorable twinning boundary for systems with this orthorhombic cell. The angle can also be found in the pole figures of Fig. 4.4 (b), as each distinct orientation spot is rotated to its neighboring spot by this angle. For a perfect atomic alignment on this twinning boundary, it was simulated, that a certain shift has to be present between both neighboring grains. This shift was observed by transmission electron microscopy to match the predictions [15]. As a short summary, the following observations were made up to now:

- In situ recording of the solidification of a ten-fold symmetric front. Together with in situ X-ray diffraction the initial solidification of the B33 phase is validated [16]. If the ten-fold heat front is observed, the system solidified in the B33 phase. A subsequent transition from the HT B2 phase into the orthorhombic B33 phase, as described in Sec. 4.1, can then be ruled out.

- A ten-fold microstructure, as observed with EBSD, with all grains aligned to a common [001] direction. With the DB, it was concluded that the primary growth

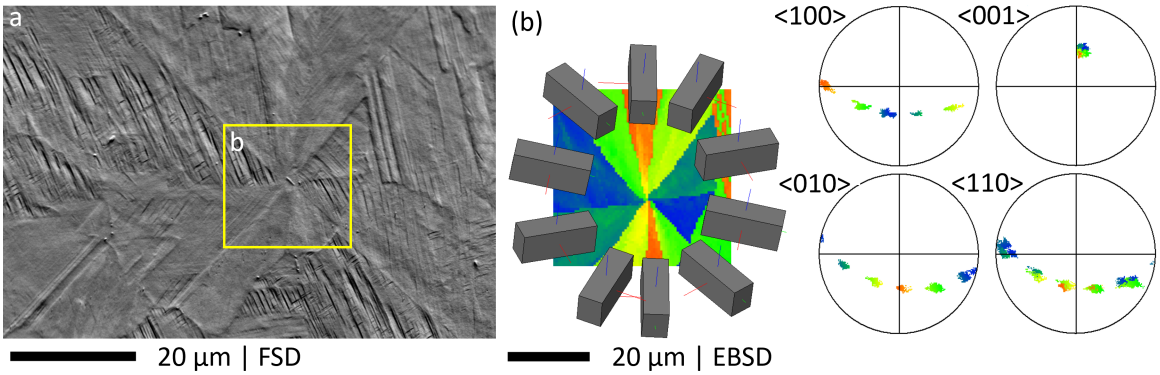

Fig. 4.4: Observed ten-fold microstructure in NiZr. **(a)** Electron image of the microstructure with the highlighted part, which was used for EBSD. **(b)** EBSD image and the corresponding pole figures with IPF coloring. Additionally the orthorhombic unit cells are aligned around the EBSD image to illustrate their common orientation around a single [001] direction.

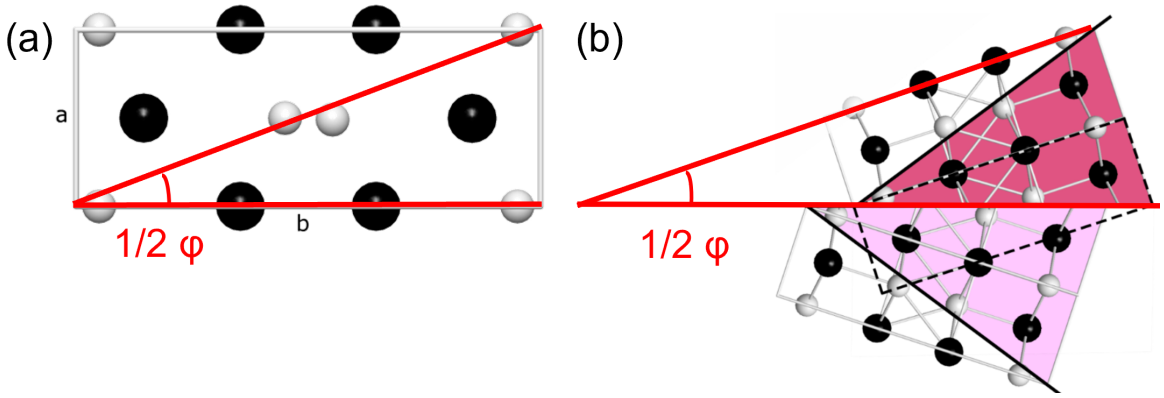

Fig. 4.5: Relation between the angle ϕ and the orthorhombic unit cell. **(a)** Unit cell top view with highlighted angle $\frac{1}{2}\phi$ between the b-axis and the diagonal. **(b)** Illustration of the grain boundary formed by the diagonal of two neighboring unit cells, resulting in a orientation change of ϕ.

direction is the [001] direction. The ten edges are formed by secondary dendrites moving in a different direction away from the primary growth direction.

- Geometric validation of the grain boundary angle ϕ between two orthorhombic grains. This results in a ten-fold symmetry in the NiZr system ($360°/\phi$, with $\phi_{NiZr} = 36.4° \rightarrow$ ten-fold symmetry).

- The shift between two neighboring grains, to realize a perfect atomic arrangement at the twinning boundary was proven by transmission electron microscopy to match the predicated value.

- Kobold observed singular nucleation events in the NiZr system. Heterogeneous nucleation was mostly obstructed, due to the experimental conditions. He also showed, that the nucleation is most probably homogeneous at high undercoolings ($\Delta T = 300$ K) [17] and it is therefore reasonably assumed, that a single nucleus grows into this microstructure.

With these observations, a nucleation and growth model, that covers the process from the onset of nucleation up to the dendritic growth that runs through the whole sample, was developed and presented [15, 16]. This model is shown, at an atomic scale, in Fig. 4.6. A core structure is visible in the center (green). From this core structure, the ten-fold twinned microstructure grows in a spiral pattern outwards. This clockwise spiraled growth continues until dendrites form. When dendritic growth takes over, each grain boundary will form the stem of a dendrite, resulting in ten dendrites, moving outwards at

the geometrically defined angle ϕ. This results in ten differently orientated grains, that are visible in Fig. 4.4.

The primary dendrite growth direction is, in the schematic of Fig. 4.6, the point of view into the image plane. Ten secondary dendrites grow outwards, constituting a grain boundary in each of their stem and therefore creating ten different grains. This schematic model was set up with the lattice parameters of the NiZr unit cell and based on energetically favorable atom positioning at the grain boundaries. The core structure (green) was constructed in the center, to be built by three consecutive decagons (in 3D: pentagonal antiprisms) and a single Zr atom in the very center. These decagons present a quasicrystalline nature and therefore a unique connection between quasicrystals and a twinned, periodic microstructure.

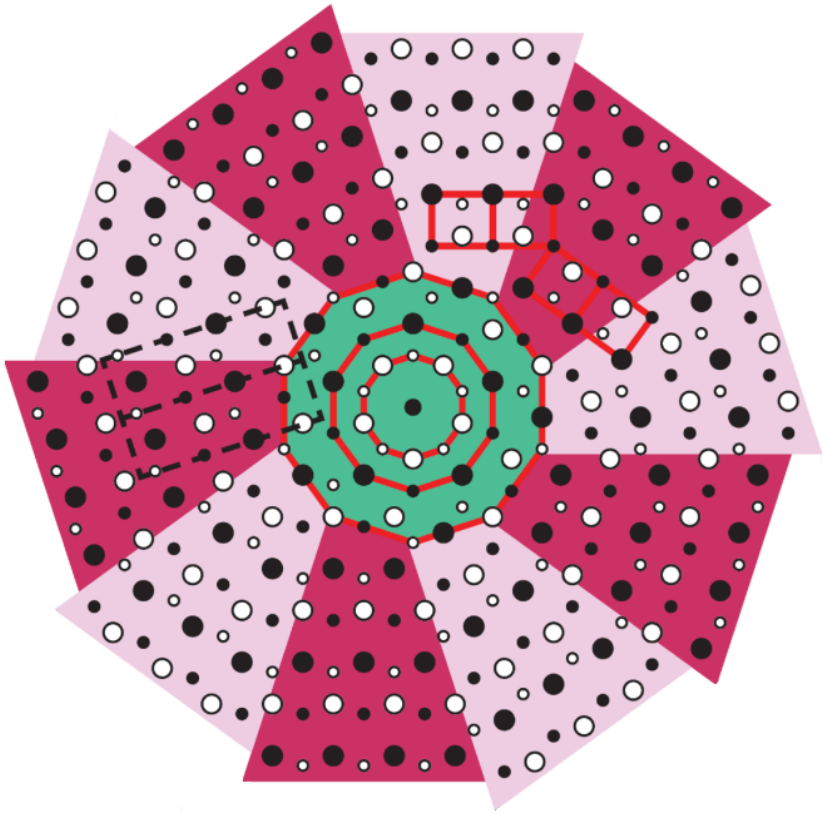

Fig. 4.6: Schematic 2D presentation of the developed nucleation and growth model at an atomic scale. From a core structure (green), the ten-fold twinned microstructure (red tones) grows outward in a spiral pattern. At a bigger scale, a dendritic growth will take over, with the grain boundaries forming the stem of each dendrite. The unit cell (black dashed lines) and symmetric relations (red lines) are highlighted to show, that the symmetry advances beyond grain boundaries. Adopted from [16].

Quasicrystal nucleation

The homogeneous nucleation in NiZr and the point symmetric microstructure, together with the icosahedral quasicrystalline (QC) core of the calculated model, left only few options of a singular nucleus structure in NiZr. Ten-fold QC were first observed in AlMn in 1985 [160], followed by several other systems, such as AlNi and AlFe [161–163] The assumption of an icosahedral nucleation into a QC core structure was therefore reasonable. An icosahedron, as shown in Fig. 2.12, is formed by a singular central atom, surrounded by 12 equidistant atoms creating the highest order locally possible. Generally, ISRO is common in metallic melts [12, 13, 164]. This is, however, not the case in the NiZr system, as Holland-Moritz showed that no ISRO is present in undercooled NiZr melts [165], explaining the well undercoolability of this system. Yet, an icosahedron still exhibits the highest local order and so, such atomic arrangements are forming and decomposing in the melt at each moment, since they do not reach the critical size to grow further. With rising undercooling, the critical radius is more likely to be exceeded and the icosahedral core grows. This implies, that the first icosahedral nucleus that is formed and can extend beyond its respective critical radius will trigger the nucleation event. Kobold showed, that the theoretical critical nucleus size compares well with the size of the (green) nucleus structure in Fig. 4.6 and consists of roughly 290 atoms.
Such ten-fold nucleation structures were also observed in rapidly quenched NiZr by heating an amorphous, melt-spun NiZr matrix [166, 167]. In Al-Fe alloys, ten-fold microtwins were explained by the decomposition of an Al-Fe decagonal quasicrystal [161].

The dendritic growth of this model

The dendritic growth, following from the presented QC nucleation and subsequent twinned growth, was evaluated in this work. The primary dendrites, growing in [001] direction, were already described. The exact direction of the secondary dendrites however, remained unknown. In general, the observed growth front of structures in the melt, such as the DB, is characterized by a simple rule: Dendrites grow into vertices. The dendritic growth forms the edges of the observed body at defined angles. The plane between dendrites will be filled usually as a flat face of the body. This can be understood easily by thinking about an octahedron, which forms by six ⟨100⟩ dendrites in a cubic crystal system. Between these dendrites, eight triangular faces are formed.

Table 4.1: Values for different ratios of the decagonal body, based on different assumptions of the growing secondary dendrite. (*) As defined by the analysis of the heat front by Kobold [16].

	DB	⟨223⟩	⟨111⟩	⟨112⟩
B [nm]	8.220	8.220	8.220	8.220
A [nm]	6.576	6.576	6.576	6.576
D [nm]	7.124	6.970	10.455	5.228
R	1.5*	1.53	1.02	2.04
γ	30°	30.5°	21.5°	38.2°

With the geometric ratios of the DB, listed by Kobold, and shown in Fig. 4.7 (a) and the first column of Tab. 4.1, the angle γ was determined. It is the angle between the (001) plane and the direction that leads into one of the vertices of the body (which must be equal to the secondary dendrite growth direction). Given the listed geometric ratios, it was calculated to $\gamma_{geo} = 30°$. When the unit cell parameters of NiZr are considered, the [223] direction will have an angle of $\gamma_{[223]} = 30.5°$. Other reasonable dendrites, as they all follow the {110} planes, are $\gamma_{[111]} = 21.5°$ and $\gamma_{[112]} = 38.2°$, but they all have a much higher deviation to the observed ratio of the DB. The {110} planes, as will be later shown in Sec. 5.2, are common twinning planes in orthorhombic alloys and are also utilized in this growth model.

Fig. 4.7 (b-e) illustrate the derivation of the secondary dendrite growth with the schematic of the growth directions into the vertices shown in Fig. 4.7 (e). In the unit cell in Fig. 4.7 (d) it is highlighted, that the [223] dendrite follows along the $(1\bar{1}0)$ plane. This can be generalized for the ten-fold symmetry, as all ⟨223⟩ directions run along a corresponding {110} plane. This is additionally shown in a stereographic projection of the CrB unit cell in App. 2.1. At last, it should be discussed, how the space, between the main dendrites is solidifying. Fig. 4.8 (a) shows an optical image of a cross-section of NiZr. It presents the same symmetric growth throughout the whole of the cross-section, as described by Kobold. Fig. 5.28 (b) gives a close up of one secondary [223] dendrite. On the central axis of this dendrite, multiple point symmetric structures can be identified. The analysis of these structures revealed, that they are in fact ten-fold dendrites, equal to the primary dendrite. These *tertiary dendrites* have the same [001] growth direction as the primary dendrite and they locally show the exact same EBSD image and pole figures of ten differently orientated grains ordered around a common [001] axis. Subsequent iterative polishing of the cross-section of an additional 50 μm each step has shown, that these structures are preserved through depth and also do not change significantly in their cross-sectional extension. This is depicted in Fig. 4.9 in four subsequent steps. The tertiary

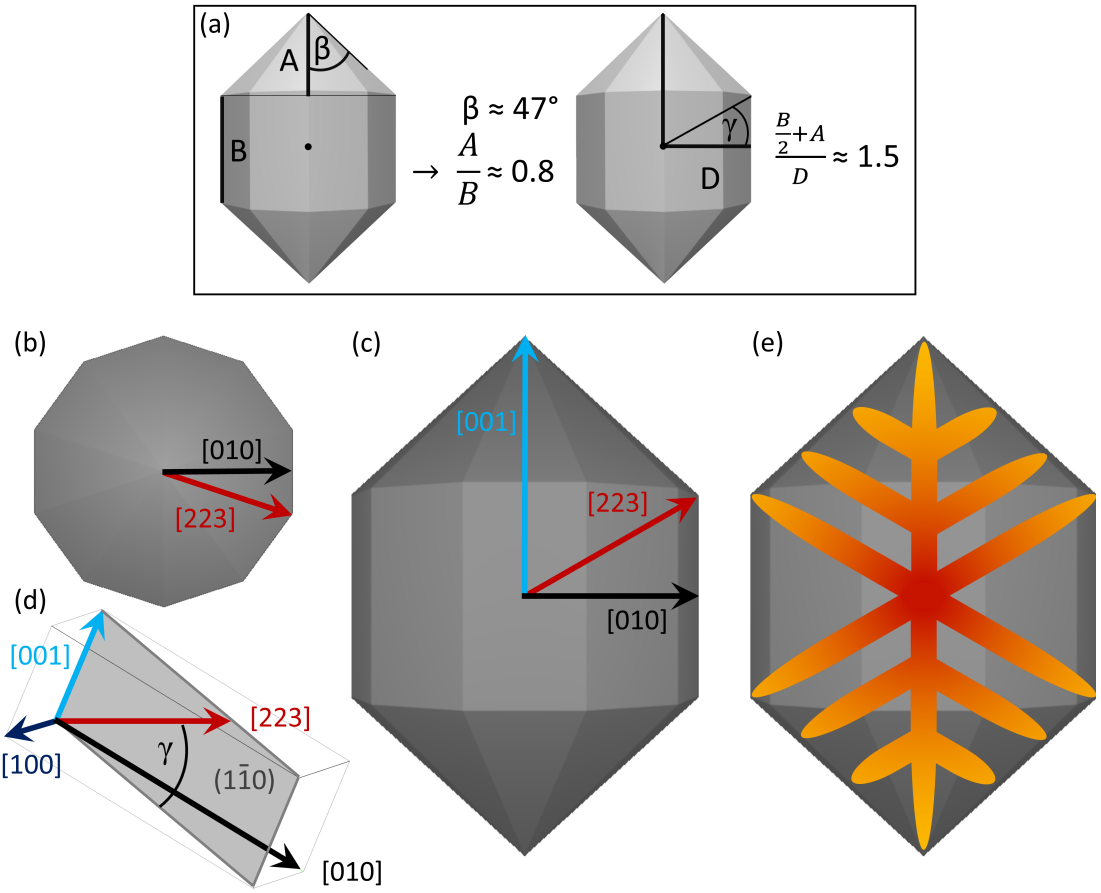

Fig. 4.7: Reconstruction of the different dendrites, that span the DB in the NiZr system. **(a)** Different geometric ratios, based on the observed heat front during recalescence; adopted from [16]. Important directions are drawn in the top **(b)** and side **(c)** view of the DB. The cross-section of the DB, shown in **(c)**, the $(1\bar{1}0)$ plane, is also highlighted in the schematic unit cell in **(d)**. **(e)** The dendrite system is visualized, spanning the DB with the main $\langle 001 \rangle$ dendrites and the secondary $\langle 223 \rangle$ dendrites.

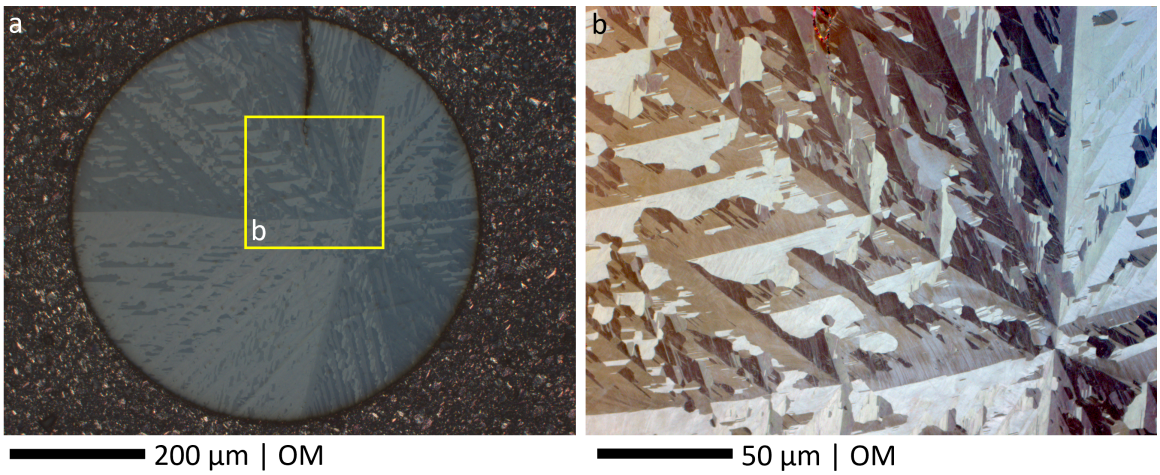

Fig. 4.8: Cross-section of a processed NiZr sample. **(a)** The cross-section shows, that the ten-fold symmetric growth structure consists through the whole visible section of the sample. **(b)** A close up view of on of the secondary dendrites with several tertiary dendrites located on its central axis.

dendrites have a shape, that can be best described cylindrical, instead of spherical. It can also be perceived, that they seem to spread only in certain, defined directions, as it is the same for each of the tertiary dendrites. This trend seems to follow the growth direction of the secondary dendrite (lower right to upper left of the images in Fig. 4.9). However, the main direction of further growth of these tertiary dendrites is aligned with the [001] growth direction of the primary dendrite.

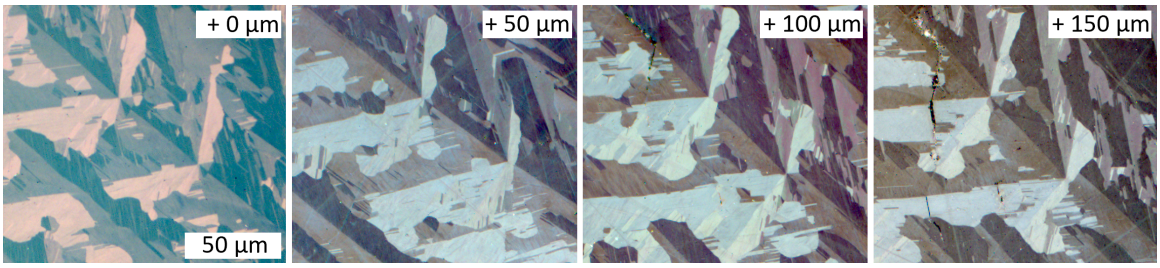

Fig. 4.9: Two tertiary dendrites followed in consecutive images, each presenting a cross-section polished by additional 50 μm. Both dendrites persist and are therefore expected to have a cylindrical shape.

4.2.1 Crucial features of the nucleation and growth model

Based on the findings for the NiZr prototype system [15, 16], that were presented in the last section, the symmetric nucleation and growth model is characterized by five crucial features, that are found to be necessary for its formation and observation. These are:

1. **Deep undercooling and singular nucleation.** A singular nucleus was necessary to observe the subsequent structure and the heat front during the in situ analysis. It was also shown, that the ten-fold microstructure for NiZr was only present at large undercoolings. A nucleation study was conducted to show, that at $\Delta T = 300\,\mathrm{K}$ homogeneous nucleation is reached in the NiZr system [17]. It is likely, that a singular core nucleated and propagated through the sample, before a second nucleation event occurs. As described, the undercooled melt of NiZr showed no ISRO. It was therefore assumed that, close to homogeneous nucleation, the icosahedral core forms through random chance by the atoms in the melt. In this instance, a nucleation event is triggered.

2. **Nucleus based on an icosahedron.** The icosahedron is basis for the growth of the QC core structure. This core grows to a certain size and will then transition into the dendritic 10-fold microstructure with the CrB-type orthorhombic lattice. Icosahedrons show pentagonal and decagonal symmetry elements [168] and are an ideal nucleus for the 10-fold macroscopic growth structure.

3. **Solidification within the CrB-structure (B33 phase).** During recalescence from the undercooled melt, the solidification must set in within a thermodynamically stable regime of the orthorhombic B33 phase.

    a) **Lattice parameter ratio a/b.** The grain boundary angle (GBA) between two grains is a direct consequence of this ratio. The lattice, and inherently the atomic spacing, is responsible for the n-fold symmetric outcome. With an angle of 36.4°, NiZr is an ideal system, as it results in a ten-fold symmetry, which is in accordance with the core structure of the icosahedral QC.

    b) **Twinned dendrites.** The ten secondary dendrites, growing outwards from the primary [001] dendrite into the ⟨223⟩ directions. Each are formed by a twin boundary in their stem. The ten-fold symmetry is therefore present from the

onset of solidification as it is imprinted into the structure already with the growing dendrites.

4. **Orientation around a common [001] direction.** A key characteristic of this model is the alignment of the ten grains around one [001] direction. Generally, only one primary [001] direction is observed, which is direct evidence of a singular nucleation event. Multiple [001] directions would not be inconsistent with the proposed model, as long as the grains in these different growth domains are orientated around their respective primary dendrite in the discussed relations. However, observability would be highly obstructed in such cases.

5. **Stable B33 phase during cooling.** Solid phase transitions are common in many alloy systems. This can become problematic, and will impede observations, if the former structure is no longer recognizable or if the transition induces tensions.

With these crucial features defined, other systems can be evaluated. Chap. 5 assesses several different CrB-structured alloys and studies their accordance to these features. It is later discussed, in Sec. 5.5, whether the symmetric nucleation and growth model of NiZr can be understood and treated as a universal growth model for CrB-structured alloys, and possibly other orthorhombic structures, or if each alloy has its own unique characteristics.

4.3 Structure variants

As the symmetry of the grown grain structure is based on the lattice parameter ratio a/b of the orthorhombic B33 phase, theoretically other symmetries can be calculated. Based on the Eq. 4.3, different angles are presented in Tab. 5.1, which lists several alloy systems, their respective lattice parameters and the expected symmetry. It was shown, that at least the even variants 8- and 12-fold[3] are symmetrically possible, as visualized in Fig. 4.10 [15, 16]. It can be seen in both images, that the chirality of the spiraled growth (see Sec. 4.2) can change. The core structure and size can also change in relation to the NiZr prototype model in Fig. 4.6. A theoretical 2D arrangement was also prepared for uneven 9-fold symmetry, as seen in the right part of Fig. 4.11. In practice, uneven symmetry, and also even symmetries deviating from 10-fold, may cause growth barriers

3 Note, that for no system with CrB-structure, the a/b ratio results in a 12-fold symmetry. The geometrically calculated symmetries range from 8- to 11-fold and were presented in [16].

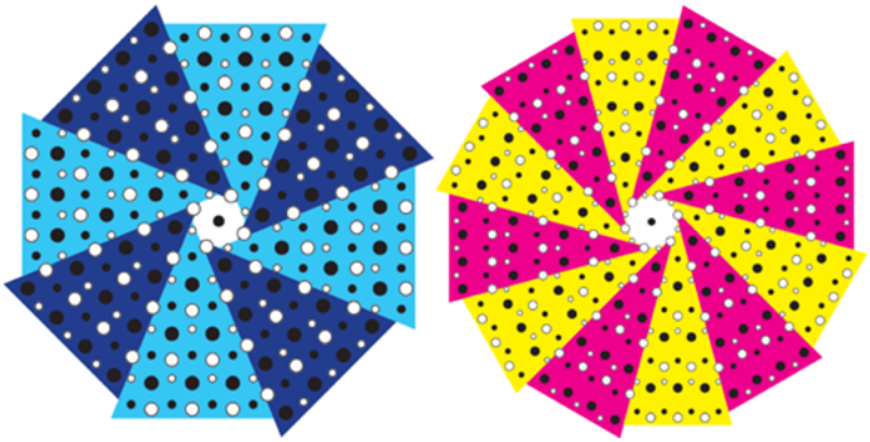

Fig. 4.10: Two 2D simulations of possible 8- and 12-fold symmetries, taken from [16]. The difference in chirality of both examples is visible as well as the spiral nature of the atomic arrangements.

for this model. It is based on a decagonal symmetry emerging from the icosahedral nucleus. As shown in Fig. 2.12, ten out of the 20 faces of the icosahedron are positioned on an outer ring, while 2x5 faces are connected to the upper and lower edge of the cluster. It was already discussed in Sec. 2.5, that ISRO is the basis for the QC core structure and that several alloy systems are known to nucleate these QC from the ISRO. The ten-fold symmetry may therefore be the ideal case of this nucleation and growth model.
Other n-fold symmetries could be based as well on the icosahedral core structure and only result in different macroscopic symmetry due to growth defects imposed by the orthorhombic unit cell parameters. They could also be explained by other QC cores, as five-, eight- and 12-fold QC have been described. [168, 169]. These may form based on other SROs present in the melt of different systems. Which nucleation case is most plausible within the proposed growth model will be discussed in detail during the assessment of the model in Sec. 5.5.

Fig. 4.11 also indicates the cell structure of the CrB-structure (highlighted in green), as well as other symmetric elements (orange), similar to Fig. 4.6. It can be seen, that with lower symmetry, geometric distortions might be induced. In the eight-fold example it is clearly visible, that the alignment of the atoms to the cell structure is shifted. It will be discussed later, e.g. in Sec. 5.3 for the proposed eight-fold NiB system, how these distortions influence the model in its macroscopic growth. The nine-fold example in Fig. 4.11 shows, that an uneven symmetry can be constructed, at least geometrically and in 2D. It will be discussed later, mainly for the NiGd system (Sec. 5.2), which practical problems are connected with an uneven symmetric growth. Even symmetries always show $\frac{n}{2}$ visible

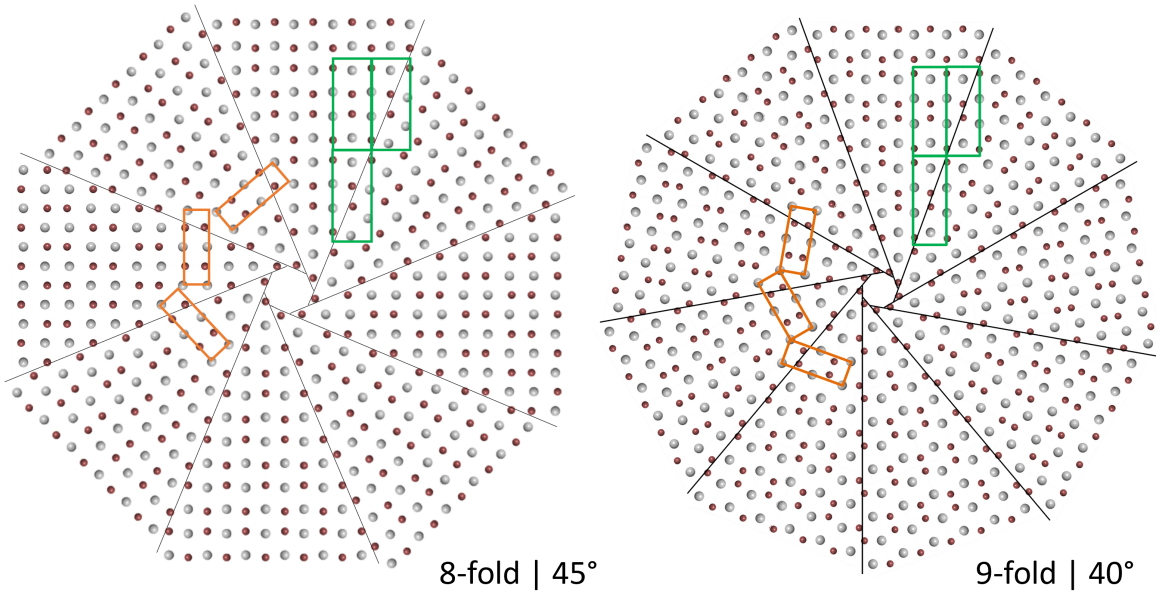

Fig. 4.11: 2D geometric simulation of possible 8- and 9-fold symmetric growth structures. Cell structures (orange) and symmetric formations (green) that are also found in Fig. 4.6 are highlighted to visualize, that the twinning grain boundaries impose no energetic boundary for the atomic layout. However, with lower symmetry, as seen in the 8-fold example, the alignment becomes shifted.

different crystal orientations, since the ones that are directly opposing each other, are orientated in the same crystallographic orientation. This is not the case in uneven symmetric structures. They will have n different orientations.

CHAPTER 5

Universal growth mechanism in CrB-structured alloys

The main objective of this work was to study the existence of the $Ni_{50}Zr_{50}$ nucleation and crystal growth model, described in the previous chapter (Chap. 4), in other systems of the orthorhombic CrB-phase (B33 structure type). It is proposed, that this growth model may represent a universal mechanism in this crystal structure, and maybe even other orthorhombic structures. The assessment was done by in situ HSC observations of the solidification and the following microstructure analysis with optical- and electron microscopy methods. In Sec. 4.2, crucial features were established, that are necessary for the growth model. These are mainly relevant parameters for the formation of such growth, but also essential to observe and investigate the grown structures. Each system analyzed in this work, was assessed based on these features. This assures a consistent evaluation, which is done in Sec. 5.5. A complete list of all features found in each respective system is found in Tab. 5.3. Additionally, relevant observed phenomena, that influence to growth model, are also discussed in the respective sections. In particular, the B2-B33 solid-solid transition, described already in Sec. 4.1, is evaluated in Sec. 5.1.2, due to its presence in the Ni(Zr,Hf) systems. To get an overview of the studied systems, Tab. 5.1 introduces them together with their respective lattice parameters. These are used to calculate expected values for the grain boundary angle and the proposed symmetry.

The alloy systems were chosen based on *Pearson*[1] data, regarding the formation of the B33 phase. It was also considered whether the systems are already known to be processable in levitation experiments, as well as the viability of their practical handling, i.e. radioactive, poisonous and highly reactive elements were drawn out. The focus of this work was set to systems with CrB-type structure (B33 phase), which was introduced in Sec. 4.1. These systems are the most comparable with the NiZr. The main difference should be the atomic spacing and therefore their lattice parameters, resulting in different n-fold symmetries in the proposed growth model. Additionally, ternary alloys were investigated. In these systems, constituent B was substituted with a third element C, so that: $A_{0.5}B_{0.5-x}C_x$. $FeZr_3$ was the first system tested, that solidifies in a different orthorhombic structure

1 Pearson's Crystal Structure database; Release 2018-22 [170].

(Re_3B-type).

Tab. 5.1 shows the calculated and expected grain boundary angles (GBA) ϕ for each alloy system. Most CrB-structured alloys have an a/b ratio, that results in a nine- or ten-fold symmetry, eight- or eleven-fold structures are the exception, but possible, as seen here with NiB or AlHf. Additionally, the a/b ratio only rarely concludes to a value near a full integer. In practice, there is a certain deviation, which one could interpret to induce tensions and difficulties during the proposed growth mechanism. This will be looked upon in each system's section, as well as in the final assessment of the proposed model.

Table 5.1: Alloy systems investigated in this work with their respective lattice parameters. The expected grain boundary angle and symmetry based on the symmetric growth model are also given. The angle ϕ is calculated with Eq. 4.3.

System	Lattice parameters			Ref.	Ratio	Calc.	Sym.	
	a [nm]	b [nm]	c [nm]		a/b	ϕ [°]	Calc.	Expected
NiZr	0.3268(8)	0.9937(4)	0.4101(5)	[159]	0.329	36.42	9.88	10-fold
NiHf	0.3220(5)	0.9820(6)	0.412(1)	[159]	0.328	36.32	9.91	10-fold
NiZrHf	0.32154	1.00246	0.41070	[171]	0.321	35.59	10.12	10-fold
NiB	0.2936(5)	0.7396(2)	0.2967(5)	[172]	0.397	43.30	8.31	8-fold
NiGd	0.3778	1.0365	0.4221	[173]	0.365	40.06	8.99	9-fold
AlY	0.3884(2)	1.1522(4)	0.4385(2)	[174]	0.337	37.24	9.67	10-fold
SiZr	0.3757	0.9915	0.374	[175]	0.379	41.52	8.67	9-fold
PdZr	0.33305(3)	1.0304(1)	0.43745(4)	[176]	0.323	35.80	10.06	10-fold
PdHf	0.329	1.021	0.438	[177]	0.322	35.70	10.08	10-fold
AuGd	0.376	1.094	0.464	[178]	0.344	37.97	9.48	9-fold
$FeZr_3$	0.33249(2)	1.09731(7)	0.88066(5)	[179]	0.303	33.71	10.68	11-fold
CoZr	0.325	0.971	0.419	[180]	0.335	37.04	9.72	10-fold
NiCoZr	0.325	0.971	0.419	[180]	0.335	37.04	9.72	10-fold
PdCoZr	0.333	1.030	0.437	[181]	0.323	35.80	10.06	10-fold
AlZr	0.3361(1)	1.0884(3)	0.4273(1)	[182]	0.309	34.34	10.48	10-fold
AlHf	0.3253	1.0822	0.4280	[183]	0.301	33.50	10.75	11-fold

5.1 The ten-fold $Ni_{50}Hf_{50}$ system

NiHf was chosen, because Zr and Hf have very similar properties and are almost completely miscible [184]. According to the growth model, it is expected to solidify in a

ten-fold symmetry, with the grain boundary angle of 36.3° fitting slightly better to such a model, than the angle of 36.4° in NiZr. It was possible to reach undercoolings of up to 460 K with NiHf, which was substantially higher than $\Delta T = 300$ K for NiZr. The HSC recordings during these high undercoolings revealed a heat front, that is already known from the NiZr system. It is reconstructed in Fig. 5.1 to represent the decagonal body (DB) as well. The front was not as sharp as in NiZr, but distinct features, such as the peaks from the edges of the DB were clearly assigned. It is also shown, best in Fig. 5.1 (c), that the DB exhibits similar growth angles, of its central axis in relation to the central axis of the sample, that are present as well in NiZr. This tilt is responsible for a characteristic elongation of the heat front on one side (blue arrow) and a compression on the opposite site. The DB was shown to be the geometrical body spanned by the dendrites growing in NiZr (see Sec. 4.2). Its presence in the NiHf system is a first validation of the assumption of a ten-fold growth in this alloy.

The subsequent optical analysis revealed several symmetric growth structures in one cross-section of a processed sample. At least one of these structures was always identified in a given specimen. Shown in Fig. 5.2, these structures have ten-fold symmetry and are

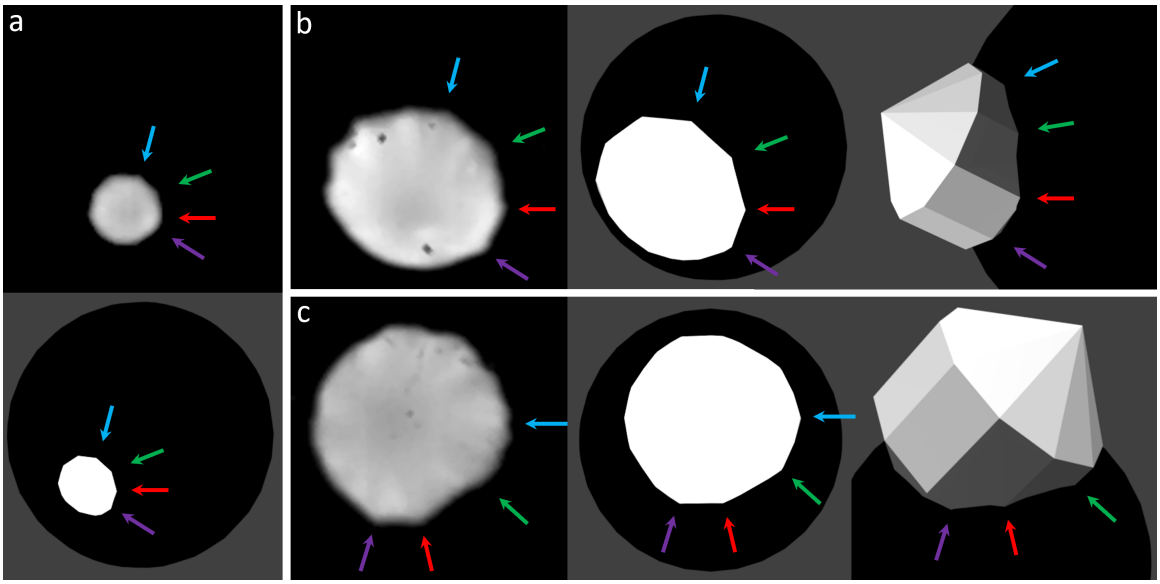

Fig. 5.1: Three consecutive stages of the observed heat fronts (black background) and the simulated growth fronts (gray background) in the NiHf system. Part (a) and (b) are taken from the heat front of a sample undercooled 445 K, which is also shown in Fig. 5.3. The sample in part (c) is undercooled 431 K. Differently colored arrows indicate to definitive features of the growth body, which was used for the NiZr system as well [16] (described in Sec. 4.2). In the right corner of part **(b)** and **(c)**, the simulated body is visualized to highlight the formation of said features.

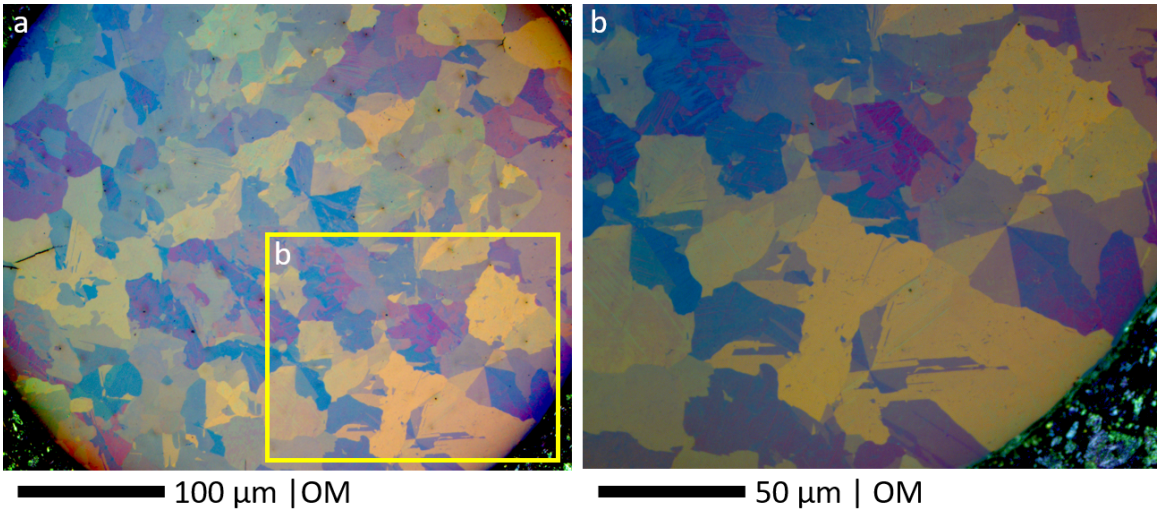

Fig. 5.2: OM images of a cross-sectional area in NiHf. This sample was undercooled $\Delta T = 418\,\mathrm{K}$. **(a)** The whole sample is shown, with several symmetric structures present, embedded in an undefined grain structure. **(b)** Highlight of three visible symmetric structures.

distributed statistically over the whole visible area. This is clearly contrary to the findings in NiZr. No singular growth can be identified in the microstructure, even though the heat front clearly showed a singular growth from one nucleation event.

The growth structures appeared to be of ten-fold symmetry in optical microscopy. EBSD analysis was performed to determine the grain boundary angle and the orientations of respective grains. Fig. 5.3 shows such analysis. The common orientation around the [001] direction, as well as the clearly defined grain rotation around this primary growth direction are both identified clearly. Surprisingly, the [001] direction was identical even in other symmetric growth structures of one specimen. A common growth front can therefore be assumed, albeit that it is not observed visibly. The expected GBA is not highlighted here, but it met the expected angle between two neighboring grains of $36° \pm 2°$. The EBSD image (b) additionally shows a grayed out, differently orientated, B33 phase. It is noticeable, that these structures seem to follow a direction roughly perpendicular to the respective grains ⟨100⟩ directions. They are also vaguely visible in the OM image (a). The whole microstructure of NiHf was ideally expected to show features of a singular dendritic growth from a central point, such as in NiZr and shown in Fig. 4.8 (a). Kobold has also investigated the NiHf system, but hasn't identified symmetric structures in the microstructure [16]. The common orientation around the [001] direction was present as well in his pole figures, but only for a small, limited number of differently orientated

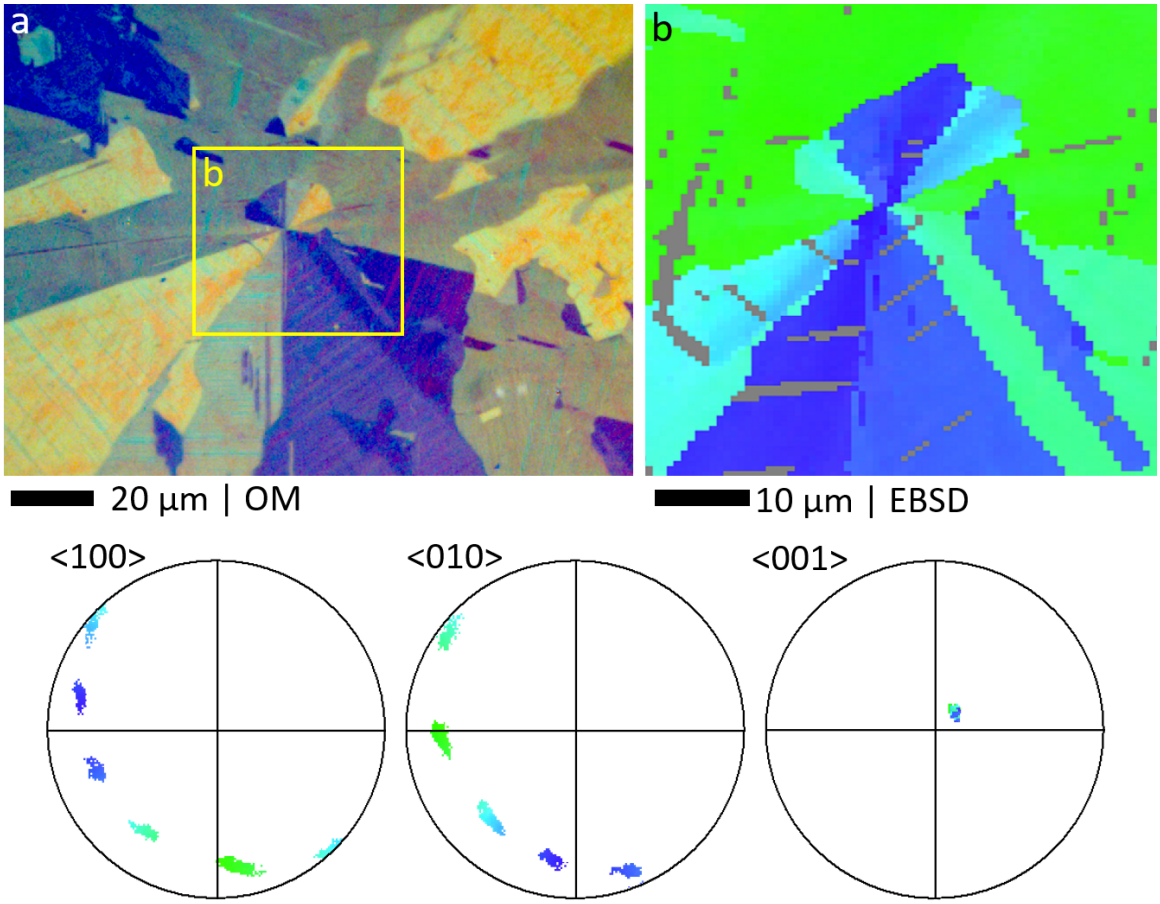

Fig. 5.3: OM and EBSD image, as well as corresponding pole figures, of a NiHf sample, that was undercooled 445 K below T_L. Both images show the same symmetric structure, which presents ten differently orientated grains with one common [001] direction.

grains. He proposed, that the size difference of the unit cells of both systems may explain the difference in behavior. He also described an unknown phase that showed up during the cooling after the solidification. By looking into the phase diagram of NiHf (App. 3.2), intermetallic NiHf has a SST, where β-NiHf (HT B2 phase) will transition into α-NiHf (B33 phase) [185]. Kobold has set this transition to 1430 K, based on phase diagrams from Nash [186] and Okamoto [187]. Together with a more recent analysis of Wang [188], an updated phase diagram of NiHf is shown in Fig. 5.4, with the SST line connecting $Ni_{11}Hf_9$ and $NiHf_2$ at 1423 K.

Experimental observations in the NiHf system

With the discrepancies between the results within the microstructure and the observations of the HSC recordings, it is assumed, that the SST has a certain influence in the

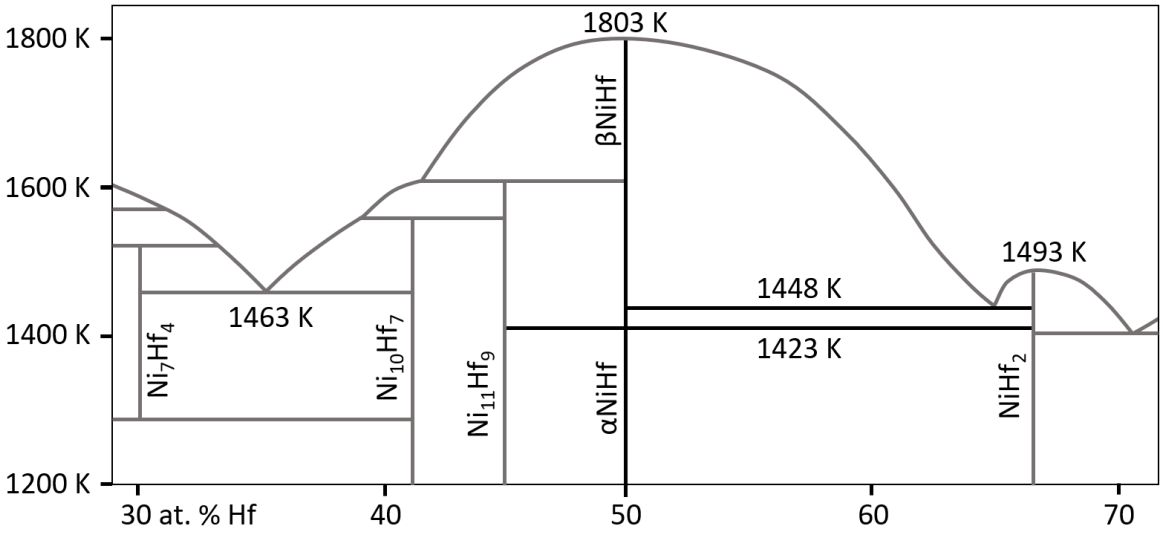

Fig. 5.4: Extract of the updated NiHf phase diagram after Okamoto, Nash and Wang. The SST transition is at 1423 K, above which the HT B2 phase of β-NiHf is stable. The B33 phase is stable below this temperature.

solidification process of this system. Fig. 5.5 shows three different undercooling cycles, processed with NiHf. In each cycle, a substantial undercooling below T_L is visible, as well as the subsequent SST during the cooling phase. It is important to realize, that the nucleation of the liquid-solid transition can happen above (a) or below (b) the transition temperature T_{SST}. This implies different initial nucleation of either the B2 phase, which is thermodynamically stable above the SST, or B33, which is stable below the SST. In Fig. 5.5 (a), the temperature of the specimen reached below the SST with $\Delta T = 422$ K and the B2→B33 transition was undercooled 44 K. It starts at 1419 K and ends at 1443 K in a steady rise, which is probably related to the eutectic line at 1448 K. In Fig. 5.5 (b), the system nucleated above the SST with $\Delta T = 348$ K and must therefore solidify in the stable B2 phase. The B2→B33 transition is undercooled 74 K and the temperature does not rise any further than to T_{SST}. In Fig. 5.5 (c), with $\Delta T = 460$ K, the B2→B33 transition does not reach its transition temperature anymore. The main undercooling (liquid-solid transition) in Fig. 5.5 (a) and (c) shows in fact hypercooling, as the latent heat is not sufficient to reach back to the equilibrium melting temperature either.

The hypercooling limit was set to 362 K for $Ni_{50}Hf_{50}$. It could not be calculated with the necessary certainty, due to lack of literature regarding this system and discrepancies of available data with the observations in this work. It is calculated with $\Delta T_{\mathrm{hyp}} = \Delta H_f / C_p$.

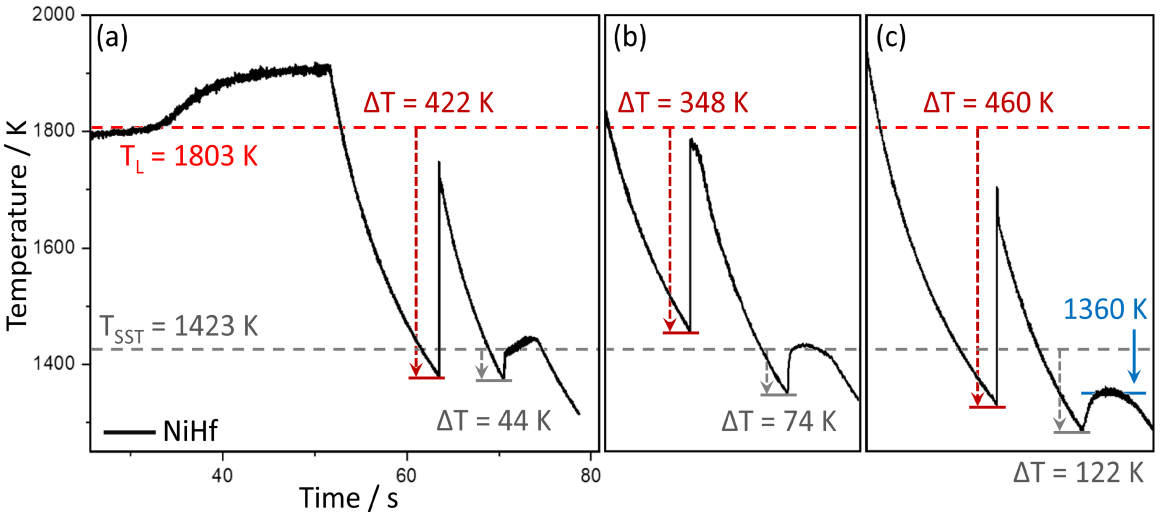

Fig. 5.5: Three TTPs of NiHf. The liquidus temperature T_L and the transition temperature T_{SST} are highlighted by a dashed line, red and grey respectively, in each cycle. Additionally, the respective undercoolings of the liquid-solid and the solid-solid transition are marked. **(a)** Typical cycle, with the undercooling reaching below the SST. **(b)** Sample triggered above the SST, to provoke an initial solidification in B2. **(c)** The SST was undercooled enough, so that its energy release is not sufficient to reach back to its transition temperature.

The specific heat capacity could be determined based on

$$C_p^L(T) = \frac{-\sigma_B A \epsilon_T (T^4 - T_0^4)}{\frac{dT}{dt} m}, \tag{5.1}$$

as described by Wessels et.al. [189]. With σ_B, A, ϵ_T, dT/dt and m being the Stefan-Boltzmann constant, the sample surface area, the hemispherical emissivity[2], the cooling rate and the mass of the sample respectively. It was calculated at $\Delta T = 360$ K to $C_p^L(T) = 30.2$ J mol^{-1}K^{-1}. This seems to be a reasonable value for an intermetallic system, with similar values in other alloys [190]. With literature data setting the enthalpy of fusion to values around -50 kJ mol^{-1} (-48.3 kJ mol^{-1} in [191]), the hypercooling limit would be calculated with $\Delta T = 1600$ K, which is not realistic. ΔT_{hyp} was therefore only determined experimentally from the TTP. Calculating the enthalpy of formation with the parameters worked out in this work, results to

$$\Delta H_f = \Delta T_{\mathrm{hyp}} \cdot C_p = 362 \text{ K} \cdot 30.2 \text{ J mol}^{-1}\text{K}^{-1} = 10.93 \text{ kJ mol}^{-1}. \tag{5.2}$$

It can also be shown in the HSC recordings, that indeed hypercooling is observed: Fig. 5.6

2 The exact emissivity is unknown. A value of 0.28 is set based on experimentally used values for the NiZr system.

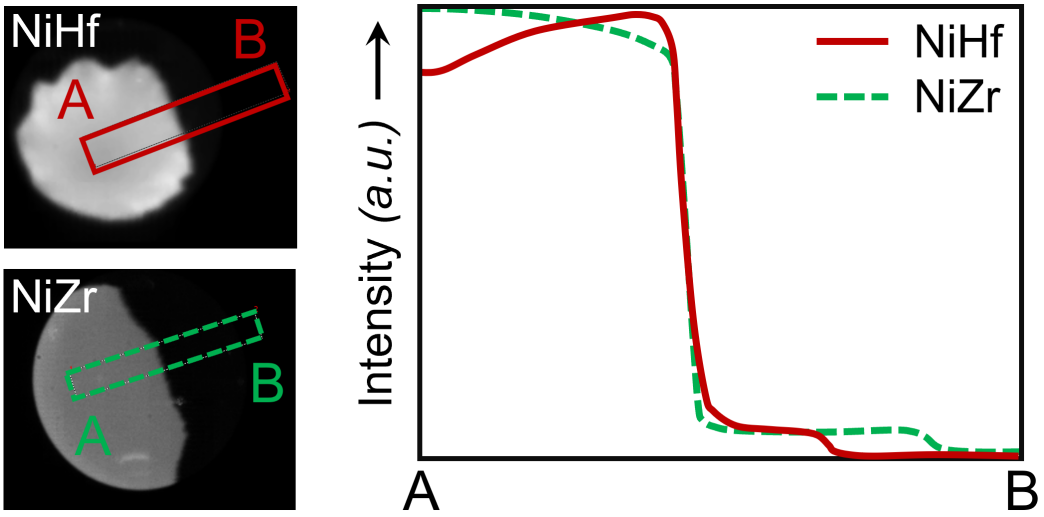

Fig. 5.6: NiHf and NiZr heat fronts and the respective pixel intensity of the HSC recording. The edge of the heat front is visible as a steep incline of a rising temperature. The undercooled liquid has a certain brightness as well and beyond the specimen, the intensity drops to a background level.

shows two heat fronts, the first from NiHf, the second from NiZr. Both recordings are analyzed by utilizing the pixel intensities and relating those to the temperature of the sample. It was shown, that the conversion from intensity to temperature follows a linear correlation [192] and was done previously to differentiate undercooling and hypercooling [193]. As in hypercooling, per definition, the whole of the system solidifies within the recalescence, the temperature should fall again after the initial rise to the equilibrium melting temperature (red line). In the undercooling case (green, dashed line), the temperature will stay at T_m during the post-recalescence plateau. This is exactly what can be observed in the upper left of the intensity plot of Fig. 5.6 for both systems. NiZr does not reach hypercooling and stays on a certain temperature level, whereas NiHf cools down immediately again.

With the premise, that a different initial phase forms the microstructure, depending on whether the system nucleated above or below the SST, different heat fronts, depicted in Fig. 5.7, were evaluated. Fig. 5.7 (a) shows the observed heat front corresponding to the TTP in Fig. 5.5 (a). The undercooling reached below the SST and B33 nucleation is possible. The first two frames show the propagation in the shape of the DB, as presented already in Fig. 5.1. However, after roughly 15-25% of the solidification, visible spikes shoot forward on the edge of the heat front (highlighted by yellow arrows). Fig. 5.7 (b)

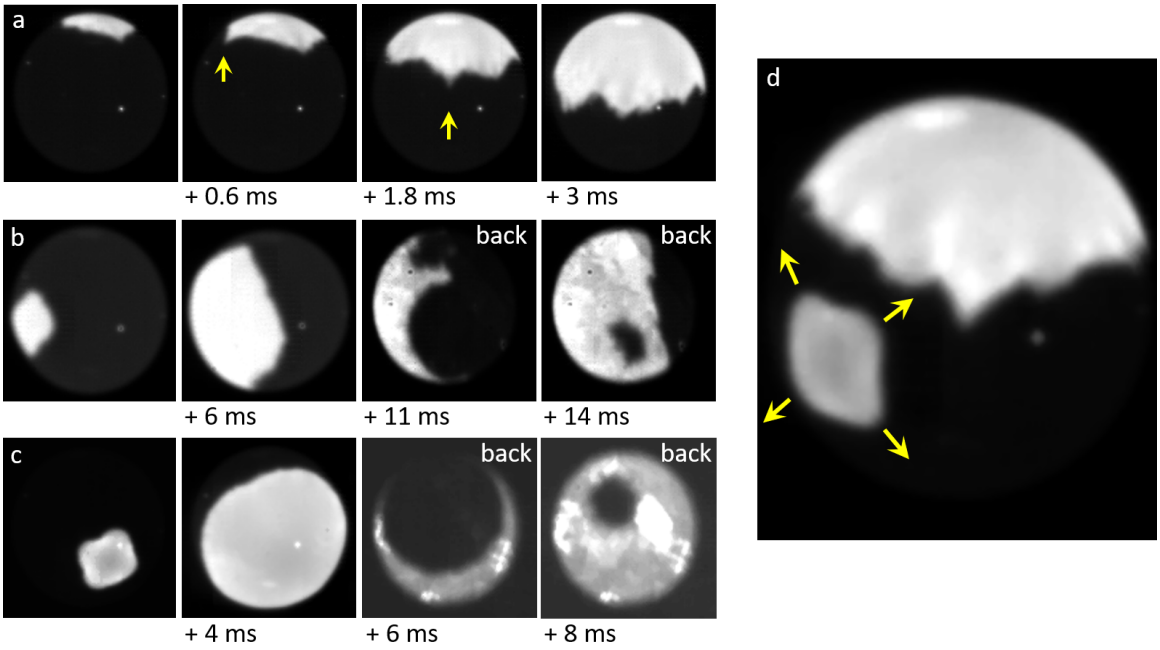

Fig. 5.7: Comparison between observed heat fronts in NiHf. **(a)** Heat front during a B33 initial nucleation. At first it shows features of the ten-fold front presented in Fig. 5.1. After a certain propagation, spikes shoot forward (yellow arrows). **(b)** Four-fold heat front from a sample, undercooled to $\Delta T = 348\ \mathrm{K} < \Delta T_{\mathrm{hyp}}$. Its nucleation sets in above the SST. **(c)** Four-fold front in a sample, that exceeds the hypercooling limit with $\Delta T = 441\ \mathrm{K}$ and nucleates below the SST. **(d)** Two independent heat fronts with the upper one being the initial front. The second front has a clearly four-fold shape.

corresponds to the TTP of Fig. 5.5 (b), in which the initial nucleation occurs above the SST ($\Delta T = 348$ K). A solidification of the B2 phase is expected. The front shows a four-fold shape in the beginning, that propagates further through the sample with features associated with cubic systems. At this point, it should be pointed out, that above the SST solely the B2 phase is stable and able to nucleate. Below the SST however, both phases can nucleate. At an exemplary undercooling of 400 K, the B33 phase is undercooled merely 20 K, whereas the B2 phase is undercooled 400 K and has therefore a much higher driving force for transition. This is shown in Fig. 5.7 (c), with a reached undercooling of $\Delta T = 441$ K, already far below the SST. Still, a four-fold shape can be identified in the first frame, continuously changing into a spherical front. In hypercooling, spherical fronts are commonly described within the recalescence [122]. The initial four-fold shape in this case is a quite interesting and new phenomenon, that needs to be looked upon in the near future. In this context, the first front of Fig. 5.7 (a) is certainly interesting as well, as it also sets in within the hypercooling regime.

At last, Fig. 5.7 (d) validates the claim, that both, the B2 and the B33, phases can nucleate

below the SST. It shows two nucleation events, independent of each other. The first, upper one, shows the front described in Fig. 5.7 (a), whereas the second one clearly corresponds to the four-fold shape denoted to the B2 nucleation. With the analysis of pixel intensities, as presented already in Fig. 5.6, it turns out, that the temperature in the melt stayed at the reached undercooling of $\Delta T = 445$ K and both nucleation events occur without knowledge of the other.

Multiple nucleation modes

Different nucleation modes are observed, dependent on the respective undercooling, the initially nucleating phase and the SST. To get an overview of these modes, they are shortly summarized and presented in Tab. 5.2. Each mode will be analyzed regarding their microstructures and especially the first one will be assessed on its connection to the proposed growth model, as it is the only mode, where an initial B33 phase nucleation is observed. It is important to point out, that, independent of the nucleation mode, each specimen goes through the B2→B33 transition after solidification. Therefore, the observed microstructure is always present in the B33 phase. The initial growth can however be traced, e.g. when preferential orientations are present.

- **Mode 1:** The undercooling reaches below the SST and the initial nucleation happens in the B33 phase. This takes place below ΔT_{hyp}. This is the only mode, where symmetric structures and a common [001] direction are found in the microstructure.

- **Mode 2:** Nucleation occurs above the SST and not in the hypercooling regime. The B2 phase is stable and has to be the initial phase.

Table 5.2: Different solidification modes observed in the NiHf system, highly depending on the respective undercooling. s.c.: single crystal. (*) The mode features equal observations as already presented for other modes.

Mode	Nucl.	ΔT [K]	$> \Delta T_{\mathrm{hyp}}$	$> T_{\mathrm{SST}}$	$\mathrm{SST_{hyp}}$[1]	Fig. 5.5	Fig. 5.7	Remarks
1	B33	422	✓	✓	✗	(a)	(a)	one [001]
2	B2	348	✗	✗	✗	(b)	(b)	poly B2
3	B2	441	✓	✓	✗	(a)*	(c)	poly B2
4	B2	460	✓	✓	✓	(c)	(c)*	s.c. B2

[1] Denotes, if the B2→B33 transition during cooling was pseudo-hypercooled. The term is defined and discussed later in this section, but the general idea is, as in liquid-solid transition hypercooling, that the latent heat is not sufficient to heat the sample to its transition temperature.

- **Mode 3:** Similar in undercooling as mode 1. It nucleates below the SST and ΔT_{hyp}. However, the initial nucleation happens in the B2 phase and not in the B33 phase.

- **Mode 4:** This is a special case, as it only differs to mode 3 in the fact, that the B2→B33 transition during cooling was pseudo-hypercooled (The term will be defined later, in the paragraph of mode 4). During the transition, the temperature does not reach T_{SST}. Additionally, the microstructure reveals a different orientation relation, than in the other B2 nucleated modes.

Mode 1 - B33 initial nucleation

With respect to the proposed growth model for CrB-structured systems, this nucleation mode is the most relevant, as it is the only one, where an initial nucleation of the B33 phase is expected. In this mode, the undercoolings reach below the SST and it is thermodynamically possible to nucleate in the B33 phase. With rising temperatures from the latent heat however, the B33 phase must transition into the B2 phase, which is subsequently transformed back into the B33 phase during cooling. The exact growth mechanisms and transitions are now presented, to get plausible explanations for the existence of the observed multiple growth structures, together with the common orientation around a single [001] direction, even after passing through two SSTs.
It needs to be discussed, why there is not a single initial growth structure present, as shown in the NiZr prototype, and also how the information of the initial B33 growth would be saved through two transitions (B33→B2→B33). Likely, as shown in Fig. 5.7 (a), the dendritic front of the B33 nucleation gets disturbed at some point and the dendritic structure cannot grow freely throughout the sample. This can explain multiple growth structures, despite disturbances, as these are most likely remnants of the tertiary dendrites grown in the proposed growth model (see Sec. 4.2). It is however unclear, how the B33 growth is disturbed. Basically, there are two options regarding the initial nucleation and growth through the melt.

- **Solidification in B33 and a subsequent transition into B2.** At nucleation, when the undercooling temperature is below T_{SST}, the B33 structure is thermodynamically stable and upon nucleation its dendrites will grow throughout the sample. This structure will then, after a certain time transition into the B2 structure. This option is unlikely, as it would result in a parted recalescence, where a first peak would be

visible for the B33 nucleation and afterwards, a higher peak marks the B2 nucleation and release of latent heat back to the melting temperature. Even when setting the pyrometer to a 5000 Hz resolution, it was not possible to capture any discrepancies in the recalescence.

- **Immediate B33→B2 transition during growth right at the dendrite tip.** The initial nucleation occurs, according to the proposed model. The secondary dendrite growth directions are immediately set regardless of future transitions. The dendrites keep growing through the sample and are almost immediately transitioned into the B2 structure. This can explain a common orientation from a previously shared singular growth and several symmetric structures by imposed tensions during the transition. This option will be discussed further, as it can also explain the disturbances observed in the HSC recordings, if the B2 dendrites overtakes the B33 dendrite at some point.

Based on the models by Lipton, Trivedi and Kurz, regarding the dendrite tip growth and temperature [42, 43] the following model for the almost immediate transition during the dendritic growth is presented. Fig. 5.8 shows a scheme of the B33 dendrite growing into the liquid phase. The transition into the B2 phase follows directly. According to the dendrite tip model, the temperature of the undercooled melt rises just in front of the dendrite tip to finally reach the interface temperature T_i.
It was shown by Lum and Matson [194], that the distance between the visible heat front in the HSC recordings and the actual growth interface can be calculated by

$$d = \frac{\alpha_T}{v}, \tag{5.3}$$

with the dendrite tip velocity v. They calculated $d = 3.2\ \mu$m for pure Ni. In NiZr, the thermal diffusivity is $\alpha_T = 3 \times 10^{-6}$ ($m^2 s^{-1}$)[158]. With a growth velocity of $v(\Delta T) = 0.52$ m/s the distance can be calculated to 6.92 μm. Other intermetallic, binary alloys usually have thermal diffusivities ranging from $10^{-6} - 10^{-5}$ ($m^2 s^{-1}$) [195–197] and have growth velocities of roughly the same magnitude. Similar values for the distance between the observed heat front and the actual interface can therefore be expected in NiHf. In conclusion, the temperature in the majority of the remaining melt is not rising during the recalescence. Only when a dendrite is actually in close proximity it will influence the melt.

During the initial nucleation, B33 is the thermodynamically stable phase and as its dendrites grow through the melt, the solid phase will reach to the transition temperature

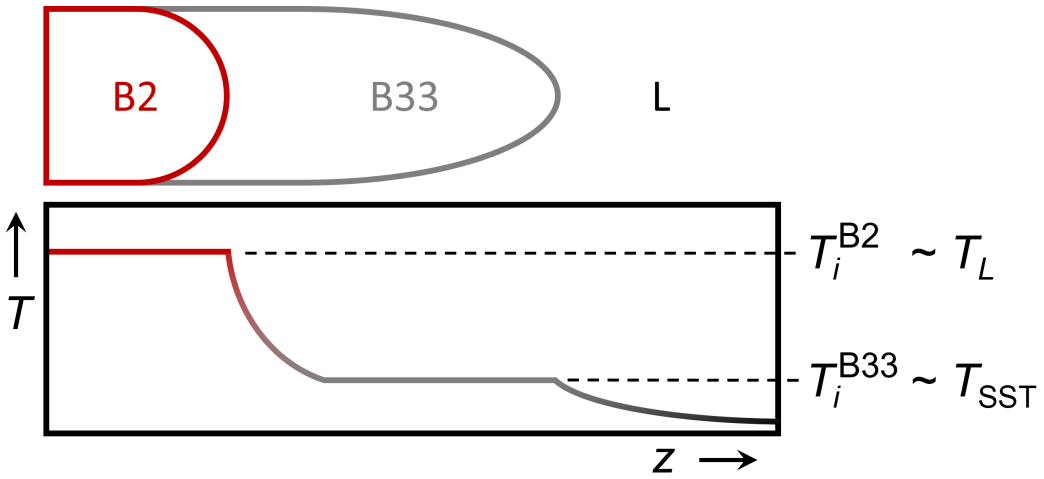

Fig. 5.8: Model for the SST within the dendritic growth. The initial B33-structured dendrite is growing into the undercooled melt and imposes its growth directions into the solid part. The solid phase has reached the transition temperature of B33→B2. With the transition into B2, the latent heat is fully released heating the sample up until recalescence has passed.

up to which the B33 phase is stable. In Fig. 5.8 this is marked as T_i^{B33}. Now both phases can principally coexist. After a certain time, the first transition into the B2 phase will occur and it will release the remaining latent heat of the system. This, in turn, will favor the B2 transition, as the energy barrier gets lower. The B33 dendrite is consequently transitioned into a B2 structure almost immediately after it has grown. This transition will release the mayor part of the stored latent heat and heat the sample up. In principle, it would rise up to the equilibrium melting temperature. However, since this happens in hypercooling, only the recalescence spike is visible in the TTP. Phase changes, during the recalescence, were also observed recently in pure Si [198].

This mechanism, of a dendrite growing and transitioning basically simultaneous, is of course difficult to capture. The nature of this nucleation mode would imply, that there is always only a tiny amount of B33 phase present. With temporal resolutions of 5000 Hz in the pyrometer or pixel intensities in the HSC recordings, this phenomenon can not be resolved in the recalescence. In principle, a short hold at the transition temperature would be expected. A similar parted recalescence was shown most recently by Kreischer and Volkmann, in FeCo, where the first phase solidified to its transition temperature and after about 0.13 ms, the second phase solidified. This led to clear steps in the observed recalescence and also validates the assumption, that the first phase will not heat up the solid part back to the equilibrium melting temperature of the system [199]. The difference here is, that the time, between the two events, must be much shorter and therefore the transition must occur directly behind the growing B33 dendrite. In turn, the fraction of

B33 phase present at any given moment of the recalescence must be proportionally small as well.

It can also be considered, that a growth front, that consists of two, almost simultaneously, growing phases can explain the heat fronts observed in NiHf. They are always more blurry than the ones recorded in NiZr, or, as will be presented later, in NiZrHf. Also, the, seemingly, ten-fold front, that is connected to the DB, gets distorted during growth. It can usually only be observed for the first 15-25% of the growth through the specimen with the same heat front shape as in NiZr. After this, the front is changed, as spikes will outrun the general front and a new shape is formed. (This was presented already in Fig. 5.7 (a).) It is an option, that the B2 dendrite growth overtakes the B33 growth under certain conditions, at least partially. This would result in a small shift of the dendrite growth direction. As it was already discussed, the growth follows the $[223]_{B33}$ direction for the B33 structured secondary dendrites. With a transition to the B2 structure, the inherent monoclinic symmetry (see. Sec. 4.1) transitions into the B2 lattice. With the presumption, that the growth direction has to be preserved, the closest crystallographic direction of the B2 phase is the $[113]_{B2}$ direction. This is shown in detail in App. 2.2. This shift, and a possibly different growth velocity, are a reasonable explanation for such spikes.

Additionally, this explanation for the distorted heat front is also supported by a first optical analysis regarding the fraction of symmetric structures within the microstructure of NiHf. The premise is, that all symmetric structures have formed, e.g. as the primary, or the tertiary dendrites (see Sec. 4.2), from the initial B33 growth. If, at some point, the B2 dendritic growth dominates, no new n-fold growth structures should be formed. A sample with several visible growth structures, seen in Fig. 5.2, is analyzed as follows: The cross-section, as well as each growth structure, were approximated with a circular surface area. This way a surface fraction of these structures could be calculated. The surface fraction is equal to the volume fraction (proportionality factor = 1). It was calculated to $11\% \pm 4\%$. A large error estimation was chosen, as its quite difficult to assume the exact size of the symmetric structures. This fraction was then compared to the fraction of the heat front that is not yet disturbed by the overtaking B2 structure. It was observed to usually range from 15-25%. Even considering the large deviations possible in assessing the structural fraction, this is an indication that the symmetric structures may only grow until the B2 growth takes over and other directions are possibly favored.

Mode 2 - B2 nucleation above T_{SST}

For this mode, nucleation is expected to set in above the SST. In this region, the B33 phase is not stable, so it is only possible to start nucleation in the B2 phase. Under equilibrium conditions, near the melting temperature, this would be the standard sequence for solidification as well. After nucleation and the following recalescence, the temperature rises to T_L until the solidification is finished. The temperature will then drop until the sample reaches the transition temperature, at which the microstructure transitions from the B2 into the B33 phase.
This mode was deliberately provoked, to get a more concise picture of the different possible microstructures. A NiHf specimen was undercooled to $\Delta T = 348$ K, which is just above the SST (see Fig. 5.5 (b)). It was then triggered to solidify at this exact undercooling. This way, it could be ensured, that the sample will nucleate fully within the B2 phase. It can be noted, that this undercooling is already quite substantial and that the HT cubic B2 phase seems to be not affine to nucleate at this temperature.
Fig. 5.9 shows an EBSD image, and its pole figures, of this sample. At first glance, the microstructure seems to be similar to Fig. 5.2. A large distribution of small grains is visible in the EBSD image, which are seemingly unrelated to each other. The pole figures reveal several [001] directions without any noticeable ordering of other orientations. No symmetric structures or implied overlaying grain orientations can be perceived. The pole figures also differ substantially to the ones shown before, where the system solidified below the SST. Such a microstructure is expected in this mode. The sample only experienced one transition during cooling (B2→B33) and cannot have any connections to the proposed growth model of the B33 structure, since it is thermodynamically ruled out, that nucleation would occur in the B33 phase.

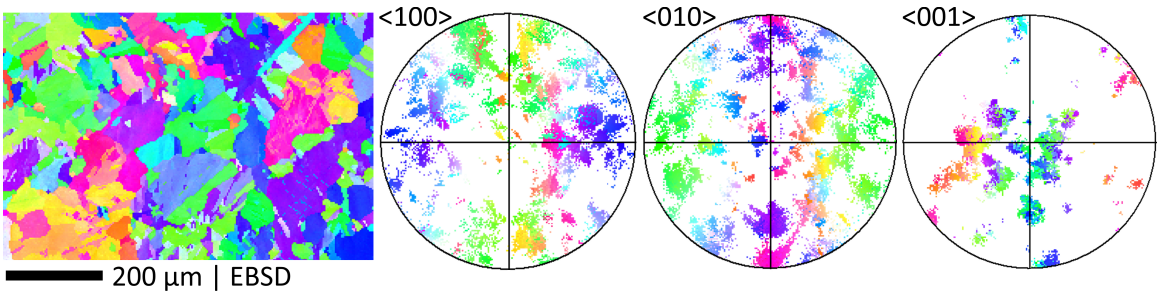

Fig. 5.9: EBSD pattern and corresponding pole figures with IPF coloring. This NiHf sample was undercooled 348 K and solidification was deliberately triggered. This way, it was assured that the melt never reached the SST (nucleation mode 2).

Mode 3 - B2 nucleation below T_{SST}

In this mode, the initial nucleation of the B2 phase was observed, while the undercooling reached below the SST. Fig. 5.10 shows an exemplary microstructure from such nucleation. The EBSD image shows no symmetric structures, but a rather randomly distributed grain structure. No special orientation relations can be perceived in the pole figures, as well. Especially, there is no preferential [001] direction or any visible ordering of other directions around one of the ⟨001⟩ directions. This kind of microstructure, similar to mode 2, is expected with an initial B2 nucleation. The distinction to mode 2 is, that this mode nucleated below the SST, where the B33 phase would be stable as well. One additional point is, that mode 3 nucleated in the hypercooling regime and that there are small variations between the two microstructures, as mode 2 consists of smaller grains and they show greater deviations in their orientation. With these observations however, there seems to be no significant difference between both options for the initial B2 nucleation.

Mode 4 - B2 nucleation below T_{SST}, with a pseudo-hypercooled B2→B33 transition

Another unexpected observation was made in the TTP of Fig. 5.5 (c). The set transition temperature T_{SST} (Fig. 5.4) is underlying each of the cycles as a dashed gray line at 1423 K. It can now be seen, that the SST itself was undercooled $\Delta T_{SST} = 44 - 122$ K in the three cycles, with cycle (c) having the highest undercooling of $\Delta T = 122$ K. In this cycle, the transition does not reach T_{SST}. A certain plateau can still be perceived at 1360 K, 63 K below the equilibrium transition temperature. Solid-solid transitions generally release about 6 – 10 times less energy, than liquid-solid transitions. This is based on findings regarding the $\beta \rightarrow \alpha$ transition in pure elemental melts of Zr [78], and several intermetallic transitions, as in CuZr [200], Cu-Au [91] or Ti-Al alloys [86]. Additionally, SSTs normally run slower than LSTs. Together with the high cooling rate, the relatively small and slow energy release during the transition apparently is not sufficient to reach T_{SST}.
In liquid-solid transitions a similar effect is known as hypercooling and is explained with the finite amount of the enthalpy of fusion, which at some point (hypercooling limit ΔT_{hyp}) is not sufficiently anymore to reach the transition temperature. The entirety of the melt will solidify during the recalescence and no plateau is observed. The temperature will decrease again, after reaching a high spike in the recalescence. Hypercooling might therefore not be the right term to describe the observed phenomenon. Although, the phenomenon is similar to hypercooling in the sense, that both transitions cannot reach

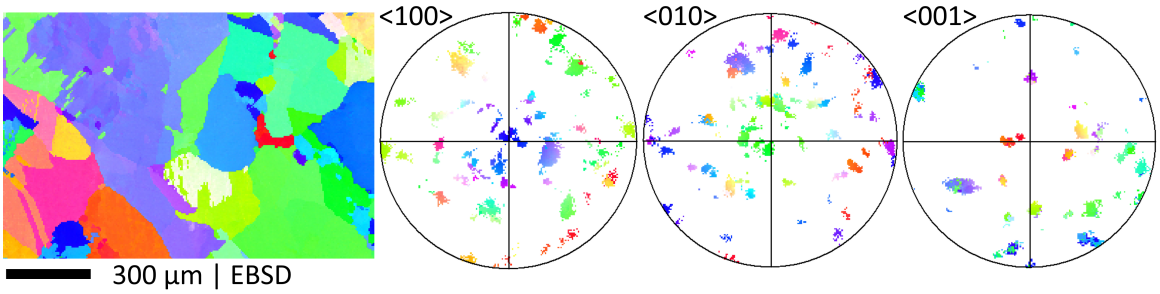

Fig. 5.10: EBSD image and pole figures of NiHf in nucleation mode 3. The sample nucleated in B2 structure and shows no preferential directions or symmetric microstructures.

their respective equilibrium transition temperature, the post-recalescence plateau in the SST is much more the expression of the exothermic reaction during an ongoing cooling of the sample. The observation is therefore denoted as *pseudo-hypercooling* to respect, that it distinctly differs from the known hypercooling phenomenon.
With even deeper undercoolings, it is also possible, that the absolute temperature, and therefore the inherent energy, is not sufficient anymore to fully complete the transition and to, partially, quench it in.

Fig. 5.11 shows an EBSD image and the corresponding pole figures of the respective sample, that is presented with the TTP in Fig. 5.5 (c). Here, a color representation was chosen, that is fixed on a standard orientation and colors the rising deviation from this orientation (blue→green→yellow→red). Black areas in this image are therefore just not represented by the color scheme. The whole analyzed cross-sectional area exhibits the B33 phase. It is clear however, that the sample solidified entirely in the B2 structure. This can be deducted, as only three different B33 phase orientations are present in the pole figures[3]. These are highlighted by the red arrows in the ⟨100⟩ pole figure. They have their origin in a single cubic B2 phase orientation. Consequently, the initial B2 phase has grown as a single crystal. Upon transition, the B33 structure was formed, orientated in either of the six available space directions possible with the initial cubic structure (see Sec. 4.1). This type of transition is also shown in an analysis of CoZr in App. 5.3, which will be covered in Sec. 5.1.2.
In contrast to the other examples of an initial B2 nucleation presented with Fig. 5.9 and Fig. 5.10, this growth mode results from a single crystal growth of B2. This is the direct consequence of the observation of three B33 directions. The only apparent difference to

3 The ⟨110⟩ pole figure naturally shows two sets for each B33 orientation.

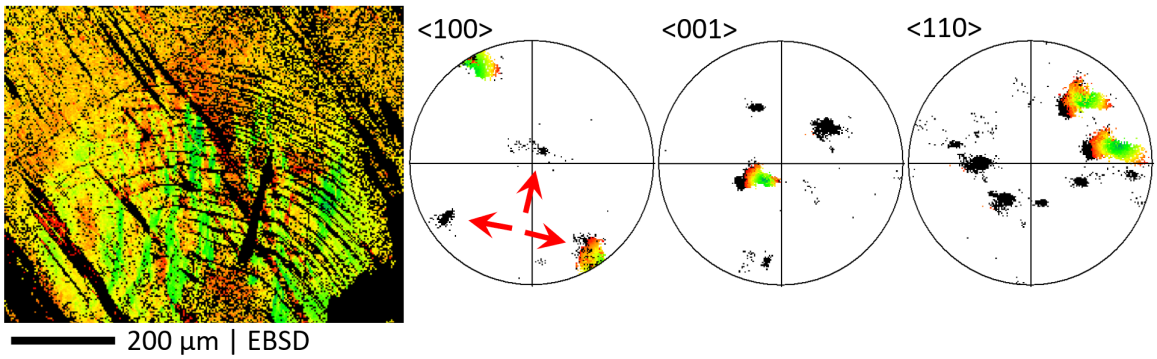

Fig. 5.11: EBSD image and selected pole figures of the sample presented in Fig. 5.5 (b). The color presentation focuses heavily on a fixed direction, whereas other directions are not present (black), to highlight the deviations within the microstructure. The apparent B33 structure can be reconstructed to the pre-transition B2 structure, as only three main directions are present in the microstructure (red arrows).

the growth modes (2) and (3) is the pseudo-hypercooled SST. Given, that the SST occurs only after the initial nucleation, it cannot be the cause for the initial single crystalline B2 growth. The exact reason for the appearance of this mode remains unknown, but it can be suspected, that it is either a plain statistical occurrence, or due to the overall deep undercooling reached in the SLT. This was the deepest undercooling, $\Delta T = 460\,\mathrm{K}$, reached in NiHf.

Connection of NiHf to the proposed growth model

Nucleation mode 1 is clearly connected to the proposed growth model. However, the fact, that the initial B33 structure must pass two SSTs, is a huge disadvantage, especially considering the observability and the microstructure analysis. The main difference to the findings of Kobold, regarding the NiHf system, is, that his experiments did not reach undercoolings below the SST. The observations made by Kobold for the NiHf system can therefore be explained by an initial nucleation and growth in the B2 structure (mode 2), as this phase was thermodynamically stable during the onset of solidification. A subsequent SST from B2 into the B33 phase (see Sec. 4.1) results in the microstructure he described and as it was described for nucleation mode 2 and 3 (Fig. 5.9 and Fig. 5.10). In this work, the onset of solidification in nucleation mode 1 takes place in a temperature region below the SST. Therefore, the B33 phase should be thermodynamically stable. B33 was observed to nucleate and it was explained, how the first transition from B33→B2 is passed already during the dendritic growth. Despite the transition, the relevant directions

and symmetric structures are already imprinted into the microstructure, even if at some point during growth solely B2 dendrites remain. As in all other nucleation modes, the B2→B33 transition is passed during cooling. This transition disturbs the microstructure even further, but still, symmetric growth structures are found, as well as a common orientation around a single growth direction. Most likely, these symmetric structures are remnants of the initially present tertiary dendrites, as they are found at any point within the microstructure.

5.1.1 Pseudo-binary $Ni_{50}Zr_{25}Hf_{25}$

The nucleation and growth in NiHf clearly show most of the defined crucial features, that were observed in NiZr. It was therefore interesting to see the behavior of the solidification mechanisms when both system are brought together. For this work, the intermediate composition of $Ni_{50}Zr_{25}Hf_{25}$ was chosen, to advance the approach from Kobold, who tried to replace the Zr content with Hf in small amounts according to $Ni_{50}Zr_{50-x}Hf_x$, with $x = 1, 2.5, 5, 10$ at.% Hf. These compositions will be denoted in this work based on their Hf content, e.g. $Ni_{50}Zr_{45}Hf_5$ is written as Hf_5.
Kobold was mainly interested in the *migration* of the SST from NiHf to NiZr, since it cannot be observed anymore in NiZr - with the exception of occasional spikes in the post-recalescence plateau and metastable B2 nucleation. He showed, that the absolute temperature of the SST rises with declining Hf-fractions. This indicates, together with the observations in NiZr, that the SST has migrated to an absolute temperature that is just above the liquidus temperature in NiZr. Only the B33 structure can solidify thermodynamically stable in the NiZr system, as was also calculated by Sun et al. [151]. The assumption of a stable B33 and a metastable B2 phase in NiZr is validated by the pseudo-binary phase diagram, shown in Fig. 5.12 [201]. It shows the liquidus and solidus lines for the LST and the transus temperatures of the SST between the NiHf and the NiZr systems. The upper transus line, which marks the $\beta_1 \rightarrow \beta_1 + \phi$ transformation, is denoted as B2-transus in this work. The lower one ($\beta_1 + \phi \rightarrow \phi$) will be referred to as B33-transus. The SST transition is shown to have a slightly rising absolute temperature with a more substantial rise towards higher Zr-fractions. At roughly $NiZr_{47}Hf_3$, the SST forms a peritectic reaction with the solidus temperature of the LST. This is in line with the findings of Kobold, who has observed the SST in Hf_{10} and Hf_5 compositions, but not anymore in $Hf_{2.5}$ and Hf_1 fractions. With his observations, Kobold calculated an interpolated liquidus temperature

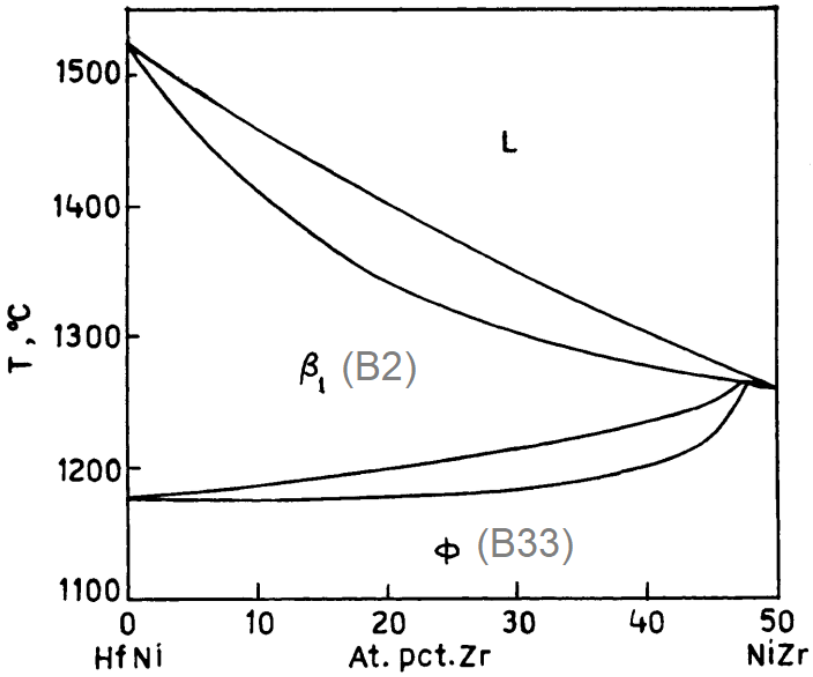

Fig. 5.12: Pseudo-binary phase diagram between NiHf and NiZr, adopted from [184, 201]. It shows the liquidus and solidus from solidification, as well as the range of the SST. Close to $Ni_{50}Zr_{50}$ the SST reaches a peritectic reaction with the solidus line of the liquid-solid transition. The HT cubic B2 phase is marked as β_1 and B33 phase is denoted as ϕ.

plot for the pseudo-binary range. With his interpolation a liquidus temperature could be set for $Ni_{50}Zr_{25}Hf_{25}$ of $T_L = 1418$ K. The calculated parameters and other observations of this work are plotted onto the pseudo-binary phase diagram to visualize the new data. This is shown in Fig. 5.13 with the diagram from [184] underlying in grey. It can be noted, that the absolute value of the maximal observed undercoolings only changes slightly over a broad range of the diagram and only drops when approaching the binary NiZr system. Still, as calculated by Kobold [16], $\Delta T_{\mathrm{hyp}} = 346$ K in NiZr (1166 K absolute value) is not reachable by levitation, since the observed undercoolings for NiZr are based on homogeneous nucleation.

NiZrHf was successfully undercooled to $\Delta T = 378$ K. A typical cycle with heating and undercooling is shown in Fig. 5.14. The SST can be identified, already during heating, as a visible kink in the curve. The sample is then hypercooled below the SST and the SST itself is undercooled 66 K as well. The graph is quite similar to the curves observed with NiHf. The resemblance continues with the observed heat front, depicted in Fig. 5.15. The frames show basically the same front, that is observed in NiZr and NiHf and which deter-

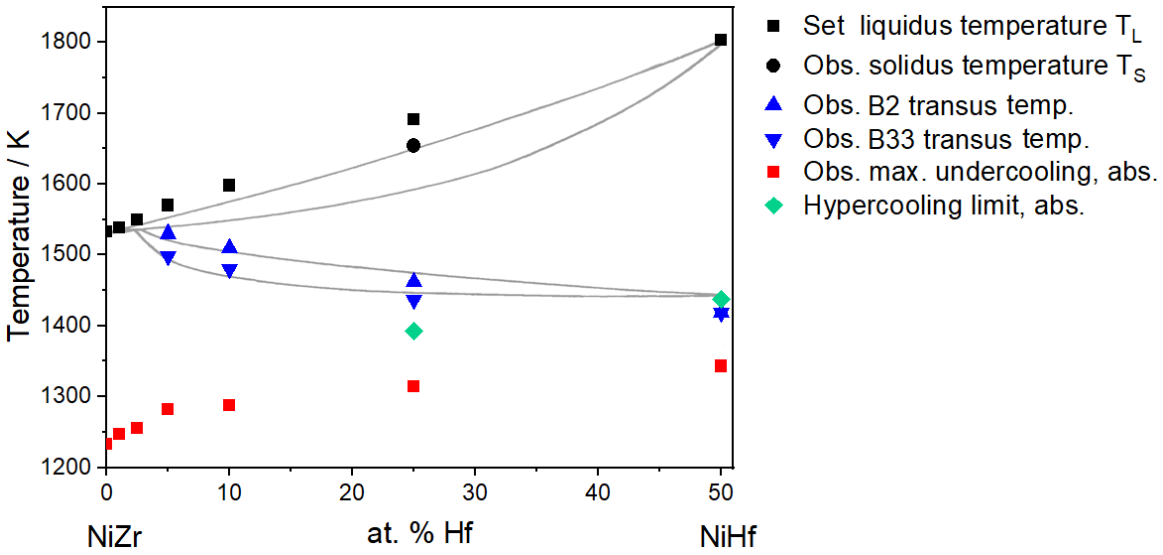

Fig. 5.13: Data plot based on the pseudo-binary phase diagram, presented in Fig. 5.12. It is underlying this plot in gray. Multiple parameters were extracted from experiments, as well as the work of Kobold [16](Hf$_1$ - Hf$_{10}$).

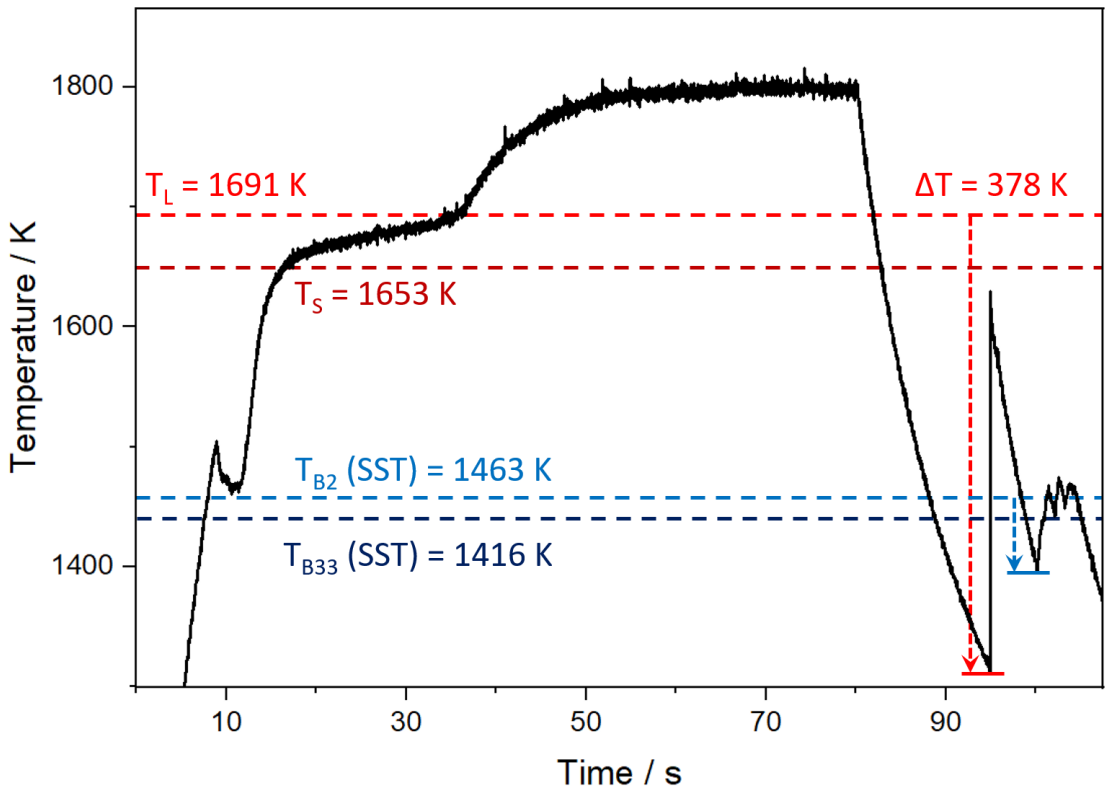

Fig. 5.14: Heating cycle of a NiZrHf specimen, undercooled $\Delta T = 378\ \mathrm{K} > \Delta T_{\mathrm{hyp}}$. The relevant temperatures of both transitions, as well as the undercooling, are highlighted.

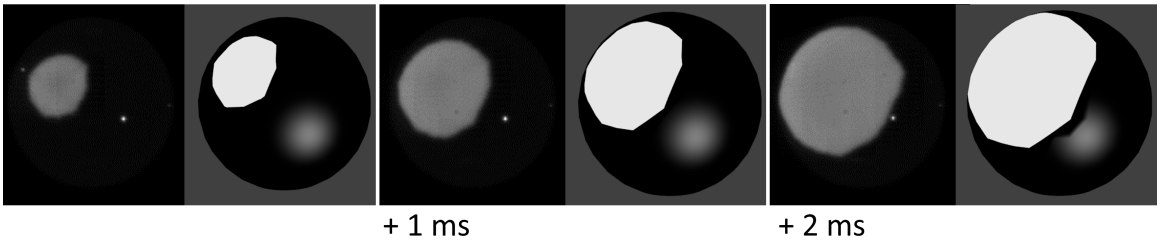

Fig. 5.15: NiZrHf heat front (black background) and corresponding simulated front (gray background) based on the decagonal body. The heat front can be characterized by the same features, that are also found in the analysis of the NiHf and NiZr heat fronts (see Fig. 5.1).

mines the decagonal body (DB) growing through the systems. Unlike in the NiHf system, where the front is distorted by the B33→B2 transition, the front was observed to be stable during the whole process. It is possible, that the Zr fraction has a stabilizing effect in this system. The surface of the processed NiZrHf specimen shows a ten-fold point symmetric dendritic structure, highlighted in Fig. 5.16 (a). Such surface features were observed in NiZr as well. Image (b) shows the cross-section of the sample. Although, there are no clear and straight grain boundaries, an underlying preference can be identified in the orientations. A common center can be marked (center of image (c)), from where the grain structures move away radially. Presumably, the SST is responsible for these shifts and restructuring. Without it, this cross-section could certainly not be differentiated from examples in NiZr. Despite the SST, image (c) shows an EBSD image of the central structure, with the corresponding pole figure. The common [001] direction is present, as well as ten differently orientated grain directions around the growth direction (blue color set). A second area can be identified (red IPF coloring) on the left upper side of the sample (image region (d)). Similar to Fig. 5.7 (d), this sample experienced two independent nucleation events, with the difference that in this case, both events nucleated in the B33 phase. It is shown in Fig. 5.16 (d), that they have different [001] orientations, seemingly random to each other, but both share the features of the proposed growth model.
NiZrHf samples were also triggered to nucleate above their respective transitions temperatures, in order to force the B2 phase nucleation. The observed heat fronts did not differ from the four-fold fronts described for NiHf. Microstructure analysis of these samples revealed a grain structure, with no apparent preference direction, as it was the case with growth mode (2) and (3) in the NiHf system.

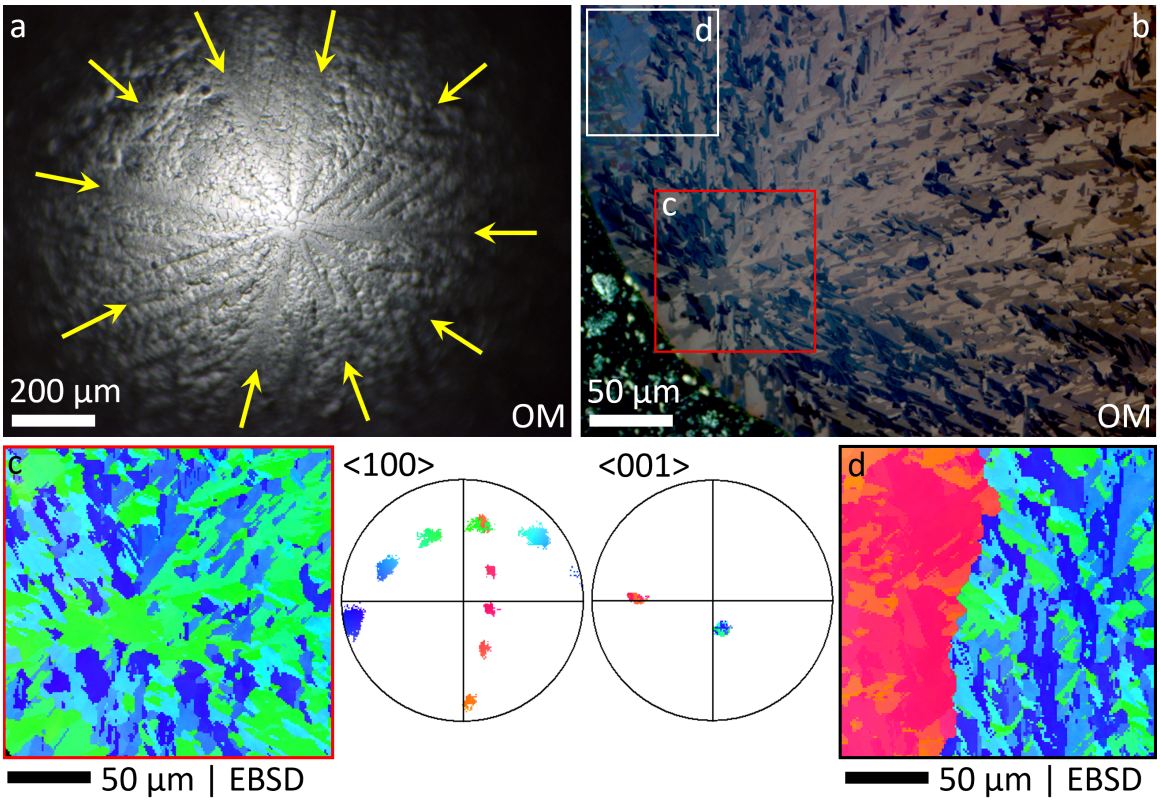

Fig. 5.16: Microscopic analysis of NiZrHf, undercooled 378 K. **(a)** OM image of a ten-fold surface structure. **(b)** Cross-section with grains visibly orientated towards a common center. **(c)** EBSD image of the assumed center. The corresponding pole figures show a common orientation around the [001] direction. **(d)** A second regime with a different [001] direction adjacent to the first one.

5.1.2 B2↔B33 solid phase transition in the Ni(Zr,Hf) systems

As explained in Sec. 5.1, a presumably realistic option for the dendritic growth during solidification with an initial B33 phase nucleation, that would be coherent with the proposed growth model, would run through the following steps:

1. Nucleation must initiate below the transition temperature of the SST. An initial B33 solidification sets in, since this is the thermodynamically stable phase.

2. The B33 dendrites set up the directions of growth and define the macroscopically visible heat front shape of the decagonal body (DB). They heat up the solidified parts to the respective SST temperature.

3. The B33→B2 transition follows, almost instantly, after the initial B33 growth. Growth directions are mostly preserved, with small deviations and shifts. The temperature rises, back to the equilibrium melting temperature, but due to hypercooling it is not reached.

4. After the recalescence, 100% of the specimen must be present in solid phase (hypercooling) and in the B2 structure (temperature).

5. During cooling, the sample goes through the SST again, this time reordering atoms from B2→B33. After that the sample will cool down to RT.

It is quite special, that the ten-fold growth, which is visible during the HSC recordings and also preserved on the surface of NiZrHf, can still be found in the microstructure, at least partially, as discussed in the previous sections. However, it was always a possibility, that the symmetric structures, found in different systems (NiZr, NiHf, NiZrHf), are formed solely by the SST[4]. Although the relevance of the initial phase was already partly discussed in the last two sections, it will be compressed here, to get a concise picture.

- Nucleation of the B33 phase and the subsequent transition into the B2 structure was presented to mostly preserve the dendritic growth direction. The ongoing heat front of the DB and presented microstructures can be reasonably explained by the dendritic model discussed with Fig. 5.8.

4 Relates to the second SST, during cooling after the recalescence (B2→B33).

- The investigated samples would be (and are) significantly different, when the initial phase is the B2 structure (by chance or by triggering). There is either a random grain orientation present (growth modes 2 and 3) or highly defined orientation relation (mode 4), due to an initial B2 single crystal.

The transition from a single crystal B2 structure into B33 was observed as well in the CoZr system (App. 5.3). Interestingly, both systems show the same orientation relations. Both transitions occur from a single crystal with a certain orientation. Therefore, the B33 phase can only be constructed on three possible orientations.

Lastly, it will be discussed, that the B33→B2 transition, does not alter growth directions significantly. High alterations would be problematic, as they would impede the analysis of the proposed growth model. The orthorhombic B33 lattice, the monoclinic sub-symmetry and the B2 structure[5] are compared, based on their orientation to each other. It is shown in a stereographic projection in App. 2.2, that the $[111]_{B33}$ and the $[113]_{mon}$ directions are identical. However, as discussed in Sec. 4.2, to form the DB based on the ratio given by Kobold [16], the $[223]_{B33}$ direction needs to be inherent to the dendrite growth. The $[111]_{B33}$ direction deviates about 8° from this orientation. A DB with secondary dendrites in the $[111]_{B33}$ direction would result in a highly compressed shape. Since Kobold calculated the ratio of the DB based on HSC observations, a certain deviation might be tolerable.
A 9° shift during the transition from $[223]_{B33}$ to $[113]_{B2}$ is also an option, as there are no other possible orientations in the near vicinity. Another point is, that after the transition, the present phase is naturally the B2 structure and not the monoclinic symmetry element. This relation is also highlighted in App. 2.2 by a green dashed arrow.
All together, it can be noted, that the proposed B33 growth direction $[223]_{B33}$, the $[111]_{B33}$ direction and the possibly subsequent $[113]_{mon}$ and $[113]_{B2}$ directions all run along the same plane in 3D space, which is the $(1\bar{1}0)_{B33}$ plane. A transition from either B33 growth direction into the B2 growth direction seems plausible. The dendrites would maintain their orientation, and even a shift by 8° would be possible as the form of the body is preserved. Only the proportions would change, the 10-fold heat front can still be observed.

With this comparison, it becomes clear, that there must be a mechanism, that preserves

5 The structures were introduced in Sec. 4.1.

the initial B33 structure through two solid-solid transitions, to be observable in the microstructure later on. A preferred, singular, [001] direction is only present, when B33 nucleation initialized the growth. This common growth direction is then preserved through the B33→B2 transition and the B2→B33 transition during cooling. Other features, such as the underlying orientation towards a common center in NiZrHf or the symmetric structures found in NiHf, are only present together with the presented growth mode 1 and initial B33.

Determining the initial nucleation phase

The initial phase during recalescence will be investigated further in future studies. Although the observations imply an initial B33 nucleation, this can not be claimed with absolute certainty. The temporal resolution of the pyrometer during ESL processing was set to 5000 Hz for the NiHf experiments. This was the maximal setting. The goal was, to identify a kink during the recalescence that would indicate a phase transition. Unfortunately, no deviations in the recalescence rise could be found. So, there either are none, since the B33 fraction can be tiny, or they just cannot be depicted. Even at these high temporal resolutions it is questionable, if the pyrometer can detect those small deviations within such steep rises, even in optimal conditions.
Scattering experiments, preferably at a synchrotron facility, can improve the temporal resolution to at least 10.000 Hz, which should be sufficient. For such high temporal resolutions, there most likely have to be compromises in the angular resolution of the resulting count spikes. However, the experiment can be set up to present only a small angular distribution and the diffraction patterns of both phases (B2 and B33) differ enough to distinguish the two (calculated patterns are found in App. 4.1 and App. 4.2). The main spike in both patterns seems to be roughly the same angle (110_{B2} at 38° and 111_{B33} at 36°), however, with mentioned small angular distribution they can be differentiated clearly. It is however questionable, if any B33 pattern can be detected. The discussed dendritic model (Fig. 5.8) implies, that the B33 dendrite is almost immediately transitioned into the B2 structure after growth.

5.2 Uneven nine-fold $Ni_{50}Gd_{50}$

NiGd was one of the first alloy system tested, with an expected (calculated) uneven symmetry. Hence, a lot of experiments were performed with this system. The lattice parameters, presented in Tab. 5.1, result in an angle of 40.1° and a 9-fold symmetry. The phase diagram, presented in App. 3.4, depicts NiGd as an intermetallic line component without additional solid phase transitions. This section will present multiple different examples, that express several of the crucial features, defined for the growth mechanism in the NiZr system. It will also be shown, that the uneven symmetry creates practical barriers during the solidification process.

The NiGd system was thoroughly processed and investigated in ESL, TEMPUS and DSC. As a rare-earth element, Gd has a high affinity to oxidization [202]. The specimens were prepared and alloyed in a glove box under protective atmosphere. The achieved undercoolings did not exceed $\Delta T = 90\,\mathrm{K}$. It was not achieved to remove impurities and oxides from the surface of the specimens. Only at temperatures significantly above T_L (more than 400 K), the oxides began to melt. At these temperatures, evaporation has already reached a considerable amount, so that the sample could not be held in this range for long. However, during cooling, the oxides re-solidified on the surface again, about 100 K above T_L. This is visible in Fig. 5.18 (a) with the oxides being brighter than the liquid sample itself. Fig. 5.17 shows these oxides or impurities on the surface of NiGd and in

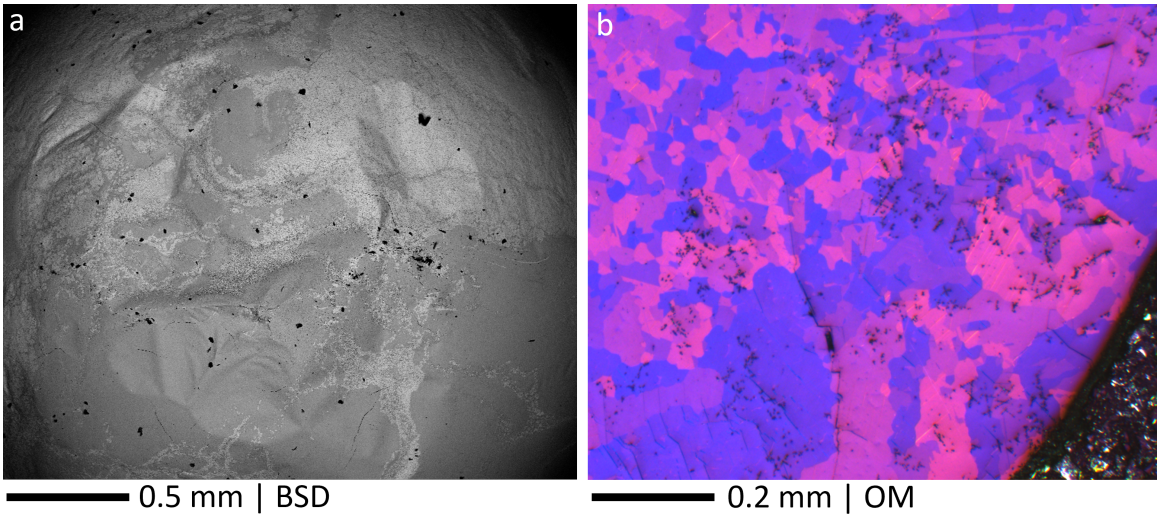

Fig. 5.17: Oxides and impurities in NiGd. **(a)** The surface of a specimen after levitation. The upper half of the sample is covered by a thin film of a different substance. **(b)** Cross-section with several precipitations.

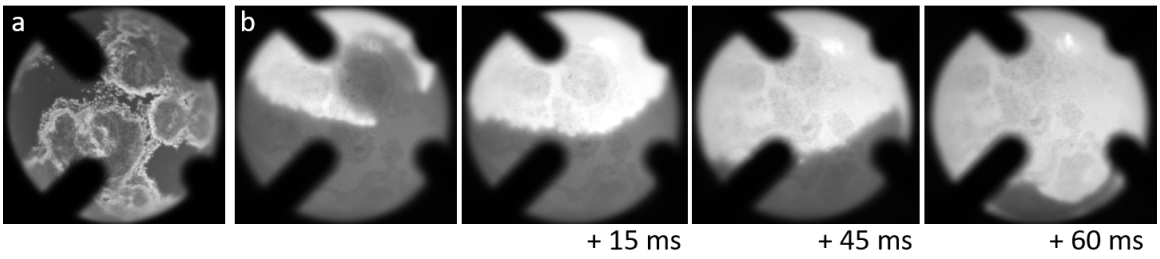

Fig. 5.18: HSC observations of NiGd during a parabolic flight. **(a)** Re-solidifying oxides on the surface of the molten specimen. **(b)** Consecutive frames of the heat front, observed through the oxide layer on the surface.

the microstructure. The surface film appears to be very thin and it was indeed observed, that with every consecutive heating cycle, the amount of material on the surface got smaller. The impurity layer could not be removed completely and it does not stay solute in the sample. At the latest, the solute impurities separate during the solidification process. It is likely, that they promote heterogeneous nucleation and prevent deeper undercoolings. In EML processing during a parabolic flight it was possible to capture a good view of the systems heat front in a sample, that undercooled 41 K. The heat front was observed through the, already solidified, oxide layer and had a slow growth velocity of $v = 3.15\ \mathrm{cm/s} \pm 0.1\ \mathrm{cm/s}$, as shown in Fig. 5.18 (b). The exact shape however, could not be determined, since there were not enough different perspectives of this front. The velocity was therefore only calculated with the FL-method and stands as a first fit for the respective magnitude.
The microstructure of these samples revealed several structures that seem to represent the symmetric growth according to the proposed model. Two distinct examples are shown in the upper right of Fig. 5.19 (a) and in the two EBSD images. It is visible in the OM image, that they are separated about 100 μm to each other and that they are embedded into a microstructure, that consists of a seemingly unrelated grain distribution. The pole figures reveal, that all grains visible in the EBSD images are ordered in nine different directions around one common [001] direction. Both symmetric structures are depicted in the two EBSD images, showing grain structuring towards a common central point. It needs to be particularly noted, that the pole figures represent both EBSD images. This means, that both growth structures, and in fact the whole visible cross-section, share the same set of nine differently orientated grains, all ordered around the common [001] direction. The GBA between any of these nine grain orientation matches the expectations of $40° \pm 2°$.

Overall, in the NiGd samples assessed this work, many of these growth structures can

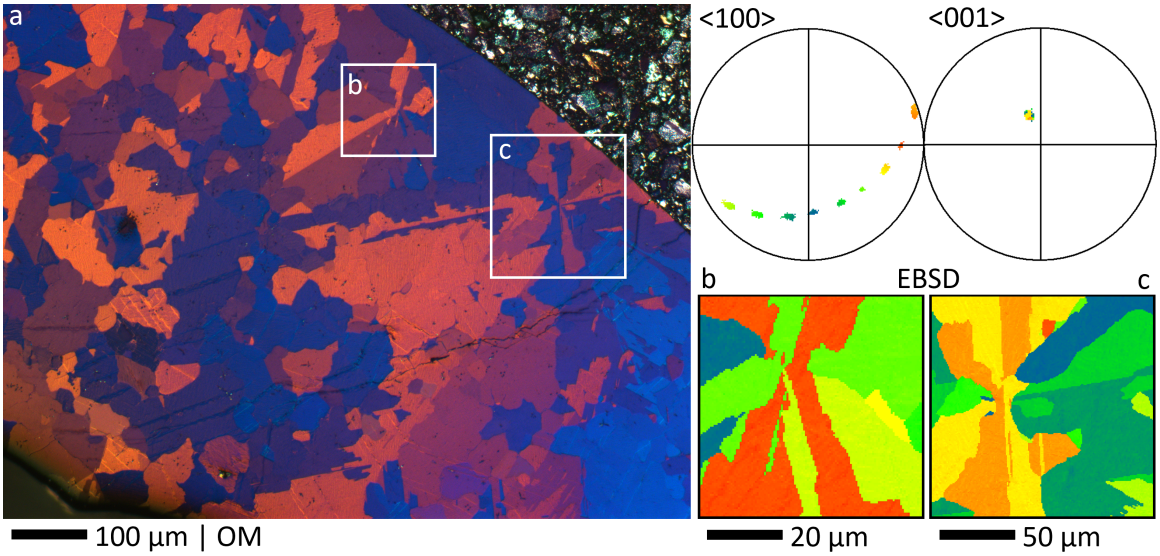

Fig. 5.19: NiGd sample, which was levitated in TEMPUS during a parabolic flight campaign and reached $\Delta T = 35\,\mathrm{K}$. **(a)** Two growth structures are visible in the cross-section of the sample. Images **(b)** and **(c)** depict the structures in EBSD. The pole figures show, that both structures have one identical set of differently orientated grains around a common [001] direction.

be identified. As will be shown later in Fig. 5.22, they are distributed quite randomly across the cross-sectional area. In contrast to the distorted examples of Fig. 5.19 (b) and (c), these symmetric structures were also observed with absolutely straight grain boundaries, orientated towards a common central point. This is visualized in Fig. 5.20. Seven consecutive grains are visible, each orientated to its neighbors by the proposed grain boundary angle of 40°. Unfortunately, it seems as if the grain in the bottom of the picture has overgrown the two left, differently orientated, grains that are missing in the EBSD image and the pole figures. This is also indicated by the angle between this grain and the dark green grain in the lower left, which is 120°. Most notably, the visible grains are all ordered around the common [001] direction.

Several of the crucial features for the growth model can be observed in the presented examples, such as the common growth direction and the GBA between two neighboring grains. It is however quite difficult to connect these pieces, especially considering the relatively low undercoolings on the one hand, and on the other, that there is a multiple of circular growth structures. Even though they partly present exactly the mechanism, that is proposed, it needs to be discussed, why there are several, seemingly randomly distributed ones across the sample. Fig. 5.21 shows EBSD images of an ESL processed sample, that

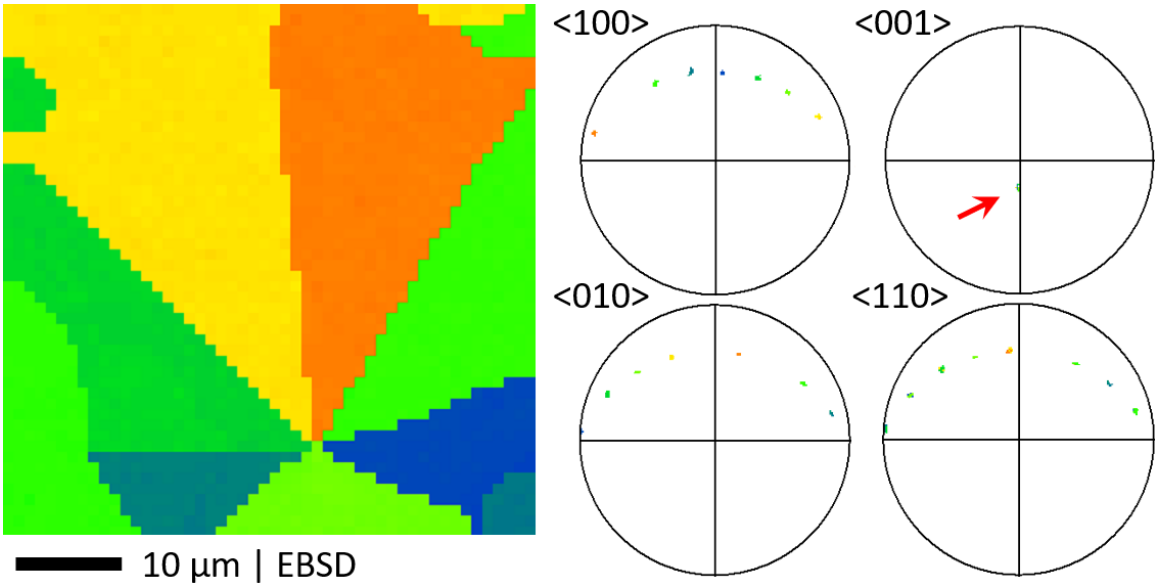

Fig. 5.20: Symmetric structure in a NiGd sample that undercooled 42 K. It shows an almost full symmetric center, but only seven different orientations are visible in the EBSD image, as well as in the ⟨100⟩ and ⟨010⟩ pole figure. All grains are orientated in the typical common [001] direction.

undercooled to $\Delta T = 90$ K. Two growth structures are visualized, that are directly neighboring each other. Images (b) and (c) each highlight one of these two structures in color, while the rest of the respective image is grayed out. Grain boundaries, where the expected angle ($40° \pm 2°$) is met, are highlighted in white in image (a). In this cross-sectional view, both growth structures are separated through a thin line of a different interphase (dark gray in image (a)). The corresponding pole figures to images (b) and (c) both show a nine fold symmetry of grains ordered around a central [001] direction. As already presented in Fig. 5.19, both growth structures share one exact set of nine differently orientated grains. Both are orientated in the exact same [001] direction. Although neither structure is complete, the existing grains have overlaying symmetry, as they share the same spots in either ⟨100⟩ pole figure. These findings indicate towards a shared origin of both structures. This means, that they are connected somehow and may have grown based on a single nucleation.

The presented observations are only partly in accordance with the proposed growth model. Especially the fact, that multiple, seemingly randomly distributed, symmetric structures are found in one sample, as seen in Fig. 5.22 is contrary to the nucleation mechanism of the model. The mechanism depends on a singular nucleation to be easy

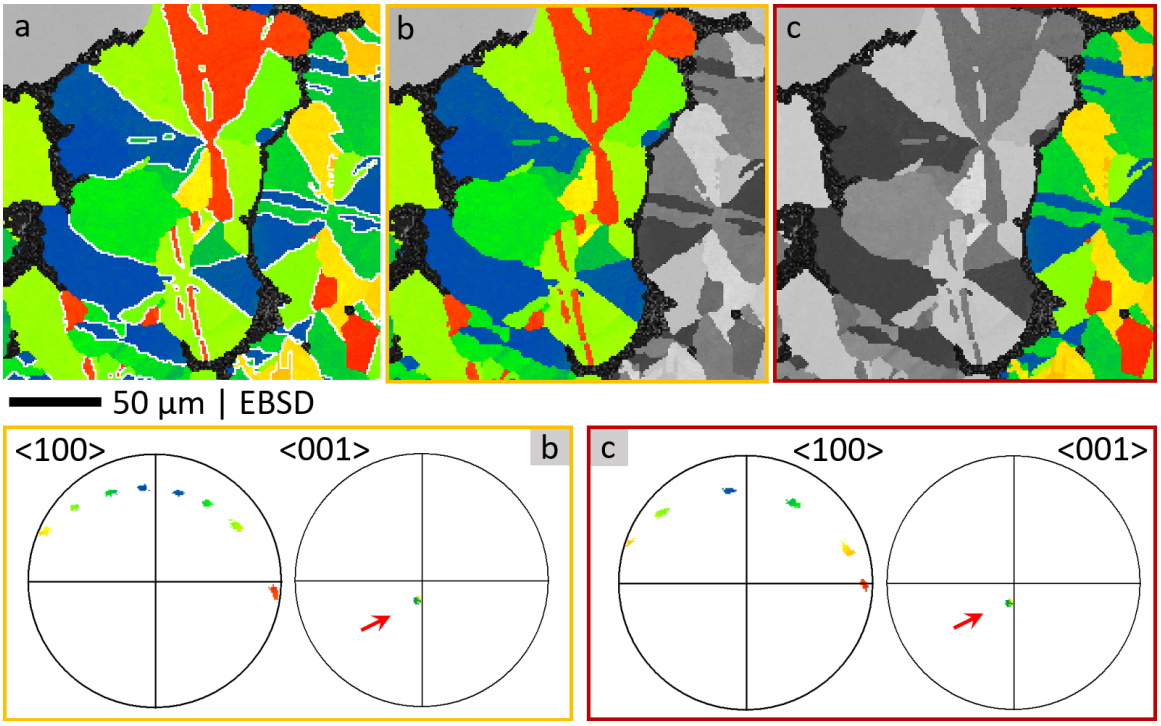

Fig. 5.21: ESL processed NiGd sample that reached $\Delta T = 90$ K. The corresponding pole figures depict the typical orientation relations, as found in other NiGd samples. **(a)** IPF coloring of two symmetric structures. Grain boundaries, that show the expected angle, are colored in white. Different phases are greyed out. Frames **(b)** and **(c)** each show one of the structures highlighted. Both structures exhibit the exact same set of orientations as is visualized below in respective pole figures. Certain orientations are missing in either of the parts.

observable. Multiple growth structures can emerge, when several nucleation sites are present. However, such growth structures would then have a random distribution of [001] directions. They would not all show a single [001] direction, as it is the case in NiGd. The structures found in NiGd could be explained as the tertiary dendrites of the growth model, as it was presented in Sec. 4.2, however, this would raise the question, why the primary and secondary dendrite structures are not visible anymore.

Heterogeneous growth front

A different growth mode needs to be considered to get these observations in accordance with the model. It is proposed, that a heterogeneous growth front grows through the melt with a defined [001] direction. Heterogeneous growth is implied by the relatively low undercoolings reached. However, no primary core structure is formed, but instead a

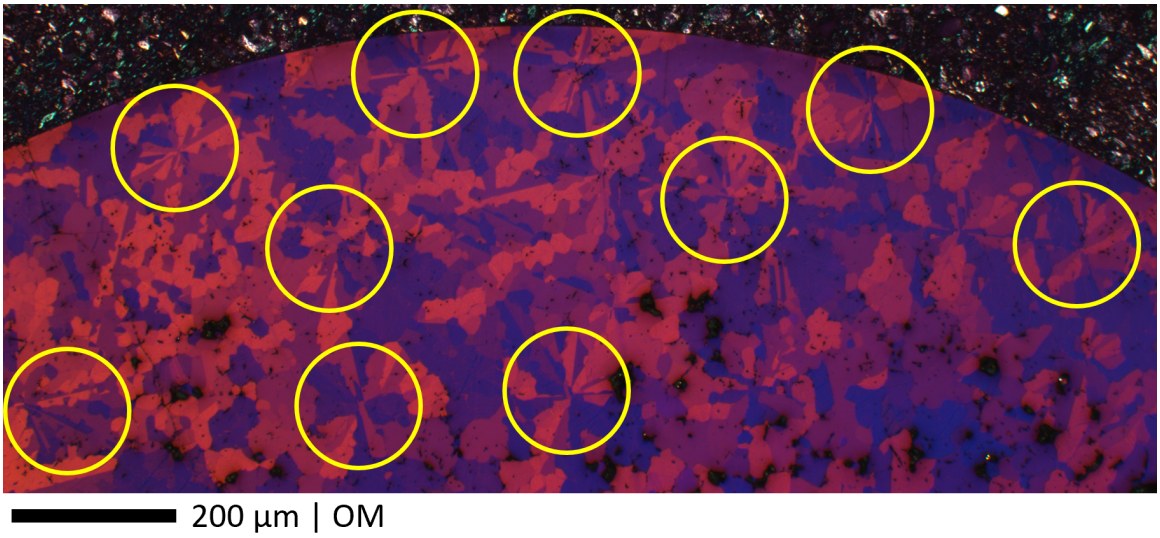

Fig. 5.22: OM image of a NiGd cross-section. This sample was processed during a parabolic flight inside TEMPUS and reached $\Delta T = 45\,\mathrm{K}$. Several symmetric growth structures can easily be observed and are highlighted with yellow circles.

growth front propagates through the melt and multiple small core structures are formed. Kobold showed, that the orthorhombic cell of CrB-structured systems has geometric features that translate to icosahedrons and decagons [16]. Such geometric links can also be identified in other orthorhombic phases [203, 204], as well as in monoclinic phases [205]. The monoclinic Gd-oxide Gd_2O_3 structure could be an option, to act as a heterogeneous nucleation site in NiGd. A pentagonal or decagonal local symmetric structure can also easily be built, e.g. by stacking faults within the regular growth front.

Assuming a solidification front running through the melt and the formation of a symmetric structure within this growth front, it can be understood, that this structure will have to compete its growth with the regular growing solidification front. This can be an explanation for the mostly distorted and only partially visible structures. One indication, that this assumption of a heterogeneous growth front, might by valid, are the observed structure shapes. They were analyzed on whether they have a spherical shape or if they are propagating through the sample. It is presented in Fig. 5.23, where one such structure was observed, as the cross-section was polished repeatedly, that a somewhat cylindrical shape is present. The structure is basically preserved in depth. This makes sense, since the structure competes with the surrounding solidification front and can only expand freely in the only direction, where the liquid phase is still present. As this is also the growth direction of the heterogeneous growth front, all of the observed growth structures are aligned in their [001] direction.

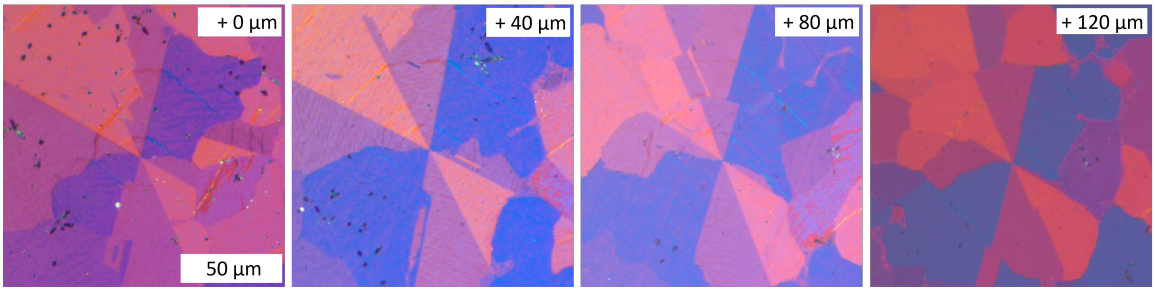

Fig. 5.23: Consecutive images of one growth structure in NiGd. With each frame, additional $40\,\mu$m were polished of, to get an impression of the 3D behavior of these structures. It becomes visible, that these are not spherical, but more of a cylindrical shape.

Similar cyclic twinning structures are observed in tin based solder alloys with a six-fold symmetry. They are based on one nucleation event as well. However, they do not depend on an icosahedral nucleus and a QC core structure, but instead on a hexagonal bypyramidal dodecahedron[6] at the center [206]. It is argued, that this structure is locally easier to build than the Sn unit cell, but it possibly needs impurities for nucleation as well.

In fcc-structured Au and Al-Zn alloys, icosahedral twinning was shown by Kurtuldu and Rappaz [207, 208], based on certain additives, such as Ir or Cr particles. An icosahedron is proposed to be the basis of an icosahedral QC that is triggered by the addition of said dopants. This enhances the heterogeneous nucleation and improves grain refinement. In contrast to the proposed growth model in this work, the growth in these alloys is dependent on these additives. Without them, such twinning based in the icosahedral-QC core structure was not observed. Twinning is also described for all facets of the icosahedral QC core, whereas the orthorhombic structure and the singular growth direction of the proposed growth model only allow that the ten outer facets[7] of the icosahedron could be utilized. Another important difference is, that they do not observe a common [001] direction, together with the preferred growth around this central axis. In general, the pole figures presented by Kurtuldu et al. cannot be connected to an n-fold growth around a central [001] direction. It is therefore unlikely, that the presented twinning enhancement, based on dopants, is connected to the proposed growth model in this work, but it can support the proposed modification of the model in NiGd.

6 Two hexagonal pyramids, which share a common base.

7 As shown in Sec. 2.5 and Fig. 2.12, the icosahedron has 20 triangular facets. In the proposed growth model, the C_5 symmetry axis of the icosahedron is aligned to the primary [001] direction of growth. Outer facets are the ones, that are not in contact with the respective C_5 axis (highlighted in green in Fig. 2.12 (b)).

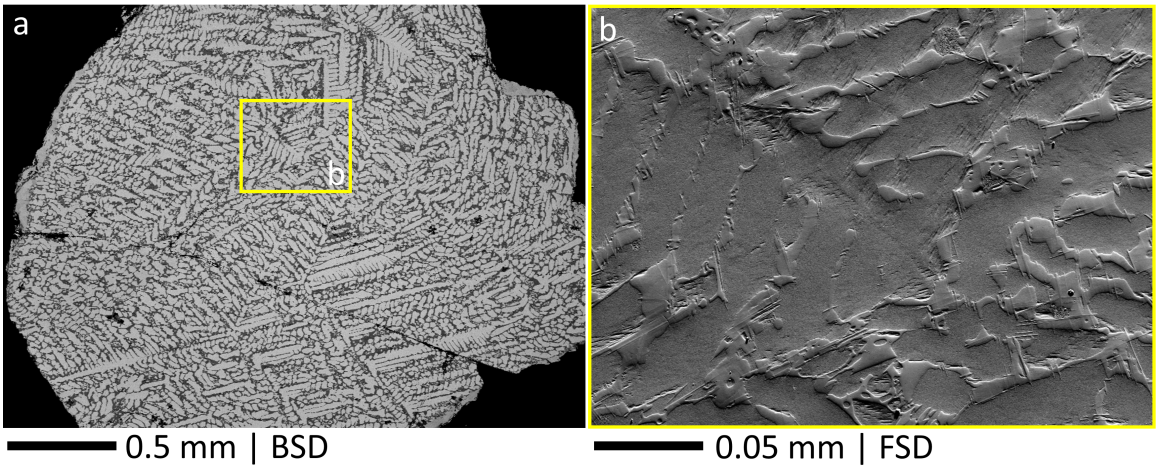

Fig. 5.24: SEM images of the DSC processed $Ni_{44}Gd_{56}$ sample. **(a)** The dendritic structure is visualized well, since the composition deviation results in multiple phases. **(b)** A seemingly symmetric dendrite is highlighted and used for further analysis.

Secondary dendrite growth plane

Another feature, that connects NiGd to the proposed growth mechanism of NiZr, are the growing dendrites. In NiZr it was shown by Kobold [16], that the stem of each of the secondary dendrites (see Sec. 4.2) is built by the boundary between two neighboring grains. Twinned dendrites are a common growth feature in fcc-alloys [207, 209–211]. They are known to have a growth advantage against non-twinned dendrites, for example in Al-alloys [212, 213]. Such a twinned dendrite was also found in a NiGd sample, that was processed in a DSC. It was embedded in borosilicate glass to prevent a direct contact to the crucible. Glass itself is usually not a nucleation site for other systems. Additionally, it was assumed, that the molten glass will absorb the oxides on the surface of NiGd samples. For this experiment, different compositions were chosen, to provoke the formation of second phases. By this, it was possible to visualize the dendrites of the main phase, as can be seen in Fig. 5.24 (a). In these experiments, only marginal undercoolings could be achieved. One particular dendrite, that visually seems to be symmetrical, was chosen for a further analysis. This dendrite is highlighted in Fig. 5.24 (b). The interphase is also clearly visible. In the center of the dendrite, some kind of boundary can be vaguely perceived. The following EBSD analysis in Fig. 5.25 revealed, that this dendrite is a perfect example of a twinned dendrite in general, and also especially in relation to the proposed growth model. It is formed by two B33 structured grains, that are both orientated in the same [001] direction, as deducted from the respective ⟨001⟩ pole figure. The orientation relations

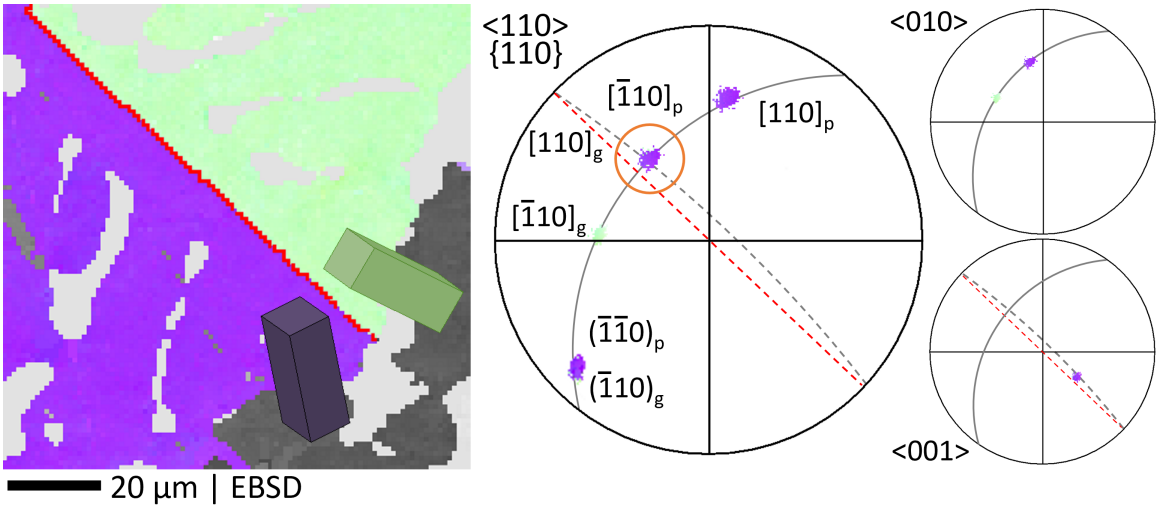

Fig. 5.25: EBSD image and pole figures of the dendrite shown in Fig. 5.24. The dendrite is split in two parts. The pole figures visualize the relation between both parts, as they are angled 40° to each other (red line in EBSD image: $40° \pm 2°$) and share a ⟨110⟩ direction and a {110} plane. These particular results will be published in [214].

between both parts have been thoroughly analyzed to show:

- The two parts of the dendrite are angled 40° to each other. This is indicated by the red line in the center of the dendrite, that shows $40° \pm 2°$, as well as directly visible in the ⟨010⟩ pole figure.
- Both parts share a common ⟨110⟩ direction. This is the $[110]_g$ for the green part, and the $[\bar{1}10]_p$ for the purple part. They are marked in the pole figure with an orange circle.
- As they share a common ⟨110⟩ direction, they must share a {110} plane. The $(\bar{1}10)_g$ and $(\bar{1}\bar{1}0)_p$ planes indeed share the same orientation. The analyzed dendrite grows along this plane, which supports the previously made assumption, that the secondary dendrites in the proposed growth model grow along {110} planes in ⟨223⟩ directions (Sec. 4.2).

The two unit cells of both parts are also depicted. It can be understood, that both {110} diagonals of these cells follow the same 3D plane. The (110) twinning plane is common in orthorhombic alloys, as in cyclic twinning around a shared [001] direction. An example would be the aragonite in natural shells [215], which is structured in the orthorhombic B27 phase (Cmcn, space group 62) or the tin-based solder alloys [206], already introduced earlier.

The secondary dendrite direction was discussed in Sec. 4.2 and it was set to the ⟨223⟩ directions of the cell, as they best fit to the ratio of the DB. This dendrite was selected, as it was visually determined, that it lied almost perfectly symmetric within the cross-sectional area. This can be validated by looking at the crystallographic directions of said dendrites. By plotting the crystal orientation onto a stereographic projection, which is shown in App. 2.3, it becomes clear, that the $[22\bar{3}]$ direction runs almost perfectly perpendicular to the axis of this point of view. This serves as another validation of the dendritic growth, originally described by Kobold, on which the proposed growth model is based.

Altogether, the NiGd system showed unique features due to the uneven symmetry with its 40° GBA. Additionally, only small undercoolings were reached. However, the system exhibits some of the defined crucial features of the proposed growth model. Symmetric structures, with the expected GBA, all orientated around a common growth direction, were found to be essential in the growth of this system. Unlike in the previously presented systems, a singular growth from a central nucleation site could not be determined. At least not, regarding the structures connected to the proposed growth model. It is however proposed, that a heterogeneous growth front propagates through the system. As it was discussed in this section, stacking faults or other impurities probably lead to several heterogeneous nucleation sites for new symmetric structures. With the general propagation of the growth front, they are all aligned in the same growth direction and have only a limited size distribution. This leads to difficulties in the construction of the nine-fold symmetric structures. They can only be observed partly, with distortions, or with parts, that are overgrown by differently orientated grains. Considering an icosahedral QC core, as in the prototype model, it seems plausible, that the core in NiGd is based on the icosahedron as well. This would impose growth problems during the transition from the core structure to the nine-fold twinned growth and could very well be another cause for incomplete symmetric structures. In principle, another, nine-fold, QC structure could act as the core structure. However, such a QC structure is yet to be discovered.
The NiGd system and its solidification process can be described with the nucleation and growth model by adapting the heterogeneous growth front and several nucleation events for the symmetric structures. Even without this adaption, some crucial features, as the GBA and the common growth direction, are present in the NiGd system, despite the very low undercoolings reached.

5.3 Eight-fold $Ni_{50}B_{50}$

The NiB intermetallic alloy is one of the few systems, for which an eight-fold symmetry is expected, according to the proposed growth model. The exact angle, based on the systems lattice parameters, is 43.3° with a theoretical symmetry of 8.31. In the NiZr system, the theoretical symmetry was 9.88. Together with expected distortions due to tensions, as explained in Sec. 4.3, this deviation may disturb the proposed growth mechanism. However, as seen in Fig. 4.10 and 4.11, geometrically, eight-fold symmetric growth should be possible. In practice, NiB proved to be quite difficult in handling, regarding the preparations, as well as the actual levitation. Impurities on the surface of all NiB samples interfered with the active PSD system of the ESL experiment, since it can't predict the behavior of the sample anymore. Multiple attempts with different elemental boron batches were carried out. It turned out, that even the purest batches (up to 5N elemental boron, powder) were not free from boron oxides. The powder additionally proved to be difficult to handle in the alloying process as well.
Eventually, NiB was successfully levitated and heated above its melting temperature. Fig. 5.26 shows an excerpt of the NiB phase diagram (found in full in App. 3.3). It can be seen, that the NiB phase is stable below a peritectic temperature of 1316 K. Above this line, elemental boron is still present in crystalline form. In levitation experiments, the system had to be heated at least to 1348 K to reach a fully molten state. After reaching a state, where the specimen is completely liquid, it was overheated substantially above

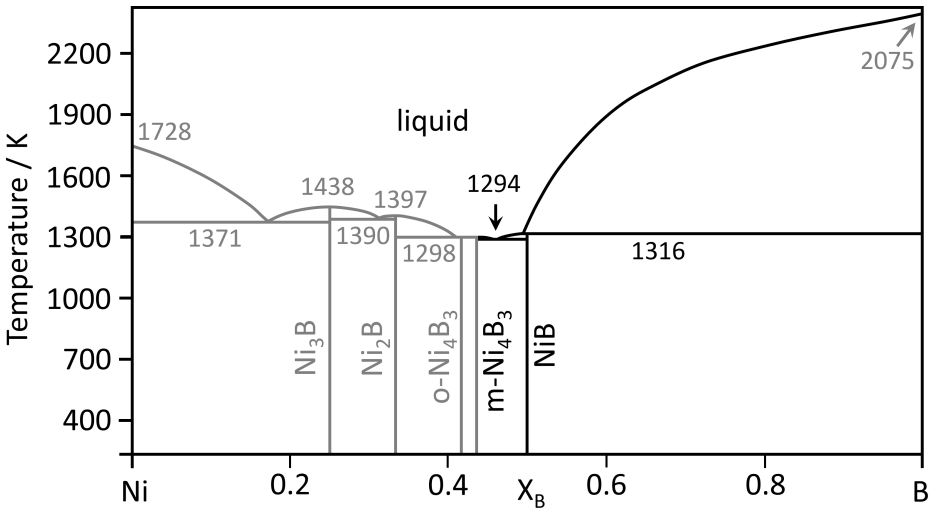

Fig. 5.26: Adopted and simplified Ni-B phase diagram, from [216, 217]. The NiB phase is stable below a peritectic line at 1316 K.

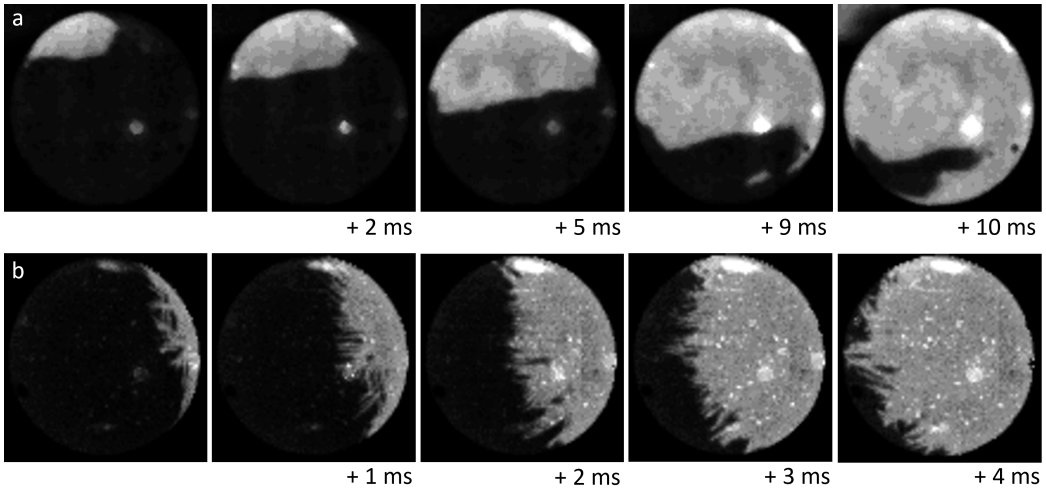

Fig. 5.27: Two different types of heat fronts observed in NiB. The samples reached an undercooling of 80 K and 82 K, respectively. **(a)** Heat front with a clear contrast to the liquid phase. Several kinks are visible, which indicates to a specific shape. **(b)** Heat front made up visibly by several small spikes. The white dots distributed above the surface are impurities with a different emissivity.

the melting temperature. Temperatures of 1700 – 1800 K were reached with the goal of evaporating the impurities floating visibly on the surface. Evaporation of the elemental constituents was of no concern in this system, even at the described temperatures. The impurities evaporated neither and there was also only a very limited degree of dissolving into the specimen. Despite these obstacles, NiB was undercooled, up to $\Delta T = 82$ K. During the recalescence, different types of heat fronts were observed. They are presented in Fig. 5.27, with (a) showing a clear and smooth heat front, as it was present as well in previously described observations. Several edges and spikes are visible and in the lower part of the fourth frame a dendrite is seen poking through the surface from within the sample. This heat front could be observed in a few HSC recordings and seems to indicate towards a characteristic body shape growing in NiB. Unfortunately this body, or specific dendrites, could not be simulated, as there were not enough different perspectives of this heat front. Sequence (b) shows a heat front, made up from several small needle-like structures. They are either growing fast enough, so that the dissipated heat is distributed slower and no clear front is formed, or they break through the surface from within the sample. Both samples reached almost the same undercooling, but (b) was faster by a factor of 2. Exactly, sample (a) showed a growth velocity of $v_{(a)} = 36.15$ cm/s $\pm$ 1 cm/s, while sample (b) had $v_{(b)} = 47.83$ cm/s $\pm$ 1 cm/s[8].

8 The velocities were obtained using the FL method, as introduced in Sec. 3.2.4, since specific dendrite directions could not be deducted.

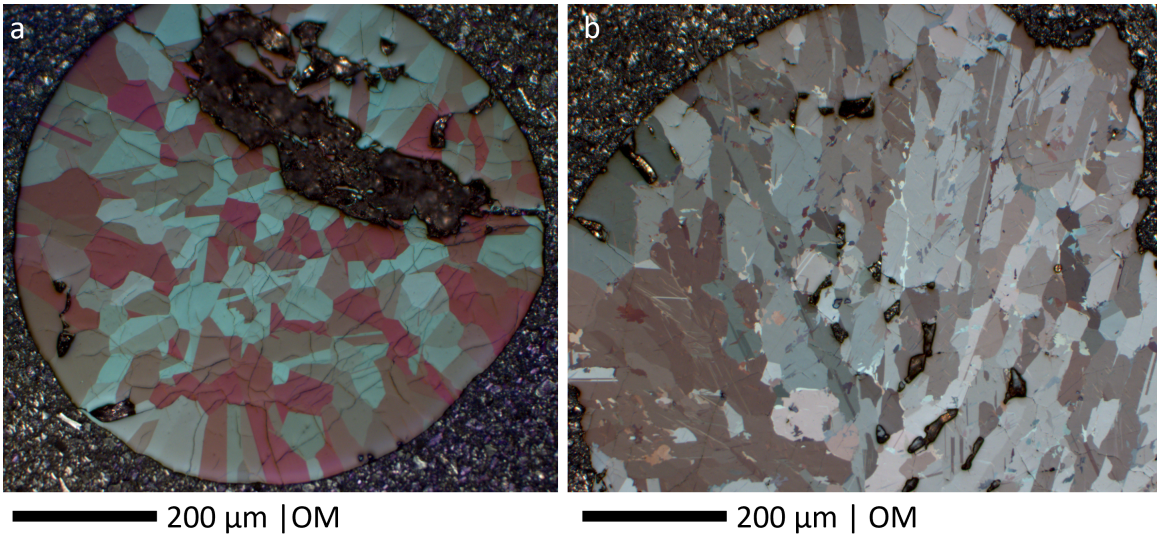

Fig. 5.28: Cross-sections of both samples, which are presented as well in Fig. 5.27, respectively. **(a)** Compact grain structure with no visible symmetric resemblance. **(b)** Large grains, seemingly orientated outwards from a single point. Both microstructures show straight grain boundaries.

Both samples are analyzed optically by looking into their cross-section. In Fig. 5.28 (a), compact grains are shown, with no visible link to the observed heat front, like a symmetric grain orientation. Fig. 5.28 (b) exhibits elongated grains, that seem to have originated from a single symmetric point. Both cross-sections show straight grain boundaries, which are most likely twinning boundaries. The cross-section of Fig. 5.28 (b) surprisingly corresponds with sequence (b) from Fig. 5.27. To get a better understanding of these structures, they were analyzed with EBSD. Fig. 5.29 shows grain structures, as seen in Fig. 5.28 (a), in an EBSD image with IPF coloring and corresponding pole figures. The gray areas correspond to a different, not indexed, phase. Red markings highlight grain boundaries with an angle of $45° \pm 2°$. The pole figures show, that the different grains are all more or less orientated around a common [001] direction. The ⟨100⟩ and ⟨010⟩ pole figures show much higher deviations of the orientations, but it can be determined, that there are preferred directions. Even in NiB samples with a relatively low undercooling, already some of the crucial features (Sec. 4.2.1) of the proposed mechanism can be identified. These are:

- Solidification within the B33 structure, which is assumed, based on its subsequent observation in the microstructure and the fact, that a HT B2 phase is not described for this system. A solid phase transition (SST) from a HT B2 to the B33 phase could be traced back in the analysis of the B33 microstructure, as was shown for Ni(Zr,Hf)

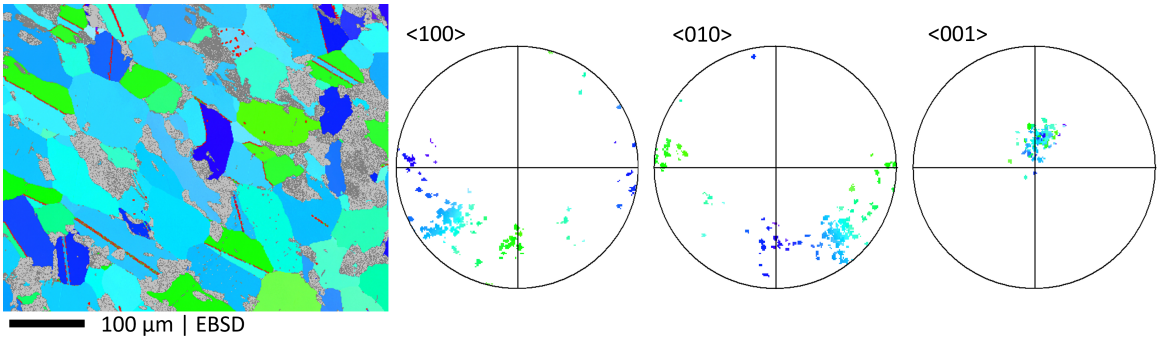

Fig. 5.29: EBSD image and pole figures with IPF coloring of a NiB sample, undercooled 79 K. Red lines highlight a grain boundary angle of $45° \pm 2°$.

from Sec. 5.1 on.

- The lattice parameter ratio a/b is observed directly through the grain boundaries, exhibiting a 45° angle, which is expected in the NiB system (Tab. 5.1).
- Although, the grains display a certain spread in the ⟨001⟩ pole figure, the preference of a common [001] direction is observed.

The first crucial feature, a deep undercooling and possible homogeneous nucleation, was not reached with NiB in this work. However, another microstructure was observed, that resembles the NiZr growth, but with an eight-fold symmetry. It was in fact found in a sample that undercooled just 43 K and is presented in Fig. 5.30. The IPF coloring helps to identify four differently colored orientations within the microstructure visible in this cross-section. The grain structure is visibly connected to a symmetric central point, although it is highly distorted. It can be seen, that directly opposing grains share the same orientation. Fig. 5.30 (b) is the same image but grayed out to highlight the grain boundaries with different colors for different angles. As before, an angle of $45° \pm 2°$ is colored red. All of the mayor grain boundaries exhibit this angle. Additionally, four distinct orientations can be seen in the ⟨100⟩ and ⟨010⟩ pole figures. Each of the differently orientated grains shares the common [001] direction. This observation of a cross-section, that is covered in full with a symmetric growth structure, out of a common central point, despite the small undercooling reached, is fascinating. In the NiZr prototype, singular nucleation was possible not at last because of the deep undercooling together with homogeneous nucleation. However, growth according to this model, was observed at lower undercoolings as well. The important factor here, as also defined previously, is the occurrence of only one singular nucleation event, that has time to propagate through the whole sample, before another nucleus grows. Without this singular nucleation,

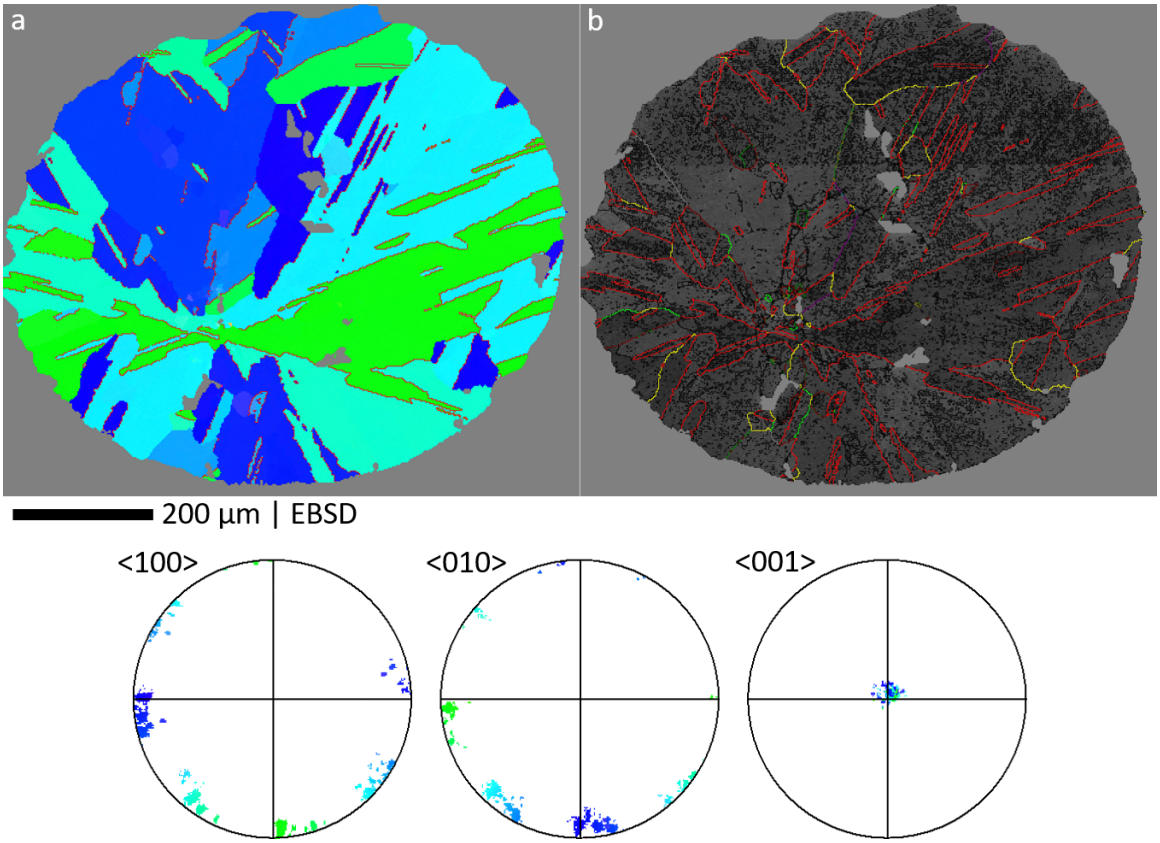

Fig. 5.30: EBSD image and the corresponding pole figures of a NiB sample, processed in ESL and undercooled 43 K. **(a)** The cross section shows a distorted point symmetric structure orientated around a common [001] direction. **(b)** The image highlights the grain boundaries with a red color if the angle is $45° \pm 2°$.

observability would be highly decreased. However, it was a rare event. Much more common were microstructures as presented in Fig. 5.29.

The crucial features of the proposed model are mostly met in the NiB system. A common, singular growth direction was observed with eight different grain orientations and the expected GBA around this common axis. It is interesting, that such features could be observed at only 43 K. Homogeneous nucleation can most certainly be discarded in this case. As discussed, it is however sufficient, that one singular nucleus grows through the sample, before other nucleations occur. If deeper undercoolings can be reached with this system in future works, most certainly even more connections to the symmetric growth model would arise. The twinning boundaries in NiB show large deviations and shifts. As it was discussed already in Sec. 4.3, lower symmetric structures are assumed to have more of such distortions. It was shown that symmetric elements, such as the orthorhombic

unit cell, can extend along the boundaries in the ten-fold symmetric structure. With lower symmetries, the atom positioning gets shifted, which is proposed to result in a more disturbed microstructure. In principle, other grain boundaries, such as in cyclic twinning, could be inserted into the structure to counteract the atom shift. This was however not observed, as mainly the expected 45° boundary was present in the examined samples.

5.4 Additional investigated CrB-structured systems

This section will give a brief overview of different systems, that were processed during this work, but did not show the proposed growth or could not be undercooled enough.

Palladium-Hafnium ($Pd_{50}Hf_{50}$)

PdHf was successfully processed to reach $\Delta T = 333$ K. The heat front visible in Fig. 5.31 reveals a four-fold initial front that seems to change shape into an octagon in the second frame. The shape was not analyzed further, but it may be the same shape, which is also present in PdZr, as shown in Sec. 6.1. This would represent a rhombic dodecahedron, which is a cubic body. According to [218] and the phase diagram (App. 3.6), the cubic B2 phase is stable above 870 K. This excludes the system from further analysis regarding the B33 growth model. However, with the growth velocity at 48 cm/s ± 1 cm/s and the assumed shape, a dendritic growth velocity can be calculated for the comparison in Sec. 6.1.1.

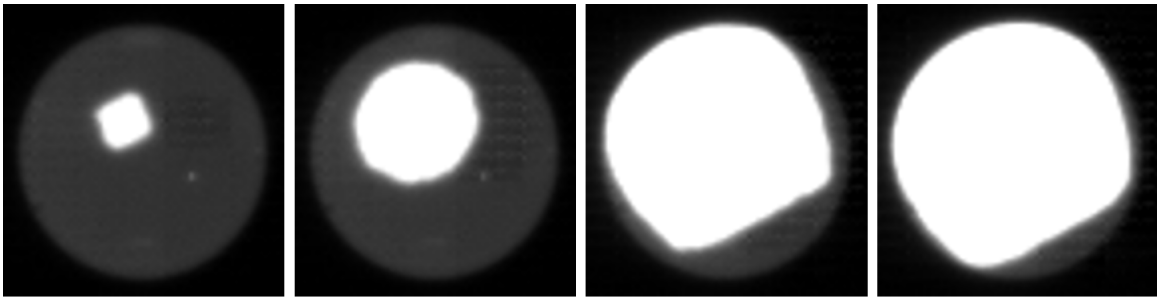

Fig. 5.31: Propagating heat front on a PdHf sample, levitated in ESL. The first frame gives the impression of a four-fold front, whereas the second frame change more into an octagon.

Palladium-Zirconium ($Pd_{50}Zr_{50}$)

As implied in the previous section for PdHf, it was possible in PdZr to construct the growing crystal structure from the propagating heat front, as it is presented later in Sec. 6.1. The stable phase upon solidification is the cubic B2 phase with a melting temperature of 1873 K, as seen in the phase diagram (App. 3.5) [219]. Later on, at 902 K there is a first solid-solid transition into the B33 phase, which will however transform again at 473 K into a monoclinic phase [220]. It is also assumed in literature that another transitions takes place between B2 and B33 with the intermediate orthorhombic B19 or B19' phases. Although, the alloy was undercooled up to 330 K, with the presented stable HT B2 phase, it is not practically possible to solidify in any other phase.

Iron-Zirconium ($Fe_{25}Zr_{75}$)

The presence of the proposed growth model was shown solely in systems with the orthorhombic CrB-structure. It is interesting to determine, whether it can be observed in other structures as well. The $Fe_{25}Zr_{75}$ was chosen for a first investigation. In a first optimistic thought, it was assumed, that the crystal structure can be understood as *pseudo-binary*, where half of the atom sites of constituent A in the unit cell are occupied by constituent B as well. It solidifies in the orthorhombic Re_3B-structure, which has, just as the CrB-structure, the space group type Cmcm, No. 63. It contains 16 atoms in its unit cell and has the lattice parameters: $a = 0.33249(2)$ nm, $b = 1.09731(7)$ nm and $c = 0.88066(5)$ nm [179]. In the phase diagram, in App. 3.11, it can be seen, that the $Fe_{25}Zr_{75}$ phase is stable for the whole existing range. In relation to CrB-structured unit cells, the parameter c is roughly doubled in size. Pseudo-tenfold twins have, however,

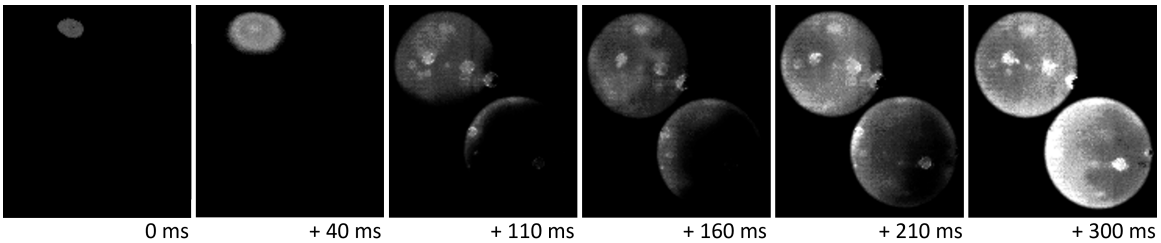

Fig. 5.32: Propagation of the heat front in a $Fe_{25}Zr_{75}$ sample. Overall the growth velocity is especially low and the front becomes blurred. Only high contrast settings allow further analysis. After about 150 ms a second heat event can be identified propagating through the whole sample itself.

been observed in sputtered, amorphous Cr-C films [221]. $Fe_{25}Zr_{75}$ was successfully undercooled in ESL to $\Delta T = 195\,K$. At first the heat front grows in hexagonal shape, as can be seen in Fig. 5.32 It propagates very slow and becomes blurred. A second event can be observed vaguely, following the first heat front, after about 160 ms. This second event happened during the observed recalescence, which lasted for 280 ms in the temperature-time profile. This time period corresponds with the total propagation of the first heat front, which is 274 ms, resulting in a growth velocity of only 1.49 cm/s ± 0.02 cm/s. The microstructure however shows none of the characteristics previously discussed necessary for the symmetric growth model. The grains visible in the EBSD image all have roughly the same orientation, only shifted by small angle grain boundaries.

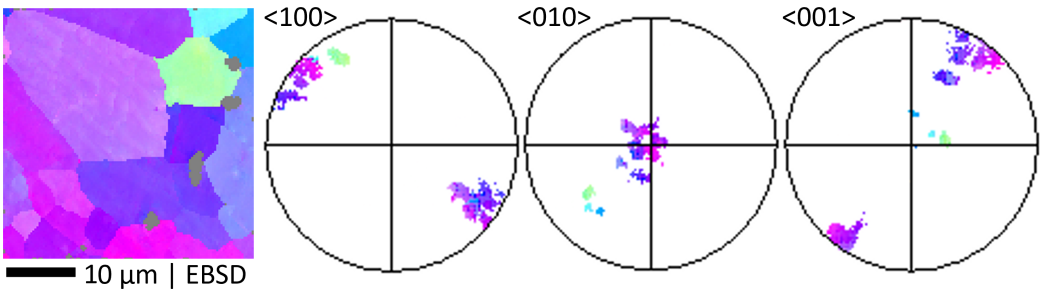

Fig. 5.33: EBSD image of $Fe_{25}Zr_{75}$ with corresponding pole figures. The grains are shifted to each other by small angle grain boundaries. This creates the spread of each distinct direction in the pole figures.

Gold-Gadolinium ($Au_{50}Gd_{50}$)

AuGd is an interesting system, as its proposed symmetry was calculated to 9.48, so its almost perfectly between two integers, which could result in several possible outcomes of the microstructure. In practice, due to the density of gold, it was not successfully levitated in ESL or ground EML. It was processed during a PF flight campaign in the TEMPUS experiment. The upper left of the image is not visible, due to a positioning element in the TEMPUS levitator. It was possible to reach $\Delta T = 80$ K. The video reveals a four-fold initial heat front, probably representing a cubic dendritic growth. This is pictured in Fig. 5.34. According to the system's phase diagram (App. 3.12) the HT B2 phase (β-AuGd) is stable in the achieved undercooling region. Only with $\Delta T > 110$ K the system will solidify in the B33 phase (α-AuGd). It may be interesting to reconsider processing AuGd again during a PF campaign to reach deeper undercoolings, as the necessary region is not far fetched with the undercoolings already reached. Especially with the expected symmetry between two integers it may be interesting to analyze.

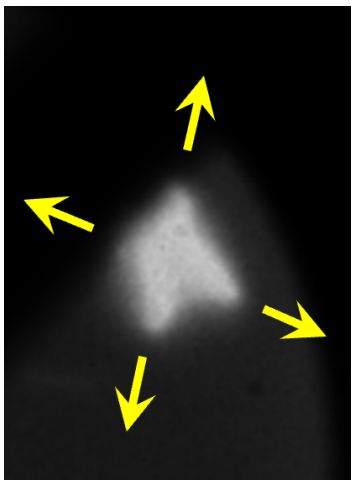

Fig. 5.34: Four-fold front on the surface of AuGd during a parabolic flight. The four dendrite directions are highlighted with yellow arrows.

Aluminium-Zirconium ($Al_{50}Zr_{50}$) and Aluminium-Hafnium ($Al_{50}Hf_{50}$)

AlZr was already tested by Kobold. It showed an unusually high evaporation of Al, even below its melting temperature. Kobold was barely able to melt down AlZr and only with a high compositional change during the process. The AlHf was tested in this work for the sake of completeness. With a more than 300 K higher melting temperature [222], in comparison to AlZr, the evaporation was even worse. High evaporation in AlHf started at roughly 1700 K. Interestingly, this is comparable to AlZr, where Kobold reported the onset of evaporation at roughly 100 K below the melting temperature. This would be at an absolute temperature of 1660 K. So, the absolute temperature is roughly the same, which hints to the reason being an intensive property of the aluminium. Both systems cannot be processed in vacuum at such temperatures without significantly changing the composition. With the experiences made with glass embedding and DSC experiments in NiGd, such experiments may be promising future projects.

Aluminium-Yttrium ($Al_{50}Y_{50}$)

After AlZr and AlHf could not be levitated in ESL, due to their high evaporation, AlY was considered, as its melting temperature is considerably lower at 1410 K [223]. According to the phase diagram (App. 3.7), AlY solidifies as a line component and there are no SST known. It was possible to undercool AlY to $\Delta T = 85$ K, however, similar to NiB and NiGd, a thick oxide layer caused problems in levitation and undercoolability. Yttrium was already processed completely within a glove box to reduce oxidization as much as possible. An iterative process proved most successful to reach these undercoolings. After each melting during ESL levitation, the sample was taken out and its surface was polished and cleaned in an ultrasonic bath. With each iteration, deeper undercoolings were reached. However, this is a very time-consuming process. It will be considered to work with this system in future ESL experiments, as the results are promising. AlY is a subject to fly on a near-future PF campaign, since EML convections should help to dissolve the impurities on the surface and the μg environment improves stable levitation. The microstructure analysis proved the B33 phase to be present. Since no SST is reported, this is probably also the phase in which the solidification occurs. The grain structure however, is highly distorted, which indicates high tensions within the sample. The pole figures reveal the common orientation around the [001] direction. The GBA between different grains seems hardly pronounced as the different ⟨100⟩ and ⟨010⟩ directions are very close to each other and do not show the complete set for the proposed ten-fold symmetry. The pole figures could also be interpreted basically as a single crystal, that exhibits large distortions in two axis.

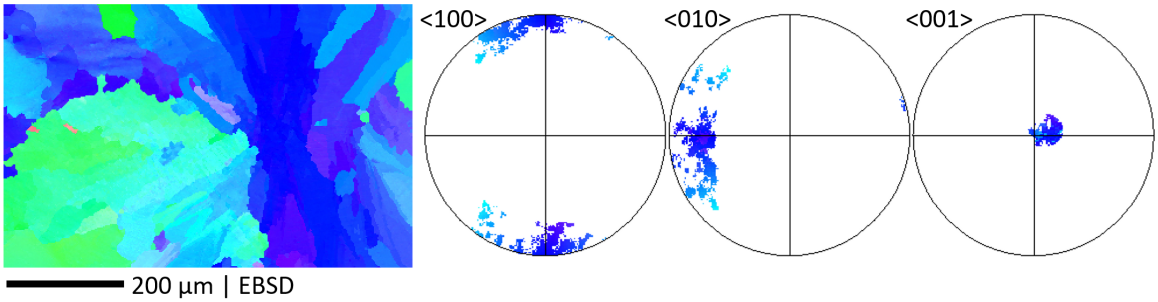

Fig. 5.35: EBSD Image of an AlY sample, that reached $\Delta T = 85$ K. A common [001] direction is visible.

Silicon-Zirconium ($Si_{50}Zr_{50}$)

According to the phase diagram (App. 3.8) SiZr has a melting temperature of 2483 K [224]. Down to 1723 K, the B33 phase is stable in β-SiZr. Below this SST, another orthorhombic phase (FeB prototype) will be stable. Due to the high temperatures, it was not possible to overcome the melting plateau in this system, even with both 75 W lasers at full power in the ESL experimental setup. A sample, taken from the arc-melting furnace after alloying, was nevertheless analyzed. As seen in Fig 5.36 (b), the microstructure consists mainly of B33 structure (yellow phase) and an arrangement of B2 structured (green phase) dendrites. These dendrites have no visible connection, but seem to be ordered, as they appear somehow periodic. Both, the presence of B2 and B33 are basically unexpected at RT. At first, the IPF colored microstructure in Fig. 5.36 (a) shows no similarity with symmetric structures, as they are expected by the proposed growth model. The pole figures however, reveal an ordered structure around a common [001] direction. A directional or

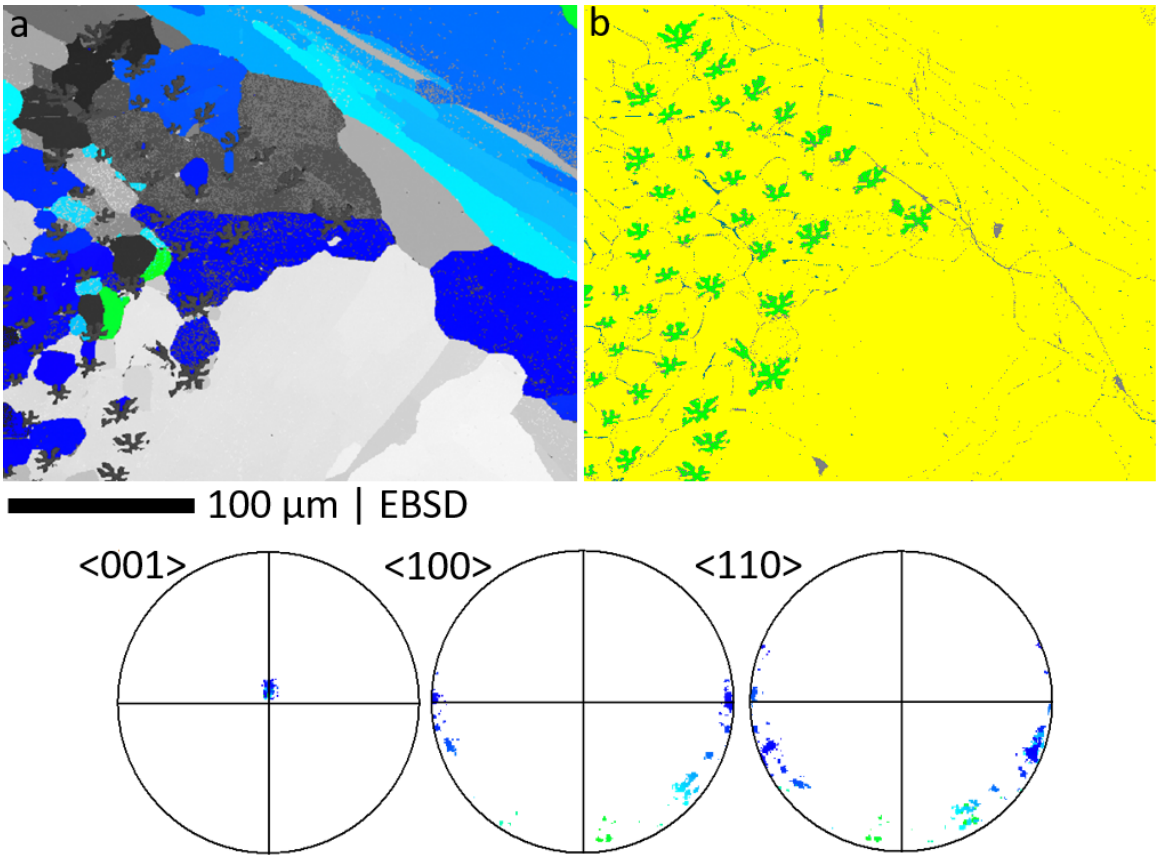

Fig. 5.36: EBSD images of SiZr from arc-melting. **(a)** IPF colored image with corresponding pole figures below. No visible resemblance with symmetric structures can be seen, but the pole figures reveal an ordered growth around the typical common [001] direction. **(b)** Phase image, showing the B33 phase in yellow and B2 dendrites in green.

ordered growth can be caused by the copper crucible in the arc-melting furnace, which rapidly dissipates large amounts of heat from the sample, basically in one direction. This creates a higher nucleation pressure near the crucible, where the temperatures are lower. Additionally, the ⟨100⟩ and ⟨110⟩ pole figures imply a grain ordering around this [001] direction. It can also be perceived, that there are preferred directions. SiZr is expected to show a nine-fold symmetry, according to the growth model. The GBA relation can be found between certain grains of this sample. Even though it was not undercooled, or could freely solidify, this shows, that SiZr solidification occurs within the B33 structure, and also that the expected grain boundary angle holds as a twinning angle. This is an ideal system for future experiments that can handle such elevated temperatures. The system solidifies stable in the B33 structure, which is also observable later on in the microstructure analysis. Even without undercooling, some of the crucial features of the growth model can be perceived already.

5.5 Assessment of a universal model in the CrB-type structure

This chapter presented several systems and discussed them in relation to the defined crucial features, that are necessary to describe the respective system's nucleation and growth with the proposed model, that was presented in Sec. 4.2. This section will give a final assessment of all investigated systems to get an overview on whether each system obeys to these features and if the proposed model can therefore be classified as a universal nucleation and growth mechanism in CrB-structured systems, or not. Tab. 5.3 includes every system investigated during this work, lists the observed features and relevant parameters and evaluates the system to the model. It differentiates between B2 and B33 nucleation and also considers the SST as part of the solidification process.
The initial growth model of the NiZr prototype system should exhibit the initial B33 nucleation, ten-fold symmetry in the HSC recordings, and a visible ten-fold microstructure, throughout the whole sample (from a singular growth structure), that shows the expected GBA. This GBA is 36° for a ten-fold microstructure. These characteristics are all present in respective EBSD image and pole figures, e.g. as one special [001] direction is present. In the line of NiZr, all these features are checked and the system can be classified with the nucleation and growth model.
Most systems always exhibited at least a selection of the crucial features, whereas in others, some features were not observable, e.g. due to a SST. The one feature, that every system exhibits, regardless of whether the system nucleated in the B33 phase, or it is formed by the SST during cooling, is the GBA. The angle is highly preserved, as it is based on the lattice parameter ratio a/b and is present in every system, that exists in B33 phase at RT. It is clearly an angle, that exhibits a low interfacial energy and is advantageous for twinning. This is also supported by the geometric relations between the atoms in the lattice, that extend even over the grain boundaries, as it was shown in Sec. 4.3. With regard to the discussions, made in each of the systems sections, the nucleation and growth in the following systems can be described by the proposed model:

- **NiHf** is very similar to the NiZr prototype system. It presents a ten-fold symmetry, reaches especially high undercoolings and shows the same heat front as NiZr. Unfortunately, the perfect growth structure could not be observed in the analysis of this system, since the B2→B33 SST restructures the growth orientation of the different grains to a certain degree. Nevertheless, remnant ten-fold structures, from

the previously present tertiary dendritic branches of the model, are observed and EBSD proves the expected orientation relations. This system is clearly defined by the nucleation and growth mechanism, although it is not easily analyzed as such.

- **NiZrHf** presents similar results to NiZr and NiHf. The front is more stable in contrast to NiHf, the macroscopic growth structure reveals a singular growth origin and the orientation relations fit to the expected values. The solid-solid transition, described in NiHf, is present as well. It is also clearly connected to the proposed model.

- The **NiGd** system was special, as it revealed an uneven symmetry, that proved problematic to form practically, due to the discrepancy to the proposed icosahedral core structure, and also due to low undercoolings reached. Therefore, a new growth mechanism was presented, to adapt the model to new undercooling regimes and to get multiple symmetric structures in accordance with model. Nevertheless, EBSD and the corresponding pole figures showed the existence of nine-fold symmetric growth. The system is definitively correlated to the model, even though not as initially proposed.

- **NiB** showed an eight-fold symmetry, that has grown throughout the whole sample in a point symmetric structure. It solidified in the B33 phase and no SST disturbs the growth. The counter point however, is a relatively low undercooling and most probably no homogeneous nucleation. As discussed in Sec. 5.3 though, the nucleation must not occur homogeneous. It is sufficient, if only a singular nucleus can grow through the sample, before statistically other nuclei emerge. This system can clearly be connected to the nucleation and growth mechanism.

- **AlY** and **SiZr** could not be analyzed in full detail up to now. They are promising systems, that may very well be connected to the proposed model, but need further investigations. In first analysis both systems showed clearly, that the common [001] direction is present, even if no substantial undercooling is reached. SiZr additionally shows indications to a nine-fold symmetry, as the GBA matches the expectation with 40°.

Icosahedral nucleus

The quasicrystalline core structure, in the NiZr prototype system, is based on an icosahedral nucleus. It has pentagonal and decagonal symmetry elements and sets a perfect basis for a ten-fold symmetric growth. It was shown, that other ten-fold systems (NiHf, NiZrHf) exhibit the defined crucial features and can be described by the proposed growth model,

Table 5.3: Listing of observed and significant features in each system. (☆) Nucleation and growth can be described with the symmetric growth model. (A) Levitation difficult, due to oxides/impurities on surface. (B) n-fold geodesics on surface. (C) Deliberately triggered to nucleate in B2 phase. (D) Density too high for ground levitation and was only successfully levitated during parabolic flight. Symbols in brackets imply, that the observed feature cannot be assigned definitively.

System	ΔT_{max}[1] [K]	ΔT_{min}[2] [K]	Observed phases		Observed symmetry features							Singular structure	Notes	
			Nucleation	SST[3]	HSC	Sym. (MS)	Sym. (PF)	n-fold	GBA[4]	ϕ [°][5]	[001]			
NiZr	300	125	B33	✗	✓	✓	✓	10	✓	36	✓	✓	☆	B
NiZr	35	–	B2	✓	✗	✗	✗	–	✓	36	✗	–		C
NiHf	*466	360	B33	✓	✓	✓	✓	10	✓	36	✓	✗	☆	B
NiHf	*345	–	B2	✓	✗	✗	✗	(10)	✓	36	✗	–		C
NiZrHf	*378	228	B33	✓	✓	✓	✓	10	✓	36	✓	✓	☆	B
NiZrHf	169	–	B2	✓	n.d.	✗	(✓)	(10)	✓	36	✗	–		C
NiB	82	◇45	B33	✗	n.d.	✓	✓	8	✓	45	✓	✓	☆	A
NiGd	92	◇35	B33	✗	n.d.	✓	✓	9	✓	40	✓	✗	☆	A
AlY	85	n.d.	n.d.	✗	✗	✗	(✓)	10	✓	36	(✓)	✓	(☆)	A
SiZr	n.d.	n.d.	n.d.	✓	n.d.	✗	✓	9	✓	40	(✓)	n.d.	(☆)	
PdZr	330	–	B2	✓	–	–	–	–	n.d.	–	n.d.	–		
PdHf	333	–	B2	n.d.	–	–	–	–	n.d.	–	n.d.	–		
AuGd	80	–	B2	✓	✓	✗	n.d.	–	n.d.	–	✓	–		D
$FeZr_3$	195	–	–	n.d.	✗	✗	✗	–	✗	–	n.d.	✓		
CoZr	419	–	B2	✓	✓	✓	–	4	✓	–	✓	✓		B
NiCoZr	334	–	B2	✓	✓	✓	–	4	n.d.	–	n.d.	n.d.		
PdCoZr	*408	–	B2	✓	✓	✓	–	4	n.d.	–	n.d.	n.d.		

[1] The maximal undercooling achieved in the respective system during this work. (*): $\Delta T > \Delta T_{hyp}$.
[2] Refers to the minimal undercooling that was necessary (or just practically achieved [°]) to observe any features of the symmetric growth mechanism.
[3] Cooling through a **S**olid **P**hase **T**ransition from high temperature B2 phase to B33.
[4] **G**rain **B**oundary **A**ngle ϕ of two grains with a common [001] direction.
[5] Observed angles usually deviate ±2° from the theoretical angle.

despite the difficulties due to the present solid phase transition. Other symmetries, such as nine-fold (NiGd) and eight-fold (NiB), definitively show enough evidence, that their growth can also be described by the model, albeit with some modifications. However, what remains to be explained is, how such macroscopic structures are built based on the icosahedral and quasicrystalline core structure of the model. Three reasonable concepts are presented:

- **Icosahedral core** The icosahedron is always the basis for this solidification model. As soon as it forms in an undercooled melt, the core structure of the proposed model is built. With the transition to the n-fold twinned microstructure, the lattice parameter ratio sets the grain boundary angle and further growth must happen in the now defined symmetry.

- **Different SRO or nucleus** An elegant solution would be the formation of such a growth structure directly and without obstacles from a SRO in the melt or a nucleus, that has the same symmetry pattern. It seems unlikely, that each system has its own SRO that coincidentally matches the macroscopic symmetry of the growth. However, for some systems, this might be possible, as some n-fold variants are possible based on other quasicrystalline structures (see Sec. 4.3).

- **Heterogeneous growth front** This concept was discussed regarding the findings in the NiGd system. It is a modification to the prototype model, as it allows several symmetric structures to be present in a single specimen and at relatively low undercoolings. Here, the symmetric structures are formed, due to stacking faults or impurities, within the main growth front. This can explain the existence of several structures, as well as their orientation in the common growth direction.

The first option is the most likely solution, as the icosahedral ordering in the melt has the highest symmetry possible, is shown to exist in many systems and was presented as the nucleation site of the proposed model in the NiZr prototype system, although especially in NiZr no ISRO was determined in the melt. The possibility that this core structure forms the basis as well in other n-fold symmetric systems was discussed in the NiGd section (Sec. 5.2). It is assumed, that the transition from the decagonal core structure to the n-fold twinned crystal structure will then induce growth defects. In conclusion, optically visible symmetric structures are only found partially and not in full.
This work showed the importance of the non-equilibrium conditions for such phenomena, namely the deep undercoolings. Some of the investigated systems may need to be

processed again to reach higher undercoolings, where they are more likely to solidify from a singular nucleation event. In other systems, deeper undercoolings will trigger a nucleation in the B33 phase, instead of B2, and therefore the growth of the symmetric growth model. Altogether, deeper undercoolings may lead to different nucleation and microstructures in some of the presented systems. A reassessment can be considered in future works.

Chapter 6

Growth dynamics and microstructure evolution

6.1 Crystal shapes

This chapter shortly describes selected systems, where the reconstruction of the growth front into a 3D body was successful, but the systems themselves were not relevant in context of the assessed growth model presented in this work. To analyze the growth velocities of specific dendrites in a given system, it must be known, which dendrite is primarily growing and in which crystallographic direction. Analyzing only the heat fronts, that are visible during recalescence, is not sufficient. The growing crystal needs to be considered. The shape of the real crystal can be simulated with a geometric body that intersects a sphere to the point at which it fits to the observed heat front. This might be trivial in some cubic systems, when the growing crystal is literally a cube, as presented for $Co_{50}Ti_{50}$ in this section. By knowing the crystal shape, its orientation in the specimen can be concluded and dendrite directions identified. In the case of CoTi, which is shown in Fig. 6.1, it is the ⟨111⟩ dendrite that spikes through the surface, creating a three-fold shape. The red arrow shows the opposite ⟨111⟩ dendrite of the shape as it penetrates the surface on the backside. With both of these fixed points, the growth velocity, presented in Sec. 6.1.1 were calculated and the other listed velocities were calculated by the same scheme.

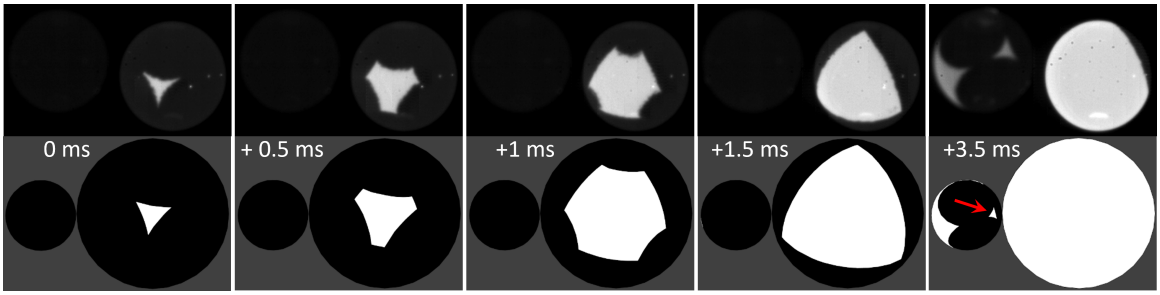

Fig. 6.1: Heat front of solidifying CoTi with the respective simulation below each frame. The red arrow marks the sport, where the ⟨111⟩ dendrite pierces through the backside.

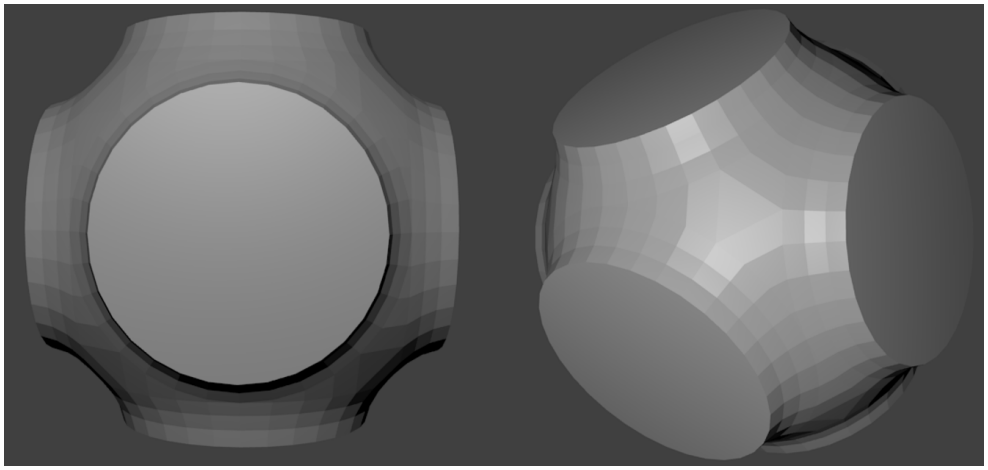

Fig. 6.2: Simulation of the 3D body growing through CoZr, based on the heat front propagation observed in HSC recordings. The heat front is presented in App. 5.1.

Cobalt-Zirconium ($Co_{50}Zr_{50}$)

The propagation of an observed heat front of CoZr can be seen in App. 5.1, at $\Delta T = 401$ K. The simulated body, that best represents this growing heat front is shown in Fig. 6.2. It has basically a cubic shape, but with the eight edges cut out. This is particularly strange, as such a cubic body is generally spanned by the respective system's ⟨111⟩ dendrites. However, exactly the tips of these dendrites must be missing here in the macroscopic shape. Another option, that was discussed, but not concluded to a final evaluation, is the growth of dendrites in several, lower symmetric, directions that span this body in a *sea-weed*-like growth pattern. The exact growth mechanism at play here remains unknown. A further analysis of the present phases in CoZr is made in Sec. 6.2.

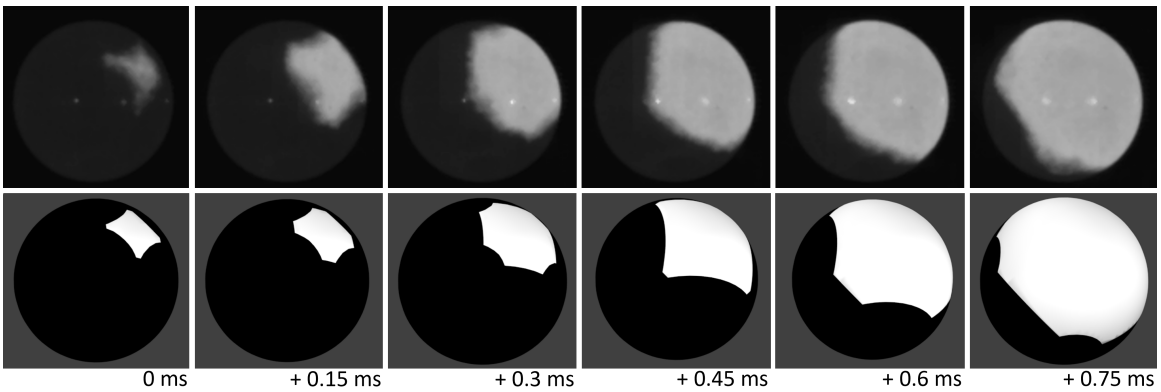

Fig. 6.3: Heat front propagation (black background) and corresponding simulated front (gray background) of the solidification in PdZr. Note, that the simulated front perfectly mimics the change from a four-fold structure, to an octagonal structure and back again to four-fold.

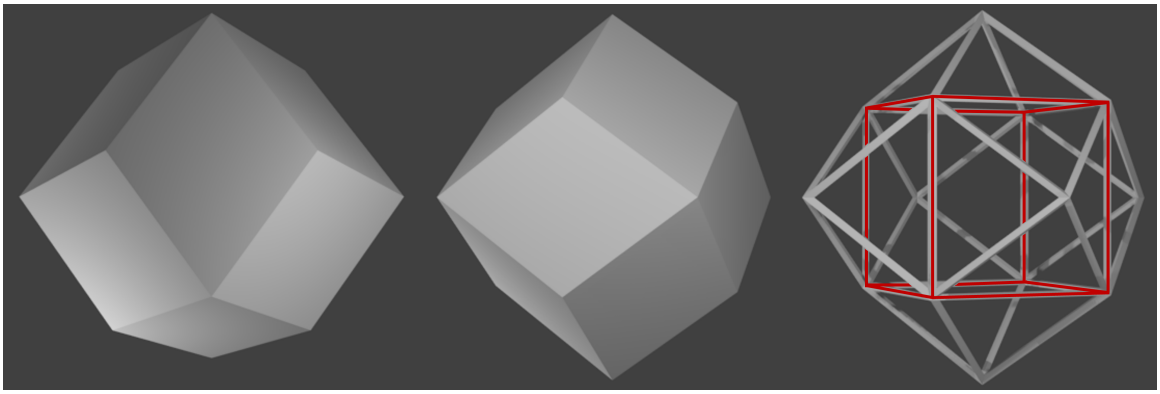

Fig. 6.4: Simulated 3D shape of a rhombic dodecahedron. The inherent cubic structure is highlighted in red. This body fits to the heat front simulation of the PdZr solidification.

Palladium-Zirconium ($Pd_{50}Zr_{50}$)

As previously presented in Sec. 5.4, PdZr solidifies in the cubic B2 structure. This can be supported with the analyzed growth structure. Fig. 6.3 shows the observed heat front on the sample's surface during recalescence. In the first frame, a four-fold front is clearly perceived. This is however changing rapidly and in frame 3 the shape can be interpreted as an octagon. Only to then change again into a four-fold front, and so on. The respective simulated growth front is depicted below each frame. This front was simulated by a rhombic dodecahedron, which has 12 congruent rhombic faces. Such a body, with faces that only have small deviations regarding their relative orientation, is the only way to simulate heat fronts, that seem to be changing back and forth. This change is a visual confirmation of the body's faces running through the sample's surface. In Fig. 6.4 the inner cubic structure of the rhombic dodecahedron can be seen highlighted in red. The six tips, at which four rhombi meet respectively, correspond to the ⟨100⟩ directions of the B2 lattice structure. This is also the orientation visible in Fig. 6.3. With the observed growth front, a growth velocity for the ⟨100⟩ dendrites was calculated to be 235 cm/s ± 25 cm/s at $\Delta T = 330\,\mathrm{K}$. A second orientation of the rhombic dodecahedron growing in PdZr could be identified as shown in Fig. 6.5. A hexagonal heat front is visible on the surface. This happens if the rhombic dodecahedron has one of its ⟨111⟩ axes orientated towards the surface of the sample. This axis is also the one pointing into the sample, growing directly through it. With this observed orientation of the heat front, the growth

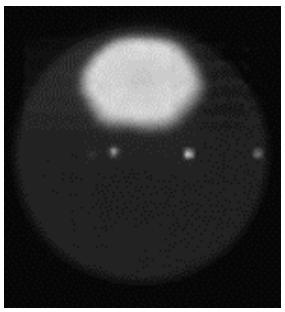

Fig. 6.5: Hexagonal heat front on PdZr. This indicates to a <111> dendrite being in the center.

velocity for the ⟨111⟩ dendrites was calculated as 110 cm/s ± 10 cm/s at $\Delta T = 300\,\mathrm{K}$.
As the shape of the rhombic dodecahedron has spikes in the position of the ⟨100⟩ and ⟨111⟩ dendrites, presumably both types of dendrites are growing in this system, to form the 3D shape.

6.1.1 Growth velocity

Based on the observed shapes and determination of respective growing dendrites, a small compilation is presented here, for the growth velocities in systems, where they were not mentioned before.

Table 6.1: Growth velocities of specific dendrites in the analyzed systems.

System	dendrite	$\Delta T/\mathrm{K}$	$v/\mathrm{cm\,s^{-1}}$	T_m
CoTi	⟨111⟩	294	107 ± 1	1427 K [225]
PdHf	⟨100⟩	333	48 ± 1	1883 K [218]
PdZr	⟨100⟩	330	235 ± 25	1873 K [220]
PdZr	⟨111⟩	300	110 ± 10	1873 K [220]
CoZr	⟨111⟩	395	46 ± 1	1643 K [226]
$FeZr_3$	n.d.	195	1.49± 0.02	1213 K [227]
AuGd	n.d.	80	86 ± 1	1858 K [228]
NiTi	spherical	375	63 ± 1	1583 K [229]

6.2 Quasi-binary variants of CoZr

The transition between the cubic B2 and the orthorhombic B33 (CrB) structure was discussed previously. It was stated, that both phases are thermodynamically close. In the CoZr system, the B2 phase was more stable from upon solidification, which was shown by X-ray scattering experiments at the ESRF synchrotron[1]. This is depicted in Appendix 5.2. From the moment of recalescence down to 773 K only the B2 phase was observed. The microstructure in the subsequent analysis showed, however, only the B33

1 The **E**uropean **S**ynchrotron **R**adiation **F**acility is a particle accelerator placed in Grenoble, France. High energy X-rays are scattered at interaction with the sample. Diffraction angles, as described in Sec. 2.7, are characteristic for different phases.

phase. Either there is an unknown solid phase transition between room temperature and 773 K, or the sample preparation, especially the embedding, induced tensions, which in turn promotes a transformation. Preparation with cold embedding and ion etching showed, that the latter was not the case. A solid phase transition must be present below 500°C. The stability of both phases is subject of discussion [148, 180]. The observed B33 microstructure was analysed by EBSD and it could be determined, that the orthorhombic structure transitioned from a single B2 crystal. This is seen in App. 5.3. The surface of the sample shows the remnant of the B2 structure that solidified at first. After transition into the B33 phase, only two different orientations can be found throughout the sample. This hints to a fixed relation between both phases. This relation was already described in Sec. 4.1; as discussed there, the B2 symmetry element can be found in the B33 phase after being rotated by 45° and slightly compressed in the c-axis[2]. The figure of App. 5.3 and the depicted B33 microstructure can now be understood as the transition from B2 into B33 in the two only possible free directions. Both phases share the same [100] direction. Depending on the local tension field, the transition will occur in either one of the directions. The EBSD image also shows such alternation of both possible transition directions.

It was shown in $Ni_{40}Co_{60}Zr$, that the CrB-structure is stable [230]. The quasi-binary alloys $Ni_{25}Co_{25}Zr$ and $Pd_{25}Co_{25}Zr$ were investigated, but both showed the same heat front as CoZr, which is characteristic for the cubic phase and therefore indicates to the growth of the B2 phase. Fig. 6.6 shows a comparison of the three heat fronts that are observed in CoZr, NiCoZr and PdCoZr. As indicated by the red arrows, different features, that define the shape of the CoZr heat front (shown in detail in Sec. 6.1), are found in all three systems, even though they appear to have different size ratios. Additionally, the heat fronts of the quasi-binary systems become spherical after propagating roughly $\frac{1}{3}$rd of the sample. In the CoZr system, a four-fold structure was clearly visible on the surface and the microstructure was partly distorted by martensitic transformations. For NiCoZr and PdCoZr (Fig. 6.7) this was the case within the whole sample. No features could be identified on the surface of these systems.

2 The transition also implements a shift of $b = \frac{a}{2}\langle 100\rangle$. The B2 and the B33 phase elements can not be found simultaneously within the microstructure.

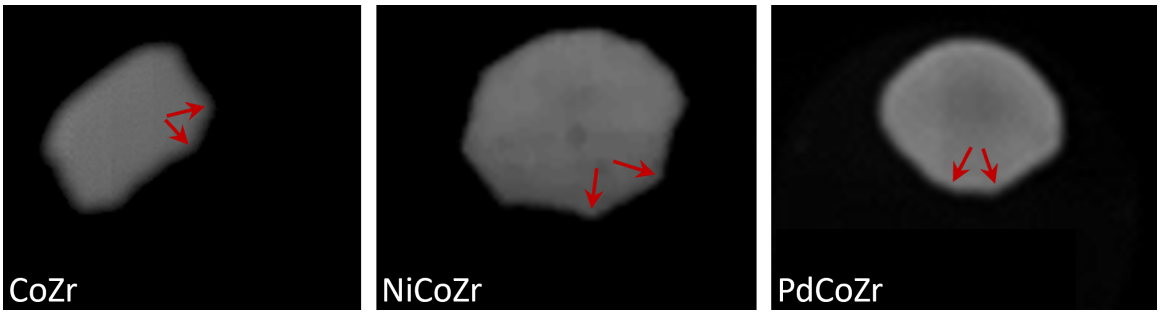

Fig. 6.6: Heat fronts of the three different CoZr systems. Although the ratios of the visible features vary, they can be identified to roughly the same shape. Red arrows mark kinks, that are visible in all three systems.

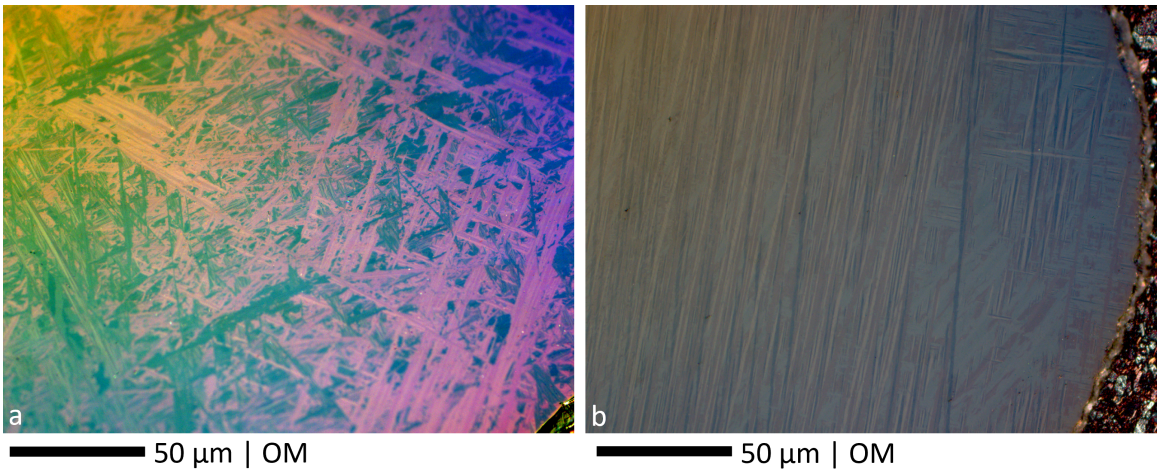

Fig. 6.7: Optical microscope images of NiCoZr (a) and PdCoZr (b). Both show extensive martensitic transformations.

CHAPTER 7

Conclusion

The nucleation and crystal growth mechanisms under non-equilibrium conditions were analyzed for several intermetallic systems. With high-purity elements and containerless processing, mainly by electrostatic levitation, these intermetallic melts were undercooled substantially below their equilibrium melting temperature. Nucleation, dendritic growth and the microstructure evolution could be observed in situ through HSC recordings and a cross-section was prepared for analysis by optical microscopy and electron backscatter diffraction.

The systems were investigated to assess the existence of a universal nucleation and growth model, that was proposed to be present in orthorhombic, CrB-structured alloys. It is based on the work of Kobold for the $Ni_{50}Zr_{50}$ system [16], which was taken as a prototype system. One characteristic of the model, is a ten-fold symmetric grain structure around a common central growth axis. The ten-fold symmetry was found to be based on the lattice parameter ratio a/b of the orthorhombic unit cell of the CrB-structure. With different lattice parameters, different n-fold symmetries were proposed in other CrB-structured systems. Several crucial features were defined, based on the NiZr prototype system, that are necessary to form such micro- and macroscopic growth structures. The most important features are the singular nucleation and growth direction, the icosahedral basis and the solidification within the CrB-structure, as it sets the lattice parameters.

Based on the lattice parameter ratio, different systems were selected for investigation in this work, to evaluate them based on the defined crucial features. This work focuses mainly on the Ni(Zr,Hf) systems. With an expected ten-fold symmetry, they seemed to be perfect systems to replicate the findings of NiZr and show the universal nature of the proposed model. However, a solid-solid phase transition (SST), from the HT cubic B2 into the orthorhombic B33 phase (CrB-structure) was observed and found to be a substantial disturbance factor during the growth process.

In $Ni_{50}Hf_{50}$, four different nucleation modes were determined, which are mainly dependent on whether the respective undercooling is below or above the transition temperature of the SST. In one mode, the system initially nucleates in the B33 phase. It must then pass the SST two times, first during the initial dendritic growth as latent heat is released and

afterwards when cooling down (B33→B2→B33). Remarkably, symmetric structures and a common growth direction are still observed in the subsequent microstructure analysis. It was shown, that an initial nucleation in the B2 structure, as presented in the other nucleation modes, does not result in such structures, but rather in a wide distribution of random orientations within one microstructure. These results, together with the in situ observations of the growth front, led to the conclusion, that the NiHf system would be a perfect twin of the NiZr system, if the SST would not be present. The transition impedes the analysis of the initial growth to a substantial degree.
The $Ni_{50}Zr_{25}Hf_{25}$ system revealed a much more stable growth front, resembling the NiZr front even better. Its microstructure showed a singular growth throughout the whole sample with a single growth direction. Overall, the microstructure was distorted and shifted, as the same SST, present in NiHf, is also observed in this system. However, it has a much smaller disturbing effect.

With the basis of an icosahedral QC as a nucleus for the proposed growth model, ten-fold symmetric growth is the ideal case. Different symmetries either need another QC core structure or will run into growth problems, when transitioning from the QC core structure to the n-fold symmetric crystalline growth. This work shows, that symmetries deviating from the ten-fold prototype, are possible. However, their growth is not based on all of the defined crucial features and modifications to the model are presented to express a realistic approach to a universal nucleation and growth model.
Nine-fold $Ni_{50}Gd_{50}$ was the first uneven symmetry investigated. Due to the oxidative nature of rare earth elements and impurities within the alloy it was not possible during this work to reach substantially high undercoolings in this system. Still, certain crucial features, presenting the common [001] growth direction and the nine-fold symmetry ordered around this central axis, are shown. The model was extended to include the growth of these structures from a general heterogeneous growth front. Stacking faults, due to pentagonal and decagonal elements of the CrB unit cell, or oxides with similar symmetric element could act as nucleation sites for new symmetric structures.
$Ni_{50}B_{50}$ was investigated and an eight-fold symmetric growth structure was found, that has propagated through the whole specimen. In the nature of the proposed model, lower symmetries can lead to higher distortions of the grain boundaries, as the symmetry elements (e.g. the unit cell), that exist even across the grain boundaries, will get shifted more and more. This is observed in NiB, with many visible shifts of the straight grain boundaries and deviations in the respective orientations of these grains. Just as in NiGd,

this was already observed in relatively low undercooling regimes. It was shown, that the original premise of the proposed model, regarding homogeneous nucleation must not be met. It is however important, that only a singular nucleation event propagates through the sample, in order to observe the growth based on this model. It needs to be investigated further in future works, what exactly causes the QC core structure in this case - assuming that such a core forms.

The proposed nucleation and growth model is based on an icosahedral core and therefore has an optimal symmetry, which is the ten-fold one. Alloy systems, where a ten-fold symmetric growth is expected, will exhibit the same phenomena, that were observed in the NiZr prototype. NiHf would probably show the exact behaviour as NiZr, if there was no SST present. Alloy systems with deviating symmetries either need a new basis for a nucleus structure, or must adapt during the transition from the QC core to the twinned microstructure. This adaptation leads to defects, where no complete symmetric structures can be found.
All in all, the nucleation and growth model is at least relevant in several CrB-structured alloys. It has universal characteristics, as many of the defined crucial features are observed in all investigated systems. Each system shows its own characteristic behaviour, but the underlying mechanism, especially the GBA at the diagonal of the orthorhombic unit cell and the orientation around a single growth direction are found in all analyzed systems.

Bibliography

[1] K. F. Kelton and A. L. Greer, *Nucleation in Condensed Matter.*, 1st edition (Pergamon Mat. Series, 2010). ISBN 978-0-080-42147-6 1, 14, 16

[2] D. G. Fahrenheit, *Experimenta & observationes de congelatione aquae in vacuo factae a d. g. fahrenheit.* R. S. S. Phil. Trans **33**, 78 (1724). DOI:10.1098/rstl.1724.0016 1, 5

[3] D. Turnbull and J. C. Fischer, *Rate of Nucleation in Condensed Systems.* J. Chem. Phys. **17**, 71 (1949). DOI:10.1063/1.1747055 1, 11, 14, 15

[4] D. Turnbull, *Formation of Crystal Nuclei in Liquid Metals.* J. Appl. Phys. **21**, 1022 (1950). DOI:10.1063/1.1699435 1, 5, 8, 11, 15, 16, 28

[5] M. Volmer and A. Weber, *Keimbildung in übersättigten Gebilden.* Z. Phys. Chem. **119U**, 277 (1926). DOI:10.1515/zpch-1926-11927 1, 11, 13

[6] B. Feuerbacher, *Phase formation in metastable solidification of metals.* Mat. Sci. Rep. **4**, 1 (1989). DOI:10.1016/S0920-2307(89)80008-8 1

[7] D. M. Herlach and B. Feuerbacher, *Non-equilibrium solidification of undercooled metallic melts.* Adv. Space Res. **11**, 255 (1991). DOI:10.1016/0273-1177(91)90293-S 1

[8] J. Kepler, *Strena seu de Nive sexangula*, 1st edition (G. Tampach, Frankfurt, 1611). DOI:10.3931/e-rara-478 2

[9] T. C. Hales, *A Proof of the Kepler Conjecture.* An. Math. **162**, 1065 (2005). DOI:jstor.org/stable/20159940 2

[10] F. C. Frank, *Supercooling of liquids.* Proc. Roy. Soc. Lond. A **215**, 43 (1952). DOI:10.1098/rspa.1952.0194 2, 28

[11] D. Holland-Moritz, *Short-range order and solid–liquid interfaces in undercooled metallic melts.* Mat. Sci. Eng.: A **304-306**, 108 (2001). DOI:10.1016/S0921-5093(00)01460-X 2, 28

[12] T. Schenk, D. Holland-Moritz, R. Simonet, R. Bellissent, and D. M. Herlach, *Icosahedral Short-Range Order in Deeply Undercooled Metallic Melts.* Phys. Rev. Lett. **89**, 075507 (2002). DOI:10.1103/PhysRevLett.89.075507 62

[13] D. Holland-Moritz, T. Schenk, R. Simonet, R. Bellissent, P. Convert, T. Hansen, and D. M. Herlach, *Short-range order in undercooled metallic liquids.* Mat. Sci. Eng.: A **375-377**, 98 (2004). DOI:10.1016/j.msea.2003.10.056 2, 62

[14] D. Shechtman, I. Blech, D. Gratias, and J. W. Cahn, *Metallic Phase with long-Range Orientational Order and No Translational Symmetry.* Phys. Rev. Lett. **53**, 1951 (1984). DOI:10.1103/PhysRevLett.53.1951 2

[15] W. Hornfeck, R. Kobold, M. Kolbe, M. Conrad, and D. M. Herlach, *Quasicrystal nucleation and Z module twin growth in an intermetallic glass-forming system.* Nat Commun **9**, 4054 (2018). DOI:10.1038/s41467-018-06597-0 3, 55, 58, 59, 60, 66, 67

[16] R. Kobold, *Crystal growth in undercooled melts of glass forming Zr-based alloys.*, dissertation, Ruhr-Universität Bochum (2016), DOI:urn:nbn:de:hbz:294-49382 3, 45, 55, 57, 58, 59, 60, 61, 63, 64, 66, 67, 68, 73, 74, 90, 91, 95, 102, 104, 131

[17] R. Kobold, M. Kolbe, W. Hornfeck, and D. M. Herlach, *Nucleation study for an undercooled melt of intermetallic NiZr.* J. Chem. Phys. **148**, 114502 (2018). DOI:10.1063/1.5018135 3, 17, 56, 58, 60, 66

[18] D. R. H. Jones and G. A. Chadwick, *An expression for the free energy of fusion in the homogeneous nucleation of solid from pure melts.* Phil. Mag. **24**, 995 (1971). DOI:10.1080/14786437108217064 8

[19] C. V. Thompson and F. Spaepen, *On the approximation of the free energy change on crystallization.* Acta Metall. **27**, 1855 (1979). DOI:10.1016/0001-6160(79)90076-2

[20] H. B. Singh and A. Holz, *Stability limit of supercooled liquids.* Sol. St. Comm. **45**, 985 (1983). DOI:10.1016/0038-1098(83)90973-0 8

[21] R. Hultgren, P. D. Desai, D. T. Hawkins, M. Gleiser, and K. K. Kelly, *Selected values of the thermodynamic properties of binary alloys.* (National Standard Reference Data System, USA, 1973) 8

[22] J. H. Perepezko and J. S. Paik, *Thermodynamic properties of undercooled liquid metals.* J. Non-Cryst. Sol. **61-62**, 113 (1984). DOI:10.1016/0022-3093(84)90538-6 8

[23] J. A. Dantzig and M. Rappaz, *Solidification.*, 2nd edition (EPFL Press Imprint, 2016). ISBN 978-2940222971 9, 10, 16

[24] M. C. Flemings, *Solidification processing.* Met. Mat. Trans. B **5**, 2121 (1974). DOI:10.1007/BF02643923 10

[25] R. Becker and W. Döring, *Kinetische Behandlung der Keimbildung in übersättigten Dämpfen.* Ann. Phys. **416**, 719 (1935). DOI:10.1002/andp.19354160806 11, 13

[26] Y. B. Zeldovich, *On the theory of new phase formation; cavitation.* Acta Phys. USSR **18**, 1 (1943). DOI:10.1515/9781400862979.120 11

[27] R. Becker, *On the formation of nuclei during precipitation.* Proc. Phys. Soc. **52**, 71 (1940). DOI:10.1088/0959-5309/52/1/309 14

[28] D. A. Porter and K. E. Easterling, *Phase transformations in metals and alloys.*, 2nd edition (Chapman & Hall, 1992). ISBN 978-1-489-93051-4, DOI:10.1201/9781003011804 14, 15, 17, 56

[29] J. Brillo, A. I. Pommerich, and A. Meyer, *Relation between self-diffusion and viscosity in dense liquids: New experimental results from electrostatic levitation.* Phys. Rev. Lett. **107**, 165902 (2011). DOI:10.1103/PhysRevLett.107.165902 14

[30] M. Volmer, *Über Keimbildung und Keimwirkung als Spezialfälle der heterogenen Katalyse.* Z. Elektrochemie **35**, 555 (1929). DOI:10.1002/bbpc.192900026 15

[31] T. Young, *An essay on the cohesion of fluids.* Phil. Trans. R. Soc. Lond. **95**, 65 (1805). DOI:10.1098/rstl.1805.0005 15

[32] J. H. Perepezko, *Kinetic processes in undercooled melts.* Mater. Sci. Eng. A **226–228**, 374 (1997). DOI:10.1016/S0921-5093(96)10647-X 16

[33] V. P. Skripov, *Homogeneous nucleation in melts and amorphous films.*, Current Topics in Materials Science, 2nd edition (North-Holland Publ. Comp., 1977). ISBN 978-0-720-40740-2 17

[34] V. P. Skripov, V. G. Baidakov, and A. M. Kaverin, *Nucleation in superheated argon, krypton and xenon liquids.* Phys. A **95**, 169 (1979). DOI:10.1016/0378-4371(79)90049-9 17

[35] C. V. Thompson and F. Spaepen, *Homogeneous crystal nucleation in binary metallic melts.* Acta Metall. **31**, 2021 (1983). DOI:10.1016/0001-6160(83)90019-6 17

[36] D. M. Herlach, P. K. Galenko, and D. Holland-Moritz, *Metastable solids from undercooled melts.*, 1st edition (Pergamon Mat. Series, 2006). ISBN 978-2940222971 17, 20

[37] F. Spaepen, *A structural model for the solid-liquid interface in monatomic systems.* Scripta Metall. **23**, 729 (1975). DOI:10.1016/0001-6160(75)90056-5 18

[38] F. Spaepen and R. B. Meyer, *The surface tension in a structural model for the solid-liquid interface.* Scripta Metall. **10**, 37 (1976). DOI:10.1016/0036-9748(76)90323-9 19

[39] C. V. Thompson, *Crystal nucleation in easy glass-forming metallic alloys.*, dissertation, Havard University, USA (1982) 18, 19

[40] D. Holland-Moritz, *Ordnungsphänomene, fest-flüssig Grenzfläche und Phasenselektionsverhalten in unterkühlten Metallschmelzen.* (Ruhr-Universität Bochum, 2003) 19

[41] J. Lipton, M. E. Glicksman, and W. Kurz, *Dendritic growth into undercooled alloy metals.* Mat. Sci. Eng. **65**, 57 (1984). DOI:10.1016/0025-5416(84)90199-X 20

[42] J. Lipton, M. E. Glicksman, and W. Kurz, *Equiaxed dendrite growth in alloys at small supercooling.* Metall. Mat. Trans. A **18**, 341 (1987). DOI:10.1007/BF02825716 82

[43] J. Lipton, W. Kurz, and R. Trivedi, *Rapid dendrite growth in undercooled alloys.* Acta Metall. **35**, 957 (1987). DOI:10.1016/0001-6160(87)90174-X 20, 82

[44] W. J. Boettinger, S. R. Coriell, and R. Trivedi, *Rapid solidification processing: principles and technologies IV.* (Claitor's Baton Rouge, LA, p. 13, 1988) 20

[45] W. Kurz and D. J. Fischer, *Fundamentals of solidification.*, 3rd edition (Trans Tech Publ., Switzerland, 1992). ISBN 978-0-878-49522-1, DOI:10.4028/www.scientific.net/RC.35 21, 22

[46] H. W. Wilson, *Xx. on the velocity of solidification and viscosity of super-cooled liquids.* The London, Edinburgh, and Dublin Phil. Mag. and J. Sci. **50**, 238 (1900). DOI:10.1080/14786440009463908 21

[47] J. Frenkel, *Note on a relation between the speed of crystallization and viscosity.* Phys. Z. Sowjetunion **1**, 498 (1932) 21

[48] K. A. Jackson, *The Interface Kinetics of Crystal Growth Processes.* Interface Sci. **10**, 159 (2002). DOI:10.1023/A:1015824230008 22

[49] M. Barth, B. Wei, and D. M. Herlach, *Crystal growth in undercooled melts of the intermetallic compounds FeSi and CoSi.* Phys. Rev. B **51**, 3422 (1995). DOI:10.1103/PhysRevB.51.3422 22

[50] M. J. Aziz and W. J. Boettinger, *On the transition from short-range diffusion-limited to collision-limited growth in alloy solidification.* Acta Metall. Mat. **42**, 527 (1994). DOI:10.1016/0956-7151(94)90507-X 23

[51] G. P. Ivantsov, *Diffusion supercooling in the crystallization of a binary alloy.* Dokl. Akad. Nauk USSR **81** (1951) 23, 25

[52] D. A. Kessler, J. Koplik, and H. Levine, *Pattern selection in fingered growth phenomena.* Adv. Phys. **37**, 255 (1988). DOI:10.1080/00018738800101379 23, 26

[53] D. A. Kessler, J. Koplik, and H. Levine, *Geometrical models of interface evolution. III. Theory of dendritic growth.* Phys. Rev. **31**, 1712 (1985). DOI:10.1103/physreva.31.1712 23, 26

[54] E. Ben-Jacob, N. Goldenfeld, B. G. Kotliar, and J. S. Langer, *Pattern Selection in Dendritic Solidification.* Phys. Review Lett. **53**, 2110 (1984). DOI:10.1103/PhysRevLett.53.2110 23

[55] J. S. Langer, *Lectures in the theory of pattern formation.* (Chance and Matter, Conference Proceedings, 629, 1987) 23

[56] A. Barbieri and J. S. Langer, *Predictions of dendritic growth rates in the linearized solvability theory.* Phys. Rev. A **39**, 5314 (1989). DOI:10.1103/PhysRevA.39.5314 23

[57] E. Ben-Jacob and P. Garik, *The formation of patterns in non-equilibrium growth.* Nature **343**, 523 (1990). DOI:10.1038/343523a0 23

[58] W. A. Tiller, *The science of crystallization - microscopic interfacial phenomena*, 1st edition (Cambridge University Press, 1991). ISBN 978-0-5213-8827-6 23

[59] E. Ben-Jacob, R. Godbey, N. D. Goldenfield, J. Koplik, H. Levine, T. Mueller, and L. M. Sander, *Experimental Demonstration of the Role of Anisotropy in Interfacial Pattern Formation.* Phys. Rev. Lett. **55**, 1315 (1985). DOI:10.1103/PhysRevLett.55.1315 23

[60] P. R. Sahm, I. Egry, and T. Volkmann, *Schmelze, Erstarrung, Grenzflächen.*, 1st edition (SpringerVerlag Berlin-Heidelberg, 1999). ISBN 978-3-540-41566-4, DOI:10.1007/978-3-642-58523-4 23, 51

[61] R. Kirchheim, *Phase Transformations in Multicomponent Melts.* (Ed. D. M. Herlach, John Wiley & Sons, 2009). ISBN 978-3-527-62405-8 24

[62] C. Herring, *Surface Tension as a Motivation for Sintering.* (SpringerVerlag Berlin-Heidelberg, 1999). ISBN 978-3-642-64188-6, DOI:10.1007/978-3-642-59938-5_2 24

[63] C. Herring, *The use of classical macroscopic concepts in surface energy problems.* Struc. Prop. Sol. Surf. **1**, 72 (1953). DOI:1953spss.conf...72M 24

[64] J. J. Hoyt, M. Asta, and A. Karma, *Atomistic and continuum modeling of dendritic solidification.* Mat. Sci. Eng. Rep. **41**, 121 (2003). DOI:10.1016/S0927-796X(03)00036-6 24, 25

[65] K. A. Jackson, *Growth and perfection of crystals.* (Liquid metals and solidification: Conference Proceedings, R. H. Roberts, B.W. Turnbull (eds.), 1958) 25

[66] K. A. Jackson, *The present state of the theory of crystal growth from the melt.* J. Cryst. Growth **24-25**, 130 (1974). DOI:10.1016/0022-0248(74)90290-5 25

[67] G. P. Ivantsov, *Temperature field around a spherical, cylindrical, and needle-shaped crystal, growing in a pre-cooled melt.* Dokl. Akad. Nauk. USSR **58**, 567 (1947). DOI:1985tfas.rept..567I 25, 26

[68] A. Papapetrou, *Untersuchungen über dendritisches Wachstum von Kristallen.* Z. Krist. **92**, 89 (1935). DOI:10.1524/zkri.1935.92.1.89 25

[69] S. C. Huang and M. E. Glicksman, *Overview 12: Fundamentals of dendritc solidification - i. Steady-state tip growth.* Acta Metall. **29**, 701 (1981). DOI:10.1016/0001-6160(81)90115-2 25

[70] M. E. Glicksman, R. J. Schaefer, and J. D. Ayers, *Dendritic growth-a test of theory.* Metall. Trans. A **7**, 1747 (1976). DOI:10.1007/BF03186673 25, 26

[71] J. S. Langer and H. Müller-Krumbhaar, *Theory of dendritic growth—I. Elements of a stability analysis.* Acta Metall. **26**, 1681 (1978). DOI:10.1016/0001-6160(78)90078-0 26

[72] J. S. Langer and J. Müller-Krumbhaar, *Stability effects in dendritic crystal growth.* J. Crys. Growth **42**, 11 (1977). DOI:10.1016/0022-0248(77)90171-3 26

[73] S. McFadden, P. L. Schaffer, R. H. Mathiesen, and D. J. Browne, *Analysis of an equiaxed dendrite growth model with comparisons to in-situ results of equiaxed dendritic growth in an Al-Ge alloy.* Mat. Sci. Forum, C.P. 654–656 (2010). DOI:10.4028/www.scientific.net/MSF.654-656.1359 26

[74] S. McFadden and D. J. Browne, *A generalised version of an ivantsov-based dendrite growth model incorporating a facility for solute measurement ahead of the tip.* Comp. Mat. Sci. **55**, 245 (2012). DOI:10.1016/j.commatsci.2011.12.011 26

[75] U. Bisang and J. H. Bilgram, *Shape of the tip and the formation of sidebranches of xenon dendrites.* Phys. Rev. E **54**, 5309 (1996). DOI:10.1103/PhysRevE.54.5309 26

[76] S.-C. Huang and M. E. Glicksman, *Overview 12: Fundamentals of dendritic solidification—I. Steady-state tip growth.* Acta Metall. **29**, 701 (1981). DOI:10.1016/0001-6160(81)90115-2 26

[77] G. Mie, *Zur kinetischen Theorie der einatomigen Körper.* Ann. Phys. **316**, 657 (1903). DOI:10.1002/andp.19033160802 26

[78] S. Klein, *Nucleation in undercooled melts of pure zirconium and zirconium based alloys.*, dissertation, Ruhr-Universität Bochum (2016), DOI:urn:nbn:de:hbz:294-30208 26, 86

[79] D. Nelson and F. Spaepen, *Polytetrahedral Order in Condensed Matter.* Solid State Phys. **42**, 1 (1989). DOI:10.1016/S0081-1947(08)60079-X 26, 27

[80] C. Kittel, *Einführung in die Festkörperphysik.*, 15th edition (De Gruyter Oldenbourg Verlag, 2013). ISBN 978-3-486-59755-4 28

[81] D. Holland-Moritz, D. M. Herlach, and K. Urban, *Observation of the undercoolability of quasicrystal-forming alloys by electromagnetic levitation*. Phys. Rev. Lett. **71**, 1196 (1993). DOI:10.1103/PhysRevLett.71.1196 28

[82] A. D. Cicco, A. Trapananti, S. Faggioni, and A. Filipponi, *Is There Icosahedral Ordering in Liquid and Undercooled Metals?* Phys. Rev. Lett. **91**, 135505 (2003). DOI:10.1103/PhysRevLett.91.135505 28

[83] E. J. Mittermeijer and F. Sommer, *Solid state phase transformation kinetics: a modular transformation model.* Int. J. Mat. Res. **93**, 352 (2002). DOI:10.3139/ijmr-2002-0064 28, 29

[84] F. Liu, F. Sommer, and E. J. Mittermeijer, *An analytical model for isothermal and isochronal transformation kinetics.* J. Mat. Sci. **39**, 1621 (2004). DOI:10.1023/B:JMSC.0000016161.79365.69 28

[85] W. Bleck, *Werkstoffkunde Stahl*, 5th edition (Verlagsgruppe Mainz, 1611). ISBN 978-3-896-53820-8 28, 29

[86] B. Distl, K. Hauschildt, F. Pyczak, and F. Stein, *Solid-Solid Phase Transformations and Their Kinetics in Ti-Al-Nb Alloys.* Metals. **11**, 1991 (2009). DOI:10.3390/met11121991 29, 86

[87] Y. Mnyukh, *Hysteresis of Solid-State Reactions: Its Cause and Manifestations.* Am. J. Cond. Matter Phys. **3**, 142 (2013). DOI:10.5923/j.ajcmp.20130305.05 29

[88] S. Suzuki and H. K. D. H. Bhadeshia, *Reversibility of the allotriomorphic ferrite and austenite transformations.* Mat. Sci. Eng. A **186**, 157 (1993). DOI:10.1016/0921-5093(94)90315-8

[89] I. Medved and A. Trnik, *DSC Investigations of the Phase Transition in the High Strength Steel S960QL.* Adv. Mat. Res. **1126**, 148 (2015). DOI:10.4028/www.scientific.net/AMR.1126.148 29

[90] S. Leoni, *Solid–Solid Phase Transitions: Interface Controlled Reactivity and Formation of Intermediate Structures.* Chem. Eur. J. **13**, 10022 (2007). DOI:10.1002/chem.200701078 29

[91] G. Miranda, F. S. Silva, and D. Soares, *Solid State Transformations and Equilibrium Crystal Structures of an Au-Cu Alloy with Shape Memory Effect.* Adv. Mat. Forum VI **730**, 859 (2012). DOI:10.4028/www.scientific.net/MSF.730-732.859 29, 86

[92] G. Miranda, F. S. Silva, and D. Soares, *New enthalpies determination and in situ X-ray diffraction observations of order/disorder transitions in* $Au_{0.5}Cu_{0.5}$. Acta Mater. **47**, 2539 (1999). DOI:10.1016/S1359-6454(99)00089-0 29

[93] J. J. Metois and J. C. Heyraud, *The overheating of lead crystals.* J. Phys. **50**, 3175 (1989). DOI:10.1051/jphys:0198900500210317500 29

[94] W. H. Bragg and W. L. Bragg, *The reflexion of x-rays by crystals.* Proc. R. Soc. Lond. A. **88(605)**, 428 (1913). DOI:10.1098/rspa.1913.0040 30

[95] M. Etter and R. E. Dinnebier, *A Century of Powder Diffraction: a brief History.* Z. Anorg. Allg. Chem. **640**, 3015 (2014). DOI:10.1002/zaac.201400526 30

[96] N. N. Greenwood and A. Earnshaw, *Chemistry of the Elements.*, 2nd edition (Butterworth-Heinemann, 1997). ISBN 978-0-7506-3365-9, DOI:10.1016/C2009-0-30414-6 31

[97] S. Cotton, *Lanthanide and Actinide Chemistry.* (John Wiley & Sons, 2006). ISBN 978-0-470-01005-1, DOI:10.1002/0470010088

[98] J. C. Slater, *Atomic radii in crystals.* J. Chem. Phys. **41**, 3199 (1964). DOI:10.1063/1.1725697 31

[99] A. J. Rulison, J. L. Watkins, and B. Zambrano, *Electrostatic container-less processing system.* Rev. Sci. Instr. **68**, 2856 (1997). DOI:10.1063/1.1148208 33

[100] S. Earnshaw, *On the nature of the molecular forces which regulate the constitution of the luminiferous ether.* Trans. Camb. Philos. Soc **7**, 97 (1842) 33

[101] W. K. Rhim, M. Collender, M. T. Hyson, W. T. Simms, and D. D. Elleman, *Development of an electrostatic positioner for space material processing.* Rev. Sci. Instr. **56**, 307 (1985). DOI:10.1063/1.1138349 33

[102] W. K. Rhim, S. K. Chung, M. T. Hyson, and D. D. Elleman, *Charged Drop Levitators and their Applications.* Proc. Mat. Res. Soc. Symp. **87**, 103 (1987). DOI:10.1557/PROC-87-103 33

[103] T. Meister, *Aufbau und Regelung eines elektrostatischen Levitators.*, dissertation, Ruhr-Universität Bochum (2001), DOI:urn:nbn:de:hbz:294-2069 33, 36

[104] T. Meister, H. Werner, G. Lohöfer, D. M. Herlach, and H. Unbehauen, *Gain-scheduled control of an electrostatic levitator.* Control Eng. Pract. **11**, 117 (2003). DOI:10.1016/S0967-0661(02)00102-8 33

[105] T. Meister, G. Lohoefer, and H. Unbehauen, *Development of an electrostatic levitator for containerless processing.* In: L. Schultz et al. (Eds.): Mat. Dev. Proc., Euromat 99 **8**, 136 (2000). DOI:10.1002/3527607277.ch22 36

[106] D. M. Herlach, R. F. Cochrane, I. Egry, H. J. Fecht, and A. L. Greer, *Containerless processing in the study of metallic melts and their solidification.* Int. Mat. Rev. **38**, 273 (1993). DOI:10.1179/095066093790326267 33

[107] A. Einstein, *Über einem die Erzeugung und Verwandlung des Lichtes betreffenden heuristischen Gesichtspunkt.* An. Phys. **4**, 132 (1905). DOI:10.1002/andp.19053220607 34

[108] C. Panofen, *Nukleation und Wachstum von unterkühlten Silizium-, Silizium-Cobalt und Silizium-Germanium-Schmelzen.*, dissertation, Ruhr-Universität Bochum (2006), DOI:urn:nbn:de:hbz:294-15635 36

[109] P. R. Rony, *The electromagnetic levitation of metals.* Tech. Rep., UCRL-11411, California Univ., Berkeley (1964). DOI:10.2172/4035813 38

[110] G. Lohöfer, *Theory of an Electromagnetically Levitated Metal Sphere I: Absorbed Power.* SIAM J. Appl. Math. **49**, 567 (1989). DOI:10.1137/0149032 39

[111] G. Lohöfer, *Force and torque of an electromagnetically levitated metal sphere.* Quart. Appl. Math. **51**, 495 (1993). DOI:jstor.org/stable/43637940 39

[112] D. M. Herlach, *Containerless Undercooling and Solidification of Pure Metals.* Ann. Rev. Mater. Sci. **21**, 23 (1991). DOI:10.1146/annurev.ms.21.080191.000323 39

[113] G. Lohöfer, P. Neuhaus, and I. Egry, *TEMPUS: a facility for measuring the thermophysical properties of undercooled liquid metals.* High Temp. High Press. **23**, 333 (1991) 39

[114] M. Planck, *Zur Theorie des Gesetztes der Energieverteilung im Normalsprektrum.* Phys. Bl. **4**, 146 (1900). DOI:10.1002/phbl.19480040404 41

[115] W. Wien, *Ueber die Energievertheilung im Emissionsspektrum eines schwarzen Körpers.* An. Phys. **294**, 662 (1896). DOI:10.1002/andp.18962940803 41

[116] E. Tiesinga, P. J. Mohr, D. B. Newell, and B. N. Taylor, *CODATA Recommended Values of the Fundamental Physical Constants: 2018.* J. Phys. Chem. **50**, 033105 (2021). DOI: 10.1063/5.0064853 43

[117] W. Dokko and R. G. Bautista, *The normal.* Metall. Mater. Trans. B **11**, 309 (1980). DOI: 10.1007/BF02668416 43

[118] S. Krishnan, C. Anderson, J. K. R. Weber, P. C. Nordine, W. H. Hofmeister, and R. J. Bayuzick, *Optical properties and spectral emissivities at 632.8 nm in the titanium-aluminum system.* Metall. Trans. A **24**, 67 (1993). DOI:10.1007/BF02669604

[119] S. Krishnan and P. C. Nordine, *Optical properties of liquid aluminum in the energy range 1.2–3.5 eV.* Phys. Rev. B **47**, 11780 (1993). DOI:10.1103/PhysRevB.47.11780 43

[120] X. H. Lin and W. L. Johnson, *Formation of Ti–Zr–Cu–Ni bulk metallic glasses.* J. Appl. Phys. **78**, 6514 (1993). DOI:10.1063/1.360537 43

[121] T. Volkmann, G. Wilde, R. Willnecker, and D. M. Herlach, *Nonequilibrium solidification of hypercooled Co–Pd melts.* J. Appl. Phys. **83**, 3028 (1998). DOI:10.1063/1.367057 44

[122] P. Fopp, *Investigation of the effect of the hypercooling limit on the crystal growth velocity of intermetallic alloys.*, dissertation, RWTH Aachen University (2020), DOI:10.18154/RWTH-2020-08169 44, 79

[123] W. Wien, *Eine neue Beziehung der Strahlung schwarzer Körper zum zweiten Hauptsatz der Wärmetheorie.*, 2nd edition (Vieweg+Teubner Verlag, Wiesbaden, 1893). ISBN 978-3-528-06840-0, DOI:10.1007/978-3-663-13885-3_12 44

[124] *Blender 3D creation suite software.* https://www.blender.org/about/license/ . (02.04.22) 45

[125] E. S. Watson and M. J. O'Neill, *Differential microcalorimeter.* Patent US3263484A (1962) 46

[126] G. Höhne, W. F. Hemminger, and H.-J. Flammersheim, *Differential Scanning Calorimetry.*, 2nd edition (Springer Berlin (Verlag), 2003). ISBN 978-3-540-00467-7, DOI:10.1007/978-3-662-06710-9 46

[127] F. Gillessen and D. M. Herlach, *Crystal Nucleation and Glass-forming Ability of Cu-Zr in a Containerless State.* Mat. Sci. Eng. **97**, 147 (1988). DOI:10.1016/0025-5416(88)90030-4 47

[128] J. Gao, T. Volkmann, and D. M. Herlach, *Metastable solidification of NdFeB alloys by drop-tube processing.* J. Mat. Res. **16**, 2562 (2001). DOI:10.1557/JMR.2001.0351 47

[129] R. B. Bird, W. E. Stewart, and E. N. Lightfoot, *Transport phenomena*, 2nd edition (John Wiley & Sons, New York, 2006). ISBN 978-0-470-11539-8 47

[130] L. Reimer, *Scanning Electron Microscopy.*, 2nd edition (Springer-Verlag Berlin Heidelberg, 1998). DOI:10.1007/978-3-540-38967-5 49

[131] H. Alexander, *Physikalische Grundlagen der Elektronenmikroskopie.*, 1st edition (Vieweg+Teubner Verlag, 1997). ISBN 978-3-519-03221-2, DOI:10.1007/978-3-663-12296-8 49

[132] D. Bell and A. Garratt-Reed, *Energy Dispersive X-ray Analysis in the Electron Microscope.* (Garland Science, 2003). ISBN 978-3-642-83613-8, DOI:10.4324/9780203483428 50

[133] J. I. Goldstein, D. E. Newbury, R. Michael, and N. Ritchie, *Scanning electron microscopy and x-ray microanalysis.* (New York: Plenum Press, 1981). DOI:10.1007/978-1-4939-6676-9 50, 53

[134] S. Nishikawa and S. Kikuchi, *Diffraction of Cathode Rays by Mica.* Nature **121**, 1019 (1928). DOI:10.1038/1211019a0 50

[135] A. Morawiec, *Orientations and Rotations*, 1st edition (Springer-Verlag, 2003). ISBN 978-3-540-40734-8, DOI:10.1007/978-3-662-09156-2 51, 53

[136] E. Boehm-Courjault, F. Gonzales, A. Jacot, F. Kohler, A. Mariaux, C. Niederberger, M. A. Salgado-Ordorica, and M. Rappaz, *EBSD: a powerful microstructure analysis technique in the field of solidification.* J. Microsc. **233**, 160 (2009). DOI:10.1111/j.1365-2818.2008.03107.x 53

[137] G. Gottstein, *Materialwissenschaft und Werkstofftechnik.*, 4th edition (Springer-Verlag Berlin Heidelberg, 2014). ISBN 978-3-642-36602-4, DOI:10.1007/978-3-642-36603-1 53

[138] O. Teppo and P. Taskinen, *Properties of chromium boride and sintered chromium boride.* JOM **1**, 198 (1949). DOI:10.1007/BF03398095 55

[139] A. J. Frueh, *Confirmation of the structure of chromium boride, CrB.* Acta Cryst. **4**, 66 (1951). DOI:10.1107/S0365110X51000118 55

[140] A. J. Frueh, *Structural investigation of Cr_2B_3, Cr_3B_3, and CrB by single-crystal diffractometry.* J. Sol. St. Chem. **68**, 61 (1987). DOI:10.1016/0022-4596(87)90285-4 55

[141] P. K. Liao and K. E. Spear, *The B-Cr (Boron-Chromium) system.* Bull. Al. Phase Diagr. **7**, 232 (1986). DOI:10.1007/BF02868996 55

[142] N. Hatcher, O. Y. Kontsevoi, and A. J. Freeman, *Role of elastic and shear stabilities in the martensitic transformation path of NiTi.* Phys. Rev. B **80**, 144203 (2009). DOI:10.1103/PhysRevB.80.144203 56

[143] G. Liu, H. Liu, X. Feng, and S. Redfern, *High-pressure phase transitions of nitinol NiTi to a semiconductor with an unusual topological structure.* Phys. Rev. B **97**, 140104(R) (2018). DOI:10.1103/PhysRevB.97.140104 56

[144] X. Huang, G. Ackland, and K. Rabe, *Crystal structures and shape-memory behaviour of NiTi.* Nature Mater. **2**, 307 (2003). DOI:10.1038/nmat884 56

[145] A. J. Frueh, *Resolving quandaries surrounding NiTi.* Appl. Phys. Lett. **101**, 081907 (2012). DOI:10.1063/1.4747488 56

[146] J. B. Haskins, A. E. Thompson, and J. W. Lawson, *Ab initio simulations of phase stability and martensitic transitions in NiTi.* Phys. Rev. B **94**, 214110 (2016). DOI:10.1103/PhysRevB.94.214110 56

[147] M. Krcmar, G. D. Samolyuk, and J. R. Morris, *Stacking faults and alternate crystal structures for the shape-memory alloy NiTi.* Phys. Rev. Mat. **4**, 103606 (2020). DOI:10.1103/PhysRevMaterials.4.103606 56

[148] W. F. Lu, C. J. Li, B. Sarac, D. Sopu, J. H. Yi, J. Tan, M. Stoica, and J. Eckert, *Structural, elastic and electronic properties of CoZr in B2 and B33 structures under high pressure.* J. Al. Comp. **705**, 445 (2017). DOI:10.1016/j.jallcom.2017.02.085 56, 129

[149] T. Niersbach(Schulzendorff), *Analysis of Crystal Growth in Intermetallic Alloys with CrB-Structure from Levitated Undercooled Melts.* (Master thesis. RWTH Aachen University, 2018) 56, XXXI

[150] D. Quirinale, G. Rustan, S. Wilson, M. Kramer, A. Goldman, and M. Mendelev, *Appearance of metastable B2 phase during solidification of $Ni_{50}Zr_{50}$ alloy: electrostatic levitation and molecular dynamics simulation studies.* J. Phys.: Cond. Matter **27**, 085004 (2015). DOI:10.1088/0953-8984/27/8/085004 56

[151] Y. Sun, F. Zhang, H. Song, M. I. Mendelev, C. Z. Wang, and K. M. Ho, *Competitive B2 and B33 Nucleation during solidification of $Ni_{50}Zr_{50}$ Alloy: Molecular Dynamics Simulation and Classical Nucleation Theory.* J. Phys. Chem. C **123**, 6685 (2019). DOI:10.1021/acs.jpcc.9b00439 57, 89

[152] P. Fopp, M. Kolbe, F. Kargl, R. Kobold, W. Hornfeck, and T. Buslaps, *Phase selection in hypercooled alloys.* J. Al. Comp. **834**, 154439 (2020). DOI:10.1016/j.jallcom.2020.154439 57

[153] E. Parthé, *The CrB and related structure interpreted by periodic unit-cell twinning of close-packed structures.* Acta Cryst. B**32**, 2813 (1976). DOI:10.1107/S0567740876008959 57

[154] B. G. Hyde and S. Andersson, *Inorganic Crystal Structures.* (John Wiley & Sons, New York, 1989). ISBN 978-0-471-62897-2, DOI:10.1002/crat.2170250611 57

[155] J. Morris, M. Krcmar, and C. Fu, *The Role of Phase Stability in Ductile, Ordered B2 Intermetallics.* MRS Online Proc. **980**, 610 (2006). DOI:10.1557/PROC-980-0980-II06-10 57

[156] G. V. Kurdjumov and G. Sachs, *Über den Mechanismus der Stahlhärtung.* Z. Phys. **64**, 325 (1930). DOI:10.1007/BF01397346 57

[157] E. C. Bain, *The Nature of Martensite Trans.* AIME, Steel Div. **70**, 25 (1975) 57

[158] R. Kobold, W. W. Kuang, H. Wang, W. Hornfeck, M. Kolbe, and D. M. Herlach, *Dendrite growth velocity in the undercooled melt of glass forming $Ni_{50}Zr_{50}$ compound.* Phil. Mag. Let. **97**, 249 (2017). DOI:10.1080/09500839.2017.1330561 58, 82

[159] M. E. Kirkpatrick, D. M. Bailey, and J. F. Smith, *The structures of $NiZr_2$, NiZr and their Hafnium Analogs.* Acta Cryst. **15**, 252 (1962) 58, 72

[160] L. Bendersky, *Quasicrystal with One-Dimensional Translational Symmetry and a Tenfold Rotation Axis.* Phys. Rev. Lett. **55**, 1461 (1985). DOI:10.1103/PhysRevLett.55.1461 62

[161] K. K. Fung, X. D. Zou, and C. Y. Yang, *Transmission electron microscopy study of $Al_{13}Fe_4$ tenfold twins in rapidly cooled Al–Fe alloys.* Phil. Mag. Lett. **55**, 27 (1987). DOI:10.1080/09500838708210436 62

[162] X. Z. Li and K. H. Kuo, *Decagonal quasicrystals with different periodicities along the tenfold axis in rapidly solidified Al-Ni alloys.* Phyl. Mag. Lett. **58**, 167 (1988). DOI:10.1080/09500838808214749

[163] S. Ebalard and F. Spaepen, *Long-range chemical ordering in Al-Cu-Fe, Al-Cu-Mn, and Al-Cu-Cr quasicrystals.* J. Mat. Res. **5**, 62 (1990). DOI:10.1557/JMR.1990.0062 62

[164] G. W. Lee, A. Gangopadhyay, K. F. Kelton, R. W. Hyers, T. J. Rathz, J. R. Rogers, and D. S. Robinson, *Difference in Icosahedral Short-Range Order in Early and Late Transition Metal Liquids.* Phys. Rev. Lett. **93**, 037802 (2004). DOI:10.1103/PhysRevLett.93.037802 62

[165] B. Nowak, D. Holland-Moritz, F. Yang, T. Volkmann, T. Kordel, T. Hansen, and A. Meyer, *Partial structure factors reveal atomic dynamics in metallic alloy melts.* Phys. Rev. Mat. **1**, 025603 (2017). DOI:10.1103/PhysRevMaterials.1.025603 62

[166] W. J. Jiang, K. Hei, Y. X. Guo, and K. H. Kuo, *Tenfold twins in a rapidly quenched NiZr alloy.* Phil. Mag. A **52**, 53 (1985). DOI:10.1080/01418618508242136 62

[167] A. Cziraki, B. Fogarassy, K. Tompa, and R. Nauta, *On the formation of a phase with tenfold symmetry in amorphous Ni-Zr alloys.* Phase Trans. **44**, 131 (1993). DOI:10.1080/01411599308210266 62

[168] W. Steurer, *Quasicrystals: What do we know? What do we want to know? What can we know?.* Acta Cryst. **A74**, 1 (2018). DOI:10.1107/S2053273317016540 66, 68

[169] N. Wang, H. Chen, and K. H. Kuo, *Two-dimensional quasicrystal with eightfold rotational symmetry.* Phys. Rev. Lett. **59**, 1010 (1987). DOI:10.1103/PhysRevLett.59.1010 68

[170] P. Villars and K. Cenzual, *Pearson's Crystal Data: Crystal Structure Database for Inorganic Compounds (on DVD).* ASM International, Materials Park, Ohio, USA (2018-22) 71

[171] T. B. Flanagan, H. Noh, and S. Luo, *The Thermodynamic Characterization of ZrCo-H, HfCo-H, HfNi-H and Zr_{1-x}HfxNi(Co) Alloy-H Systems.* J. Al. Comp. **677**, 163 (2016). DOI:10.1016/j.jallcom.2016.03.207 72

[172] Z. Malik, A. Grytsiv, P. Rogl, G. Giester, and J. Bursik, *Phase relations and structural features in the system Ni–Zn–B.* J. Sol. St. Chem. **198**, 150 (2013). DOI:10.1016/j.jssc.2012.09.042 72

[173] J. A. Blanco, J. C. G. Sal, J. Rodriguez, D. Gignoux, D. Schmitt, and J. Rodriguez-Carvajal, *Magnetic and electrical properties of $GdNi_{1-x}Cu_x$ compounds.* J. Phys. Cond. Mat. **4**, 8233 (1992). DOI:10.1088/0953-8984/4/42/012 72

[174] T. Dagerhamn, *X-ray studies on the yttrium-aluminium system.* Ark. Kem. **27**, 363 (1967) 72

[175] A. Raman and K. Schubert, *Über den Aufbau einiger zu $TiAl_3$ verwandter Legierungsreihen.* Z. Metallkd **56**, 44 (1965). DOI:10.1515/ijmr-1965-560108 72

[176] L. A. Bendersky, J. K. Stalick, R. Portier, and R. M. Waterstrat, *Crystallographic structures and phase transformations in ZrPd.* J. Al. Comp. **236**, 19 (1996). DOI:10.1016/0925-8388(96)80046-6 72, XXX

[177] S. Hisada, M. Matsuda, K. Takashima, and Y. Yamabe-Mitarai, *Structural analysis and martensitic transformation in equiatomic HfPd alloy.* J. Sol. St. Chem. **258**, 712 (2018). DOI:10.1016/j.jssc.2017.12.002 72

[178] O. D. McMasters, K. A. Gschneidner, G. Bruzzone, and A. Palenoza, *Stoichiometry, crystal structures and some melting points of the lanthanide-gold alloys.* J. Less Com. Met. **25**, 135 (2011). DOI:10.1016/0022-5088(71)90125-1 72

[179] W. Liu, O. D. Feya, T. T. Debela, J. R. Hester, C. J. Webb, and E. M. Gray, *Experimental and computational modelling study of Ni substitution for Fe in Zr_3Fe and its hydride.* J. Al. Comp. **781**, 131 (2019). DOI:10.1016/j.jallcom.2018.12.054 72, 113

[180] M. Matsuda, T. Nishimoto, K. Matsunaga, Y. Morizono, S. Tsurekawa, and M. Nishida, *Deformation structure in ductile B2-type Zr-Co-Ni alloys with martensitic transformation.* J. Mater. Sci. **46**, 4221 (2011). DOI:10.1007/s10853-010-5236-3 72, 129

[181] M. Matsuda, T. Nishimoto, Y. Morizono, S. Tsurekawa, and M. Nishida, *Enhancement of ductility in B2-type Zr–Co–Pd alloys with martensitic transformation.* Intermetallics **19**, 894 (2011). DOI:10.1016/j.intermet.2011.02.006 72

[182] F. Stein, G. Sauthoff, and M. Palm, *Phases and phase equilibria in the Fe–Al–Zr system.* Int. J. Mat. Res. **95**, 469 (2004). DOI:10.1515/ijmr-2004-0096 72

[183] K. Schubert, H. G. Meissner, M. Pötzschke, W. Rossteutscher, and E. Stolz, *Einige Strukturdaten metallischer Phasen (7).* Naturwissenschaften **49**, 57 (1962). DOI:10.1007/BF00595382 72

[184] K. P. Gupta, *The Hf-Ni-Zr (Hafnium-Nickel-Zirconium).* J. Ph. Eq. **22**, 73 (2001). DOI:10.1361/105497101770339333 72, 90

[185] A. Berche, J. C. Tedenac, and P. Jund, *Phase diagram and enthalpy of formation of Hf-Ni-Sn.* Comp. Mat. Sci. **125**, 271 (2016). DOI:10.1016/j.commatsci.2016.08.042 75

[186] P. Nash and A. Nash, *The Hf-Ni (Hafnium-Nickel) system.* Bull. Al. Diagr. **4**, 250 (1983). DOI:10.1007/BF02868664 75

[187] H. Okamoto, *Hf-Ni (Hafnium-Nickel).* J. Ph. Eq. **14**, 769 (1993). DOI:10.1007/BF02667895 75, XXIV

[188] T. Wang, Z. Jin, and J. Zhao, *Experimental Study and Reassessment of the Ni-Hf Binary System.* Z. Metallk. **92**, 441 (2001) 75

[189] V. Wessels, A. K. Gangopadhyay, K. K. Sahu, R. W. Hyers, and S. M. C. et.al., *Rapid chemical and topological ordering in supercooled liquid $Cu_{46}Zr_{54}$.* Phys. Rev. B **83**, 094116 (2012). DOI:10.1103/PhysRevB.83.094116 77

[190] P. Fopp, M. Kolbe, F. Kargl, R. Kobold, and W. Hornfeck, *Unexpected behavior of the crystal growth velocity at the hypercooling limit.* Phys. Rev. Mat. **4**, 073405 (2020). DOI:10.1103/PhysRevMaterials.4.073405 77

[191] Q. Guo and O. J. Kleppa, *Standard enthalpies of formation of some alloys formed between group IV elements and group VIII elements, determined by high-temperature direct synthesis calorimetry: II. Alloys of (Ti, Zr, Hf) with (Co, Ni).* J. Al. Comp. **269**, 181 (1998). DOI:10.1016/S0925-8388(98)00246-1 77

[192] J. E. Rodriguez, C. Kreischer, T. Volkmann, and D. M. Matson, *Solidification velocity of undercooled Fe–Co alloys.* Acta Mater. **122**, 431 (2017). DOI:10.1016/j.actamat.2016.09.047 78

[193] K. Nagashio and K. Kuribayashi, *Rapid solidification of $Y_3Al_5O_{12}$ garnet from hypercooled melt.* Acta Mater. **49**, 1947 (2001). DOI:10.1016/S1359-6454(01)00107-0 78

[194] J. W. Lum, D. M. Matson, and M. C. Flemings, *High-Speed imaging and analysis of the solidification of undercooled nickel melts.* Metall. Mater. Trans. B **27**, 865 (1996). DOI:10.1007/BF02915616 82

[195] Y. Ruan, L. Li, Q. Gu, K. Zhou, N. Yan, and B. Wei, *Thermal expansion and thermal diffusivity properties of Co-Si solid solutions and intermetallic compounds.* J. Chem. Thermo. **102**, 1 (2016). DOI:10.1016/j.jct.2016.06.029 82

[196] B. Sundqvist, *Thermal diffusivity and thermal conductivity of Chromel, Alumel, and Constantan in the range 100–450 K.* J. Appl. Phys. **72**, 539 (1992). DOI:10.1063/1.351885

[197] A. Hazotte, B. Perrot, and P. Archambault, *High temperature thermal diffusivity of nickel-based superalloys and intermetallic compounds.* J. Phys. IV France **03**, C7 (1993). DOI:10.1051/jp4:1993754 82

[198] J. T. Okada, P. H. Sit, and R. I. et.al., *Phase relation between supercooled liquid and amorphous silicon.* Appl. Phys. Lett. **116**, 093705 (2020). DOI:10.1063/1.5129059 83

[199] C. Kreischer and T. Volkmann, *Transformation kinetics of the metastable bcc phase during rapid solidification of undercooled Fe-Co alloy melts.* Materialia **20**, 101211 (2021). DOI: 10.1016/j.mtla.2021.101211 83

[200] S. Pauly, *Phase formation and mechanical properties of metastable Cu-Zr-based alloys.*, dissertation, Technische Universität Dresden (2010), DOI:urn:nbn:de:bsz:14-qucosa-39545 86

[201] N. N. Eremenko, E. L. Semenova, L. A. Tretyachenko, and V. M. Petyukh, *Interaction of equiatomic binary compounds in ternary systems formed by 4-group transition metals with nickel.* Neorganicheskie Mat. **28**, 1173 (1992). DOI:INIS-Reference:24046537(no.real.DOI) 89, 90

[202] J. C. Bünzli and V. Pecharsky, *Handbook on the Physics and Chemistry of Rare Earths*, 1st edition (North-Holland, 2016). ISBN 978-0-444-63699-7 97

[203] D. W. Deng, Z. M. Mo, and K. H. Kuo, *Crystal structure of the orthorhombic Al_4(Cr,Fe) approximant of the Al–Cr–Fe decagonal quasicrystal.* J. Phys.: Cond. Mat. **16**, 2283 (2004). DOI:10.1088/0953-8984/16/13/009 102

[204] J. Grin, U. Burkhardt, M. Ellner, and K. Peters, *Crystal structure of orthorhombic Co_4Al_{13}.* J. Al. Comp. **206**, 243 (1994). DOI:10.1016/0925-8388(94)90043-4 102

[205] M. J. Cooper, *The structure of the intermetallic phase θ(Cr-Al).* Acta Cryst. **13**, 257 (1960). DOI:10.1107/S0365110X60000571 102

[206] L. P. Lehman, Y. Xing, T. R. Bieler, and E. J. Cotts, *Cyclic twin nucleation in tin-based solder alloys.* Acta Mater. **58**, 3546 (2010). DOI:10.1016/j.actamat.2010.01.030 103, 105

[207] G. Kurtuldu, A. Sicco, and M. Rappaz, *Icosahedral quasicrystal-enhanced nucleation of the fcc phase in liquid gold alloys.* Acta Mater. **70**, 240 (2014). DOI:10.1016/j.actamat.2014.02.037 103, 104

[208] G. Kurtuldu and M. Rappaz, *Probability of twin boundary formation associated with the nucleation of equiaxed grains on icosahedral quasicrystal templates.* IOP Conf. Ser. Mat. Sci. Eng. **84**, 012012 (2015). DOI:10.1088/1757-899X/84/1/012012 103

[209] S. Henry, M. Rappaz, and P. Jarry, ⟨110⟩ *dendrite growth in aluminum feathery grains.* Metall. Mat. Trans. A **29**, 2807 (1998). DOI:10.1007/s11661-998-0321-9 104

[210] M. A. Salgado-Ordorica and M. Rappaz, *Twinned dendrite growth in binary aluminum alloys.* Acta Mater. **56**, 5708 (2008). DOI:10.1016/j.actamat.2008.07.046

[211] G. Kurtuldu, P. Jarry, and M. Rappaz, *Influence of Cr on the nucleation of primary Al and formation of twinned dendrites in Al-Zn-Cr alloys: Can icosahedral solid clusters play a role?* Acta Mater. **61**, 7098 (2013). DOI:10.1016/j.actamat.2013.07.056 104

[212] L. Yang, S. Li, Y. Li, K. Fan, and H. Zhong, *Study of growth advantage of twinned dendrites in aluminum alloys during Bridgman solidification.* J. Mat. Res. **34**, 240 (2019). DOI:10.1557/jmr.2018.344 104

[213] M. A. Salgado-Ordorica, A. B. Phillion, and M. Rappaz, *Morphology and Growth Kinetic Advantage of Quenched Twinned Dendrites in Al-Zn Alloys.* Metall. Mat. Trans. A **44**, 2699 (2013). DOI:10.1007/s11661-012-1539-0 104

[214] T. Niersbach, M. Kolbe, M. Becker, and F. Kargl, *Twinned dendrites in CrB-structured intermetallic NiGd.* IOP Conf. Ser.: Mater. Sci. Eng. (2022). Accepted. 105

[215] J. He, S. Zhao, Z. Wei, and U. Bismayer, *Mesoscale twinning in shells of Pinctada martensii.* Z. Krist. **231**, 673 (2016). DOI:10.1515/zkri-2016-1989 105

[216] O. Teppo and P. Taskinen, *Thermodynamic assessment of Ni-B phase diagram.* Mat. Sci. Tech. **9**, 205 (1993). DOI:10.1179/mst.1993.9.3.205 107

[217] W.-H. Sun, Y. Du, Y. Kong, H.-H. Xu, W. Xiong, and S.-H. Liu, *Reassessment of the Ni-B system supported by key experiments and first-principles calculation.* Int. J. Mat. Res. **100**, 59 (2009). DOI:10.3139/146.101786 107, XXV

[218] J. K. Stalick and R. M. Waterstrat, *Crystal Structures and Phase Equilibria in the Hafnium-Palladium System.* J. Ph. Eq. Diff. **37**, 416 (2016). DOI:10.1007/s11669-016-0469-8 112, 128, XXVI

[219] H. Okamoto, *Pd-Zr (Palladium-Zirconium).* J. Ph. Eq. Diff. **30**, 413 (2009). DOI:10.1007/s11669-009-9542-x 113, XXVI

[220] C. Guo, Z. Du, and C. Li, *Thermodynamic modeling of the Pd-Zr system.* Calphad. **30**, 482 (2006). DOI:10.1016/j.calphad.2006.05.005 113, 128

[221] E. Bouzy, G. L. Caer, and E. Bauer-Grosse, *Pseudo-tenfold twins in a new metastable chromium carbide and associated growth morphologies.* Phil. Mag. Let. **64**, 1 (1991). DOI:10.1080/09500839108214659 114

[222] J. L. Murray, A. J. McAlister, and D. J. Kahan, *The Al-Hf (aluminum-hafnium) system.* J. Ph. Eq. **19**, 376 (1998). DOI:10.1361/105497198770342111 115

[223] H. Okamoto, *Al-Y (Aluminium-Yttrium).* J. Ph. Eq. **29**, 114 (2008). DOI:10.1007/s11669-007-9226-3 116, XXVII

[224] H. Okamoto, *The Si-Zr (Silicon-Zirconium) system.* Bull. Al. Ph. Diagr. **11**, 513 (1990). DOI:10.1007/BF02898272 117, XXVII

[225] P. Nash, H. Choo, and R. B. Schwarz, *Thermodynamic Calculation of Phase Equilibria in the Ti-Co and Ni-Sn Systems.* J. Mat. Sci. **33**, 4929 (1998). DOI:10.1023/A:1004478101233 128

[226] X. J. Liu, H. H. Zhang, C. P. Wang, and K. Ishida, *Experimental determination and thermodynamic assessment of the phase diagram in the Co-Zr system.* J. Al. Comp. **482**, 99 (2009). DOI:10.1016/j.jallcom.2009.04.032 128

[227] M. Jiang, K. Oikawa, T. Ikeshoji, L. Wulff, and K. Ishida, *Thermodynamic calculations of Fe-Zr and Fe-Zr-C systems.* J. Ph. Eq. **22**, 406 (2001). DOI:10.1361/105497101770332965 128, XXIX

[228] H. Okamoto, *Au-Gd (Gold-Gadolinium).* J. Ph. Eq. Diff. **29**, 285 (2008). DOI:10.1007/s11669-008-9300-5 128, XXIX

[229] J. E. Garay, U. Anselmi-Tamburini, and Z. A. Munir, *Enhanced growth of intermetallic phases in the Ni–Ti system by current effects.* Acta Mater. **51**, 4487 (2003). DOI:10.1016/S1359-6454(03)00284-2 128

[230] V. G. Ivanchenko and T. A. Kosorukova, *Phase equilibria in the ZrCo-ZrNi-Zr_2Ni-Zr_2Co partial system.* Chem. Met. Al. **1**, 73 (2008). DOI:10.30970/cma1.0005 129

[231] M. J. Mehl, D. Hicks, C. Toher, O. Levy, R. M. Hanson, G. Hart, and S. Curtarolo, *The AFLOW Library of Crystallographic Prototypes: Part 1.* Comp. Mat. Sci. **136**, S1 (2017). DOI:10.1016/j.commatsci.2017.01.017 XIX, XX

[232] S. Weber, *WinWulff software*. https://www.jcrystal.com/products/winwulff . (19.04.22) XXI

[233] H. Okamoto, *Ni-Zr (Nickel-Zirconium).* J. Ph. Eq. **28**, 409 (2007). DOI:10.1007/s11669-007-9120-z XXIV

[234] P. Nash and C. S. Jayanth, *The Ni-Zr (Nickel-Zirconium) system.* Bull. Al. Ph. Diagr. **5**, 144 (1984). DOI:10.1007/BF02868950 XXIV

[235] G. Xu, Y. W. Cui, H. Fei, L. Zhang, F. Zhang, L. Liu, and Z. Jin, *Phase equilibria in the Gd-Ni binary and Mg-Ni-Gd ternary systems.* Int. J. Mat. Res. **103**, 1179 (2012). DOI:10.3139/146.110756 XXV

[236] H. Okamoto, *Co-Zr (Cobalt-Zirconium).* J. Ph. Eq. **32**, 169 (2011). DOI:10.1007/s11669-010-9838-x XXVIII

[237] O. L. Semenova, V. M. Petyukh, and O. S. Fomichev, *The Quasibinary ZrCo-ZrNi Phase Diagram.* Powder Metall. Met. Ceram. **56**, 210 (2017). DOI:10.1007/s11106-017-9888-2 XXVIII

[238] H. Okamoto, *Fe-Zr (Iron-Zirconium).* J. Ph. Eq. **14**, 652 (1993). DOI:10.1007/BF02669163 XXIX

[239] M. Bououdina, B. Lambert-Andron, B. Ouladdiaf, S. Pairis, and D. Fruchart, *Structural investigations by neutron diffraction of equi-atomic Zr–Ti(V)–Ni(Co) compounds and their related hydrides.* J. Al. Comp. **356-357**, 54 (2003). DOI:10.1016/S0925-8388(03)00166-X XXX

Appendix

1 Crystallographic structures

CsCl (B2) Structure:

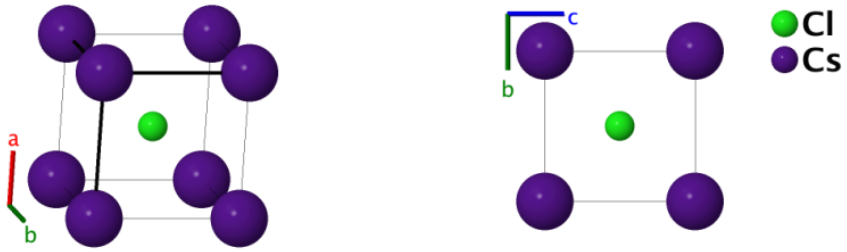

Prototype	:	CsCl
***Strukturbericht* designation**	:	B2
Pearson symbol	:	cP2
Space group number	:	221
Space group symbol	:	$Pm\bar{3}m$

Basis vectors:

		Lattice Coordinates		Cartesian Coordinates	Wyckoff Position	Atom Type
$\mathbf{B_1}$	=	$0\,\mathbf{a_1} + 0\,\mathbf{a_2} + 0\,\mathbf{a_3}$	=	$0\hat{\mathbf{x}} + 0\hat{\mathbf{y}} + 0\hat{\mathbf{z}}$	$(1a)$	Cs
$\mathbf{B_2}$	=	$\frac{1}{2}\,\mathbf{a_1} + \frac{1}{2}\,\mathbf{a_2} + \frac{1}{2}\,\mathbf{a_3}$	=	$\frac{1}{2}\,a\,\hat{\mathbf{x}} + \frac{1}{2}\,a\,\hat{\mathbf{y}} + \frac{1}{2}\,a\,\hat{\mathbf{z}}$	$(1b)$	Cl

The different parameters and classifications of the B2 phase were adopted from [231].

CrB (B33) Structure:

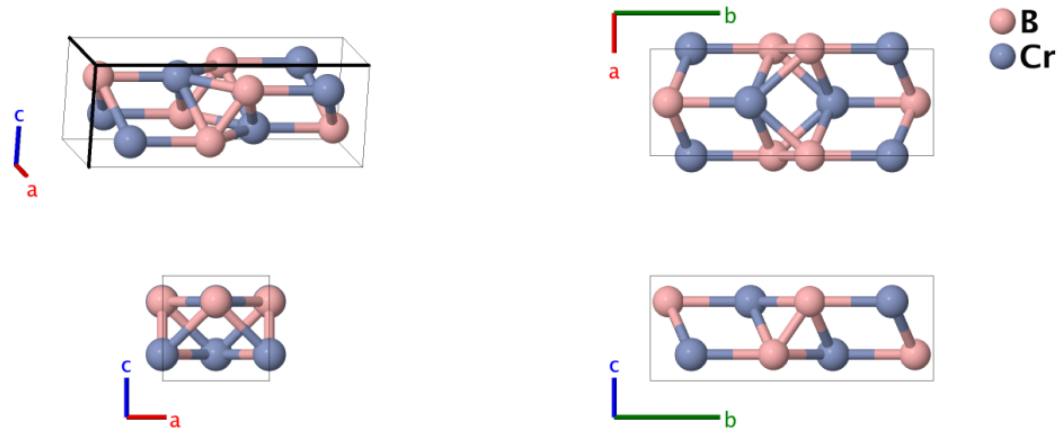

Prototype	:	CrB
***Strukturbericht* designation**	:	B33
Pearson symbol	:	oC8
Space group number	:	63
Space group symbol	:	Cmcm

Basis vectors:

		Lattice Coordinates		Cartesian Coordinates	Wyckoff Position	Atom Type
$\mathbf{B_1}$	=	$-y_1\,\mathbf{a_1} + y_1\,\mathbf{a_2} + \frac{1}{4}\,\mathbf{a_3}$	=	$y_1\,b\,\hat{\mathbf{y}} + \frac{1}{4}\,c\hat{\mathbf{z}}$	$(4c)$	B
$\mathbf{B_2}$	=	$y_1\,\mathbf{a_1} - y_1\,\mathbf{a_2} + \frac{3}{4}\,\mathbf{a_3}$	=	$-y_1\,b\,\hat{\mathbf{y}} + \frac{3}{4}\,c\hat{\mathbf{z}}$	$(4c)$	B
$\mathbf{B_3}$	=	$-y_2\,\mathbf{a_1} + y_2\,\mathbf{a_2} + \frac{1}{4}\,\mathbf{a_3}$	=	$y_2\,b\,\hat{\mathbf{y}} + \frac{1}{4}\,c\hat{\mathbf{z}}$	$(4c)$	Cr
$\mathbf{B_4}$	=	$y_2\,\mathbf{a_1} - y_2\,\mathbf{a_2} + \frac{3}{4}\,\mathbf{a_3}$	=	$-y_2\,b\,\hat{\mathbf{y}} + \frac{3}{4}\,c\hat{\mathbf{z}}$	$(4c)$	Cr

The different parameters and classifications of the B33 phase were adopted from [231].

2 Stereographic projections of $Ni_{50}Zr_{50}$ and $Ni_{50}Gd_{50}$

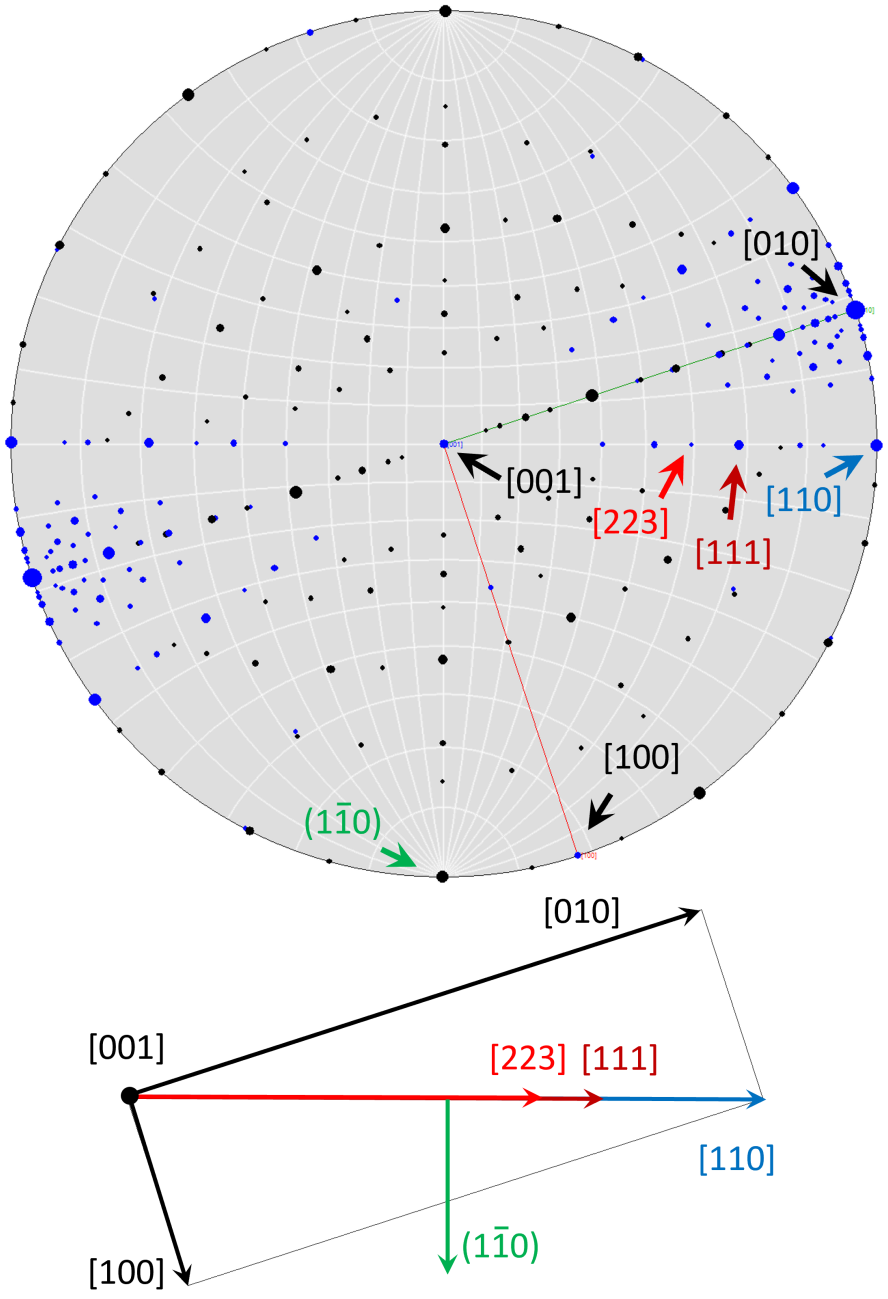

Fig. 1: Visualization of several directions (blue dots) and plane normals (black dots) of the NiZr orthorhombic unit cell (CrB, B33) in a stereographic projection with Wulff net. Important directions are highlighted to show, that $\langle 110 \rangle$ and $\langle 111 \rangle$ directions both follow along the $\{110\}$ planes. The $(1\bar{1}0)$ plane is represented by its normal. Projection plotted with *WinWulff* [232].

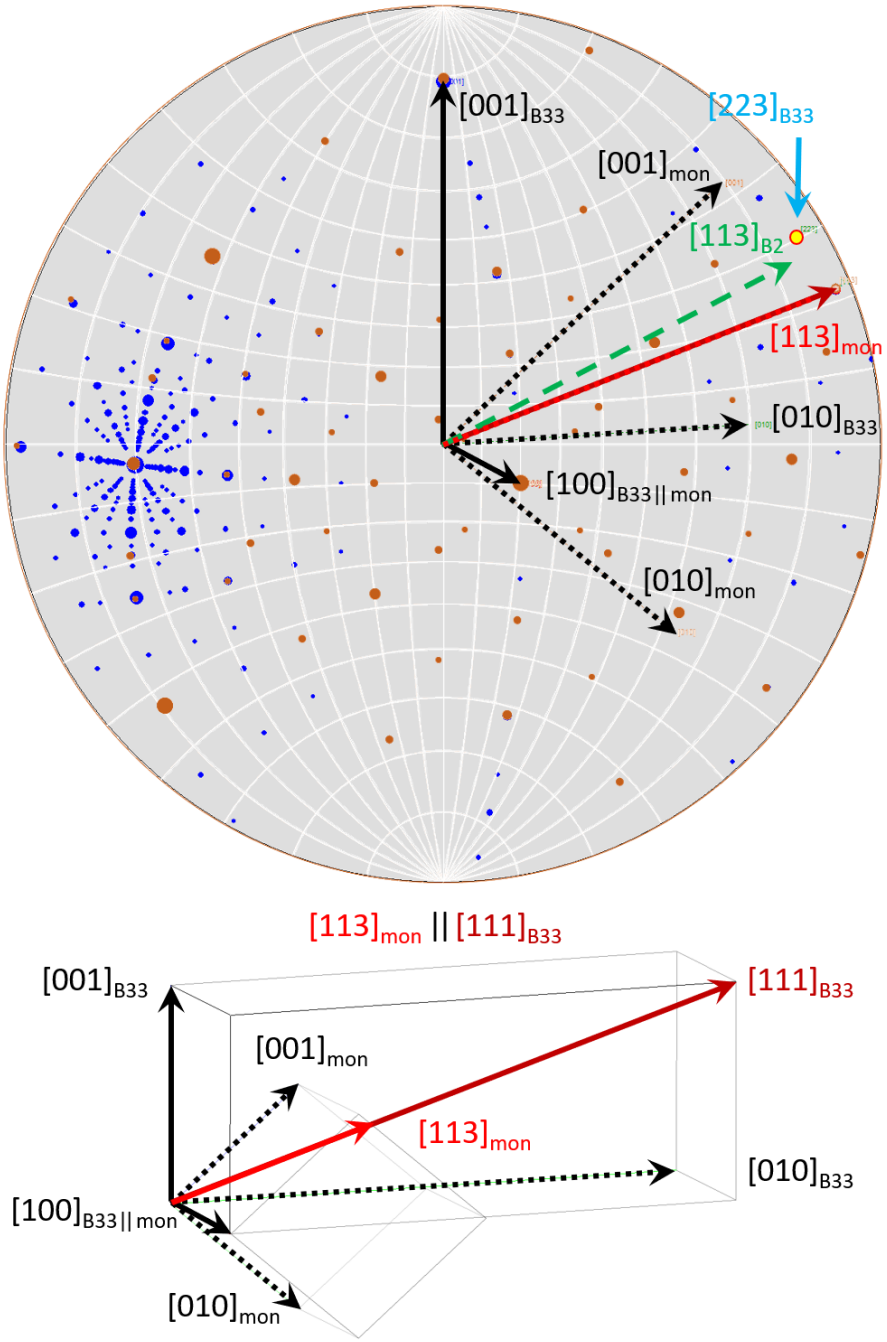

Fig. 2: Overlay of the stereographic projections for the orthorhombic NiZr unit cell (blue dots) and the monoclinic cell (symmetry element) (orange dots), based on the former cubic cell within the orthorhombic lattice. Different directions are highlighted to show the position of the monoclinic cell element in the orthorhombic lattice and the position of equal directions. Additionally, the $[113]_{B2}$ direction and the $[223]_{B33}$ are highlight and are remarkably close.

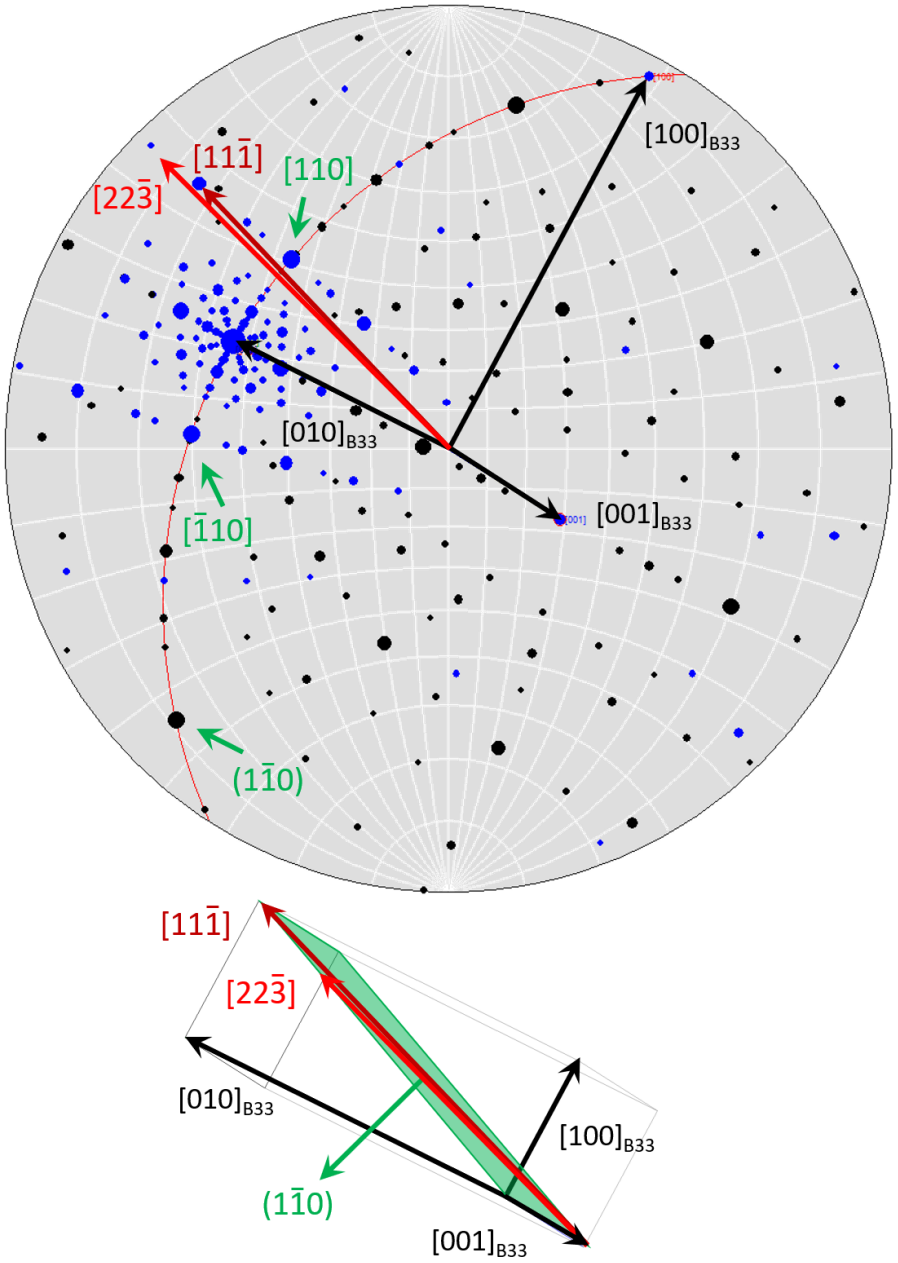

Fig. 3: Stereographic projection of the green (upper) part of the twinned NiGd dendrite in Fig. 5.25. The secondary dendrite direction (red) runs along the $(1\bar{1}0)$ plane of the unit cell and almost perfectly perpendicular to the point of view.

3 Phase diagrams

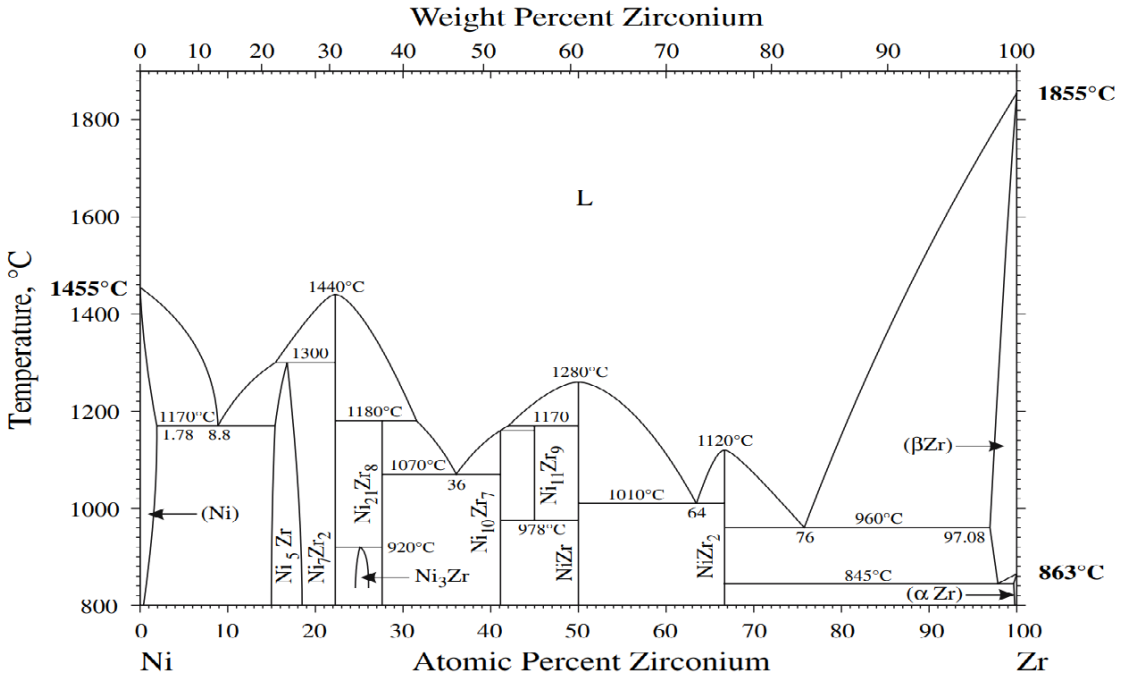

Fig. 1: Binary Ni-Zr phase diagram [233]. Note that the liquidus temperature line is drawn correctly from [234], but the indicated temperature of the NiZr phase was misread. It should state 1260 °C

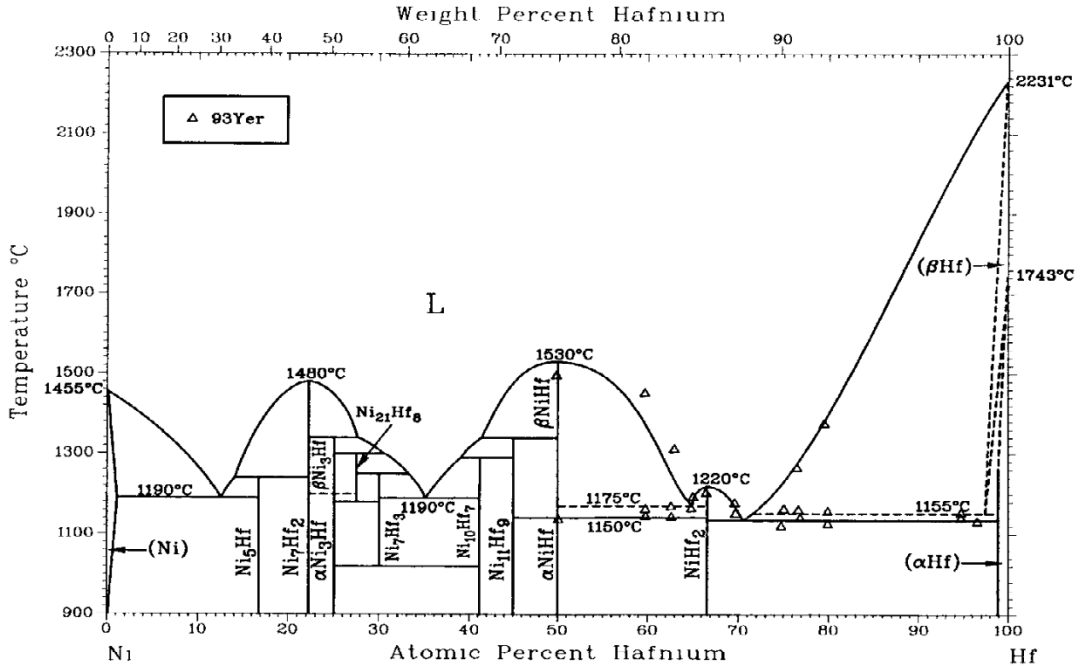

Fig. 2: The binary Ni-Hf phase diagram [187].

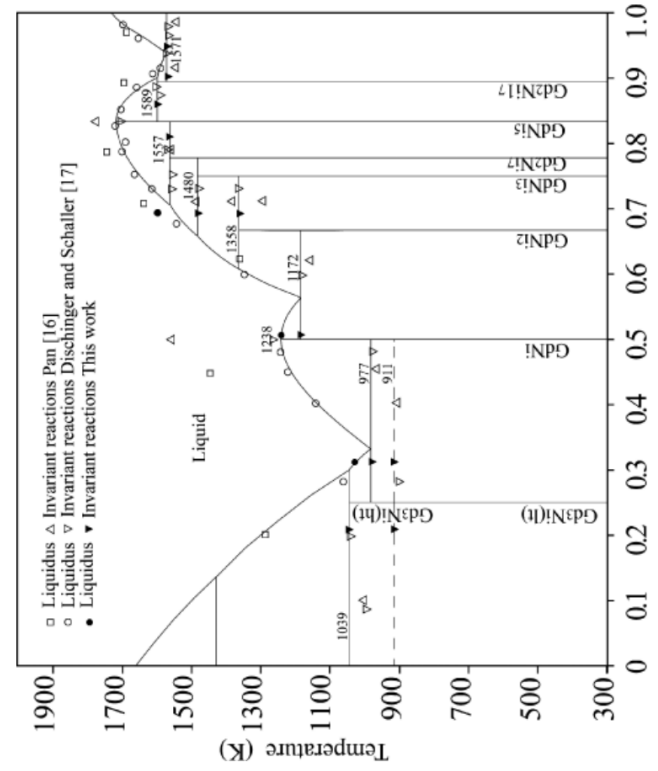

Fig. 4: The binary Ni-Gd diagram, adopted from [235]. It shows NiGd as a line component stable over the whole range up to the $T_L = 1238\,\mathrm{K}$.

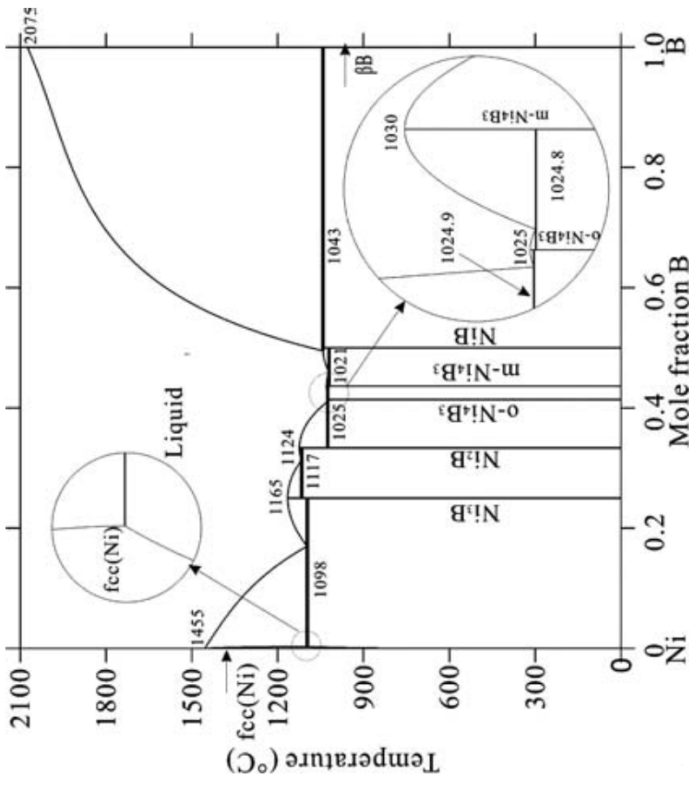

Fig. 3: The binary Ni-B phase diagram, from [217]. Incongruently melting NiB is drawn as a line component and lies beneath a peritectic line. It is stable from RT to 1316 K.

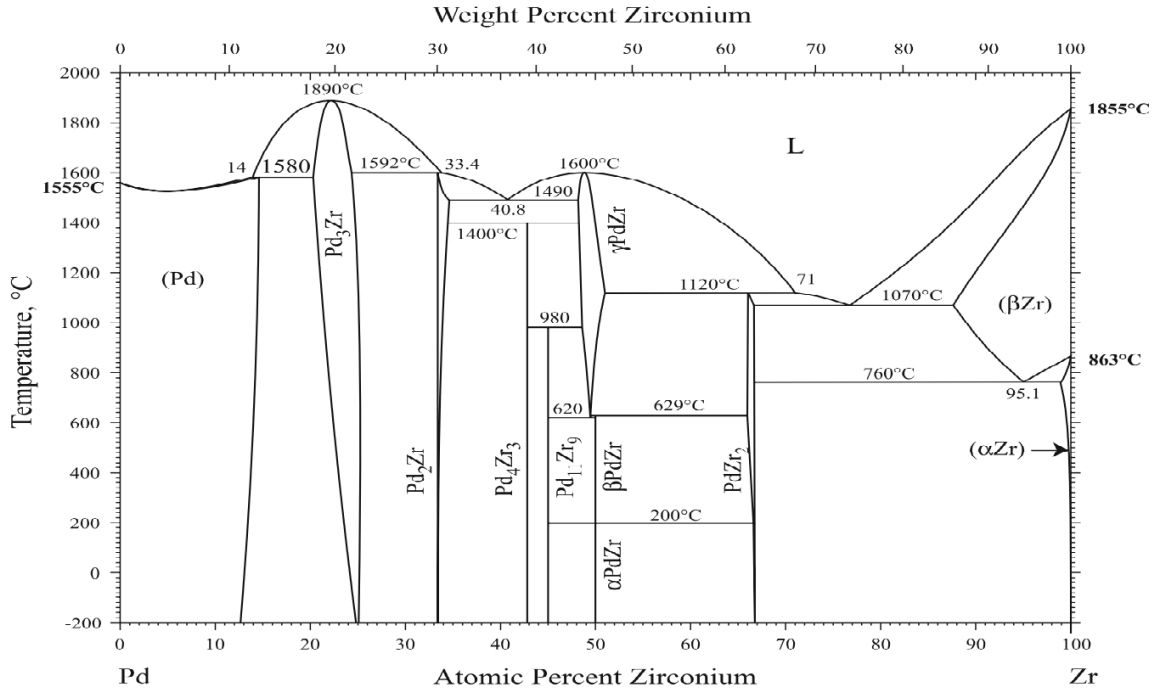

Fig. 5: Binary Pd-Zr phase diagram [219]. B33 structured β-PdZr is not stable above 902 K. Below 473 K it transitions into a monoclinic α-PdZr.

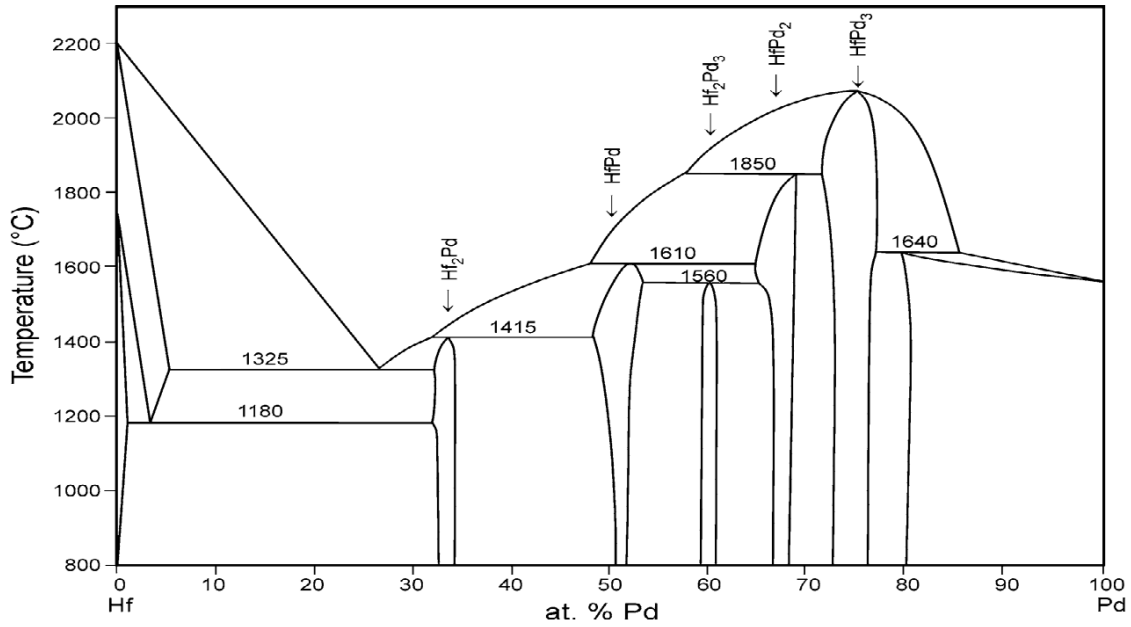

Fig. 6: Binary phase diagram of Pd-Hf [218]. The incongruently melting PdHf phase is formed by a peritectic reaction.

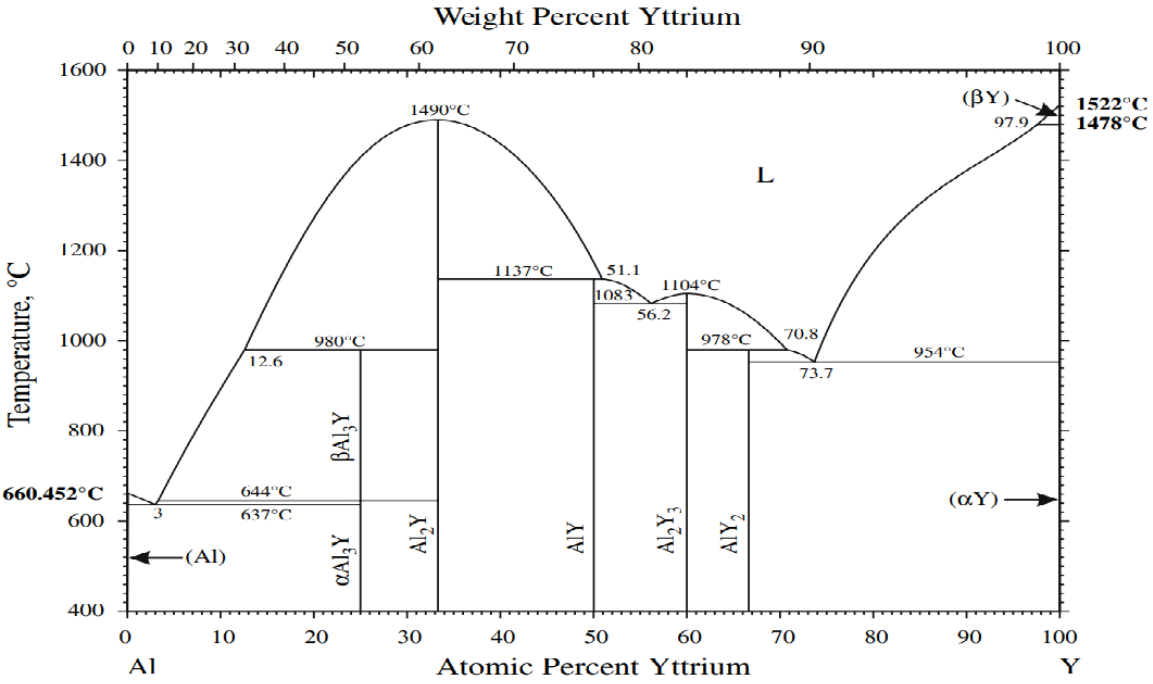

Fig. 7: The binary Al-Y phase diagram [223]. AlY is incongruently melting and formed by a peritectic reaction.

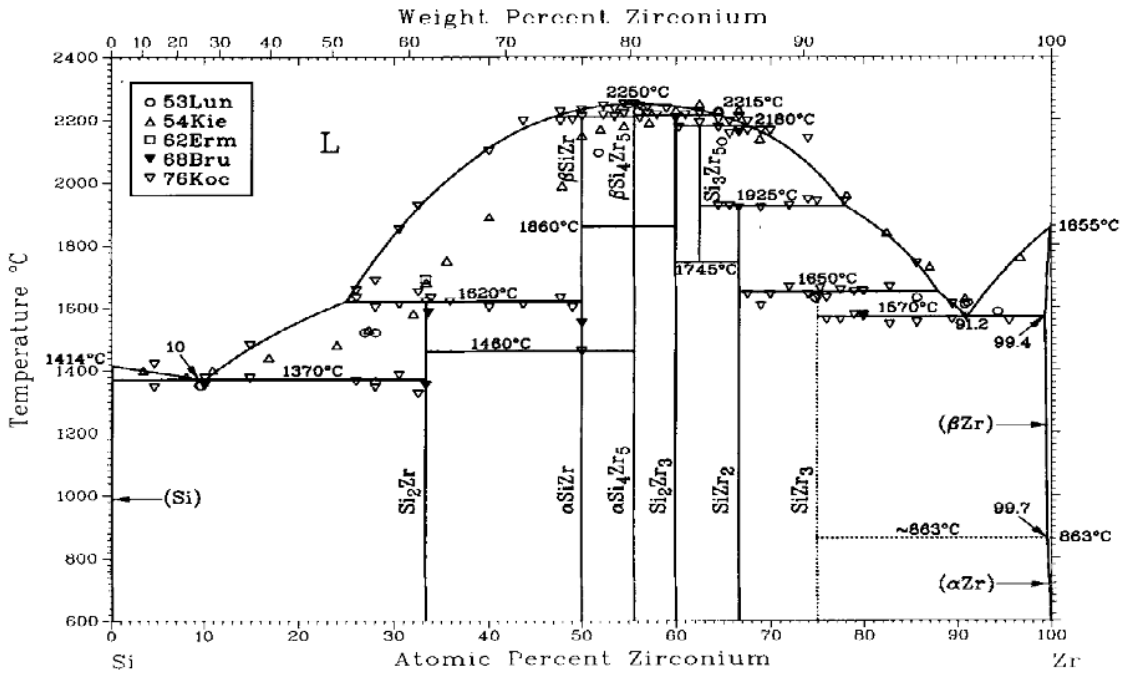

Fig. 8: Binary Si-Zr phase diagram [224].

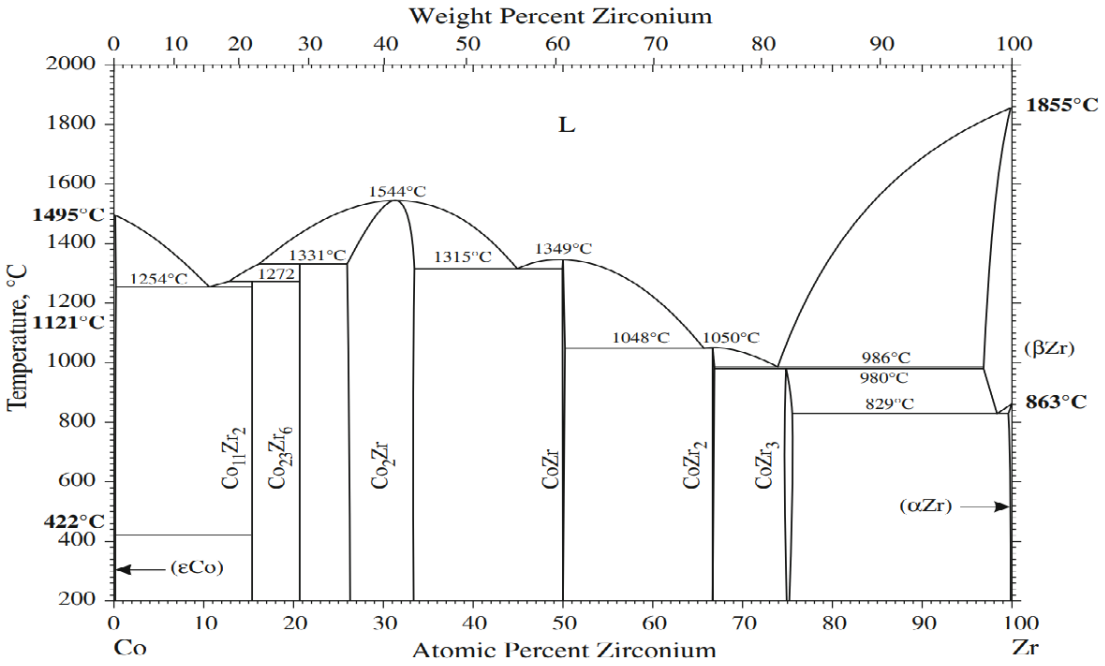

Fig. 9: Binary phase diagram of Co-Zr [236]. CoZr is a congruently melting line phase.

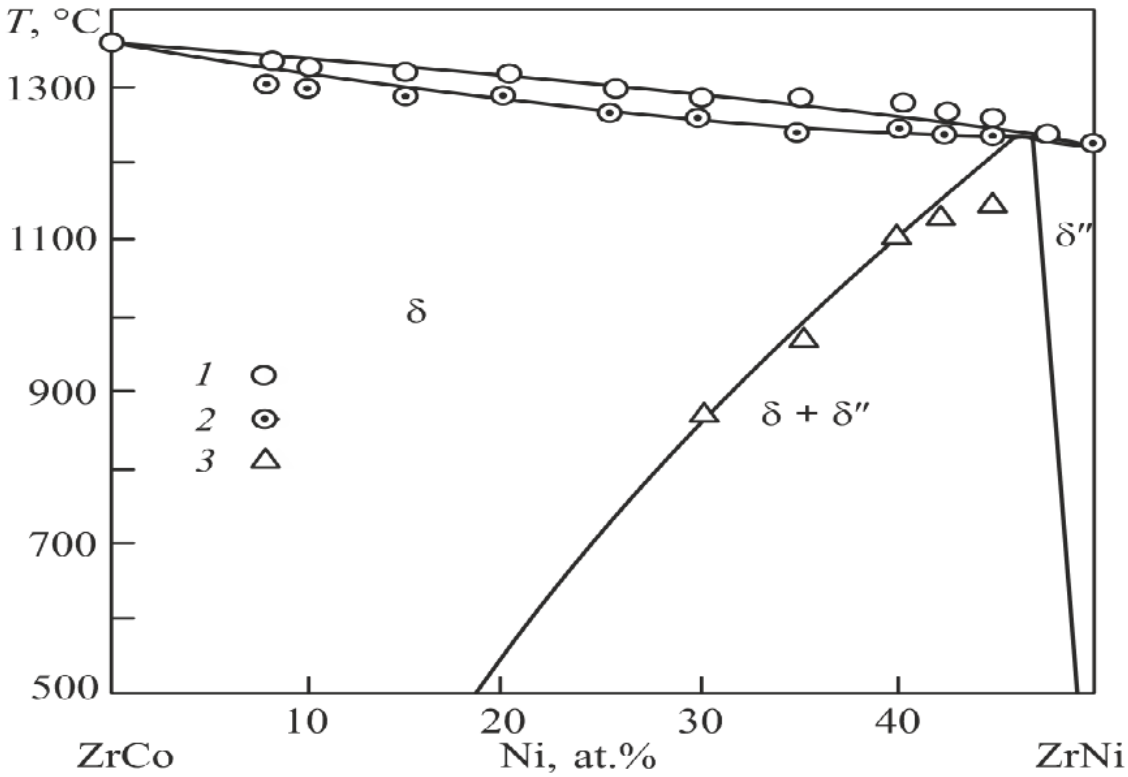

Fig. 10: Quasi-binary NiZr-CoZr phase diagram [237].

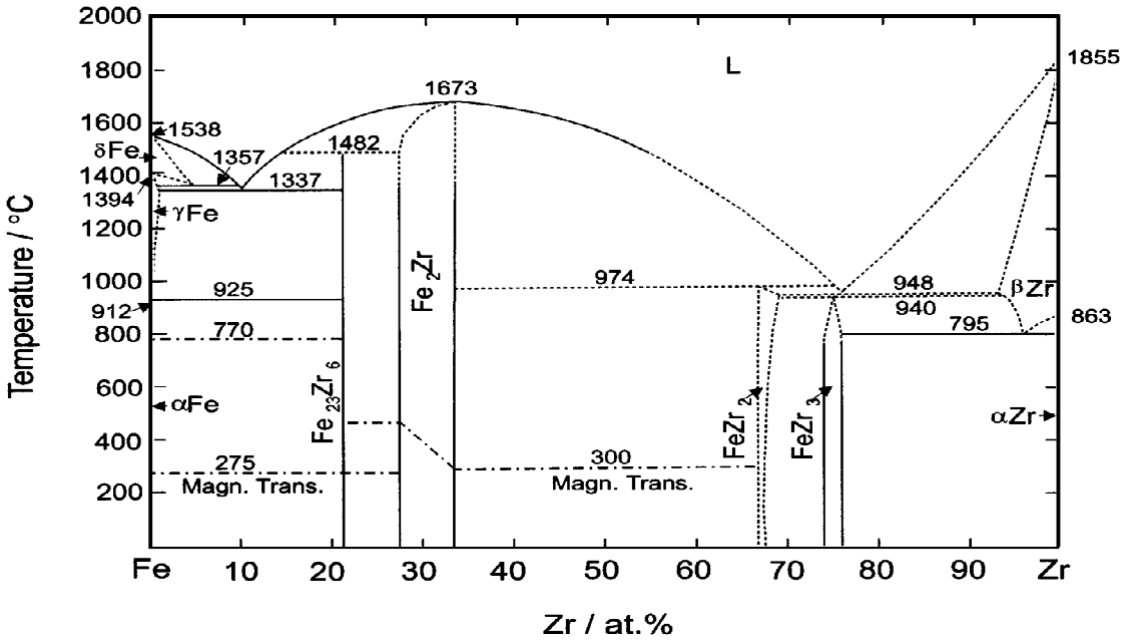

Fig. 11: Binary Fe-Zr phase diagram [227, 238].

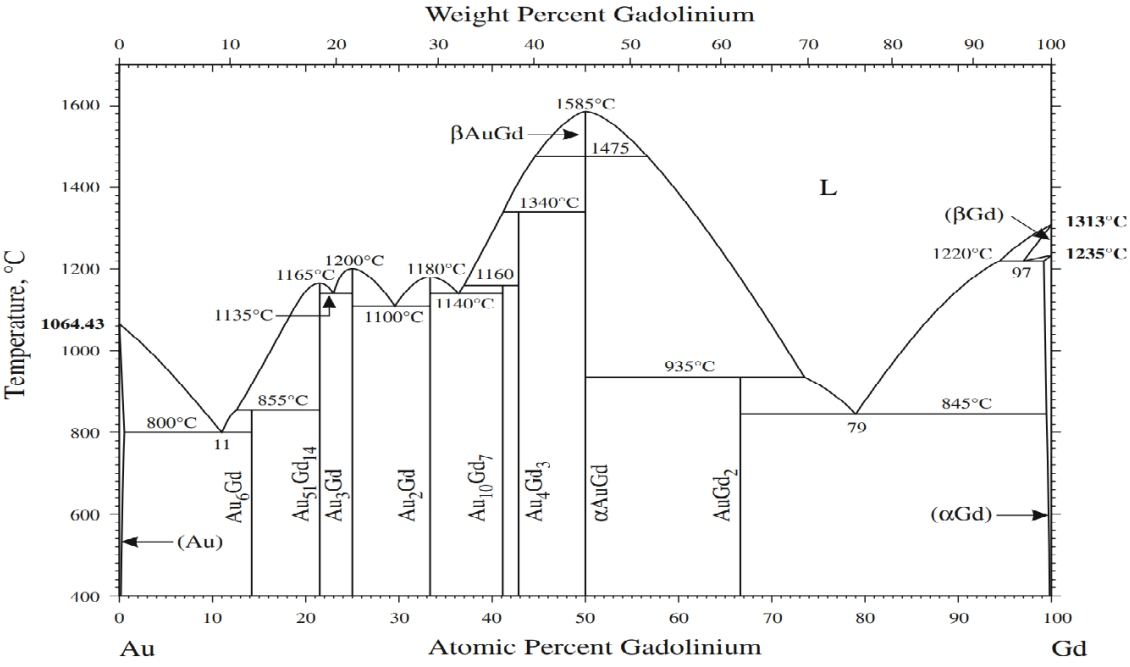

Fig. 12: The binary Au-Gd phase diagram [228]. B33 structured α-AuGd is stable below 1475° C.

4 Diffraction patterns of the B2 and the B33 phase

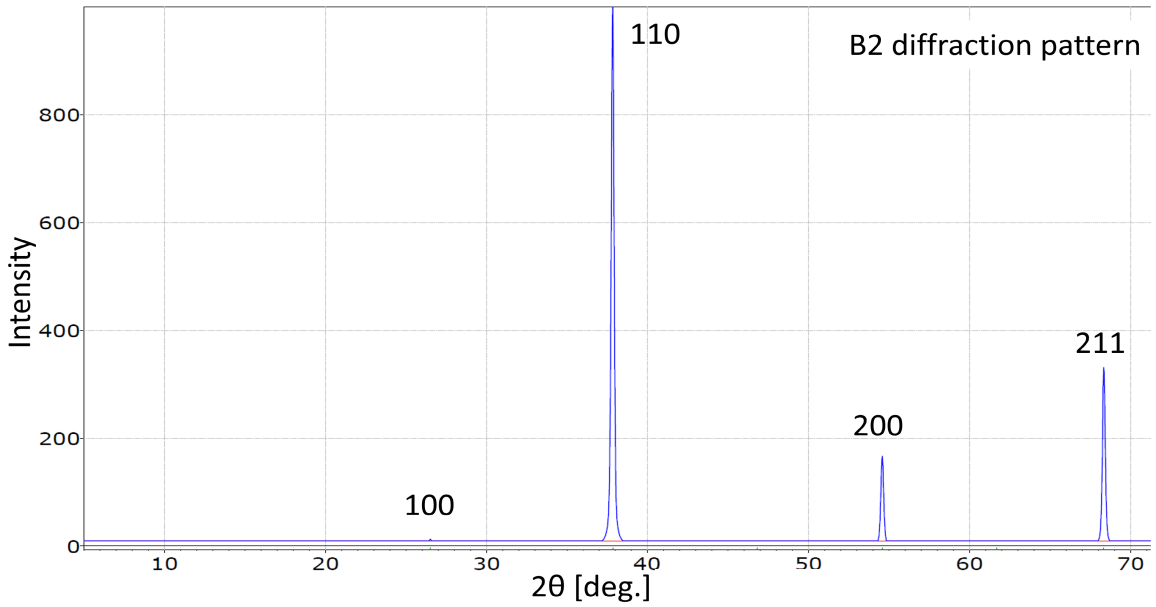

Fig. 1: Calculated diffraction pattern for the B2 phase, based on the PdZr system [176]. The data was collected at a temperature of 1073 K and with $\lambda = 0.154$ nm.

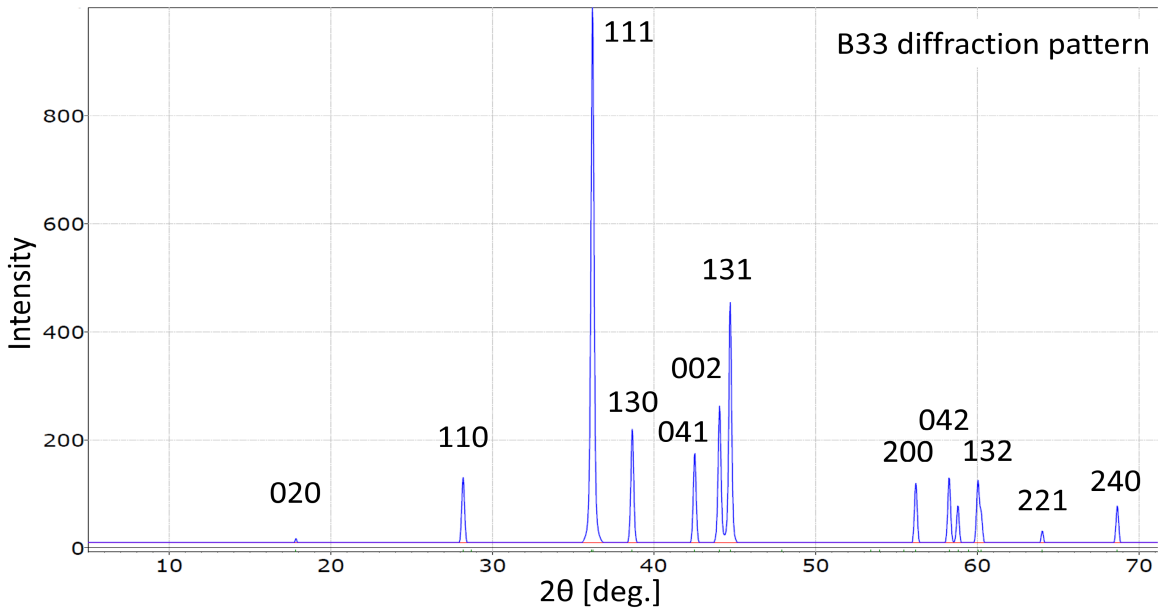

Fig. 2: Calculated diffraction pattern for the B2 phase, based on the NiZr system [239]. The data was collected with $\lambda = 0.154$ nm.

5 Analysis of the CoZr system

This section shows mentioned figures, necessary to understand the behavior of CoZr solidification, that were obtained during my master thesis [149].

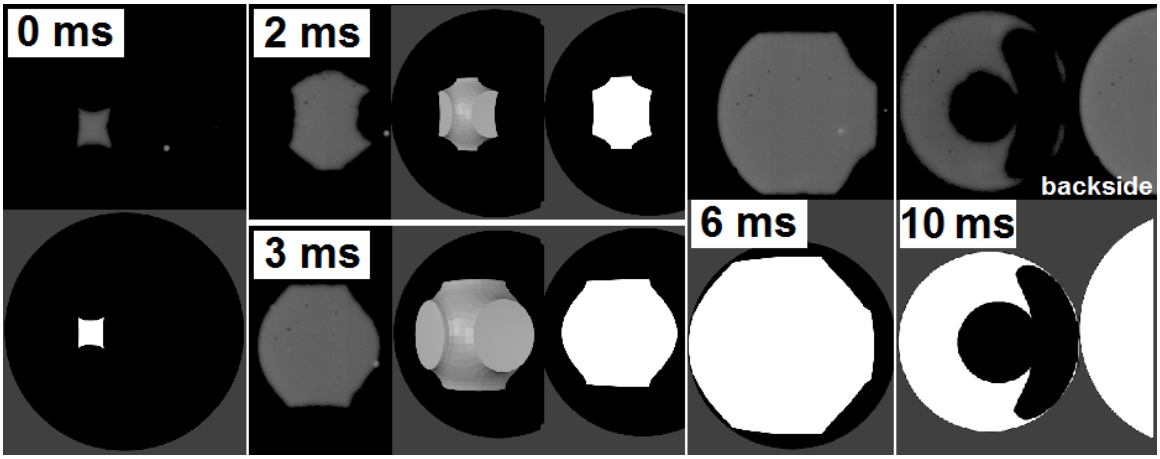

Fig. 1: Series of consecutive heat front steps and their respective simulation. The shapes could be reproduced in simulation by using the body shape shown in Fig. 6.2.

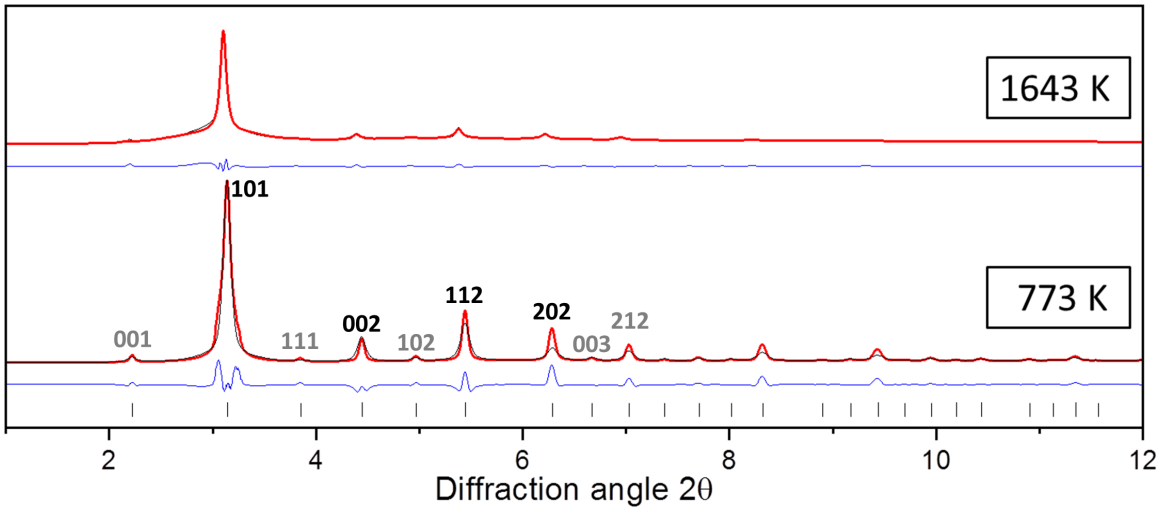

Fig. 2: Results of scattering experiments during levitation in CoZr. The upper pattern was obtained right after the recalescence. The X-ray pulses are shot every 0.5 s. Both patterns show the B2 phase characteristics.

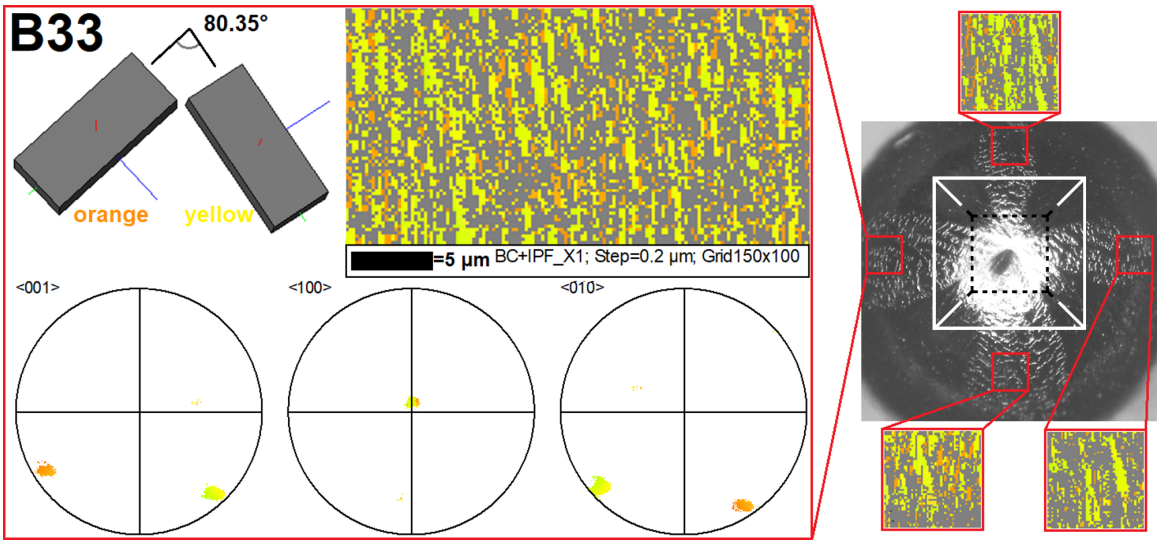

Fig. 3: EBSD image and corresponding pole figures of a CoZr sample. The structure visible on the surface is a remnant of the solidified B2 phase. The relation between both phases is shown, as only two differently orientated B33 grains can be found in the whole sample.

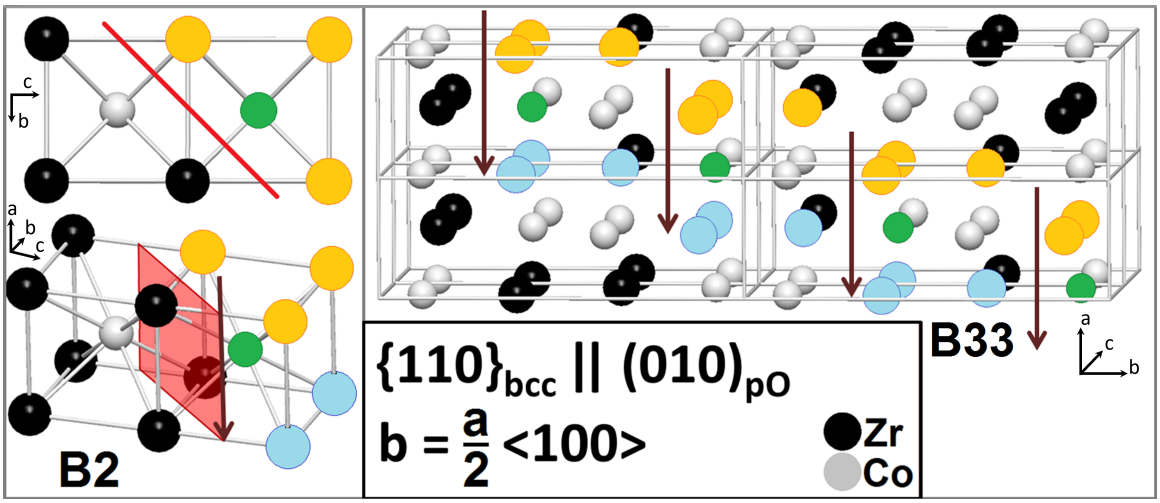

Fig. 4: The transition from B2 into B33 phase. The glide plane slide is depicted with a red arrow. Some atoms are colored to highlight the position of the B2 phase within the B33 lattice.

Publications

Publications that resulted from individual parts of this work are listed below.

- T. Niersbach, M. Kolbe, M. Becker and F. Kargl, *Twinned dendrites in CrB-structured intermetallic NiGd*. (2022) IOP Conf. Ser.: Mat. Sci. Eng. Accepted
- T. Niersbach, M. Kolbe and F. Kargl *Nucleation modes in the Ni(Zr, Hf) systems, in relation to the B2→B33 solid phase transition*. In preparation.

Acknowledgements

This work was only possible thanks to the contributions and support of colleagues, friends and family.

At first, I thank Prof. Florian Kargl for offering me to work out a PhD thesis on this interesting topic and Prof. Bührig-Polaczek, head of the Foundry Institute, to be the referee for this work at the RWTH Aachen University.

I would like to thank Prof. Andreas Meyer, and his successor Prof. Daniela Zander, for the opportunity to work at the Institute for Materials Physics in Space at the German Aerospace Center in Cologne.

I am particularly grateful to Dr. Matthias Kolbe for his supervision and support, endless discussions and deep knowledge regarding the electron microscopes and microstructure analysis. This work would not have been possible without your ongoing interest in this particular topic and the interpretation of our results. Working with you has always promoted my motivation and the drive for knowledge.

Special thanks go to Dr. Raphael Kobold, who oversaw the work as mentor, provided useful insight in his work and helped to extend my field of view in his introduction to the topic and multiple of subsequent discussions.

Additionally, thanks go to my colleagues:

Dr. Fan Yang for countless discussions and explanations regarding levitation of several alloy systems in the ESL facility.

The TEMPUS crew for several flight campaigns, where samples of this work were processed, as well as the workshop team for their most valuable work.

Dr. Thomas Werner, Dr. Maike Becker, Ali Jafarizadeh, Toni Schiller, Johanna Wilden, Juliane Baumann, Tobias Aumüller, Tiberius Blumberg, Dr. Mitja Beckers, Dr. Nuria Navarrete Argilés, Dr. Dirk Breuer, and all colleagues and former fellows from the institute, whose knowledge and social input have highly influenced my work, of course only in the best way.

Finally, i thank my family, friends and of course Julia Niersbach for their patience, emotional support and encouragement over these years.